

Kaspar Lasn

# EVALUATION OF STIFFNESS AND DAMAGE OF LAMINAR COMPOSITES

Thesis for the degree of Philosophiae Doctor

Trondheim, June 2015

Norwegian University of Science and Technology  
Faculty of Engineering Science and Technology  
Department of Engineering Design and Materials



**NTNU – Trondheim**  
Norwegian University of  
Science and Technology

**NTNU**

Norwegian University of Science and Technology

Thesis for the degree of Philosophiae Doctor

Faculty of Engineering Science and Technology  
Department of Engineering Design and Materials

© Kaspar Lasn

isbn: 978-82-326-0978-9 (print)  
isbn: 978-82-326-0979-6 (digital)  
issn:1503-8181

Doctoral theses at NTNU, 2015:161

Printed by NTNU Grafisk senter

THESIS ON CIVIL ENGINEERING F53

**Evaluation of Stiffness and  
Damage of Laminar Composites**

KASPAR LASN



EHITUS F53

**Komposiitlaminaatide jäikuse ja  
kahjustuste hindamine**

KASPAR LASN



## **Preface**

This Doctoral Thesis has been submitted to Tallinn University of Technology (TUT) and Norwegian University of Science and Technology (NTNU) simultaneously for the degree of PhD. The co-operation of two institutions in respect of the doctoral degree training has been outlined in the Cotutelle Agreement.

The research was conducted in Department of Mechanics, Faculty of Civil Engineering, TUT from 2008 to 2012 under the supervision of prof. Aleksander Klauson.

The spring semester of 2011 was spent in NTNU as an exchange PhD student. Thereafter, the research was conducted in Department of Engineering Design and Materials, Faculty of Engineering Science and Technology, NTNU from 2012 to 2015 under the supervision of prof. Andreas T. Echtermeyer.

The disputation is held on June 4<sup>th</sup>, 2015 at NTNU.

## Acknowledgements

The two most influential people for my research activities have been prof. Aleksander Klauson from Tallinn University of Technology (TUT) and prof. Andreas Echtermeyer from Norwegian University of Science and Technology (NTNU). I consider myself very fortunate for having two supervisors, whose advice often reflected two distinctly different viewpoints on the research topic. I would like to thank them both for time, guidance and solid support throughout this research.

The work for this PhD project has taken place in three European countries. In addition to aforementioned universities, some experimental measurements were also conducted in Laboratoire Ondes et Milieux Complexes (LOMC) in Le Havre, France. Professors Farid Chati and Dominique Décultot have been very kind to help conducting ultrasonic measurements; their contribution is noted in the Thesis and very much appreciated. When first starting out with practical work with laminates, the help and tips from Dr. Anthonippillai Antonarulajah and Stanislav Shchebetov, then working at NTNU, were very important and time saving. Finally, the Norwegian translation of the Abstract would be quite different (i.e. barely readable) without the linguistic help from assoc. prof. Nils Petter Vedvik, Jahn Peter Storvold and Julian Sauterleute.

I would like to thank my colleagues from TUT, NTNU and LOMC, especially those who engaged me in scientific discussions. On the whole, I would like to express my gratitude to all who have, wittingly or otherwise, helped to advance the work for this Thesis, including all teachers, professors and co-workers throughout the years.

Finally, I would like to thank my family. They have been the closest and strongest support, through all periods. My parents are my role models. My sister and brother have always been there with a good word or advice. Thank you!

Kaspar Lasn

Trondheim

March – May 2015



## **Abstract**

The elastic constants of laminated composites are required for modelling of structures or components made from these materials. The variability in manufacturing can result in different composite material properties than intended. Therefore, reliable properties are typically not just estimated, or known from experience, but measured directly from representative physical specimens. Today, the elastic characterization is still conducted by employing numerous quasi-static test methods, which require various test specimens and test set-ups, due to the inherent anisotropy of the material. Meanwhile, decades of research and development with advances in sensor technology and computing power have resulted in advanced characterization methods, e.g. based on vibration or Lamb wave propagation measurements. Several elastic constants can be measured from a single test. Application of these advanced methods makes composite elastic characterization both faster and cheaper.

This research has been conducted to compare how three independent methods can be applied for the evaluation of stiffness and damage of laminar composites. In the central part, the elastic constants of composite laminates are measured by quasi-static, natural frequency and Lamb wave propagation based methods. Then, the results from individual test methods are compared. The comparison yields good agreement for virgin laminates, but shows some discrepancies for laminates with fatigue damage.

Both static and vibration measurements of cross plied laminates provide the investigator with effective tensile or flexural stiffnesses of laminates. However, the basic building block to be characterized is a ply. Literature is scarce about systematic methods for the back-calculation of ply moduli from laminate stiffnesses. As a part of this work, a systematic approach was developed for the back-calculation of ply moduli for symmetric cross plied laminates. Both, the mean values and the coefficients of variation of moduli are evaluated, as shown by calculated examples. The input data for these calculations was obtained from quasi-static experiments.

## Sisukokkuvõte

Komposiitlaminaatide elastsusomaduste mõõtmine on vajalik, et modelleerida neist valmistatud konstruktsioonide või komponentide füüsikalist käitumist. Komposiitmaterjali valmistamiseks võib kasutada erinevaid tehnoloogiaid (näiteks vaakumlamineerimine, filamentmähkimine vms.) ja erinevaid kiud-vaik materjalisüsteeme. Arvestades, et materjal ja komponent valmivad komposiitmaterjali tahkenedes ühekorraga, tekkib erinevates oludes valmistatud materjalil mehaaniliste omaduste suhteliselt suur ebamäärasus. Komposiitmaterjali omadusi saab usaldusväärselt määrata üksnes neid otse katsekehadelt mõõtes. Komposiitide anisotroopse olemuse tõttu kasutatakse nende elastsus- ja tugevusomaduste määramiseks mitmeid purustavaid katsemeetodeid, rakendades selleks erineva kujuga katsekehi ning koormamisviise. Samas, viimaste aastakümnete jooksul toimunud kiire areng, muuhulgas mõõtesensorite ja arvutusvõimsuse kättesaadavuses, võimaldab materjali jäikusomaduste mõõtmiseks rakendada uudseid meetodeid. Sellised mõõtemetodid on tavaliselt kaudsed, põhinedes näiteks materjali omavõnkesageduste või Lamb'i laine levimise mõõtmisel. Ühe mõõtmisega saab korraga mitmeid materjali elastsuskonstante määrata. Uute mõõtemetodite rakendamine muudab komposiitmaterjalide omaduste määramise kiiremaks ja odavamaks.

Käesolev uurimistöö teostati, et võrrelda kolme sõltumatu mõõtemetodi rakendamisel leitud materjali jäikusomadusi. Mõõdeti nii väsimuskahjustustega kui ka ilma kahjustusteta komposiitlaminaate. Töö põhiosas kirjeldatakse elastsuskonstantide mõõtmist, kasutades selleks tavapärasel kvaasi-staatikal, madalatel omavõnkesagedustel ning ultrahelina leviva Lamb'i laine faasikiirustel põhinevaid mõõtmisviise. Töö lõpuosas võrreldakse tulemusi, mis on saadud kolme eelnimetatud meetodi eksperimentaalsel rakendamisel samale materjalile. Selgub, et sõltumatutel viisidel leitud elastsusomadused langevad hästi kokku, kui mõõta ilma kahjustusteta komposiite. Väsimuskahjustustega materjali mõõtmisel erinevad mõned eri viisidel leitud elastsusomadused juba oluliselt.

Kui ristkiulise laminaadi elastsusomadusi määratakse kvaasi-staatikal (tõmbekatse, paindekatse) või omavõnkesagedustel põhineva mõõtmisega, siis eksperimentaalseks tulemuseks on nn. efektiivne ehk keskmistatud laminaadi tõmbe- või paindejäikus. Samas, see laminaadi aluselement, mida mõõta soovitakse ja mis on modelleerimiseks huvipakkuv, on laminaadi üks ühesuunaline kiht. Kirjanduses on ebapiisavalt käsitletud teemaderingi, mis puudutab ühe kihi jäikuse tagasiarvutamist laminaadi jäikusest. Käesoleva uurimistöö esimeses peatükis pakutakse välja viisid, kuidas ühe kihi elastsusmooduleid saab tagasi arvutada sümmeetriliste laminaatide piki- ja paindejäikustest. Lisaks ühesuunalise kihi elastsusmoodulite keskvaärtustele on ristkiulise laminaadi puhul võimalik hinnata ka nende variatsioonikordajaid. Eksperimentidel põhinevatest näidisarvutustest leitud tulemused on oodatavas suurusjärgus.

## Sammendrag

De elastiske konstantene til komposittlaminat er nødvendig for modellering av strukturer og komponenter hvor slike laminaer inngår. Variasjoner i produksjon kan føre til egenskaper som avviker fra forventede egenskaper og pålitelige data må finnes ved direkte fysisk testing av representative prøver. Karakterisering av elastiske egenskaper foregår vanligvis ved ulike tradisjonelle kvasi-statiske metoder som for slike anisotrope strukturer vil kreve et større antall prøver og lasttilfeller. I den senere tiden har utviklingen av metoder, sensorteologi og datakraft resultert i avanserte karakteriseringsmetoder som for eksempel teknikker basert på vibrasjon eller Lamb-bølge forplantning. Ved å anvende slike metoder kan flere elastiske konstanter måles fra en enkelt prøve, noe som gir både tidsbesparelse og kostnadsreduksjon ved testing og karakterisering av kompositter.

Hovedformålet med avhandlingen var å sammenligne hvordan tre uavhengige metoder kan anvendes for å evaluere stivhet og skade i komposittlaminat. Elastiske konstanter for komposittlaminat er oppnådd med kvasi-statiske metoder, egenfrekvensanalyse og Lamb-bølgeforplantning, og resultatene fra disse metodene er sammenlignet. Det er funnet godt samsvar for laminaer uten skade mens det for laminaer med utmattingsskade ble observert avvikende resultater.

Statiske målinger og vibrasjonsmålinger av  $[0/90]$  laminat gir prinsipielt kun effektive elastiske egenskaper, mens det ofte vil være egenskaper til enkel-lag som er av interesse. Litteraturen gir lite informasjon om systematiske metoder for å regne tilbake, fra laminat til enkelt lag. Dette arbeidet har i vesentlig grad derfor lagt vekt på å utvikle en systematisk tilnærming til denne problemstillingen for symmetriske  $[0/90]$  laminat. Eksempler basert på eksperimenter viser at både gjennomsnittsverdi og variasjonskoeffisient kan evalueres.

## List of publications

This Section lists publications which have so far resulted from the work on the PhD project. The Thesis has been written as a self-sufficient monograph. All publications present the material and/or methods which are also treated in this monograph. The papers have not been added as appendices in order to avoid repetition and due to different structure the material is presented. To facilitate comprehension, the Chapters of the monograph which relate to different journal papers were added as comments in [square brackets].

### Peer-reviewed publications in international journals

- Lasn, K.; Echtermeyer, A. T.; Klauson, A.; Chati, F.; Décultot, D. An experimental study on the effects of matrix cracking to the stiffness of glass/epoxy cross plied laminates. *Composites Part B: Engineering* (subm. with a minor revision, May 2015). [Chapter 5, Appendix G]
- Lasn, K.; Echtermeyer, A. T.; Klauson, A.; Chati, F.; Décultot, D. (2015). Comparison of laminate stiffness as measured by three experimental methods. *Polymer Testing*, 44, 143-152. [Chapter 2, Chapter 3, Chapter 4, Appendix G]
- Lasn, K.; Klauson, A.; Echtermeyer, A. T. (2015). Back-calculation of ply elastic moduli for cross-ply laminates. *Mechanics of Composite Materials*, 51(1), 55-68. [Chapter 2, Appendix D, Appendix G]
- Lasn, K.; Klauson, A.; Chati, F.; Décultot, D. (2011). Experimental determination of elastic constants of an orthotropic composite plate by using Lamb waves. *Mechanics of Composite Materials*, 47(4), 435-446. [Chapter 4, Appendix G]

### Presentations at international conferences

- Lasn, K.; Klauson, A. (2011). Non-destructive identification of elastic constants by vibration measurements and optimization. In: *OAS 2011: International Conference on Optimization and Analysis of Structures*, August 25-27, Tartu, Estonia. (Eds.)E. Puman, J. Lellep., 2011.
- Lasn, K.; Klauson, A.; Chati, F.; Décultot, D. (2011). Experimental identification of elastic constants of an orthotropic composite plate. In: *Proceedings of 16th International Conference on Composite Structures (ICCS16): 16th International Conference on Composite Structures*, Porto, Portugal, June 28-30, 2011. (Eds.)A.J.M. Ferreira., 2011.
- Lasn, K.; Klauson, A.; Chati, F.; Décultot, D. (2010). The determination of mechanical properties of orthotropic composites. In: *Book of Abstracts - XVI International Conference Mechanics of Composite Materials*, 2010.

## Table of contents

Preface .....	i
Acknowledgements .....	ii
Abstract .....	iii
Sisukokkuvõte .....	iv
Sammendrag .....	v
List of publications .....	vi
Peer-reviewed publications in international journals .....	vi
Presentations at international conferences .....	vi
Table of contents .....	1
Abbreviations and notations .....	6
1 Introduction .....	10
1.1 Composite materials .....	10
1.2 Elastic constants of composite materials .....	10
1.3 Damage in composites .....	11
1.3.1 Matrix cracking .....	11
1.3.2 Delamination .....	11
1.3.3 Fiber failure .....	12
1.4 Stiffness and damage assessment methods .....	12
1.4.1 General NDT reviews .....	12
1.4.2 Stiffness assessment methods .....	12
1.5 Objectives .....	13
1.6 The scope and structure of the monograph .....	14
2 Back-calculation of ply moduli .....	15
2.1 Introduction .....	15
2.2 Length to height ratio for flexure .....	17
2.3 Solution strategies .....	18
2.3.1 The equations for symmetric cross-plyed specimens .....	19
2.3.2 The equations for symmetric balanced specimens .....	20
2.3.3 The strategies .....	21
2.4 Experimental results .....	23

2.4.1	Experimental uncertainties .....	23
2.4.2	Cross-plyed laminates .....	24
2.4.3	Symmetric balanced laminates .....	26
2.5	Estimation of ply uncertainty for cross-plyed laminates .....	29
2.5.1	The parameter $\delta$ .....	29
2.5.2	Monte Carlo simulations (MCS) .....	30
2.5.3	Estimation of ply uncertainty .....	33
3	Identification of ply moduli from vibration testing with FEA and GA .....	35
3.1	Introduction .....	35
3.2	Experiments and numerical modelling .....	36
3.3	Discrepancies of the models .....	38
3.4	Comparison of FEA trial frequencies .....	39
3.5	Sensitivity study .....	42
3.6	Inversion from experimental data .....	45
3.6.1	Approximate analytical solutions .....	45
3.6.2	FEA with SGA optimization .....	45
3.7	Summary .....	52
4	A study of wave propagation in composite plates .....	53
4.1	Introduction .....	53
4.2	Lamb waves on the unidirectional plate .....	55
4.2.1	Experimental data .....	55
4.2.2	Sensitivity analysis and simplex optimization .....	56
4.2.3	Numerical demonstration of convergence for simplex optimization .....	60
4.2.4	Optimization results .....	61
4.3	Interface waves on cross-plyed plates .....	64
4.3.1	Scholte wave .....	64
4.3.2	Rayleigh wave .....	68
5	Measurements about stiffness reduction in fatigue .....	69
5.1	Introduction .....	69
5.1.1	Selected results from static studies.....	71
5.1.2	Vibration testing studies .....	72
5.1.3	Ultrasonic testing studies .....	73
5.1.4	Summary of key issues and motivation for this study .....	76

5.2	Experimental measurements for stiffness degradation .....	77
5.2.1	Static measurements .....	77
5.2.2	Vibration measurements and optimization results .....	81
5.2.3	Wave propagation measurements.....	85
5.3	Summary of experimental observations .....	87
6	Conclusions.....	90
6.1	Achieving the objectives .....	90
6.2	Comparison of independent measurements.....	91
6.3	Novelty .....	93
6.4	Summary of findings .....	94
6.5	Future work.....	95
Appendix A	Elastic constants of anisotropic laminae.....	96
A.1	General material .....	96
A.2	Orthotropic ply .....	98
A.3	Transversely isotropic ply (hexagonal fiber packing).....	100
A.4	Plane stress ply (CLT).....	101
A.5	Strain rate influence.....	103
Appendix B	Constraints and invariants for elastic moduli .....	105
B.1	Isotropic material .....	105
B.2	Orthotropic material .....	105
B.3	Laminate constraints and invariants .....	106
B.3.1	Thermodynamic constraints for a laminate .....	106
B.3.2	Stiffness invariants for in-plane coordinate transformation.....	107
Appendix C	Micromechanics based estimation of elastic moduli.....	108
C.1	Strength of materials models (rule-of-mixtures) .....	108
C.2	Halpin-Tsai equations.....	110
C.3	Estimations for a glass-epoxy material.....	111
Appendix D	Formulas for the back-calculation of ply moduli .....	113
D.1	Symmetric cross-plyed composites .....	113
D.1.1	Single direction specimen ( <i>TF1</i> ).....	113
D.1.2	Multiple specimens .....	115
D.1.2.1	Tension-Tension ( <i>TT</i> ).....	116
D.1.2.2	Flexure-Flexure ( <i>FF</i> ).....	118

D.1.2.3	Tension-Flexure ( <i>TF2</i> ) .....	119
D.2	Symmetric balanced composites .....	119
D.2.1	Tensile stiffness.....	120
D.2.2	Flexural stiffness .....	121
Appendix E	Optimization algorithms.....	122
E.1	Nelder-Mead Simplex method.....	122
E.2	SGA .....	123
E.3	$\mu$ GA .....	125
Appendix F	Wave propagation.....	126
F.1	Isotropic media – bulk wave velocities .....	126
F.2	Orthotropic media – Christoffel equation.....	126
F.3	Guided waves in isotropic plates – Lamb waves.....	128
F.4	Guided waves in orthotropic plates .....	131
F.4.1	Solutions for the low frequency region .....	131
F.4.2	A solution for orthotropic plate in principal directions.....	132
Appendix G	Experiments and data reduction .....	134
G.1	Composite specimens .....	134
G.1.1	Glass/epoxy .....	134
G.1.2	Glass/vinylester .....	135
G.1.3	Carbon/vinylester .....	136
G.2	Static measurements .....	136
G.2.1	Tensile testing .....	136
G.2.2	Flexural testing.....	137
G.3	Vibration measurements.....	138
G.3.1	Test set-up .....	138
G.3.2	Data reduction .....	140
G.3.3	Results .....	141
G.4	Lamb wave measurements.....	143
G.4.1	Test set-up .....	143
G.4.2	Transducers .....	144
G.4.3	Laser interferometer .....	144
G.4.4	2-D FFT.....	144
References	.....	146



Curriculum Vitae.....	161
DISSERTATIONS DEFENDED AT TALLINN UNIVERSITY OF TECHNOLOGY ON <i>CIVIL ENGINEERING</i> .....	163

## Abbreviations and notations

ca.	<i>circa</i> (approximately, around, about)
<i>et al.</i>	<i>et alii</i> (and others)
e.g.	<i>exempli gratia</i> (for example)
i.e.	<i>id est</i> (that is)
etc.	<i>et cetera</i> (and so forth, and the rest)
ref., refs.	Reference(s)
2-D, 3-D	Two-dimensional, Three-dimensional
AE	Acoustic Emission
ANN	Artificial Neural Network
ASTM	American Society for Testing and Materials
BC	Boundary Conditions
CF, GF	Carbon-fiber, Glass-fiber
CI	Confidence Interval
CLT	Classical Laminate Theory
COV	Coefficient of Variation
C-scan	Through-thickness scanning of laminate with bulk waves. The reflected echo of the ultrasonic pulse (amplitude, time of travel) gives indications about damage in the material. Two dimensional image is produced from systematic measurements at various locations of the laminate plate.
DIC	Digital Image Correlation
EN	European standards for products and services
FE, FEA, FEM	Finite Element, Finite Element Analysis, Finite Element Method
<i>FF</i>	Back-calculation strategy employing two flexural stiffness measurements in perpendicular directions
<i>FFFF</i>	Boundary conditions for a rectangular plate, where all edges are completely free
FFT	Fast Fourier Transform
FRF	Frequency Response Function
FRP	Fiber Reinforced Plastic, Fiber Reinforced Polymer
GA, SGA, $\mu$ GA	Genetic Algorithm, Simple Genetic Algorithm, micro Genetic Algorithm
GFRP	Glass Fiber Reinforced Plastic
HBM	Hottinger Baldwin Messtechnik, international manufacturer on the field of testing and measurements
IEEE	Institute of Electrical and Electronics Engineers, publisher of journals and standards
ISO	International Organization for Standardization
LOMC	Laboratoire Ondes et Milieux Complexes (Waves and Complex Media Laboratory) in Le Havre, France
MATLAB	MATrix LABoratory, numerical computing environment developed by MathWorks
MCS	Monte Carlo Simulation

NDT, NDE, NDI	Non-destructive Testing, Non-destructive Evaluation, Non-destructive Inspection
PC	Personal Computer
SD	Standard Deviation
SSP	Stacking Sequence Parameter, also denoted by $\delta$
<i>TT</i>	Back-calculation strategy employing two tensile stiffness measurements in perpendicular directions
<i>TF1, TF2</i>	Back-calculation strategies employing two stiffness measurements, one from tension and one from flexure. Measurements can originate from the same principal direction ( <i>TF1</i> ) or two separate principal directions ( <i>TF2</i> )
UD	Unidirectional
USB	Universal Serial Bus, an industry standard
VARI	Vacuum Assisted Resin Infusion
<i>a, b</i>	Length and width (in-plane dimensions) of the laminate plate, or the test specimen
<i>c</i>	Constants relating to the systematic error from approximate numerical modelling (Ch. 3), coefficient for the effect from Poisson's ratios (App. D), phase velocity (elsewhere)
<i>c<sub>p</sub>, c<sub>ph</sub></i>	Phase velocity
<i>c<sub>pl</sub></i>	Plate wave velocity (long wavelength $S_0$ )
<i>c<sub>R</sub></i>	Rayleigh surface wave velocity
<i>c<sub>sch</sub></i>	Scholte interface wave velocity
<i>c<sub>p1</sub>, c<sub>L</sub></i>	Longitudinal bulk wave velocity
<i>c<sub>s1</sub>, c<sub>T</sub></i>	Shear bulk wave velocity
<i>d</i>	Thickness of the plate (only in App. F.3, F.4.2)
<i>err</i>	Error, the difference between exact and faulty/approximate values
<i>f, f<sub>i</sub></i>	Frequency, natural frequency of the <i>i</i> -th mode
<i>f<sub>pre</sub>, f</i>	Fitness before and after scaling (App. E)
<i>h</i>	Thickness of the laminate, half thickness of the plate (in App. F.3, F.4.2)
<i>i, j</i>	Summation index, index to represent a direction in Cartesian coordinate system, nodal line notation ( <i>i, j</i> ) for modes of vibration (Ch. 3, 5)
<i>k</i>	Angular wave number, ply number (Ch. 2, App. D)
<i>k<sub>r</sub>, k<sub>im</sub></i>	Real and imaginary part of the wavenumber
<i>lo, hi</i>	Plausible range of frequencies where fitness function component $w_i$ obtains non-zero values
<i>m</i>	Cosine of the ply angle (App. D), mass on the plate (App. G)
<i>n</i>	Number of specimens for one plate in one direction (Ch. 2), population size in GA (Ch. 3–5, App. E), total number of measured data points on one dispersion curve (Ch. 4), number of plies in a laminate (App. D), sine of the ply angle, number of separate measurements (App. G), number of fatigue cycles (Ch. 5)
<i>n<sub>elites</sub></i>	Number of elites in GA procedures

$n_{feval}$	Number of fitness or objective function evaluations in optimization
$n_{tot}$	Total number of fatigue cycles during specimen life until failure
$nxavg$	Fitness scaling parameter in SGA
$p_{conv}$	Probability for the convergence criterion in $\mu$ GA
$p_{cross}$	Probability of cross-over in SGA
$p_{mut}$	Mutation probability in SGA
$p, q$	Parameters in the Lamb wave dispersion equation (App. F.3)
$q$	A characteristic number representing FE mesh density
$r$	Radius of fibers
$s$	Standard deviation of the modulus of elasticity for a unidirectional ply
$t$	Time, number of generations in SGA (Ch. 3–5, App. E)
$u(t)$	Temporal accelerometer signal, in voltage
$w, \Delta w$	Deflection, change in deflection (Ch. 2); relative amplitude of frequency-wavenumber plots and weight of the data point (Ch. 4)
$w_i$	The contribution to the fitness function from the $i$ -th mode
$x, y, z$	Cartesian coordinate system for the laminate ( $z$ is out-of-plane direction)
$z_k$	Distances from the laminate midplane to the ply surfaces
1, 2, 3	Cartesian coordinate system for the ply (3-dir. is out-of-plane)
$[A], [B], [D]$	Laminate stiffness matrices
$A_{xy}, B_{xy}, D_{xy}$	Components of laminate stiffness matrices
$B$	Exponent in the Rayleigh-Lamb dispersion equation (App. F.3)
$[C], C_{ij}$	Stiffness matrix for anisotropic medium (e.g. a ply) or its component
$E, G, \nu$	Engineering constants (Young's modulus, Shear modulus, Poisson's ratio)
$\bar{E}^t, \bar{E}^f$	The (effective) tensile or flexural stiffness/modulus of the laminate
$\bar{\nu}^t, \bar{\nu}^f$	The (effective) tensile or flexural Poisson's ratio of the laminate
$F, \Delta F$	Force, change in force
$F(t)$	Temporal signal of impact hammer force, in voltage
$G$	Matrix which defines the search variable space
$L, L_i$	Span length of the beam (Ch. 2), invariant of the reduced stiffness matrix (App. B.3)
$M$	General expression for material stiffness, i.e Young's modulus, shear modulus or Poisson's ratio (see App. A.5, C.2)
$N$	Number of experimental measurements (Ch. 2)
$ObjF$	Objective function, the inverse of fitness. The goal of optimization is to minimize the objective function (or to maximize fitness).
$P_i$	Invariant of the laminate stiffness matrix (App. B.3), population (App. E)
$[Q], Q_{ij}$	Reduced stiffness matrix or its component
$R$	Distance between neighboring fibers (App. A.2), correlation coefficient (App. A.5), stress ratio ( $\sigma_{min}/\sigma_{max}$ ) in fatigue (Ch. 5)
$[S], S_{ij}$	(Reduced) compliance matrix or its component

$S_0, A_0$	Fundamental symmetric and anti-symmetric modes of the Lamb wave
$V^f, V^m$	Fiber volume fraction, matrix volume fraction
$\alpha, \beta, \eta$	Geometry coefficients of the plate, for flexural stiffness back-calculation (Ch. 2, App. D)
$\alpha, \beta, \gamma$	Material constants characterizing strain rate dependence (App. A.5)
$\psi, \xi, \chi$	Geometry coefficients of the plate, for tensile stiffness back-calculation (Ch. 2, App. D)
$\eta, \eta'$	Stress partitioning factor (App. C.1), coefficient in Halpin-Tsai equations (App. C.2)
$\Delta_i$	Difference of two $i$ -th natural frequencies, in percentage (Ch. 3)
$\delta$	Stacking sequence parameter (SSP)
$\varepsilon_{ij}, \varepsilon_i, \varepsilon, \dot{\varepsilon}$	Tensor normal strain ( $i=j$ ), engineering normal strain, strain rate (derivative with respect to time)
$\varepsilon_{ij}, \gamma_{ij}$	Tensor shear strain ( $i \neq j$ ), engineering shear strain
$\theta, \theta_k$	Ply angle in a laminate
$\xi$	A parameter in Halpin-Tsai equations (App. C.2)
$\rho$	Density of the laminate, a coefficient for Poisson's ratio influence (Appendix D)
$\rho_0$	Density of the fluid
$\rho_1$	Density of the solid
$\sigma_{ij}, \sigma_i$	Normal stress ( $i=j$ )
$\sigma_{max}, \sigma_{min}$	Maximum and minimum stress (during fatigue)
$\sigma_{ult}$	Tensile strength
$\sigma_{ij}, \tau_{ij}$	Shear stress ( $i \neq j$ )
$\omega$	Angular frequency, angular speed, equal to $2\pi f$
$\Gamma_{ij}, \Gamma_i$	Components of the Christoffel matrix or certain combinations of them (App. F.2)

# 1 Introduction

## 1.1 Composite materials

Composite materials are made from two or more different material phases. These phases remain distinct. The constituents are chosen to improve material properties in some regards. For example, improved strength and stiffness can be designed in preferred directions. Also, brittle fiber and matrix materials, both with low fracture toughness on their own, are built into a composite material with higher fracture toughness than of its constituents [1].

The stiffness and strength properties of the material depend on how the fibers are aligned. If fibers are disorganized without any directional preference, the composite is isotropic over a large enough representative volume. If fibers are organized along one single direction, the composite is unidirectional and very anisotropic. Composites are usually constructed from plies, each of which is unidirectional. These plies or laminae are the basic building blocks, stacked on top one another to form a laminate. The stacking sequence (i.e. the fiber directions of the plies) is chosen according to a specific design goal. The spatial distribution of stiffness and strength in the composite material follows from the design. Fibers provide stiffness and carry most of the load, while matrix protects the fibers and transfers loads between them.

In this work, composites are referred as laminar, long fiber (e.g. carbon, glass) reinforced materials with mostly linear elastic behavior.

## 1.2 Elastic constants of composite materials

Real materials are often anisotropic due to their internal structure, which is created either artificially or by nature (e.g. composites or timber). The objective in studying strain–stress relations is to obtain the ability to conclude deformation response from given stresses or vice versa. For anisotropic materials, generalized Hooke’s Law is applied, which requires additional elastic constants in comparison to isotropy. It should be noted that elastic constants are not constant in the strict sense, as they can be functions of e.g. temperature or strain rate and they may also change in time.

Introduction into the atomistic background and the physical basis of elastic moduli can be found e.g. in [2]. In the main part of the Thesis (Chapters 2–5), the reader is assumed to have preliminary knowledge about mechanics and notational principles of anisotropic laminae. For the convenience of the reader, three short summaries have been compiled as Appendices. Different material symmetries and customary notations are reviewed in Appendix A. The constraints and the invariants for the moduli are summarized in Appendix B. Micromechanics based estimations are discussed in Appendix C.

Three notational principles might be considered for the description of anisotropic stiffness — the stiffness tensor  $C_{ijkl}$  (can be displayed as a 9x9 matrix), stiffness matrix  $C_{ij}$  (a 6x6 matrix), or engineering constants in terms of Young’s moduli  $E_i$ , shear moduli  $G_{ij}$  and Poisson’s ratios  $\nu_{ij}$ . Relationships between these representations can be learned from Appendix A or ref. [3]. The formalism of engineering constants (sometimes called technical constants)  $E$ ,  $G$ ,  $\nu$  provides most intuitive insight for material and structural engineers. Engineering constants

are measured in simple tests, such as uniaxial tension or pure shear and therefore have clear physical meaning. The engineering constant notation has been preferred throughout the main part of the current work.

The most apparent aspect regarding composite stiffness is the number of independent elastic constants. While isotropic materials can be characterized by only two, orthotropic material requires nine independent elastic constants: three Young's moduli ( $E_1, E_2, E_3$ ), three Poisson's ratios ( $\nu_{12}, \nu_{13}, \nu_{23}$ ) and three shear moduli ( $G_{12}, G_{13}, G_{23}$ ). If a structure made of orthotropic material is designed or analyzed, all these constants need to be provided for modelling. This characterization typically requires many different experimental measurements and is costly.

### **1.3 Damage in composites**

This section briefly reviews three common damage mechanisms occurring in composite materials. In materials such as steel, damage is observed as a single separate crack and this crack propagates during service life. The phenomena in composite materials are more varied. Damage usually starts as matrix cracking and finishes as fiber failure. Complex interaction between damage mechanisms takes place in between.

#### **1.3.1 Matrix cracking**

Matrix cracking is the first type of damage to appear. It starts from resin pockets, fiber-matrix interface, locations of stress concentrations and imperfections inside the laminate. A regularly spaced network of cracks develops. The plane of the cracks is along the fiber direction. If transverse tension and/or longitudinal shear stresses dominate, the cracks are perpendicular to the plane of the ply. If transverse shear and/or transverse compression dominate, the cracks are oblique.

Matrix cracking has a limited influence on laminate stiffness. However, it is a precursor to more serious forms of damage, since the tips of matrix cracks become the initiation points for delamination and fiber failure. Matrix cracking can be detected from acoustic emission signals or visually, e.g. for glass fiber laminates.

#### **1.3.2 Delamination**

Delamination occurs in the resin rich area between plies with different orientations. It typically stems from intralaminar matrix cracks, especially at locations where two matrix cracks from two different plies meet.

The initiation and growth of delaminations is connected to out-of-plane normal and shear stresses. The most detrimental effect of delamination is the loss of compressive strength. Its influence to tensile stiffness of the laminate is negligible; influence to compressive stiffness can be significant, if delaminated areas buckle locally. The usual method for delamination detection is based on through-thickness ultrasonic wave propagation where delaminated surfaces cause echoes for the acoustic signal (C-scan).

### 1.3.3 Fiber failure

Fiber failure occurs as the last failure mechanism. It takes place at locations where local stress concentrations exceed the fiber strength inside the ply, often at the tips of matrix cracks, or where fibers themselves are weaker (weak spots are statistically distributed). Initially, fiber breaks are isolated whereas before failure they occur increasingly in clusters. In case of impact damage fiber failures can appear on the surface, directly below the striker, where high local shear stress is developed. Fiber failures change the local stiffness and strength dramatically.

## 1.4 Stiffness and damage assessment methods

Previous sections suggest that stiffness of the composite material can be linked to:

- material intrinsic properties (stiffness of a virgin material);
- material intrinsic and the damage properties (stiffness of a damaged material).

Therefore, experimental stiffness measurements can provide information about both, elastic constants for the virgin material and stiffness degradation of the damaged material. In principle, the latter measurement contains information about the type and the severity of the damage. Stiffness can be assessed in various different ways, as discussed in the following.

### 1.4.1 General NDT reviews

Some early reviews about different non-destructive testing (NDT) methods for fiber-reinforced composites were written by Scott and Scala [4], Kinra and Dayal [5] and Reynolds [6]. NDT techniques and defects in composites were reviewed by Adams and Cawley [7] and Cantwell and Morton [8]. These reviews indicate ultrasonic and low-frequency vibration based approaches (among others) as techniques used in practice and showing promise. A technology assessment about NDT methods and defects can be found in ref. [9]. Ibrahim [10] reviews NDE for thick section composites, also looking into vibration analysis, ultrasonics and strain monitoring methods. A standard guide for engineers to select NDT methods E2533 [11] has been published by ASTM, where e.g. detection possibilities regarding ultrasound methods are summarized. The use of multiple NDT methods is always recommended to strengthen the confidence in the results [12].

Pagnotta [13] reviews mixed numerical/experimental techniques for elastic modulus determination, with focus on static and vibration based approaches. Su, Ye and Lu [14] give a thorough review on Lamb wave propagation based damage identification in composites. Broda *et al.* [15] reviews the non-linear ultrasound methods (considering the opening/closing of cracks) for damage detection. Beaumont [16] looks at the big picture, focusing on structural integrity, but also briefly touching on matrix cracking, delamination and NDE.

### 1.4.2 Stiffness assessment methods

As seen from reviews, various non-destructive monitoring systems are able to detect the occurrence of material damage. Fewer systems, however can quantify the stiffness and its reduction. Standardized quasi-static test procedures exist for stiffness measurement, but usually provide only one or two constants from each measurement [17–23]. In addition,



specific specimens and specific fixtures or grips for testing machines are required for many of the tests. This makes the traditional quasi-static methods costly and inconvenient, motivating the continuing development of new methods to measure stiffness.

The advanced methods for evaluating several stiffness constants at once have not been widely accepted and they remain under development. These advanced methods can be categorized as based on three types of measurements:

- quasi-static full-field deformations of the specimen;
- natural vibration frequencies and mode shapes;
- propagation of bulk waves or ultrasonic guided waves along the specimens.

Significant data processing effort is required to actually obtain the elastic constants after each of these measurements. The inverse dynamic methods based on vibration or wave velocity measurements are quite different in terms of ease of practical application, complexity of equipment and number of obtained constants. Very few comparisons (if any) exist in the open literature about measurements conducted on the same laminate with these advanced methods. In order to have confidence in measurement methods, they should give comparable results, whether based on static, vibration or wave velocity measurements.

General reference on elastic property measurement [24] states that mean values for moduli from dynamic and static methods can differ about  $\pm 5\%$  and dynamic methods are in general more accurate. The better accuracy of dynamic techniques is partly due to the small range of strains and stresses the specimen is subjected to during testing, which is far below elasticity limit. However, possible discrepancies need to be identified and better understood for composites.

In addition, literature review revealed a small gap of knowledge. No systematic treatment for the back-calculation of elastic moduli from stiffnesses of cross-ply laminates was available in the open literature. The effective stiffnesses of cross-ply laminates can be measured by static tensile or bending tests or from natural vibrations of the laminate. Ply moduli can then be back-calculated from these laminate stiffnesses.

## 1.5 Objectives

The objectives of current work are formulated as follows.

1. To develop a method for evaluating ply moduli from measured tensile and/or flexural stiffnesses of cross-ply laminates.
2. To apply current state-of-the-art dynamic methods for the evaluation of ply elastic constants. Test methods should have experimental simplicity and possibility to obtain several elastic constants from a single measurement.
3. To compare the elastic constants obtained from previous independent test methods.
4. To quantify the influence of matrix cracking to elastic behavior.

## 1.6 The scope and structure of the monograph

The main part of the work comprises of four chapters (Chapters 2–5), elaborating on three different methods of stiffness measurement for unidirectional and cross-plyed specimens. The test methods are based on static measurements, vibration testing and wave propagation measurements. Chapters 2–4 focus on laminates without damage and Chapter 5 introduces transverse matrix cracking to cross-plyed specimens.

Chapter 2 considers the possibility to back-calculate ply properties, based on tensile or flexural stiffness measurements on laminates. Specific methods are presented to evaluate ply moduli  $E_1$  and  $E_2$  and their coefficient of variation. Calculation formulas are derived and explicitly given for some cases. For other cases, optimization is employed. In general, good experimental results are obtained from cross-plyed specimens, while symmetric balanced specimens showed too much scatter for practical applications. As a novelty, a stacking sequence parameter  $\delta$  is introduced, which is shown to control the scatter in back-calculated results.

Chapter 3 explores the possibility of obtaining elastic constants from natural frequencies measured from vibration testing. A typical test set-up is used, where a rectangular plate with all edges free boundary conditions is excited with impulse loading. Finite element analysis coupled with genetic algorithm optimization is used to determine flexural  $E_x$ ,  $E_y$  and in-plane  $G_{xy}$ . A novel definition for the fitness function is employed, accounting for previously evaluated systematic and random errors.

Chapter 4 describes various results obtained from wave propagation measurements. A novel two-stage optimization approach is described where Nelder-Mead Simplex optimization is used to identify orthotropic elastic constants from Lamb wave measurements. Young's moduli ( $E_1$ ,  $E_2$ ,  $E_3$ ) and shear moduli ( $G_{13}$ ,  $G_{23}$ ) are identified for a unidirectional plate. Scholte interface waves are detected on the surfaces of plates with transverse cracks. This demonstrates additional monitoring possibility for in-situ sensor systems — a possibility to detect changes in the surrounding gaseous environment, e.g. for monitoring of gas leaks.

In Chapter 5, transverse cracking is introduced by fatigue loading on cross-plyed specimens. Stiffness degradation of test coupons is measured by simple static testing. The stiffness degradation of a plate specimen is experimentally quantified by both vibration and Lamb wave measurements. The possibility for the experimental detection of transverse cracking is discussed, based on these experimental results.

Chapter 6 summarizes the main results and the novelty in the monograph.

Each of the Chapters 2–5 has a specific topic, which is therefore provided with a separate introduction, motivation and a literature overview. Various topics (elastic constants of anisotropic materials, micromechanics, back-calculation equations, optimization, wave propagation) are too divergent to be discussed in the main text and are therefore moved to Appendices. These Appendices include more in-depth explanations, examples, illustrations and references. Appendix G contains the description of experimental work.

## 2 Back-calculation of ply moduli

### 2.1 Introduction

One of the objectives of this work is to develop a method for evaluating ply moduli from tensile and flexural stiffnesses of cross-ply laminates. This concept has been described in general terms by e.g. Ng [25] and tensile back-calculation formulas can be found in the unpublished ref. [26] by Echtermeyer. This Chapter describes a systematic approach for back-calculation, extending it to flexural and tensile-flexural mixed measurements, and also for evaluating the coefficient of variation (COV) of the ply moduli. The derivation and details of specific equations are described in Appendix D. In addition, the possibility of generalizing a similar approach to more realistic symmetric balanced laminates is attempted and discussed.

Elaborate static test methods are available for elastic constant evaluation, based on full-field digital image correlation (DIC) measurements of either in-plane [27, 28] or out-of-plane [29] strains. Numerical FEA modelling and optimization is usually applied to solve the inverse problem for elastic constant determination. DIC technology can also be used for on-line monitoring of damage of repairs [30]. Current approach is experimentally less ambitious and does not expect full-field strain measurements. A method based on simple uniaxial tensile and flexural tests is developed.

A similar technique to what is considered here was proposed recently by Kam *et al.* [31] for the identification of four ply moduli from three-point bending of symmetric angle-ply beams. Strains need to be measured in three directions and moduli are calculated via optimization. The approach described here is based on even simpler experiments and procedures.

The ply properties are usually measured on unidirectional (UD) specimens with a well-defined geometry [17–20]. Different tests are needed to identify ply moduli as described in refs. [21–23, 32–35]. However, on some occasions only the existing laminates are available and further unidirectional specimens cannot be produced. There are also fabrics where fibers do not exist in a unidirectional form. In such cases a necessity to measure ply stiffnesses on these final laminates occurs.

Cross-ply specimens have emerged as an interesting alternative to traditional unidirectional testpieces, especially for ply strength characterization, e.g. as described in refs. [36–40]. It is argued that a ply in a cross-ply layout is more closely representative of its application in actual structural components, compared to plies tested in isolation. Cross-ply testing is reported to improve experimental strength characterization and reduce the scatter of results, due to more robust layout, making the premature failures of  $0^\circ$  plies less likely. Knowledge of ply elastic constants is necessary to calculate the strengths and these constants are currently still measured from UD specimens. Back-calculation procedures provide a way to get the ply elastic properties directly from cross-ply specimens.

Classical laminate theory (CLT) is extensively used for describing the basic mechanical behavior of laminated composite materials. Following derivations in this Chapter and in Appendix D are based on CLT. In addition, it is assumed that all plies in the laminate are

unidirectional and have been made from the same fibers. The basic building block of CLT is a ply. The out-of-plane direction is omitted by the plane stress assumption (Appendix A.4) and the ply has four elastic moduli: two Young's moduli  $E_1$ ,  $E_2$ , in-plane shear modulus  $G_{12}$  and in-plane major Poisson's ratio  $\nu_{12}$ . It is very common to estimate the effective tensile or flexural stiffness of the laminate from CLT, knowing the elastic properties and the stacking sequence of the plies. For the simple cases, reference is made to textbooks, e.g. [3, 41]. For more general cases, a derivation of effective laminate stiffnesses can be found in [42, 43].

The inverse calculation of ply moduli from effective laminate stiffnesses is not so common. The experimental work for the back-calculation of ply properties is complicated due to the stiffness coupling phenomena. In a general laminate, stiffness coupling exists between extension, shear, bending and twist. Only very specific types of layups can be tested with common tensile or flexural test set-ups. For example, if laminate is not symmetric, uniaxial tensile test causes the laminate also to bend. Such complex deformations and states of stress are difficult to experimentally measure and therefore should be avoided. It can be shown with CLT that symmetric cross-plyed layups are the most general laminates where simple tensile or flexural testing does not cause stiffness coupling issues. They possess beneficial characteristics for extension-bending ( $[B] = 0$ ), in-plane normal and shear ( $A_{xs} = A_{ys} = 0$ ) and bending-twist coupling ( $D_{xs} = D_{ys} = 0$ ) [3]. Symmetric angle ply laminates  $[\pm\theta]_s$  or their symmetric combinations with cross plies can be of practical interest because they also have ( $[B] = 0$ ) and ( $A_{xs} = A_{ys} = 0$ ). This means, uncoupled tensile testing can be carried out in their principal directions. However, it is noted that due to the angle plies in-plane shear modulus also contributes to the longitudinal stiffness.

As discussed, the test specimen should have a simple state of strain and stress for the analysis. The simplest test configurations are uniaxial tensile and flexural tests (either three-point or four-point). The stress distribution in the specimen is simple when testing in axial directions, but the test itself is much simpler when testing in flexure. Theoretically, axial and flexural tests should give the same result when measuring Young's modulus. But it is worth noting that standards and guidelines [17, 19, 36] are cautious and recommend flexural testing mainly for quality control purposes and not for obtaining design data.

It is widely recognized that composite material properties have a stochastic character [44–46] and ply Young's moduli are usually treated as having normal distribution. It was shown in [47] that material modulus uncertainty at ply level can introduce non-zero values to laminate stiffness coupling terms which are otherwise assumed to be zero. Uncertainty in ply moduli need to be accounted for the reliability analysis of any stiffness controlled design, e.g. vibration phenomena, aero elastic tailoring or buckling. It has been shown [48] that reliability can be seriously overestimated when stochastic nature of material elastic properties is not taken into account. In addition, damage from stiffness degradation is detectable with confidence only when the change in system behavior exceeds the influence of material uncertainty. Therefore, initial stiffness properties need to be known with a specified uncertainty.

## 2.2 Length to height ratio for flexure

Flexural testing requires some additional considerations when the beam is short, e.g. as discussed in [49–51]. The real deformations differ from simple mechanics of materials estimations mainly due to:

- plastic deformations (of matrix) under stress concentrations
- distribution of shear stresses in the cross section differs from parabolic near load concentrations (i.e. shear stress distribution is not uniform along beam length)

To reduce the deviations of the simple analytical model, the beam span needs to be sufficiently long in relation to the height (thickness) of the cross-section. This way, the concentrated loads will be low in magnitude (not causing significant deformations) and the non-parabolic shear stress distribution will occur more locally.

Flexural testing is further affected by through-thickness shear deformations, occurring most severely for beams with small span-to-thickness  $L/h$  ratios. The effect of shear deformation is larger when ply normal moduli are high compared to shear moduli [52]. If through-thickness shear modulus  $G_{xz}$  is known or estimated, its effect (shear deformation) can be subtracted from the total deformation. Usually,  $G_{xz} \approx G_{13} \approx G_{12}$  is a good estimation. Deformations can be calculated from beam theory, such as Mohr-Maxwell integrals, and the coefficient for shear can be taken for rectangular cross-section as  $5/6$  [53]. The “true” flexural modulus  $\bar{E}_x^{f,s}$  accounting for the shear deformation effects (thus superscript  $s$ ) becomes for three-point-bending:

$$\bar{E}_x^{f,s} = \frac{\left(\frac{L}{h}\right)^3}{4b \left[ \frac{\Delta w}{\Delta F_z} - \frac{3}{10bG_{xz}} \left(\frac{L}{h}\right) \right]} \quad (2.1)$$

where  $L/h$  is span to thickness ratio and  $\Delta w$  and  $\Delta F_z$  are the midpoint deflection and change in midpoint force, respectively. If  $G_{xz} \rightarrow \infty$ , the “true” flexural modulus in Eq. (2.1) reduces to the regular expression for “apparent” flexural modulus  $\bar{E}_x^f$  in Eq. (2.2).

$$\bar{E}_x^f = \frac{\Delta F_z}{4b\Delta w} \left(\frac{L}{h}\right)^3 \quad (2.2)$$

One can transform from “apparent” flexural modulus to “true” flexural modulus by:

$$\bar{E}_x^{f,s} = \frac{\left(\frac{L}{h}\right)^2}{4 \left[ \left(\frac{L}{h}\right)^2 \frac{1}{4\bar{E}_x^f} - \frac{3}{10G_{xz}} \right]}. \quad (2.3)$$

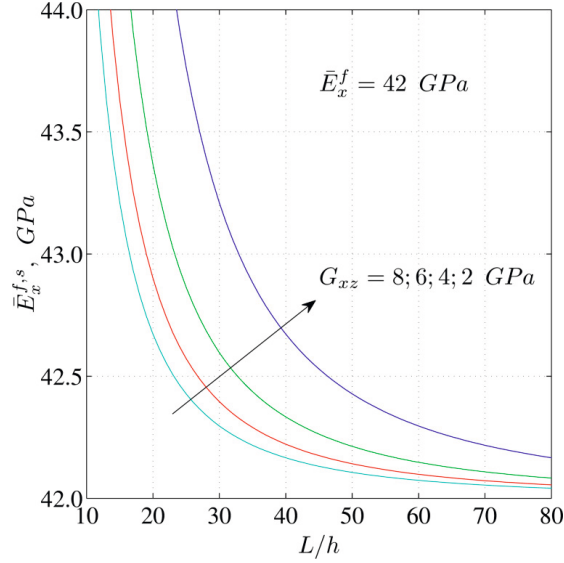


Figure 2.1. Examples of “true” flexural moduli  $\bar{E}_x^{f,s}$ , calculated for “apparent” modulus of  $\bar{E}_x^f = 42$  GPa, considering various  $G_{xz}$  values and  $L/h$  ratios by Eq. (2.3).

Figure 2.1 shows how “apparent” flexural modulus asymptotically approaches the true modulus (or vice versa) as the  $L/h$  ratio increases. Shear deformations cause the “apparent” modulus to have a slightly lower value. Standard ISO 14125 [17] sets constraints for three-point flexure as  $L/h = 20$  for glass-fiber and  $L/h = 40$  for carbon fiber specimens; ASTM standard D7264 [19] sets limit to  $L/h = 32$ . Similar values can be found from other literature, e.g.  $L/h > 40$  in [23] and  $L/h > 60$  in [52].

As an approximate estimate for glass-fiber specimens, Fig. 2.1 shows that by using Eq. (2.2) for  $L/h = 30$  specimens, the underestimation of flexural modulus is 3% at most and by using  $L/h = 60$ , it has decreased below 1%. If through thickness shear effect needs to be accounted, Eq. (2.3) can be used to convert the results. However, for very low values of  $L/h$ , it still deviates from reality due to reasons mentioned in the beginning of the current Section.

### 2.3 Solution strategies

The aim of the back-calculation is to estimate ply moduli  $E_1$  and  $E_2$  from tensile and flexural stiffness measurements  $\bar{E}^t$ ,  $\bar{E}^f$  on the laminates. Appendix D derives and discusses in detail the equations based on CLT, which connect ply moduli and laminate stiffnesses for symmetric cross-plyed and symmetric-balanced laminates.

### 2.3.1 The equations for symmetric cross-plyed specimens

In symmetric cross-plyed laminates, the in-plane shear modulus does not contribute to laminate stiffness in principal directions. The effect of varying Poisson's ratio  $\nu_{12}$  between the extremes 0 and 0.5 can be shown to influence back-calculated moduli by approx. 2% for glass-fiber or carbon-fiber laminates. The  $\nu_{12} = 0$  back-calculated moduli are always slightly larger. The influence of the Poisson's ratio depends on the specific laminate layup and the chosen strategy. For some combinations of layups and strategies, the influence of  $\nu_{12}$  exceeds 2%, especially for  $E_2$ . However, in general it is considered reasonable to either estimate the Poisson's ratio (e.g.  $\nu_{12} = 0.3$ ) or to even neglect its influence ( $\nu_{12} = 0$ ). This leaves two unknowns  $E_1$  and  $E_2$  which can be directly calculated from two measured stiffness pairs composed of tensile ( $\bar{E}_x^t, \bar{E}_y^t$ ), flexural ( $\bar{E}_x^f, \bar{E}_y^f$ ) or a mixture of these stiffnesses. Equations (2.4)–(2.5) can be applied for symmetric cross-plyed specimens measured in tension:

$$E_1 = \frac{1}{\gamma} \left[ \frac{\psi \bar{E}_x^t - \xi \bar{E}_y^t}{\psi^2 - \xi^2} - \frac{(\bar{E}_y^t \bar{\nu}_{xy}^t)^2 (\psi^2 - \xi^2)}{\psi \bar{E}_y^t - \xi \bar{E}_x^t} \right], \quad (2.4)$$

$$E_2 = \frac{1}{\gamma} \left[ \frac{\psi \bar{E}_y^t - \xi \bar{E}_x^t}{\psi^2 - \xi^2} - \frac{(\bar{E}_y^t \bar{\nu}_{xy}^t)^2 (\psi^2 - \xi^2)}{\psi \bar{E}_x^t - \xi \bar{E}_y^t} \right], \quad (2.5)$$

and Eqs. (2.6)–(2.7) for specimens measured in flexure:

$$E_1 = \frac{1}{\gamma} \left[ \frac{\alpha \bar{E}_x^f - \beta \bar{E}_y^f}{12(\alpha^2 - \beta^2)} - \frac{12(\bar{E}_y^f \bar{\nu}_{xy}^f)^2 (\alpha^2 - \beta^2)}{\alpha \bar{E}_y^f - \beta \bar{E}_x^f} \right], \quad (2.6)$$

$$E_2 = \frac{1}{\gamma} \left[ \frac{\alpha \bar{E}_y^f - \beta \bar{E}_x^f}{12(\alpha^2 - \beta^2)} - \frac{12(\bar{E}_y^f \bar{\nu}_{xy}^f)^2 (\alpha^2 - \beta^2)}{\alpha \bar{E}_x^f - \beta \bar{E}_y^f} \right]. \quad (2.7)$$

For symmetric cross-plyed pairs, such as ( $\bar{E}_x^t, \bar{E}_x^f$ ) or ( $\bar{E}_x^t, \bar{E}_y^f$ ), direct formulas for  $E_1$  and  $E_2$  were not derived. Instead, optimization can be employed, based on expressions of effective stiffnesses in Eqs. (2.8)–(2.9):

$$\bar{E}_x^t = \frac{1}{1 - \nu_{12}^2 \frac{E_2}{E_1}} \left[ \psi E_1 + \xi E_2 - \frac{(\nu_{12} E_2)^2}{\psi E_2 + \xi E_1} \right], \quad (2.8)$$

$$\bar{E}_x^f = \frac{12}{1 - \nu_{12}^2 \frac{E_2}{E_1}} \left[ \alpha E_1 + \beta E_2 - \frac{(\nu_{12} E_2)^2}{12^2 (\alpha E_2 + \beta E_1)} \right]. \quad (2.9)$$

For explanations and details about Eqs. (2.4)–(2.9), the reader is referred to Appendix D.

### 2.3.2 The equations for symmetric balanced specimens

For symmetric balanced laminates, the approach is always based on optimization with Eqs. (2.10)–(2.11). These formulas are analogous, generalized versions of Eqs. (2.8)–(2.9).

$$\bar{E}_x^t = \left\{ \begin{aligned} & [\rho(\psi E_1 + 2\chi \nu_{12} E_2 + \xi E_2) + 4\chi G_{12}] \\ & - \frac{[\rho(\chi E_1 + (\psi + \xi)\nu_{12} E_2 + \chi E_2) - 4\chi G_{12}]^2}{[\rho(\xi E_1 + 2\chi \nu_{12} E_2 + \psi E_2) + 4\chi G_{12}]} \end{aligned} \right\}, \quad (2.10)$$

$$\bar{E}_x^f = 12 \left\{ \begin{aligned} & [\rho(\alpha E_1 + 2\eta \nu_{12} E_2 + \beta E_2) + 4\eta G_{12}] \\ & - \frac{[\rho(\eta E_1 + (\alpha + \beta)\nu_{12} E_2 + \eta E_2) - 4\eta G_{12}]^2}{[\rho(\beta E_1 + 2\eta \nu_{12} E_2 + \alpha E_2) + 4\eta G_{12}]} \end{aligned} \right\}. \quad (2.11)$$

For details about Eqs. (2.10)–(2.11), the reader is referred to Appendix D.

Symmetric balanced laminates have all four ply constants contributing to its stiffness. Even if Poisson's ratio is estimated, three moduli still remain unknown. Back-calculation becomes impossible if only two experimental measurements provide the experimental data for this calculation (i.e. using similar approach as with cross-plyed specimens in Section 2.3.1). However, a different approach for presenting the results can be adopted. The equations can be solved for  $E_2$ ,  $G_{12}$ , for a given range of estimated  $E_1$  values. Each estimation of  $E_1$  enables to solve for  $E_2$  and  $G_{12}$ , introducing a pair of dots to the graph (one for  $E_2$  and one for  $G_{12}$ ), forming two solution lines as seen in Fig. 2.2.



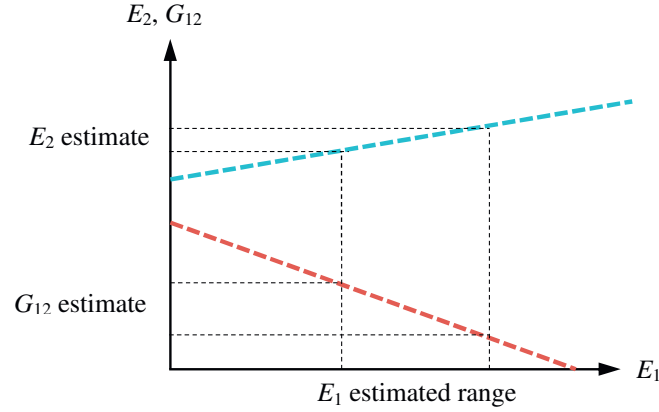


Figure 2.2. Solving for  $E_1$ ,  $E_2$ ,  $G_{12}$  from stiffnesses of a symmetric balanced laminate. Two measured laminate stiffnesses and a Poisson's ratio estimation are the required input.

### 2.3.3 The strategies

The aim of the back-calculation is to estimate ply moduli  $E_1$  and  $E_2$  from given tensile and flexural stiffness measurements on the laminates. To accomplish this, different strategies are formulated and categorized by the type of available experimental data. In each strategy, two experimentally measured stiffnesses are used to calculate either  $E_1$  and  $E_2$  (for symmetric cross-plyed specimens) or a 2-D representation as in Fig. 2.2 for symmetric balanced specimens. These two stiffnesses can be chosen from the experimental data in various ways. For a single strategy, all possible pairs of laminate stiffnesses are extracted from experimental data and thereafter solved.

Strategy *TT* is based on tensile stiffnesses measured in two principal directions of the laminate ( $\bar{E}_x^t, \bar{E}_y^t$ ), and Eqs.(2.4)–(2.5) are directly applicable. Strategy *FF* is the analogue for flexural stiffnesses measured in two principal directions of the laminate ( $\bar{E}_x^f, \bar{E}_y^f$ ) by using Eqs. (2.6)–(2.7). Strategy *TF1* assumes that both tensile and flexural stiffness are measured from the same principal direction of the laminate ( $\bar{E}_x^t, \bar{E}_x^f$  or  $\bar{E}_y^t, \bar{E}_y^f$ ). Strategy *TF2* assumes that tensile and flexural stiffness is measured on specimens originating from different directions, i.e. ( $\bar{E}_x^t, \bar{E}_y^f$  or  $\bar{E}_y^t, \bar{E}_x^f$ ). Ply moduli can be obtained from strategies *TF* by using Eqs. (2.8)–(2.9) for symmetric cross-plyed laminates, in combination with optimization. Equations (2.10)–(2.11) are used with optimization for symmetric balanced laminates, for all strategies.

A simple example is presented to explain the pairing of specimens. Consider a laminate, where six specimens (1a, 1b, 1c and 2a, 2b, 2c) are measured for both, tensile and flexural stiffness in perpendicular directions  $x$  and  $y$ , respectively. The situation is depicted in Fig. 2.3(a). For strategy *TT*, nine different tensile stiffness pairs can be formed, as shown schematically in Fig. 2.3(b), where each connecting line denotes a pairing between specimens. For convenience, this pairing is hereby denoted with braces as {1-2}. For strategy *FF*, the same nine flexural stiffness pairs {1-2} can also be formed. Strategy *TF1* employs tensile and flexural stiffnesses from the same principal direction of the laminate, and therefore eighteen

pairs ( $\{1-1\}$ ,  $\{2-2\}$ ) can be formed. Strategy *TF2* employs tensile and flexural stiffnesses from two different directions and again eighteen pairs ( $\{1-2\}$ ,  $\{2-1\}$ ) can be formed. Altogether, if  $n$  specimens are measured in both directions for tension and flexure ( $n = 3$  in Fig. 2.3(a)),  $n^2$  pairs can be formed for strategies *TT* and *FF*; and  $2n^2$  pairs for strategies *TF1* and *TF2*.



(a) Laminate and specimens

(b) Notation for specimen pairing  $\{1-2\}$ , each line shows one out of nine possible pairings

Figure 2.3. An example of specimen pairing.

Strategies *OPT* are not based on solving equations for data pairs, but on optimization, minimizing the difference between all measured and guessed moduli. These optimization strategies result only in best estimations, without evaluating the scatter of the results. Strategy *OPT\_T* employs all tensile data, strategy *OPT\_F* employs all flexural data and strategy *OPT* simply all of the measured data (tensile and flexural).

Table 2.1. The solution strategies for obtaining ply moduli.

Strategy	Measured stiffnesses	Pairing	Tension/Flexure mixing
<i>TT</i>	Spec. pair: $\bar{E}_x^t, \bar{E}_y^t$	$\{1-2\}$	No
<i>FF*</i>	Spec. pair: $\bar{E}_x^f, \bar{E}_y^f$	$\{1-2\}$	No
<i>TF1*</i>	Spec. pair: $\bar{E}_x^t, \bar{E}_x^f$ or $\bar{E}_y^t, \bar{E}_y^f$	$\{1-1\}, \{2-2\}$	Yes
<i>TF2*</i>	Spec. pair: $\bar{E}_x^t, \bar{E}_y^f$ or $\bar{E}_y^t, \bar{E}_x^f$	$\{1-2\}, \{2-1\}$	Yes
<i>OPT_T</i>	All tension: $\bar{E}_x^t, \bar{E}_y^t$	-	No
<i>OPT_F*</i>	All flexure: $\bar{E}_x^f, \bar{E}_y^f$	-	No
<i>OPT*</i>	All $\bar{E}$	-	Yes

\* - For symmetric balanced specimens, the flexural stiffnesses  $\bar{E}^f$  are analyzed with an error, due to non-zero bending-twist coupling terms  $D_{xs}$  and  $D_{ys}$ . See Appendix D.2.2 for details.

The solution strategies described above are summarized in Table 2.1 with their respective characteristics. Strategies *TT* to *TF2* are based on the measurement of two laminate stiffnesses. Ply moduli are back-calculated from one such pair. The scatter of the results from these back-calculated pairs can be visualized and analyzed. For either cross-plyed or symmetric balanced laminates, the most general and simple solution strategy is to minimize the difference between experimentally measured and guessed moduli through optimization. The differences can be summed over all tensile specimens (*OPT\_T*), over all flexural specimens (*OPT\_F*) or over all of the specimens (*OPT*).

Nelder-Mead Simplex optimization (See Appendix E.1) is employed for solving for moduli, except for strategies *TT* and *FF* for cross-plyed specimens, where explicit Eqs. (2.4)–(2.7)

exist. The principle is the same in all cases. The procedure aims to minimize the objective function  $ObjF$ , as given in Eq. (2.12). It is defined as the sum of absolute differences between the experimentally measured laminate stiffness and the corresponding guessed stiffness, calculated from guessed ply moduli.  $N$  is the total number of measurements, tensile or flexural, for a specific strategy. This optimization algorithm requires a starting value for the unknowns, providing of which is not difficult, e.g. from rule-of-mixtures type of estimations (see Appendix C).

$$ObjF = \sum_{i=1}^N |\bar{E}_i^{experiment} - \bar{E}_i^{guess}| \quad (2.12)$$

The optimization is constrained, so the objective function  $ObjF$  is given a very large value if the guessed values ( $E_1, E_2, G_{12}$ ) obtain thermodynamically implausible negative values (Table B.1 in Appendix B).

## 2.4 Experimental results

The experimental data given below will be analyzed according to the seven different strategies, as described in Table 2.1. The formulas used for back-calculation, Eqs. (2.4)–(2.11), are explained in Appendix D. Poisson's ratio value  $\nu_{12} = 0.3$  was assumed for all calculations. For the calculation of geometry coefficients  $\alpha, \beta, \eta, \psi, \xi, \chi$ , all plies are assumed to have equal and constant thickness and laminates are assumed to have no resin surface layers or other internal imperfections.

### 2.4.1 Experimental uncertainties

The uncertainties for tensile or flexural stiffness of composite specimens can result from various causes. Some more important ones are listed below.

- The production of the specimen:
  - the alignment of fibers in each single ply;
  - specimen cutting (specimen not aligned with laminate principal directions, unparallel edges, damage from cutting);
  - the internal structure of the composite (resin rich surface layers, resin rich volumes inside, voids, non-uniform ply thicknesses, uneven laminate thickness).
- The test procedure:
  - the misalignment of specimen axis with the axis of the test machine;
  - deflection from through-thickness shear in flexure;
  - large-deflection effects in flexure;
  - different test speeds (strain rates) in tension and flexure;
  - different Young's moduli in tension and compression.

Some uncertainties are connected to the fundamental nature of tensile or flexural testing. The range of strains a specimen endures during three-point flexure varies linearly both in the

through-thickness direction and also in the specimen length direction due to Bernoulli hypothesis and the shape of the bending moment diagram. Half of the beam cross-section is in tension and half in compression. In comparison, strain is theoretically assumed to be uniform throughout in the tensile test. Also, the resin surface layers have stronger influence on flexural stiffness than tensile.

#### 2.4.2 Cross-plyed laminates

The details of the glass-fiber/epoxy laminate are described in Table G.1 in Appendix G. Twelve straight sided specimens were cut from two plates (3 in all principal directions) and the same specimens were measured for tensile and flexural stiffness. The measurements were carried out below damage limit (normal strains below 0.2%), disregarding the non-linear onset region during very low strains (below 0.05%). Estimated strain rates at any single point on the specimens were below  $0.3\% \text{ min}^{-1}$ . The load to deflection ratio was obtained by least-squares linear fitting. The equipment and the procedure for tensile and flexural testing is described in Appendix G.2.

The experimental results are presented in Table 2.2. In addition to effective stiffness, the span to thickness ratio  $L/h$  is given to characterize three-point flexure. Ratios of 50 to 70 are large enough for glass-fiber/epoxy (see Fig 2.1), so the shear deformation contributions were not subtracted and the regular Eq. (2.2) was used.

Table 2.2. The effective tensile and flexural stiffnesses of glass/epoxy laminates.

Layup	Specimen	$\bar{E}_x^t$ , GPa	$\bar{E}_x^f$ , GPa	$L/h$
[90 <sub>2</sub> /0 <sub>2</sub> /90 <sub>2</sub> ]	1a	21.2	14.3	73
	1b	22.5	14.2	54
	1c	22.2	13.4	54
[0 <sub>2</sub> /90 <sub>2</sub> /0 <sub>2</sub> ]	2a	31.7	39.1	73
	2b	33.5	38.8	54
	2c	33.9	38.6	54
[0/90 <sub>4</sub> /0]	3a	22.9	32.8	72
	3b	23.7	32.7	54
	3c	21.8	31.4	53
[90/0 <sub>4</sub> /90]	4a	32.5	20.3	72
	4b	32.8	20.5	53
	4c	33.0	20.9	53

The results for the seven strategies are summarized in Fig. 2.4. The individual results from single back-calculated data pairs are displayed as dots. The arithmetic mean values are represented with horizontal lines and numerical values. If the moduli are employed to describe the tensile behavior of the laminate, the mean results from *TT* or *OPT\_T* strategy are most appropriate. Similarly, the results from *FF* or *OPT\_F* strategy are suitable when the laminate works mainly in flexure. If extensional and flexural behaviors are both structurally important, the results from *TF1*, *TF2* strategy or the mean from *TT* and *FF* are most suitable.

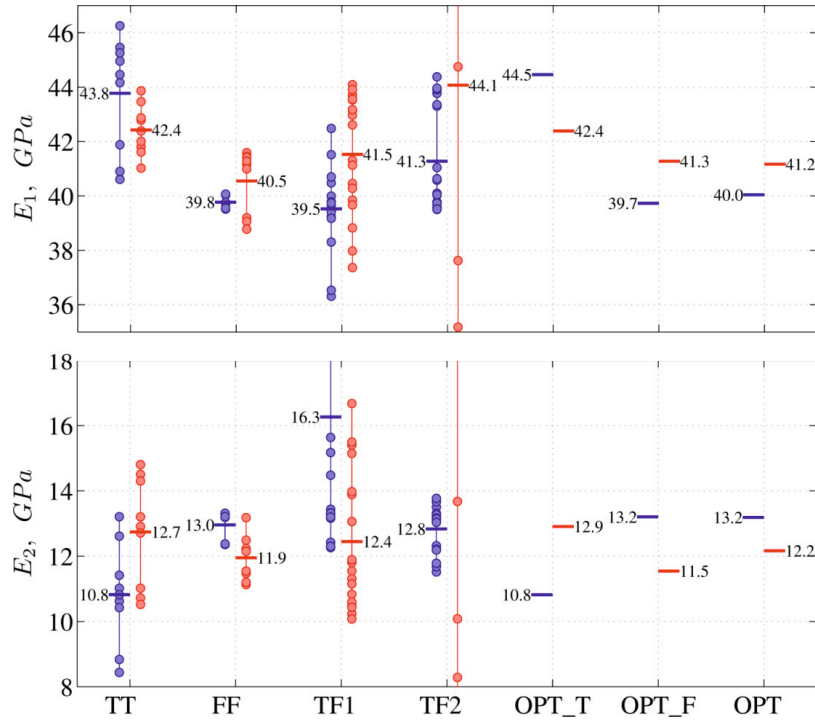


Figure 2.4. Back-calculated results for  $[90_2/0_2/90_2]$  (left, blue) and  $[0/90_4/0]$  (right, red) laminates for seven strategies (Table 2.1).

The following conclusions can be drawn from the results in Fig. 2.4.

- The results agree well and have overlapping results (also confidence intervals) with each other, for both  $E_1$  and  $E_2$ .
- There is a large difference in the scatter of individual results within different strategies. The scatter is very high for:
  - strategy  $TF1$ ,  $[90_2/0_2/90_2]$ :  $E_2$  single values range from 12.3 to 23.0 GPa (out of figure range)
  - Strategy  $TF2$  for  $[0/90_4/0]$ :  $E_1$  ranges from 18.1 to 71.1 GPa;  $E_2$  from 0.0 GPa to 54.9 GPa (out of figure range).
  - The scatter from pure tensile testing (strategy  $TT$ ) is larger than scatter from flexural testing (strategy  $FF$ )
- Compensation between  $E_1$  and  $E_2$  is observed. For example, if the obtained  $E_1$  has higher than overall average value for a specific strategy, its corresponding  $E_2$  value is lower, compared to others, and vice versa.

At this point it is unclear what causes the large scatter in some of the results (e.g.  $TF$  strategies for  $E_2$ ) and which standard deviation should be used for the ply properties. This is further investigated in Section 2.5.

### 2.4.3 Symmetric balanced laminates

#### 2.4.3.1 Glass/epoxy

The specimen details are discussed in Table G.2 in Appendix G. It is worth pointing out that the fibers used in these specimens are slightly different from the ones used in cross-plyed specimens in Section 2.4.2. Six specimens were cut from the plate (three in both principal directions) and the same specimens were measured for tensile and flexural stiffness. All measurements were carried out below damage limit (normal strains below 0.2%) and at quasi-static strain rates below  $0.3\% \text{ min}^{-1}$ ). The experimental results are given in Table 2.3. Specimens from two principal directions had different span lengths in the flexural test. This is due to the maximum size of the manufactured laminate and cut specimens. “True” flexural moduli were calculated according to Eq. (2.1) (estimated  $G_{xz} = 4 \text{ GPa}$ ), reducing the influence of different  $L/h$  ratios.

Table 2.3. Effective tensile and flexural stiffnesses of symmetric-balanced glass-fiber/epoxy laminate.

Layup	Specimen	$\bar{E}_x^t$ , GPa	$\bar{E}_x^{f,s}$ , GPa	$L/h$
[90/45/-45/0 <sub>2</sub> ] <sub>s</sub>	sbx-1	26.6	16.5	59
	sbx-2	28.9	16.2	58
	sbx-5	26.0	16.5	59
[0/-45/45/90 <sub>2</sub> ] <sub>s</sub>	sby-2	21.2	28.6	35
	sby-4	21.4	28.7	35
	sby-5	22.4	27.9	35

The experimental data in Table 2.3 was analyzed according to seven strategies (Table 2.1). For each given pair of laminate stiffnesses, a solution line for  $E_2$  and  $G_{12}$  is obtained, as introduced in Fig. 2.2. The individual solutions from specimen pairs and the envelopes for three first strategies are presented in Fig. 2.5(a). The fourth strategy had excessive scatter and was omitted from the plot. Areas where the results from three strategies overlap agree with the  $FF$  envelope are also marked by bold borders.

In optimization strategies all results from tension, flexure or combined are pooled and minimization of the objective function according to Eq. (2.12) is carried out. The results are presented in Fig. 2.5(b). All results in Fig. 2.5 are obtained for a given range of possible  $E_1$  values from 35 to 55 GPa.

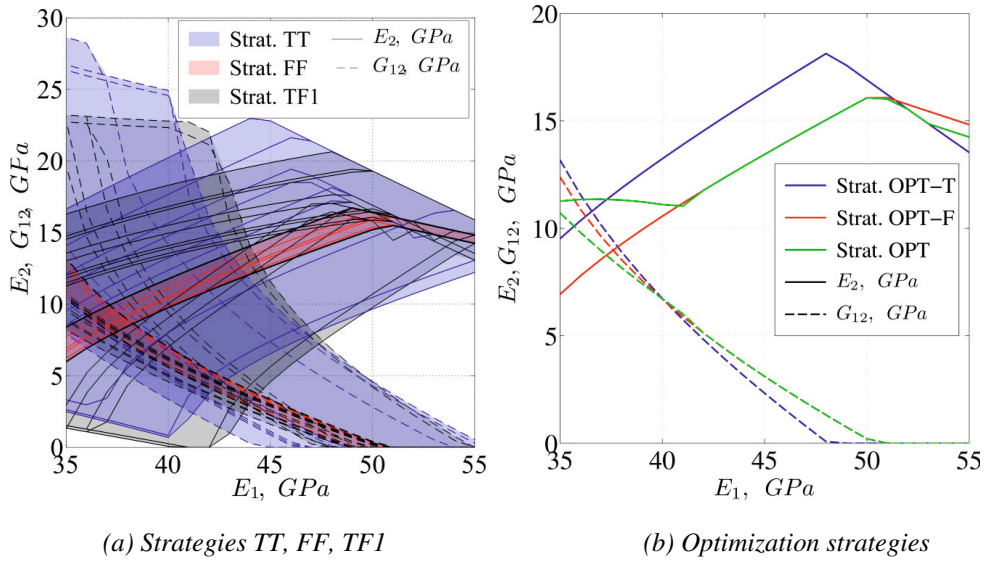


Figure 2.5. Back-calculated results for the  $[90/45/-45/0_2]_S$  glass-fiber/epoxy laminate.

The following conclusions can be drawn from the results in Fig. 2.5.

- The results from different strategies have an overlap region in Fig. 2.5(a). Given a realistic  $E_1$  range from 40 to 45 GPa in Fig. 2.5(a),(b), the estimations for  $E_2$  range from 10 to 16.4 GPa and for  $G_{12}$  from 2.2 to 7.0 GPa. These are reasonable ranges, however very wide.
- The results compare well to mean values of  $E_1 \approx 45.0$  GPa,  $E_2 \approx 12.3$  GPa,  $G_{12} \approx 3.4$  GPa, independently measured for the same material system by ASTM standards (Table G.2).
- The scatter is smallest for strategy *FF* (flexure in two directions), due to small scatter in experimental measurements (Table 2.3).
- Strategies *TT* and *TF1* have a relatively large scatter. The scatter is largest for strategy *TF2* (omitted from the plot).
- The back-calculation methods other than *FF* have little practical value here, due to the variability of experimentally measured laminate stiffnesses. Similar or even better estimates can be obtained from simple micromechanics formulas, e.g. as shown in Table C.4.

### 2.4.3.2 Carbon/vinylester

Four composite specimens were tested as part of an industry-collaboration research project. Carbon-fiber/vinylester specimens had been manufactured by an industrial partner as described in Table G.4 in Appendix G. At this stage of the project, no basic characterization of ply properties had yet been carried out. However, estimations for ply properties were needed for FE modelling. All plies,  $0^\circ$ ,  $90^\circ$ ,  $+45^\circ$  or  $-45^\circ$  have similar nominal area weight of fibers. All four specimens had the stacking sequence of  $[(+45/-45/0/90)_7 (+45/-45)]$ . It should be noted that this layout is not strictly symmetric, which means it has slight tension-flexure

coupling. The dimensions of the specimens and the  $L/h$  ratio of 42 was determined by the available component size. In order to account for through thickness shear deformation, shear modulus of  $G_{xz} = 2$  GPa was used in Equation (2.1). The results from tensile and flexural stiffness measurements are listed in Table 2.4.

Table 2.4. Effective tensile and flexural stiffnesses of balanced carbon-fiber/vinylester laminate ( $L/h = 42$ ).

Layup	Specimen	$\bar{E}_x^t$ , GPa	$\bar{E}_x^{f,s}$ , GPa
[ $(+45/-45/0/90)_7(+45/-45)$ ]	N1-1	40.0	32.1
	N2-1	40.4	31.3
	N3-2	40.3	32.2
	N4-1	39.8	33.0

Since only one type of specimen was available, strategy *TF1* (tensile and flexural stiffnesses in the same direction) was the only option to calculate with specimen pairs. The back-calculated moduli from the *TF1* and optimization strategies are plotted in Fig. 2.6.

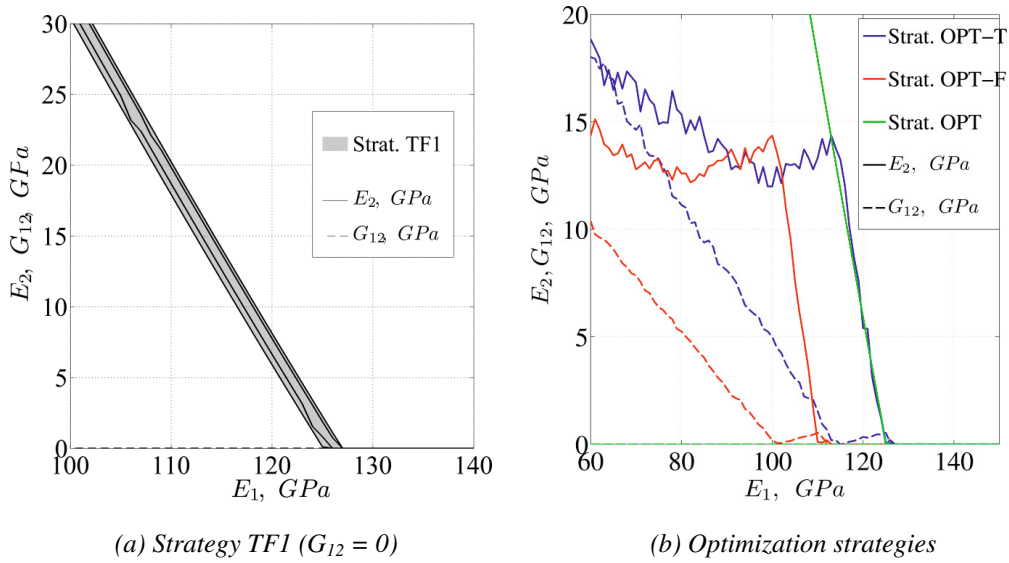


Figure 2.6. Back-calculated moduli for a [(+45/-45/0/90)<sub>7</sub>(+45/-45)] carbon-fiber/vinylester laminate.

If tensile and flexural stiffnesses are analyzed in a combined manner (strategies *TF1* and *OPT*), the shear modulus converges to value  $G_{12} = 0$ . In this specific layup, shear modulus has more influence on the flexural stiffness since  $\pm 45^\circ$  plies are the outermost. A simple interpretation of the result  $G_{12} = 0$  is that the measured flexural modulus is too low or the tensile modulus is too high, in order to obtain results which would make sense according to laminate theory. This situation is clarified further when tensile and flexural results are analyzed separately (strategies *OPT\_T* and *OPT\_F*). From tensile tests (strategy *OPT\_T*) a reasonable result could be  $E_1 = 100$  GPa,  $E_2 = 12.5$  GPa,  $G_{12} = 5$  GPa (which gives laminate



stiffnesses  $\bar{E}_x^t = 40.3$  GPa and  $\bar{E}_x^f = 37.6$  GPa with  $\nu_{12} = 0.3$ ). From flexural tests (strategy *OPT\_F*), similarly  $E_1 = 80$  GPa,  $E_2 = 12.5$  GPa,  $G_{12} = 5$  GPa (gives  $\bar{E}_x^t = 33.9$  GPa and  $\bar{E}_x^f = 31.9$  GPa with  $\nu_{12} = 0.3$ ).

It is clear that the discrepancy of results is too large to draw unambiguous conclusions. The reasons for the mismatch of the results are not clear. One factor is the un-symmetric layup — tension–bending coupling can influence the test results, especially for tensile testing. As a broad result,  $E_1 < 130$  GPa must hold, since  $E_2$  and  $G_{12}$  must be positive.

Tensile modulus of carbon fibers can be estimated from 230 to 235 GPa and the modulus of vinylster from 3 to 4 GPa [3]. Fibre volume fraction of  $V_f \approx 30\text{--}40\%$  was measured from burn-off tests (Table G.4). From simple rule-of-mixtures, approximate estimates for  $E_1$  are therefore  $230 \cdot 0.3 + 3 \cdot 0.7 = 71$  GPa to  $235 \cdot 0.4 + 4 \cdot 0.6 = 96$  GPa, which are in the same vicinity as the estimations from strategies *OPT\_T* and *OPT\_F*.

## 2.5 Estimation of ply uncertainty for cross-ply laminates

Figure 2.4 indicates that different strategies have a very different amount of scatter in the back-calculated results. The main reason for the scatter arises from the variation in experimentally measured laminate stiffnesses. Back-calculated moduli would have zero scatter in the hypothetical situation where laminate stiffness is measured with zero scatter. However, there are also other reasons besides the variation in experimental data. It is argued that the scatter in experimental laminate stiffnesses gives only the baseline scatter for the ply moduli which is further amplified depending on the layup and the strategy used in back-calculation.

In the following it is demonstrated that larger or smaller scatter of the ply moduli is obtained depending on how the experimental data is processed. That is, the intrinsic scatter of ply moduli is amplified by the back-calculation method itself. In order to investigate and verify which parameters control the scatter, numerical experiments based on Monte Carlo sampling are carried out. In the end, a procedure to evaluate the intrinsic ply modulus scatter is presented.

### 2.5.1 The parameter $\delta$

It can be shown that the influence of Poisson's ratio to the back-calculated moduli is close to negligible. If back-calculation equations (2.4)–(2.7) and (D.11) are analyzed without the influence of Poisson's ratios (assuming  $\nu_{12} = 0$ ), an interesting observation can be made. The back-calculation equations simplify to a fraction, where a linear combination of laminate stiffnesses is in the numerator and a parameter depending on the stacking sequence in the denominator. The parameter in the denominator is important, since it can act as an amplifier for the experimental uncertainties. If this parameter is small, close to zero, division with a small number results with a large influence from the experimental variability to the back-calculated moduli. This dimensionless parameter in the denominator is hereby defined as  $\delta$  for the previously defined four strategies *TT* to *TF2*:

$$\delta_{TT} = |\psi - \xi|, \quad (2.13)$$

$$\delta_{FF} = 12|\alpha - \beta|, \quad (2.14)$$

$$\delta_{TF1} = 12|\psi\beta - \alpha\xi|, \quad (2.15)$$

$$\delta_{TF2} = 12|\psi\alpha - \beta\xi|, \quad (2.16)$$

where geometry coefficients  $\psi$ ,  $\xi$ ,  $\alpha$ ,  $\beta$  can be calculated from Eqs. (D.1)–(D.4) in Appendix D. Parameters  $\delta_{TT}$  to  $\delta_{TF1}$  were obtained directly from Eqs. (2.4)–(2.7), (D.11). Parameter  $\delta_{TF2}$  has either tensile coefficients  $\psi$ ,  $\xi$  or flexural coefficients  $\alpha$ ,  $\beta$  switched, compared to  $\delta_{TF1}$ , because it has tensile and flexural stiffness from perpendicular specimens. Parameters  $\delta$ , as defined in Eqs. (2.13)–(2.16) represent the laminate layup and they can be calculated for either principal direction of the laminate, giving the same result.

### 2.5.2 Monte Carlo simulations (MCS)

The purpose of the following Monte Carlo experiments is to investigate the behavior of the mean and standard deviation of back-calculated moduli, in relation to previously defined stacking sequence parameter  $\delta$ .

Geometrically ideal (i.e. constant, equally thick plies) specimens are simulated, being composed of plies with random properties from a probability distribution. Each ply has the in-plane Poisson's ratio of  $\nu_{12} = 0.3$  and Young's moduli according to normal distributions. The moduli have mean values of  $\bar{E}_1 = 42$  GPa and  $\bar{E}_2 = 12$  GPa and standard deviations of  $s(E_1) = 2$  GPa and  $s(E_2) = 1$  GPa. The same  $E_1$  and  $E_2$  values are applied to all of the plies in a single simulated “specimen” (in one direction). However, different “specimens” have different  $E_1$  and  $E_2$ .

One can choose an arbitrary symmetric cross plied stacking sequence, composed of previously described plies with randomly chosen moduli and calculate a tensile and a flexural stiffness for this simulated “specimen”. A sample of simulated specimens is calculated for a single stacking sequence. The sample size is defined by integer  $n$ , which describes the number of specimens for one plate in one direction (which was measured for tension and flexure). The same definition of  $n$  was used in Section 2.3, where it was shown that  $n^2$  stiffness pairs can be formed for strategies  $TT$  and  $FF$ ; and  $2n^2$  pairs for strategies  $TF1$  and  $TF2$ . In order to obtain results for various layups (various parameter  $\delta$  values), 33 different stacking sequences are considered in simulations. These are all possible symmetric cross-plyed layups with less than ten plies.

Fig. 2.7 shows the arithmetic means of back-calculated moduli for strategies *TT* to *TF2*, for different sample sizes  $n$ , printed against parameter  $\delta$ . The following observations are evident.

- As sample size  $n$  increases, the uncertainty in the mean (or scatter of results) decreases, as expected.
- Ply mean moduli  $\bar{E}_1 = 42$  GPa and  $\bar{E}_2 = 12$  GPa are well captured for  $\delta > 0.4$  when  $n$  is large.
- Using parameter  $\delta$ , the scatter of the mean modulus is described similarly for all four strategies. When  $\delta < 0.4$ , the error in back-calculated mean can be large even for formidable  $n$  values (e.g.  $n = 20$  or  $n = 30$ ).

Fig. 2.8 shows the 95% confidence intervals (CI) for the standard deviation (SD) of back-calculated moduli. MCS results for different sample sizes  $n$  and strategies *TT* to *TF2* are printed against parameter  $\delta$ . Similarly to the mean modulus plots, the following observations are made.

- As sample size  $n$  increases, the confidence intervals narrow down, as expected.
- Ply standard deviations of  $s(E_1) = 2$  GPa and  $s(E_2) = 1$  GPa are well captured for  $\delta > 0.4$  when  $n$  is large.
- If sample size  $n \rightarrow \infty$ , the data from four strategies merges into one line, describing the characteristic behavior of SD in relation to parameter  $\delta$ . The back-calculated SD asymptotically approaches ply SD as  $\delta \rightarrow 1$ . The back-calculated SD becomes very large when  $\delta < 0.4$  and especially when  $\delta \rightarrow 0$ .
- Using parameter  $\delta$ , the behavior of the standard deviation is described similarly for all four strategies.

As a conclusion, Figs. 2.7–2.8 show that parameters  $\delta$ , as defined in Eqs. (2.13)–(2.16) control the scatter of the back-calculated results (mean and SD). Good estimations for ply moduli and standard deviation can be obtained if  $\delta > 0.4$ .

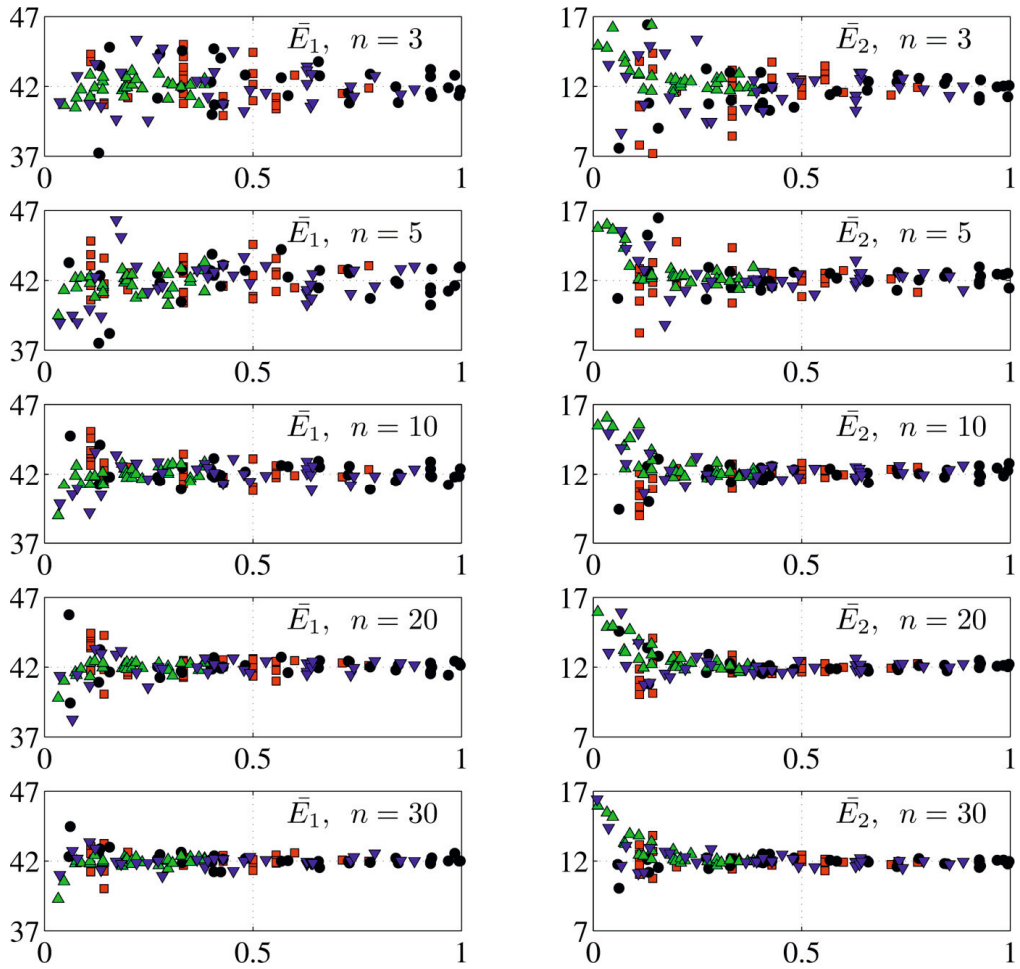


Figure 2.7. Means of back-calculated moduli  $E_1$  and  $E_2$  for different sample sizes  $n$  in MCS of strategies TT( $\square$ ), FF( $\circ$ ), TF1( $\wedge$ ), TF2( $\nabla$ ). All horizontal axes –  $\delta$ ; All vertical axes – mean  $E$  moduli (GPa).

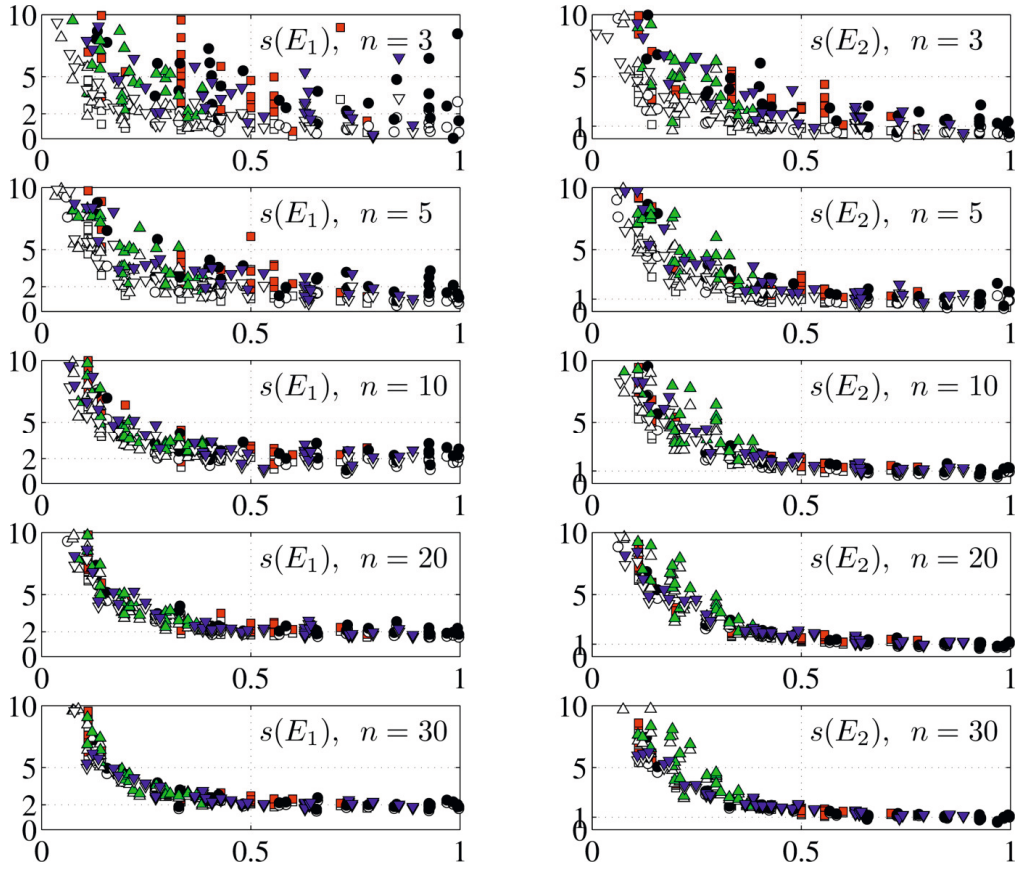


Figure 2.8. 95% CI for the SD of back-calculated moduli from MCS of strategies  $TT(\square)$ ,  $FF(o)$ ,  $TF1(\wedge)$ ,  $TF2(\nabla)$ . All horizontal axes –  $\delta$ ; All vertical axes – CI for SD (GPa). Filled markers – upper CI; empty markers – lower CI.

### 2.5.3 Estimation of ply uncertainty

The stacking sequence parameters  $\delta$  can be calculated for the cross-ply laminates given in Table 2.2, as shown in Table 2.5. The effect of parameter  $\delta$  can be seen best from the extreme values. Laminate  $[90_2/0_2/90_2]$  has  $\delta_{FF} = 0.9259$  which is very close to 1. Indeed, Fig. 2.4 confirms that this laminate has very small scatter for strategy  $FF$ . A huge scatter was observed in Fig. 2.4 for strategy  $TF2$  of laminate  $[0/90_4/0]$  because  $\delta_{TF2} = 0.0370$  is very close to zero. Figure 2.4 also shows larger scatter for strategy  $TT$ , compared to strategy  $FF$ . This can be expected, since  $\delta_{TT}$  values are smaller than  $\delta_{FF}$  values in Table 2.5.

To estimate the standard deviation (SD) of ply moduli, the confidence intervals (CI) of the SD of back-calculated moduli are plotted against parameter  $\delta$ . Figure 2.9 shows that standard deviations become large for small  $\delta$ . Confidence intervals for  $\delta_{TF2} = 0.037$  are (14.2, 28.3) for  $s(E_1)$  and (14.9, 29.7) for  $s(E_2)$  and lay out of the figure borders. However, these points with the other data points in Fig. 2.9 were used to curve fit a trend line  $s = C1 + \delta^{C2}$  for averaging purpose. The ply standard deviations can now be conservatively estimated from the upper

95% confidence interval as approximately 1 GPa for both  $E_1$  and  $E_2$ . This results with COV of 2.5% for  $E_1$  and 8% for  $E_2$ , which agrees reasonably with analogous results from the literature [48, 54].

Table 2.5. Parameters  $\delta$  for experimentally measured cross-ply specimens.

Strategy	$\delta$	
	$[90_2/0_2/90_2]$	$[0/90_4/0]$
<i>TT</i>	0.3333	0.3333
<i>FF</i>	0.9259	0.4074
<i>TF1</i>	0.2963	0.3704
<i>TF2</i>	0.6296	0.0370

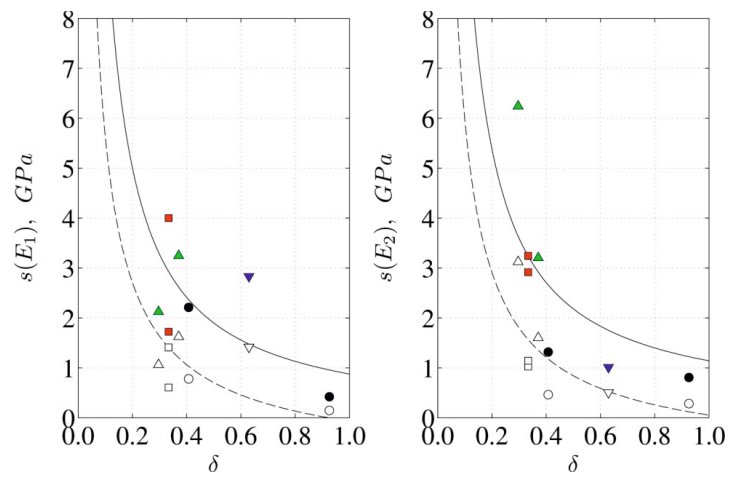


Figure 2.9. 95% CI for the SD of back-calculated moduli from experimental data and strategies *TT*( $\square$ ), *FF*( $\circ$ ), *TF1*( $\triangle$ ), *TF2*( $\nabla$ ). Filled markers – upper CI; empty markers – lower CI. (–) – upper trend line; (– –) – lower trend line.

## **3 Identification of ply moduli from vibration testing with FEA and GA**

### **3.1 Introduction**

One of the objectives of this work is to apply state-of-the-art dynamic methods for the evaluation of ply elastic constants. The final goal is to compare the results from different methods and to evaluate the potential of different methods for characterizing damage. Vibration measurement methods can be seen as intermediate dynamic techniques between static testing and wave propagation measurements. The measured natural frequencies usually span from a hundred to a few thousand hertz — a range hundred or thousand fold lower than frequencies in wave propagation measurements. The vibration test specimens are subjected to very small strains, i.e. the moduli are measured at or near the origin of the stress-strain curve. However, the strain rates are higher than quasi-static. The equipment required for vibration experiments is typically much simpler and cheaper, when compared to ultrasonic wave generation and detection.

A large number of manufacturing process parameters affects the geometry, stiffness or the density of the component. These three groups of properties determine the natural frequencies. Monitoring of natural frequencies can therefore easily reveal unwanted changes in production for quality control. Typical static test methods for stiffness (e.g. as in Chapter 2) suffer from boundary effects, non-uniform stress/strain fields, localized property measurement and high cost. Many specimens are needed to characterize various properties, which is further amplified when testing needs to be performed under different environmental conditions (high temperature, humidity). On the other hand, ultrasonic wave measurements need expensive and delicate equipment and also provide only localized properties. Vibration testing is therefore a relatively cheap and fast method to obtain global (averaged) stiffness properties of the test specimen.

Existing ASTM Standard Test Methods use continuous resonance excitation (E1875 [55]) or impulse excitation (E1876 [56]) for dynamic elastic constant measurements on (preferably isotropic) slender beam specimens. European Standard EN-843-2 [57] includes both resonance and impulse excitation methods. The measured fundamental vibrations can be of longitudinal, flexural or torsional type and these tests are usually referred as resonant beam tests in the literature. Aforementioned standards also give analytical equations for calculating elastic moduli from the fundamental resonant frequencies of slender beams. Natural frequencies from flexural vibrations have been employed to measure Young's modulus and shear modulus by Larsson [58] for free beams. A comparison between elastic moduli from in-plane and flexural vibrations of beams, strain gauge measurements and laminate theory predictions can be found in a technical memorandum [59].

A significant amount of research has been conducted about vibration testing of plates and its use for the elastic constant determination. A procedure was presented by McIntyre and Woodhouse [60] where four elastic constants are determined from the resonant frequencies of rectangular orthotropic plates with free edges. TV-holography with FEA calculations was used to determine the effective Young's moduli, shear modulus and Poisson's ratio by

Fällström and Jonsson [61]. Impulse loading on a plate with free boundary conditions was used by Pedersen and Frederiksen [62] to determine elastic constants in high temperatures. Also, a comparison between the dynamic and statically measured elastic constants is made. A numerical model for the plate and non-linear optimization (initial guess needed) was used for elastic constant determination in [63, 64]. Frederiksen showed in [65] that it is not possible to reliably estimate all 9 constants of orthotropic materials from typical vibration tests and introducing very un-sensitive constants (out-of-plane Young's modulus and Poisson's ratios) increases the uncertainty of others. A patent by Gibson and Ayorinde [66] describes a method and apparatus for deriving elastic constants from the resonance data of a freely-supported rectangular thin plate. Gibson summarized his and co-workers' vibration related research in 1990-ies in [67], which included testing for fiber distribution, elevated temperature behavior, interlaminar fracture toughness and testing of full scale components. The research by Rikards, Chate and co-workers [68–75] has focused on optimization using experiment design, where finite element analysis solutions at reference points are used to construct approximated response surfaces. A significant reduction in computational effort is reported, compared to direct optimization approaches. The elastic constants measured from three different methods (resonant frequencies of plates, resonant beam test and static testing) are compared by Lauwagie *et al.* [76]. The method to obtain elastic properties using natural frequency measurements on plates has also been applied to structural components in the construction industry [77].

Recently, researchers have started to use different versions of genetic algorithms (GA) for optimization to identify elastic constants or to detect damage, e.g. [78–82]. Although converging slowly, GA optimization does not require an initial guess and can easily escape local minima, as also discussed in Appendix E.2. A simple, however approximate analytical model for a free vibrating plate was derived by Gaul *et al.* [83] and used to obtain the elastic constants of isotropic and orthotropic plates. Commercial finite element software was used in [84] to carry out both FEA and optimization. A general overview of developments in vibration testing can be found in [13].

### **3.2 Experiments and numerical modelling**

Two types of data can in principle be obtained from vibration measurements: natural frequencies and corresponding mode shapes. Damping is hereby disregarded, similarly to numerous studies in the literature. Natural frequencies can be measured from the movements of a single point by just one accelerometer (the movements of a single point can contain all of the necessary natural frequencies). The measurement of mode shapes requires either a systematic placement of multiple sensors or non-contact measurements over a discrete grid. Constrained by the available equipment, only the natural frequencies are measured in this work. Impulse method is used for the frequency measurement since it follows simple principles and can be performed very quickly (see Appendix G.3 for the test set-up).

Each experimental frequency can only be compared to the numerical frequency with the same mode shape. Since there is no measurement of experimental mode shapes, great care must be taken when comparing frequencies. Some of the higher modes' frequencies may remain



experimentally undetected, as seen in several works in literature. The only way a more-less reliable comparison can be achieved is by employing only a small number of lowest natural frequencies and by making sure that sensor locations are well chosen. Higher mode frequencies are easier to miss, because they have numerous node lines (locations with zero displacement) and they possess less energy. If a natural frequency remains experimentally undetected, a problem occurs where compared experimental and theoretical frequencies do not belong to the same mode. This problem is discussed in ref. [81] where a strategy is suggested to overcome it.

Another issue with experimental measurements on plates is related to the boundary conditions (BC). The analytical description of plates tends to use idealized BC where constraints are either infinitely stiff or infinitely compliant. In addition, the expression of “simply supported” or “clamped” can mean four slightly different edge boundary conditions for both BC (possible to constrain in-plane displacements or in-plane forces), as discussed in [85]. Most fixed BC are troublesome to properly realize in experiments [67]. The easiest constraint to simulate in experiments is having no constraint at all. A good approximation of completely free boundary conditions (*FFFF*) can be achieved when plate is suspended by two threads, e.g. as seen in Fig. 3.1. Some testing was done with just a single thread attachment at midpoint of one edge and the differences compared to the two-thread solution were found to be negligibly small. Other researchers [83] have compared the frequencies from supporting the plate on thin needles or suspending with soft wires, and no significant difference was found. The *FFFF* boundary conditions have also been realized by supporting the plate on a cotton pad [84], suspending the plate horizontally by threads [66] or with small rubber supports at the nodal lines [61]. If the set-up from Fig. 3.1 is used for symmetric laminates ( $[B] = 0$ ), the in-plane loading from the self-weight and threads is theoretically uncoupled from small out-of-plane flexural displacements. In-plane and out-of-plane vibrations are easily separated by their magnitudes.

The placement of accelerometers and the exciting impulse for the plate needs to be on the most “flexible” location which has large out-of-plane displacements for all required low modes. Nodal lines for a specific mode are the lines with zero out-of-plane displacement. If the plate is measured or excited at a nodal line of a mode, the frequency of this mode is difficult to identify. As an example, for a free or one-end-fixed cantilever beam, a logical drive and measurement point is at the tip of the beam — all low modes have significant displacement there. Empirical observations from finite element modelling hint that the areas which have the largest displacements for rectangular plates (for a multitude of lowest modes), are the plate corners. The accelerometers were therefore attached to three corners of the plate. The plate was excited with an impulse hammer sequentially at all four corners (1, 2, 3, 4), as seen in Fig. 3.1. The mean frequency of three accelerometer measurements after four different excitations (altogether 12 data) was taken as the measured natural frequency. The details about experimental measurements are further described in Appendix G.3.

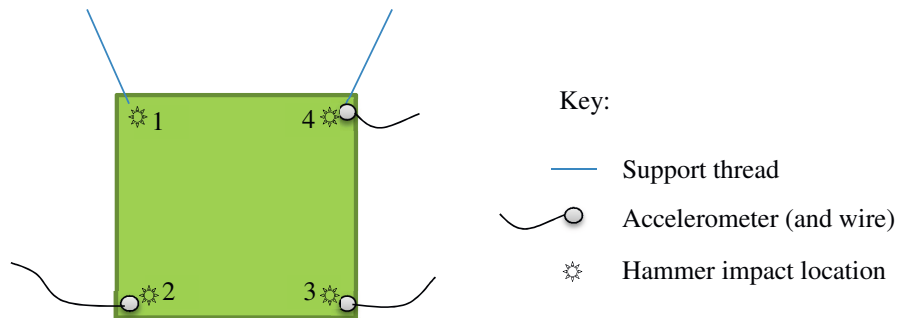


Figure 3.1. A schematic diagram of experimental set-up for vibration measurements.

An analytical or numerical model is required to calculate the natural frequencies. Some closed-form analytical solutions are available in [53, 85] for rectangular plate geometries and specific combinations of simply supported, clamped or free edge boundary conditions. An approximate analytical method for all edges free has been proposed, e.g. by Gaul *et al.* [83]. Unfortunately, no exact closed form solution is known for the rectangular *FFFF* plate, as noted e.g. by [65, 67]. Approximate analytical solutions can provide an initial guess for the optimization procedure, significantly reducing the computational effort, but actual modeling during optimization should be performed by more precise numerical means.

A popular approach among researchers is to employ finite element analysis (FEA) to calculate natural frequencies, even though it has a high computational cost. Direct optimization using FEA for forward calculations requires large computational effort. Rikards, Chate and co-workers used FEA only at reference points and response-surface approach to reduce the computational effort up to 50 to 100 times for the calculation of numerical frequencies. FEA gives almost unlimited freedom in terms of variations of specimen geometry, layup and boundary conditions while the analytical solutions are only suitable for specific set-ups.

FEA based approach is also employed in current work. A finite element toolbox, written for MATLAB by Ferreira [86] is openly available and calculates the natural frequencies for the vibrations of laminated plates. This software was slightly modified by the author to enable the calculation of *FFFF* BC, as this did not exist in the original code.

### 3.3 Discrepancies of the models

The experimental set-up (Appendix G.3) has some apparent deviations from the idealized *FFFF* linear elastic plate. These influences are assumed to be negligible in the following; however, their actual influence is currently unknown.

- A small additional mass (3.3 g) is added by mounting the accelerometers to three corners of the plate. Even though the mass of accelerometers is very small in comparison to the mass of the plates (< 0.5 %), it might be significant, considering the effective weight of the corners, relative to the whole plate.

- Mass related argument applies also to the small holes (ca. 5 mm diam.) drilled in the plate corners and edges, to provide support points for suspending threads.
- Influence from accelerometer wires and suspending threads.
- The phenomenon of damping exists in reality (inherent material damping, air, wires, threads) and tends to lower the frequencies, compared to the undamped FEA model.
- Matrix dominated moduli (such as  $E_2$ ,  $G_{12}$ ) can display viscous material properties and therefore these moduli are expected to vary with strain rate. Experimental evidence for strong strain rate dependence also exists for fiber dominated  $E_1$  in compression (see Appendix A.5).

The use of non-contact excitation and measurement devices (loudspeakers, microphones, laser scanning vibrometer, permanent magnets, etc.) could improve the experimental set-up in the future.

### 3.4 Comparison of FEA trial frequencies

The following section serves two objectives. First, there is a need to verify the implemented modifications (introducing *FFFF* boundary conditions) to the original MATLAB code of [86]. Secondly, a comparison of natural frequencies obtained from the commercial finite element software Abaqus (v. 6.12) and MATLAB FEA code gives indications of the performance and precision of the latter.

The virtual trial plate is unidirectional and orthotropic with material properties and plate characteristics (length  $a$ , width  $b$ , thickness  $h$ , density  $\rho$ ) defined in Table 3.1. Material is defined by all 9 orthotropic elastic constants in Abaqus. It is evident that through-thickness shear deformations are considered in the MATLAB FEA code which requires 6 elastic constants ( $E_1$ ,  $E_2$ ,  $\nu_{12}$ ,  $G_{12}$ ,  $G_{13}$ ,  $G_{23}$ ). Five degrees of freedom exist for each node, see Ch. 13.8 in [86] for additional details. The plate from Table 3.1 has the first five mode shapes schematically sketched in Fig. 3.2. The nodal line notation ( $i$ ,  $j$ ) is given by the number of nodal lines near-parallel to the axes 1 and 2, respectively. Numerical FEA estimations generally depend on the mesh density and the used element types. Possible numerical model errors are systematic and therefore can only be revealed from comparison with a more accurate model. Free vibration frequencies calculated by two different programs, element types and mesh densities are studied in the following.

Table 3.1. Trial plate properties.

Property	Value
$E_1$	40 GPa
$E_2, E_3$	15 GPa
$G_{12}, G_{13}, G_{23}$	5 GPa
$\nu_{12}, \nu_{13}, \nu_{23}$	0.3
$a, b$	300 mm
$h$	6.6 mm
$\rho$	1970 kg/m <sup>3</sup>

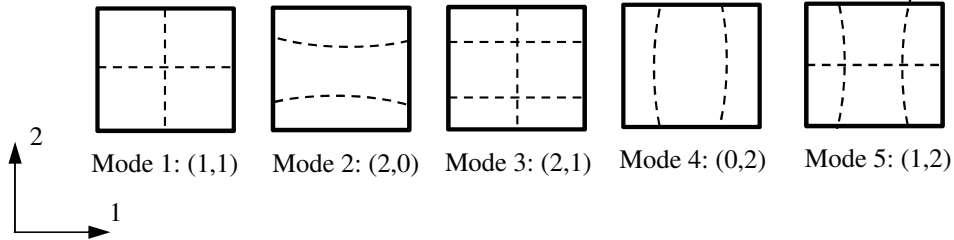


Figure 3.2. Node lines for the mode shapes of the trial plate.

Mesh is defined by the number of elements in plate length and width directions (i.e. mesh 10x10 means square elements with side lengths of 30 mm in a 30x30 cm<sup>2</sup> plate). Three-dimensional elements are brick-shaped and their mesh is described e.g. as 182x182x4 (cubes with 1.65 mm sides, since plate thickness is 6.6 mm).

The plate is modelled in Abaqus with general purpose shell elements (S4(R): 4-node rectangular linear doubly curved thin or thick shell; S8R 8-node rectangular doubly curved thick shell; both with six degrees of freedom for one node) and general purpose solid brick elements (C3D20(R): 20-node, quadratic, with three degrees of freedom for one node). The R-versions of previous elements (names ending with letter “R”) have so-called reduced integration property (fewer integration points, faster calculation) which also improves their behavior against shear locking. Further details about Abaqus element types can be found in [87].

First five calculated natural frequencies are shown in Fig. 3.3, where the horizontal axes display mesh density characteristic  $q$  in log scales (i.e. the plate in-plane mesh density is  $q \times q$ ). The mesh densities in Fig. 3.3 vary from 10x10 to 300x300 for shell elements. The results from 3-D brick elements C3D20, C3D20R agree with at least 0.01 Hz precision for two very fine meshes 136x136x6 and 182x182x4 and this is considered as “true” result and denoted by a horizontal dashed line (i.e. the characteristic  $q$  in the figure does not apply to 3-D elements).

The following observations can be made from Fig. 3.3. Firstly, MATLAB FEA code [86] behaves similarly to 4-node shell elements and almost exactly so for bending-dominated modes 2 and 4. There are some differences for modes 1, 3, 5 which have more in-plane shear ( $G_{12}$ ) contribution. For fine mesh densities, Abaqus shell and brick element results converge. For coarse mesh densities, shell and MATLAB FEA results overestimate the frequencies. This behavior is expected to be systematic (also seen in examples in [86]), i.e. true frequencies are expected to be lower than from the coarse mesh MATLAB FEA model.

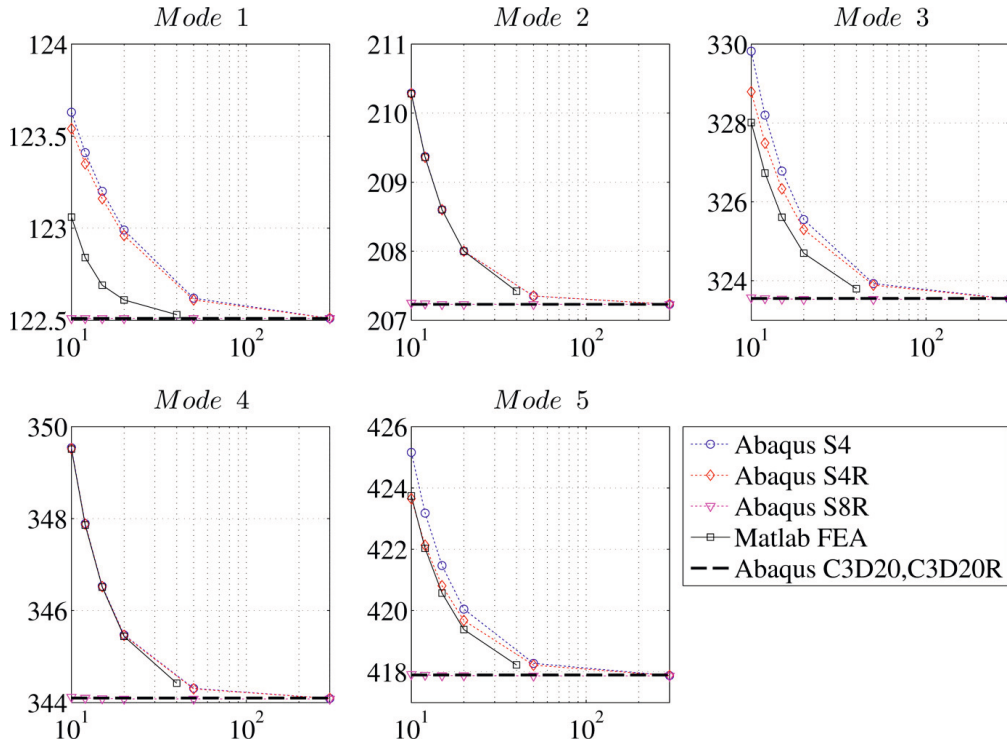


Figure 3.3. Natural frequencies of the trial plate (vert. axis, Hz) as a function of mesh density (hor. axis, characteristic  $q$  for nr. of elements).

Fig. 3.3 clearly shows that natural frequencies calculated by FEA depend on the chosen element type and mesh size. There is a considerable difference in calculation times for the MATLAB FEA already between mesh densities  $10 \times 10$  and  $12 \times 12$ , let alone  $20 \times 20$  or finer mesh. In optimization, many of these “forward” FEA calculations need to be performed and therefore a mesh density of  $10 \times 10$  is the finest that can currently be allowed for reasonable computing times on a desktop PC. The systematic error from calculating with a coarse  $10 \times 10$  mesh can roughly be evaluated from the results of the virtual trial plate (it has similar physical characteristics to the real plates). The error for the  $i$ -th mode frequency is hereby defined as the relative difference between the largest and smallest calculated frequency displayed in Fig. 3.3 as:

$$err_i = \frac{\max(f_i) - \min(f_i)}{\min(f_i)} \cdot 100\% \quad (3.1)$$

The calculated errors are presented in Table 3.2. Based on these results, a conservative range containing the true frequency and accounting for systematic errors of the FEA model, for any of the first five natural frequencies, is estimated as  $(0.98f_i, f_i)$ , where  $f_i$  is obtained by  $10 \times 10$  mesh with MATLAB FEA. That is, the true frequency can be up to 2% smaller from the frequency calculated by the approximate numerical model.

Table 3.2. Estimated errors  $err_i$  (Eq. (3.1)) from frequencies in Fig. 3.3.

Mode $i$	$err_i, \%$
1	0.9
2	1.5
3	1.9
4	1.6
5	1.7

### 3.5 Sensitivity study

Previous authors have pointed out that different modes have different sensitivities to ply moduli, e.g. [61, 77]. The trial plate (Table 3.1) was investigated by changing each of the input elastic moduli, one at a time, by  $\pm 10\%$  and visualizing the effects of this change on the six first natural frequencies. The results are calculated by the MATLAB FEA toolbox [86] on a  $10 \times 10$  mesh and shown in Fig. 3.4.

Fig. 3.4 shows that the six first modes are dominated by three elastic moduli:  $E_1$ ,  $E_2$ ,  $G_{12}$ . The influential moduli for each specific mode can be guessed from the mode shapes, which give hints about the basic forms of deformation (torsion/twist, bending in two directions) dominating the plate behavior. For example, the first mode in Fig. 3.2 displays torsion/twist and is therefore very sensitive to shear modulus  $G_{12}$ , second mode to  $E_2$  and fourth mode to  $E_1$ . This is exactly what is seen in Fig. 3.4.

In addition, it is evident that through-thickness shear moduli  $G_{13}$ ,  $G_{23}$  do not significantly influence any of the first modes. Through thickness shear moduli have significant influence for thick plates (when  $a/h$ ,  $b/h$  are less than e.g. 10). In addition, the influence of transverse shear increases for higher modes, since the number of wavelengths in the structure increases [58]. Also, in general low values of  $G/E$  increase the influence of through-thickness shear, just as previously discussed in Section 2.2. Since all plates in the experimental section are either similar or thinner than the trial plate, it can be expected that moduli  $G_{13}$ ,  $G_{23}$  are very difficult to determine from the following free vibration measurements.

Poisson's ratio  $\nu_{12}$  is a difficult property to determine because it has a generally low sensitivity to the natural frequencies, as seen in Fig. 3.4. Various researchers [13, 60, 76] discuss the length-to-breadth aspect ratio of the plate in relation to the Poisson's ratio. They state that  $\nu_{12}$  can be obtained at specific aspect ratios of specimens ( $a/b = (E_x/E_y)^{0.25}$ ). A method based on X-shaped mode shapes, rather than frequency, was proposed in [61] to measure the in-plane  $\nu$ . For isotropic plates, the frequency ratio of O and X-modes is solely determined by the Poisson's ratio, strong sensitivity of these modes to  $\nu_{12}$  also occurs for orthotropic plates, when aspect ratio  $a/b$  is chosen suitably. The reported results of identified  $\nu_{12}$  in literature sources usually have larger scatter than other constants and they do not compare as well as  $E_1$ ,  $E_2$ ,  $G_{12}$  to other independent methods.

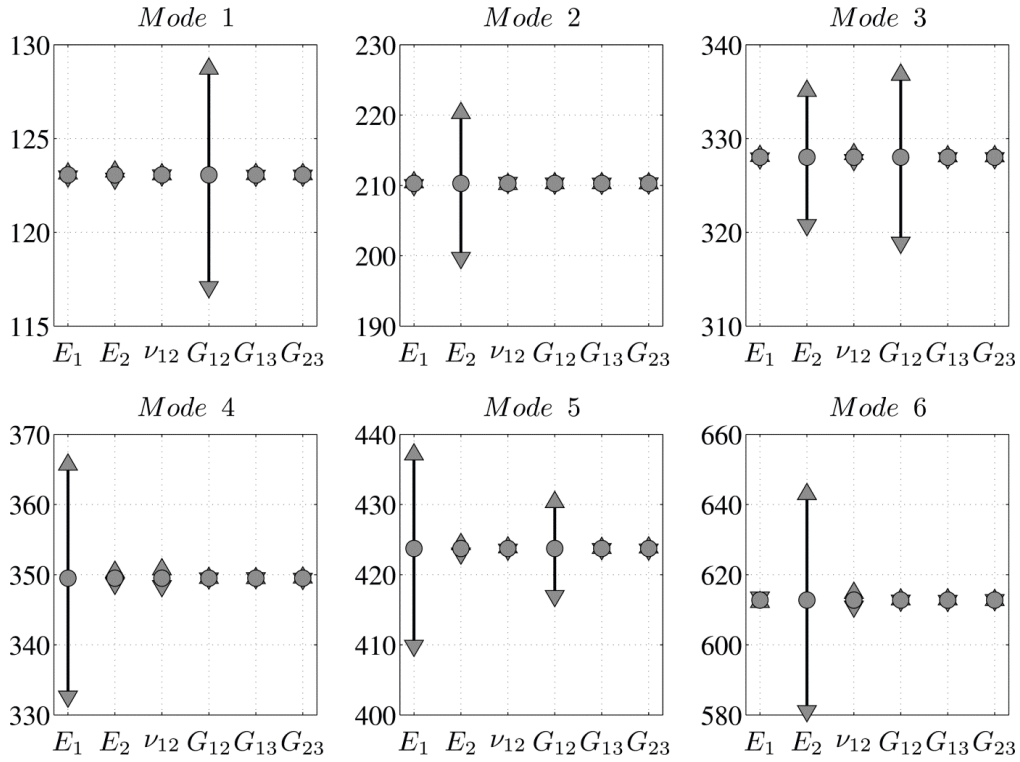


Figure 3.4. Changes to the natural frequencies (Hz) of the trial plate (o) by increasing (▲) or decreasing (▼) elastic moduli by 10%, one at a time.

Other input quantities needed to calculate natural frequencies, besides the elastic constants, are: plate length  $a$  and width  $b$ , thickness  $h$  and mass density  $\rho$ . Their sensitivity to frequencies can be investigated by exactly the same way as was done for elastic constants in Fig. 3.4. The actual amount of variability expected from these non-elastic properties is much less than  $\pm 10\%$  used for elastic moduli previously. It is estimated that in-plane dimensions  $a$  and  $b$  could vary by  $err_{ab} = \pm 0.2\%$ , thickness  $h$  and density  $\rho$  by  $err_{h\rho} = \pm 1.4\%$ . These errors are taken equal to the coefficients of variation (COV) of experimentally measured properties (Table G.5 in Appendix G.3).

The sensitivity results for non-elastic plate properties are displayed in Fig. 3.5, which displays some interesting characteristics. The variation in plate length  $a$  or width  $b$  has very little influence to the bending modes' frequencies if curvature is in the opposite direction (mode 2 for  $a$  and mode 4 for  $b$ ). Approximate analytical frequency relations [60, 83] show that plate natural frequencies are proportional to the thickness and inversely proportional to the square root of mass density. This means the variation of thickness ( $\pm 1.4\%$ ) translates directly into the same variation ( $\pm 1.4\%$ ) of natural frequencies. And the variation of density (also  $\pm 1.4\%$ ) translates into  $\left(\frac{1}{\sqrt{1.014}} - 1\right) \cdot 100\% \approx -0.7\%$  or  $\left(\frac{1}{\sqrt{0.986}} - 1\right) \cdot 100\% \approx 0.7\%$  change in natural frequencies. This behavior can be observed in Fig. 3.5.

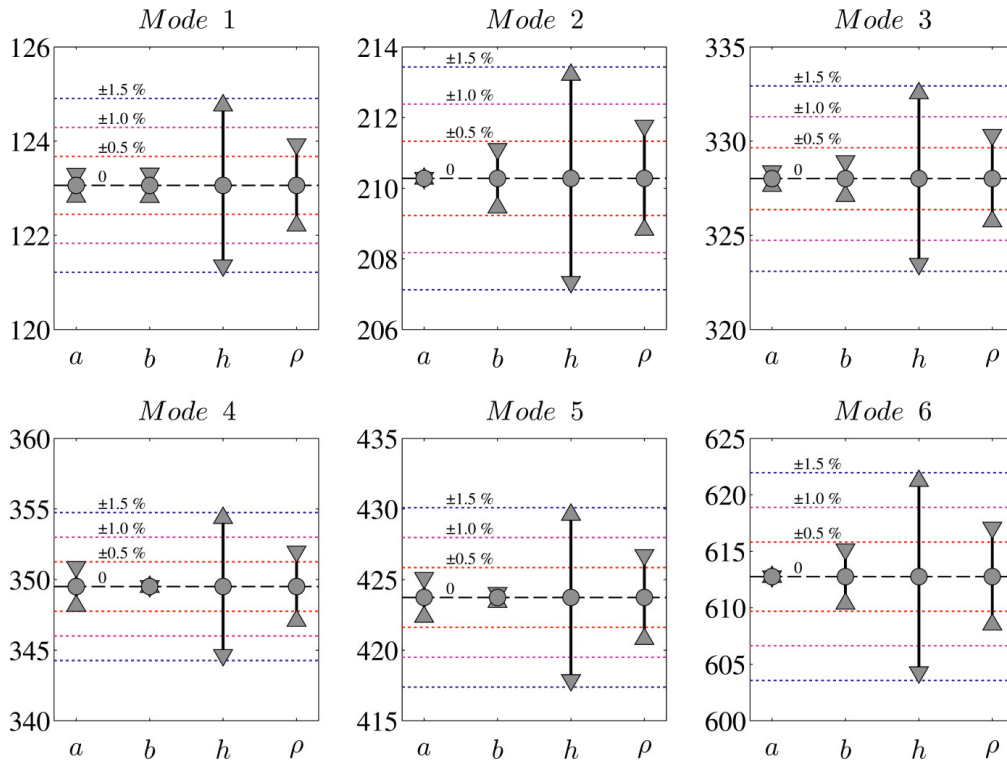


Figure 3.5. Changes to the eigenfrequencies (Hz) of the trial plate (o) by increasing ( $\wedge$ ) or decreasing ( $\vee$ ) non-elastic plate properties by a given amount, one at a time. Plate in-plane dimensions  $a, b$  are varied  $\pm 0.2\%$ , thickness  $h$  and density  $\rho$  by  $\pm 1.4\%$ .

The relationship between plate sides  $a, b$  and frequencies is more complex. However, Fig. 3.5 shows that the sum of frequency changes from the variation of both plate side lengths  $a$  and  $b$  ( $err_{ab} = \pm 0.2\%$ ) is  $2 \cdot 0.2 = 0.4\%$  for the six first modes. An explanation for this observation is unknown. Increasing the side length makes the plate more compliant and therefore lowers the frequency.

Density is here calculated from mass and volume, where the mass and mean values of length and width have low variability. Therefore, in this kind of measurement the thickness variation also causes most of the density variation (as evident in Table G.5). If measured thickness is larger than actual, the calculated density is lower than actual and vice versa. Fig. 3.5 shows that if thickness is larger and density lower, these effects add up as the combined effect to the natural frequency (the same if thickness is smaller and density higher). Based on previous discussion, the estimate for the variation of natural frequencies from the variation of non-elastic plate properties ( $a, b, h, \rho$ ) is estimated as:



$$err_{non-el} = 2err_{ab} + err_{hp} + \left( \frac{1}{\sqrt{1 - \frac{err_{hp}}{100}}} - 1 \right) \cdot 100\% . \quad (3.2)$$

This is a conservative estimate, since in reality it is unlikely that all these properties deviate in the same direction simultaneously. For the previously estimated quantities ( $err_{ab} = \pm 0.2\%$ ,  $err_{hp} = \pm 1.4\%$ ) the deviation for the frequencies becomes  $err_{non-el} = \pm 2.5\%$ . When the FEA calculated errors, as presented in Fig. 3.5 are added up, exactly the same  $\pm 2.5\%$  result is obtained for each of the six modes.

### 3.6 Inversion from experimental data

#### 3.6.1 Approximate analytical solutions

Simple analytical models from [60, 83] are hereby employed to invert the elastic constants from the exact frequencies as calculated from the numerical experiment of the trial plate (Table 3.1). In addition to density and geometry of the plate, these approaches require the natural frequencies corresponding to three specific mode shapes: torsion dominated mode (1,1) and flexure dominated modes (2,0), (0,2). Also, the coefficient  $\nu_x\nu_y$ , which is composed of Poisson's coefficients in two in-plane directions, is required beforehand.

Table 3.3 shows the results from three guesses:  $\nu_x\nu_y = 0.12$  (used in [83]);  $\nu_x\nu_y = 0.018$  (a good fit to the correct result from formulas [83]); and  $\nu_x\nu_y = 0.026$  (a good fit to the correct result from formulas [60]). It is evident that the choice of  $\nu_x\nu_y$  is fairly significant and even for a good guess, the calculated moduli remain approximate. That is, even by fine tuning the Poisson's ratio input (such information would not be available in the real case), the estimates remain approximate. However, the results in Table 3.3 also show that the estimations based on  $\nu_x\nu_y = 0$  can serve as a good initial guesses.

Table 3.3. The evaluation of elastic constants based on approximate analytical formulas [60, 83].

$$f(1,1) = 122.5 \text{ Hz}; f(2,0) = 207.2 \text{ Hz}; f(0,2) = 344.1 \text{ Hz};$$

El. constant	Ref. [83]		Ref. [60]		Correct values (Fig. 3.3)
	$\nu_x\nu_y = 0.12$	$\nu_x\nu_y = 0.018$	$\nu_x\nu_y = 0.12$	$\nu_x\nu_y = 0.026$	
$E_1$ , GPa	36.7	40.9	36.1	40.0	40
$E_2$ , GPa	13.3	14.8	13.1	14.5	15
$\nu_{12}$	0.58	0.22	-	-	0.3
$G_{12}$ , GPa	2.3	5.0	4.5	4.5	5

#### 3.6.2 FEA with SGA optimization

##### 3.6.2.1 The fitness function

A trial plate was studied in Sections 3.4 and 3.5 to obtain approximate estimations for the systematic errors and random variation of five first natural frequencies. The systematic error

arising from the FE model with a coarse mesh size was conservatively estimated as 2% at most in Section 3.4. The random scatter in natural frequencies arising from variation in non-elastic (physical) plate properties was estimated at most to  $err_{non-el} = \pm 2.5\%$  in Section 3.5. The variation from experimental measurements (repeated frequency measurements of the same kind) is estimated based on data in Table G.6 in Appendix G.3 as  $err_{exp} = \pm 0.7\%$ . Hereby, an assumption is made that the systematic error estimate and the random variation  $err_{non-el}$  obtained from the trial plate study are also valid for the current experimentally measured plates. For such case, a conservative estimate for errors in the natural frequencies (all effects simultaneously superposed) can be evaluated in Eqs. (3.3)–(3.4).

$$err_f^{syst} \leq 2\% \quad (3.3)$$

$$err_f^{rand} = err_{non-el} + err_{exp} = \pm 3.2\% \quad (3.4)$$

The mean values of experimentally measured plate data are given in Table 3.4 for three different glass-fiber plates. Plate *TR10\_2* is unidirectional and plates *TR11\_1* and *TR11\_2* are symmetric, cross-plyed. Details about the materials and production of these plates can be found in Tables G.1 and G.3 in Appendix G. Additional details about physical properties and experimentally measured natural frequencies are available in Tables G.5 and G.6.

Table 3.4. Experimentally measured data for plates.

(a) Physical properties

Plate	Layup	$a$ , mm	$b$ , mm	$h$ , mm	$\rho$ , kg/m <sup>3</sup>
<i>TR10_2</i>	[0 <sub>8</sub> ]	300	301	6.51	1953
<i>TR11_1</i>	[90 <sub>2</sub> /0 <sub>2</sub> /90 <sub>2</sub> ]	294	293	4.79	1958
<i>TR11_2</i>	[90/0 <sub>4</sub> /90]	295	297	4.81	1973

(b) Natural frequencies, Hz

Plate	Layup	$f_1^{\text{exp}}$	$f_2^{\text{exp}}$	$f_3^{\text{exp}}$	$f_4^{\text{exp}}$	$f_5^{\text{exp}}$
<i>TR10_2</i>	[0 <sub>8</sub> ]	126.8	205.6	327.4	345.3	424.1
<i>TR11_1</i>	[90 <sub>2</sub> /0 <sub>2</sub> /90 <sub>2</sub> ]	88.7	155.9	234.8	255.2	306.3
<i>TR11_2</i>	[90/0 <sub>4</sub> /90]	88.4	185.9	230.9	255.0	287.7

Based on previous error estimations, it is conservatively acknowledged that random component of error for natural frequency is at most  $err_f^{rand} = \pm 3.2\%$ . The systematic error from the FEA analysis means that “true” numerical natural frequency is in the range  $(0.98f_i^{calc}, f_i^{calc})$ .

The fitness function quantifies the difference between measured and guessed (calculated) natural frequencies. The optimization procedure aims to minimize this difference (and

maximize the fitness) in a systematic way. However, the fitness function also needs to account for the possibility that  $i$ -th natural frequency has some systematic and random errors. The mean values are more likely to be true with regard to random errors. A simple yet approximate way to account for errors and realize these principles is by using a trapezoidal distribution for the fitness, as seen in Fig. 3.6. Notations  $f_i^{exp}$  and  $f_i^{calc}$  stand for experimentally measured and guessed/calculated frequencies by the FEA, for the  $i$ -th mode. The constant  $c = 1/0.98 = 1.0204$  defines the range of frequencies ( $f_i^{exp}$ ,  $cf_i^{exp}$ ) where all results are considered correct (stems from coarse mesh FEA systematic error).

Fitness obtains a high value as the guessed/calculated natural frequencies approach the measured frequencies. The aim of the optimization is to maximize fitness (e.g. see SGA in Appendix E.2). Fitness function is defined here to be non-negative. The fitness function in Eq. (3.5) employs the sum of functions  $w_i$ , over modes  $i$  as defined by Eqs. (3.6)–(3.8). The maximum contribution from each mode to fitness can be  $w_i = 1$ . If guessed  $f_i^{calc}$  is outside the range ( $lo$ ,  $hi$ ) then  $w_i = 0$ . The maximum possible fitness in current case is equal to the number of measured modes (i.e. five).

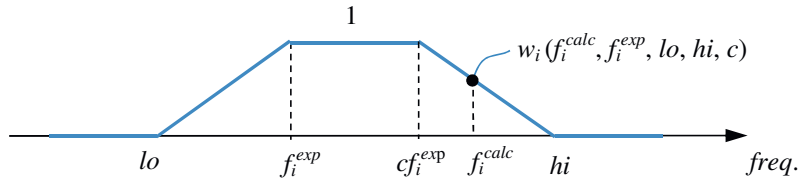


Figure 3.6. Definition of function  $w_i$ .

$$fitness = \sum_{i=1}^5 w_i(f_i^{calc}, f_i^{exp}, lo, hi, c) \quad (3.5)$$

where

$$w_i(f_i^{calc}, f_i^{exp}, lo, hi, c) = \begin{cases} 0 & \text{if } f_i^{calc} \leq lo \text{ or } f_i^{calc} \geq hi \\ \frac{f_i^{calc} - lo}{f_i^{exp} - lo} & \text{if } lo < f_i^{calc} \leq f_i^{exp} \\ 1 & \text{if } f_i^{exp} < f_i^{calc} \leq cf_i^{exp} \\ \frac{hi - f_i^{calc}}{hi - cf_i^{exp}} & \text{if } cf_i^{exp} < f_i^{calc} < hi \end{cases} \quad (3.6)$$

and

$$lo = f_i^{exp} \left( 1 - \frac{|err_f^{rand}|}{100} \right) \quad (3.7)$$

$$hi = cf_i^{exp} \left( 1 + \frac{|err_f^{rand}|}{100} \right) \quad (3.8)$$

The entire plausible range ( $lo$ ,  $hi$ ) and the fitness function components  $w_i$  are defined by:

- the mean experimental frequency  $f_i^{exp}$
- constant  $c = 1.0204$  (from systematic error  $err_f^{syst}$ )
- random error estimate  $|err_f^{rand}| = 3.2 \%$ .

The unknown variables are engineering constants  $E_x$ ,  $E_y$ ,  $\nu_{xy}$ ,  $G_{xy}$ ,  $G_{xz}$ ,  $G_{yz}$ , constrained by the thermodynamic constraints described in Appendix B.

### 3.6.2.2 SGA optimization results

The detailed description of the simple genetic algorithm (SGA) optimization can be found in Appendix E.2. It is run from a self-written toolbox in MATLAB. The experimental data was presented in Table 3.4 and the fitness function defined by Eqs.(3.5)–(3.8). The parameters for SGA based optimization are reported in Table 3.5 for all plates. Computation time is saved by narrowing the search variable ranges, based on coarse initial estimations. The resolution is defined very finely for the sensitive moduli ( $E_x$ ,  $E_y$ ,  $G_{xy}$ ), below 0.01 GPa, and very coarsely for non-sensitive constants ( $\nu_{xy}$ ,  $G_{xz}$ ,  $G_{yz}$ ). The binary string lengths designated to the variables are 10, 9, 9 digits for  $E_x$ ,  $E_y$ ,  $G_{xy}$  and 2 digits for each of the non-sensitive moduli, resulting in a 34 binary digit individual for each of the plates. All laminates are considered as homogeneous orthotropic media (i.e. a single orthotropic layer), disregarding its actual layered structure. The optimization procedure searches for the effective laminate properties (denoted by  $x$ - $y$ - $z$  axes), where  $z$  is normal to the plate.

Table 3.5. SGA parameters.

Pop. size	$n = 25$
Nr. of generations	$t = 30$
Fitness scaling parameter	$nxavg = 2$
Probability of cross-over	$p_{cross} = 90 \%$
Nr. of elites	$n_{elites} = 1$
Mutation probability	$p_{mut} = 2 \%$

SGA optimization was run consecutively 50 times for each plate inversion. The evolution of fitness can be seen in Fig. 3.7(a). Each of the 50 SGA optimizations took  $n_{feval} = nt = 25 \cdot 30 = 750$  fitness function evaluations. Figure 3.7(a) confirms that the population size and the number of generations in Table 3.5 were selected appropriately.

The maximum  $fitness = 5$  was achieved for all plates, but not in every optimization run. Only the results which reached  $fitness = 5$  are of interest, since they converged to the unity-valued region for all five mode frequencies (see Fig. 3.6). Several of these high-fitness results proved to be duplicates of each other, so only the unique high fitness results were extracted. Out of 50 runs for each plate, 33, 23 and 13 unique high fitness results were obtained for plates  $TR10\_2$ ,  $TR11\_2$  and  $TR11\_1$ , respectively. These results are multiple solutions for the defined optimization problem.

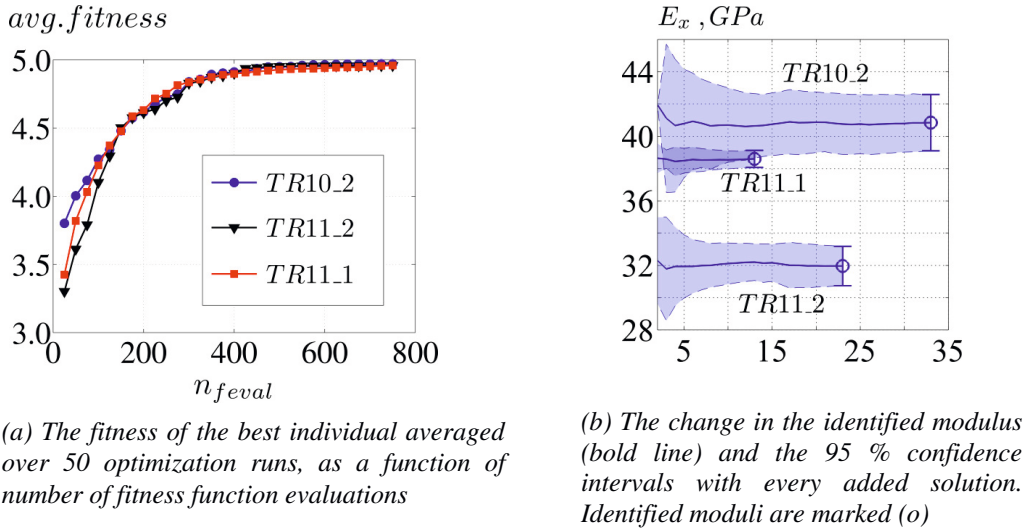


Figure 3.7 Details of SGA optimization.

The mean of unique high fitness results is defined as the identified modulus. Its coefficient of variation (COV) characterizes the spread in obtained solutions. Figure 3.7(b) shows how the mean and its estimated 95 % confidence intervals develop with every added unique high-fitness solution for modulus  $E_x$ . Similar behavior was seen for  $E_y$ ,  $G_{xy}$ . The initial fluctuations die out and a steady state is achieved after ca. 10 unique high fitness solutions, as the addition of another result does not change the mean significantly. The mean and coefficient of variation (COV) of these unique high fitness optimization results are reported in Table 3.6.

Table 3.6. Statistical data of  $q$  unique  $fitness=5$  results from 50 SGA optimizations.

El. constant	$TR10\_2$ ( $q = 33$ )		$TR11\_1$ ( $q = 13$ )		$TR11\_2$ ( $q = 23$ )	
	Mean	COV, %	Mean	COV, %	Mean	COV, %
$E_x$ , GPa	40.8	2.1	38.6	0.6	32.0	1.8
$E_y$ , GPa	15.1	1.2	14.3	1.3	21.5	1.0
$\nu_{xy}$	0.22	44.6	0.01	360.6	0.05	154.6
$G_{xy}$ , GPa	5.5	1.0	4.5	0.6	4.6	0.8
$G_{xz}$ , GPa	5.6	22.0	5.5	15.8	5.6	24.7
$G_{yz}$ , GPa	5.7	20.1	5.4	17.8	5.4	19.1

Some constants in Table 3.6 have consistently low COV, whereas others have consistently high COV. The constants with low COV are the same which had high sensitivities to natural

frequencies, as was seen in Fig. 3.4. The high COV constants inversely have low sensitivities. Although these high COV constants ( $v_{xy}$ ,  $G_{xz}$ ,  $G_{yz}$ ) were identified from a very coarse search variable range (only 2 binary digits for one constant), the main reason for the high COV value stems from their insensitivity. This assumption was confirmed by other optimizations, carried out but not reported here, where ( $v_{xy}$ ,  $G_{xz}$ ,  $G_{yz}$ ) also had fine resolution in search variable ranges.

The COV of optimization results shows which constants are identified consistently. If COV is low, the optimization results have low variability and the mean is expected to identify the corresponding elastic property. If COV is high, the optimization results have high variability i.e. the range of possible constant values is very wide. The mean values of constants which have a low COV (i.e.  $E_x$ ,  $E_y$ ,  $G_{xy}$ ) can be seen as the elastic constants obtained from vibration testing. The other constants ( $v_{xy}$ ,  $G_{xz}$ ,  $G_{yz}$ ) need some additional experimental considerations for identification.

It needs to be verified how well do the natural frequencies, calculated from the inversion results (the mean values in Table 3.6), compare to the measured natural frequencies in Table 3.4(b). First, Table 3.7 shows how the calculated values from the approximate coarse mesh MATLAB FEA compare to the measured frequencies. The quantity  $\Delta_i$  shows the difference in percentage, with respect to the measured frequency. Table 3.7 shows that all calculated values are larger than measured ( $\Delta_i$  is positive). This is expected, since the approximate MATLAB FEA calculation model is expected to overestimate the frequencies, up to 2%.

Table 3.7. Natural frequencies [Hz] as calculated by MATLAB FEA (10x10 mesh) from the mean values in Table 3.6. All results have fitness = 5.0. Quantity  $\Delta_i$  shows the relative difference, compared to the measured frequencies.

Plate	$f_1^{\text{calc}}$	$f_2^{\text{calc}}$	$f_3^{\text{calc}}$	$f_4^{\text{calc}}$	$f_5^{\text{calc}}$
TR10_2	127.6	207.8	332.6	347.2	429.0
TR11_1	89.1	157.1	238.9	256.3	311.7
TR11_2	88.8	187.6	232.1	259.4	292.2

Plate	$\Delta_1$ , %	$\Delta_2$ , %	$\Delta_3$ , %	$\Delta_4$ , %	$\Delta_5$ , %
TR10_2	0.6	1.1	1.6	0.6	1.2
TR11_1	0.5	0.8	1.7	0.4	1.7
TR11_2	0.4	0.9	0.5	1.7	1.6

Frequencies can also be calculated by using more precise numerical modelling tools. The natural vibration modes are modelled by Abaqus (v. 6.12) finite element software, using the identified elastic properties in Table 3.6 (and  $E_z = E_y$ ,  $\nu_{xz} = \nu_{yz} = 0.3$ ). The model is composed of 8-node shell elements S8R with a 20x20 mesh, which should give good accuracy (as seen in Fig. 3.3). The mode shapes of the first five modes agree with the trial plate mode shapes (Fig. 3.2) for TR10\_2 and TR11\_1. Compared to other plates, modes 3 and 4 are switched for plate TR11\_2. The results from accurate modelling are shown in Table 3.8. It is pointed out that the relative differences  $\Delta_i$ , from comparison to the measured frequencies are now both

positive and negative. This is again expected as the systematic error is removed by accurate modelling. In addition, the difference between the approximate and precise results in Tables 3.7 and 3.8 is less than 1.6 % for all frequencies, with approximate MATLAB FEA showing higher values for all cases. This is expected from the earlier estimation  $err_f^{syst} \leq 2\%$ .

Table 3.8. Natural frequencies [Hz] as calculated by Abaqus software (S8R, 20x20 mesh) from the mean values in Table 3.6. Quantity  $\Delta_i$  shows the relative difference, compared to the measured frequencies.

Plate	$f_1^{calc}$	$f_2^{calc}$	$f_3^{calc}$	$f_4^{calc}$	$f_5^{calc}$
TR10_2	127.1	204.6	328.9	344.5	423.5
TR11_1	88.7	154.7	235.6	252.5	307.3
TR11_2	88.3	184.8	228.6	255.9	288.2

Plate	$\Delta_1, \%$	$\Delta_2, \%$	$\Delta_3, \%$	$\Delta_4, \%$	$\Delta_5, \%$
TR10_2	0.2	-0.5	0.5	-0.2	-0.1
TR11_1	0.0	-0.7	0.3	-1.1	0.3
TR11_2	-0.1	-0.6	-1.0	0.3	0.2

For the last comparison, the precision of the analytical approximate formulas, as discussed in Section 3.6.1 is evaluated. The formulas given in [60] require the plate to be square and beforehand knowledge about which frequencies belong to (1,1), (2,0) and (0,2) modes. These frequencies are 1<sup>st</sup>, 2<sup>nd</sup>, 4<sup>th</sup> for plates TR10\_2 and TR11\_1 and 1<sup>st</sup>, 2<sup>nd</sup>, 3<sup>rd</sup> for plate TR11\_2, respectively. It is also assumed that Poisson's ratio coefficient  $\nu_x\nu_y = 0$ . The elastic moduli calculated from approximate analytical formulas are given in Table 3.9. Their relative difference  $\Delta$  to the mean identified constants in Table 3.6 is mostly below 10%, confirming that the approximate formulas can give fairly good estimates.

Table 3.9. Elastic moduli as calculated from approximate analytical formulas [60]. Quantity  $\Delta$  shows the difference relative to the identified constants in Table 3.6.

El. constant	TR10_2	TR11_1	TR11_2
$E_x$ , GPa	42.4	39.1	33.1
$E_y$ , GPa	15.0	14.6	21.4
$G_{xy}$ , GPa	5.0	4.1	4.2

El. constant	TR10_2	TR11_1	TR11_2
$\Delta$ for $E_x$ , %	3.9	1.2	3.4
$\Delta$ for $E_y$ , %	-0.3	2.0	-0.5
$\Delta$ for $G_{xy}$ , %	-10.3	-9.0	-8.0

### 3.7 Summary

Three general notes can be summarized from the study in Chapter 3.

- It was demonstrated that in-plane moduli  $E_x$ ,  $E_y$  and  $G_{xy}$  of an orthotropic laminate are straightforward to determine from natural frequencies of rectangular laminates. A numerical FEA model was employed for forward calculations and an optimization procedure (SGA) to solve the inverse problem.
- Literature study reveals and numerical modelling confirms that by having control over specimen geometry, additional constants could also be determined. By increasing the specimen thickness (or by employing higher modes in the procedure), through-thickness shear moduli  $G_{xz}$ ,  $G_{yz}$  can be obtained. By having control over in-plane dimensions of the rectangular specimen (length to width aspect ratio), in-plane Poisson's ratio  $\nu_{xy}$  can also be obtained.
- It is argued that systematic errors from numerical models and random errors from experimental uncertainties should be evaluated and accounted in the inversion procedure. One example, by including their effect into the fitness function, was shown in Chapter 3.



## 4 A study of wave propagation in composite plates

### 4.1 Introduction

One of the main objectives of this work is to apply current state-of-the-art dynamic methods for the evaluation of ply elastic constants. Vibration based measurement methods were reviewed and applied in Chapter 3. Another large group of methods is based on ultrasonic wave propagation. Ultrasound measurements help to determine the local stiffness properties of the specimen. No alterations are created to the specimen from the small amplitude stress waves and several moduli can be estimated simultaneously.

Through-transmission ultrasound is commonly used to detect delamination damage in composites (C-scan, pulse-echo flaw detection equipment), e.g. as discussed in [88]. It is straightforward to use normal incidence through-thickness time-of-flight measurements for the determination of through-thickness elastic moduli. The concepts of bulk waves in boundless media are reviewed in Appendices F.1 and F.2. ASTM Standards C1419, E494 [89, 90] and European Standard EN-843-2 [57] give guidance for through-thickness measurements employing longitudinal and transverse sound waves, either in transmission or pulse echo mode for elastic modulus measurement. However, as noted in [24], despite its accuracy and simplicity, the material test community has not yet adapted this technique.

More advanced techniques, based on plate wave i.e. Lamb wave propagation have become increasingly popular as tools for elastic property measurement and damage detection. Lamb wave is a common wave type used in ultrasonic NDT. The term ‘Lamb wave’ originally denoted wave propagation in a traction-free homogeneous isotropic plate in vacuum. However, the terminology has now a wider use, being applied to composite plates, plates immersed in water, shells etc. Lamb waves are dispersive, i.e. waves have different phase velocities at different frequencies. In addition, numerous different modes can be generated simultaneously. The zero-order (or sometimes referred as fundamental or first) modes of the Lamb waves,  $S_0$  and  $A_0$ , are usually employed for non-destructive testing. They are the only modes which propagate on the full spectrum of frequencies. More importantly, they usually carry the most energy and are therefore easy to experimentally detect. A short insight into Lamb wave behaviour is given in Appendix F.3 for isotropic plates. The velocity calculation for long wavelength limit and dispersion equations for UD plates are given in Appendix F.4 for orthotropic plates.

The innovation with the use of Lamb waves for structural health monitoring has resulted with numerous patents, e.g. [91–98] in last two-three decades. Damage detection has always been the primary task of ultrasonic NDT while pure stiffness determination is less studied, as it is only needed for numerical modelling purposes. The literature review about ultrasound is therefore broadly divided into two parts. The literature about stiffness determination is reviewed in this Chapter. This is because the experimental results and analysis of virgin (undamaged) plates are mainly discussed in the following. Later in Chapter 5, developments regarding transverse matrix cracking, local delamination and its influence to stiffness and ultrasonic waves are reviewed.

Wave propagation in isotropic plates is already a difficult topic, adding anisotropic behavior of the material and various damage mechanisms only increases the complexity. The textbook by Rose [99] is a well-known reference about ultrasonic waves, mostly focusing on isotropic materials. Lempriere [100] provides a good introduction into the topics of ultrasound and anisotropic materials. A short review about scientific work is provided in the following.

Dean [101] measured accurate moduli for the isotropic plate and the in-plane elastic modulus for the anisotropic plate using the fundamental  $A_0$  mode of the Lamb wave. Tang and Henneke [102] used approximate theory to calculate the dispersion curves of multilayered laminates, applicable for the low frequency, long wavelength region. Hosten *et al.* [103, 104] used water immersion and air-coupled measurements to measure the elastic constants from ultrasonic bulk waves in principal and non-principal material directions. The wave propagation characteristics in plates (for AE), based on classical and higher order plate theories, were the subject of the PhD Thesis by Prosser [105]. Rogers [106] measured the elastic constants of isotropic plates using Lamb waves, also investigating the sensitivity of the accuracy of constants to the frequency region of the dispersion curve. Wu and Liu [107] measured the elastic constants of transversely isotropic composite from a hybrid approach, a combination of bulk wave and Lamb wave ultrasound. Laser sources were used for Lamb wave generation. Castaings *et al.* [108] used bulk wave measurements to determine the complex viscoelasticity constants of composites. Among other things they showed that the real parts do not strongly depend on the imaginary parts, i.e. variations in damping do not lead to significant errors in real parts of elastic constants. Reverdy and Audoin [109] used lasers to synthesize and detect through transmission bulk waves and used these to identify the stiffness coefficients of a unidirectional composite. The inverse determination of material constants, based on  $\mu$ GA optimization and displacements recorded only at one point on the laminate is discussed in a textbook chapter and a paper on the topic [110, 111]. Rose discussed the future potential of Lamb wave based inspection application [112] and noted the benefits of using guided waves: inspection over long distances, good sensitivity to defects, ability to inspect in different environments (e.g. water) and cost effectiveness (simplicity and speed). Giurgiutiu *et al.* [113] introduced piezoelectric wafer active sensors (PWAS) as a small, inexpensive and non-invasive solution for creating sensor arrays for Lamb wave generation and detection. Van Oterloo and Dayal [114] determined the elastic constants of quasi-isotropic laminates and quantified their actual isotropy from measurements at various directions by using the low frequency region of  $S_0$  Lamb mode. Gao *et al.* [115] determined the thickness and elastic constants of an isotropic copper plate from fitting the Lamb  $A_0$  and  $S_0$  modes measured and generated by lasers. Lowe *et al.* [116] give a short overview of a decade of work and practical applications related to the general purpose computer model “DISPERSE” which was developed to study guided waves. This is well suited for applied researchers who are not interested in deriving the specific solutions themselves. Another approach for such researchers would be to use numerical commercial software, e.g. as discussed by Gómez *et al.* [117]. Predoi *et al.* [118] describe a semianalytical finite element method based dispersion curve calculation, applicable for waveguides of infinite, periodic widths. Theoretical predictions are validated by experimental measurements. Vishnuvardhan *et al.* [119, 120] apply genetic algorithms to determine the elastic constants of composites from bulk wave

velocity (oblique incidence back-reflection technique) and Lamb wave fundamental modes measurements, respectively. Tian and Yu [121] carry out the separation of the obtained multimode Lamb wave signal into desired single modes. Glushkov *et al.* [122] discuss the mathematical low cost modelling for Lamb wave velocities and apply their approach with  $\mu$ GA optimization for the determination of composite elastic moduli.

This work aims to provide a better understanding for the relationships between the engineering elastic constants of composites and the dispersion curves of the wave propagation. A novel approach is introduced into the way Simplex optimization is conducted. It is noted that only a few studies in the literature have used laser interferometer measurements for Lamb wave detection on composites. As an interesting outcome of current work, most likely due to the precise measuring equipment, Scholte waves are detected on plate surfaces in air.

The work in this Chapter includes experimental data which has been manipulated by a 2-D Fourier transform (see Appendix G.4), a technique for the analysis of multimode signals described by Alleyne and Cawley [123]. The measured time-amplitude data is transformed into wavenumber-amplitude data at discrete frequencies. This data processing helps to distinguish between different Lamb wave modes.

The general aim of the elastic constant determination is to minimize the difference between experimental and guessed dispersion curves of Lamb wave  $S_0$  and  $A_0$  modes. This inverse problem of elastic constant determination can be studied only when proper methods have been established for the forward computation (i.e. for calculation of dispersion curves from guessed elastic constants). Dispersion equations derived by Rhee *et al.* [124] were applied for this purpose, as described in Appendix F.4.2.

Three different optimization approaches were utilized — SGA,  $\mu$ GA and Nelder-Mead Simplex method with a preliminary sensitivity study. Optimization algorithms are reviewed in Appendix E. Simplex algorithm based inversion from Lamb wave data has been conducted before by Karim *et al.* [125]. They showed a continuous convergence zone in the neighborhood of the solution point in the parameter space. They also conducted a previous sensitivity study and cautioned that convergence to a false solution may result from a poor initial guess. The Simplex method based approach described in the following is different as it describes a two-step procedure, where the initial guess is greatly improved with the help of results from the previous sensitivity study and numerous pre-inversions.

## **4.2 Lamb waves on the unidirectional plate**

### **4.2.1 Experimental data**

The measured plate is a unidirectional laminate, produced by vacuum assisted resin infusion, from glass fibers and vinylester matrix. Its details are described in Table G.3 in Appendix G.1. Lamb waves are generated by a 250 kHz central frequency contact transducer on the plate edge and detected by a laser interferometer from the displacements perpendicular to the plate surface. Experimental details are described in Appendix G.4. After 2-D FFT [123], the measurements result in experimental dispersion curves as shown by contour lines in Fig. 4.1.

The local maxima are located and numbered on the plot, similar data reduction can be found in the literature e.g. [115]. The relative amplitude  $w$  of the frequency-wavenumber representation (i.e. the third dimension) can be somewhat estimated from the plot by the number of contour lines, however, the detailed data for all points is omitted for the sake of brevity.

From the general shape of the dispersion curves (see Fig. F.1(a) in Appendix F.3), one can identify the data points in Fig. 4.1 belonging to specific Lamb modes. Mode  $S_0$  is characterized by data points 1,...,14 in the fiber direction ( $0^\circ$ ) and 1,...,10 in the transverse direction ( $90^\circ$ ). Mode  $A_0$  is characterized by points 15,...,21 in the fiber direction and 11,...,16 in the transverse direction. The other data points in Fig. 4.1 belong to higher Lamb modes or are noise falsely identified as data. The thickness of the plate was measured 6.6 mm on average and the density as  $1930 \text{ kg/m}^3$ .

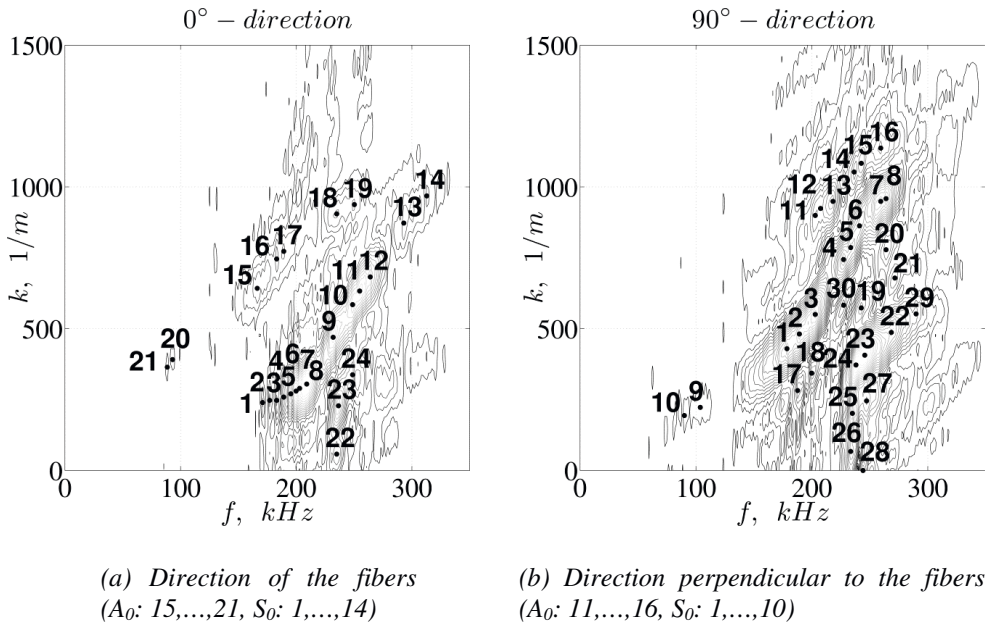


Figure 4.1. Experimental dispersion curves and local maxima for glass-fiber/vinylester plate (thickness  $d = 6.6 \text{ mm}$ , mass density  $\rho = 1930 \text{ kg/m}^3$ ).

#### 4.2.2 Sensitivity analysis and simplex optimization

The relationship between dispersion curves and elastic constants of orthotropic plates is less complex only for distinct cases. Symmetric  $S_0$  wave velocity approaches plate wave velocity  $c_{pl}$  in the low frequency region (Appendix F.4.1). Both  $S_0$  and  $A_0$  approach Rayleigh surface wave velocity  $c_R$  in the high frequency region, as explained in Fig. F.1(b) in Appendix F.3. The experimental data in Fig. 4.1 was not obtained for these low and high frequency regions.

In the intermediate frequency range, the elastic moduli can be identified from the experimental dispersion curves by using optimization. For this method, a non-negative

objective function is defined, quantifying the difference between the calculated and guessed phase velocities. As the objective function is minimized the elastic properties as search variables are identified.

For a large number of elastic constants (9 for orthotropic material), a complex form of the objective function, and thermodynamic constraints (Appendix B), the direct optimization with simplex method is impossible. This is because the obtained solution is highly dependent on the initial guess, as described in Appendix E.1. One possible way to proceed is by employing a global optimization method such as genetic algorithm (GA, see Appendix E.2), as some researches have done before [119, 120]. GA employs a search variable space rather than a single initial guess to initiate the search, but as a downside, it is much slower. A novel approach by modifying the simplex method is proposed in this work for obtaining the elastic constants. This is described in the following.

Elastic constants can be approximately estimated from previous experience, utilizing approximate formulas (Appendix C.3) or by GA which has very good initial convergence. An example of an initial guess for the moduli of the investigated UD plate is given in Table 4.1.

*Table 4.1. Estimates for the elastic constants of GF/vinylester UD plate.*

$E_1$ , GPa	$E_2$ , GPa	$E_3$ , GPa	$\nu_{12}$	$\nu_{13}$	$\nu_{23}$	$G_{12}$ , GPa	$G_{13}$ , GPa	$G_{23}$ , GPa
43.7	15.3	15.3	0.28	0.28	0.40	5.30	5.30	5.46

This estimate can be used to investigate and determine which regions in the frequency spectrum are most influenced by different elastic constants. The dispersion equations are given in Appendix F.4.2. First, phase velocities  $c_p^{(2)}$  are calculated from the constants in Table 4.1 for fundamental modes  $A_0$  and  $S_0$ . Then, each constant is reduced one at a time (the others remain the same) by a small amount (0.01 % taken here) and slightly changed phase velocities  $c_p^{(1)}$  are calculated. Similarly, each constant is then increased by 0.01% and the phase velocities  $c_p^{(3)}$  are again calculated from these sets. The quantities  $c_p^{(1)} / c_p^{(2)}$  and  $c_p^{(3)} / c_p^{(2)}$  show relative changes in phase velocities of the fundamental modes from each single elastic constant. In other words, it shows how sensitive the phase velocity is to changes in a specific elastic constant. Phase velocities  $c_p^{(1)}$ ,  $c_p^{(2)}$ ,  $c_p^{(3)}$  were calculated in the frequency range up to 350 kHz and the results for the two directions of the plate are shown in Fig. 4.2.

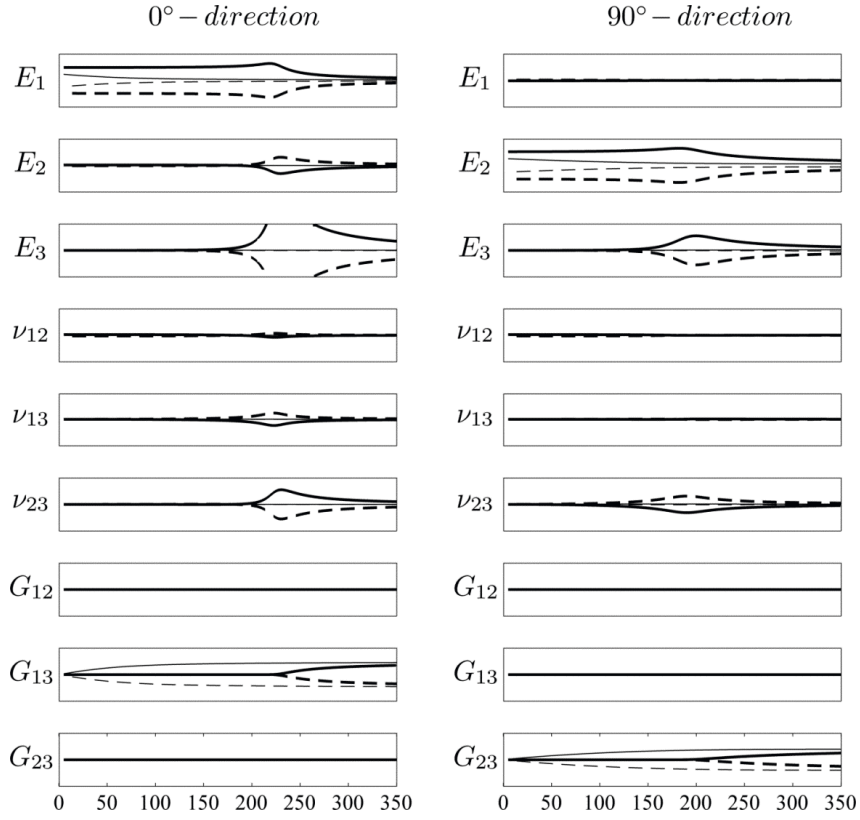


Figure 4.2. Relative change of phase velocities when each single constant is increased by 0.01% (solid line) or decreased by 0.01% (dashed line).  $S_0$  mode – thick line,  $A_0$  mode – thin line. Horizontal axis in kHz, Vertical axis displays  $c_p^{(1)} / c_p^{(2)}$  and  $c_p^{(3)} / c_p^{(2)}$  in the range  $1 \pm 0.01$  %.

From a study on isotropic plates, Rogers [106] concluded that fewer experimental data points, when selected properly, produce more accurate estimates of elastic constants than a large number of arbitrarily chosen points. It is therefore reasonable to assume that the elastic constants which have stronger influence on the phase velocity can be more easily determined from the optimization. For example, Poisson ratios  $\nu_{12}$ ,  $\nu_{13}$  and shear modulus  $G_{12}$  are unlikely to be identified from the experimental data, since they have very little or no influence on the phase velocity, compared to other constants, as seen from Fig. 4.2.

In order to improve the convergence of the simplex method, only selected experimental data points (based on their high sensitivity in a certain frequency region in Fig. 4.2) are chosen for the optimization. And optimization is initially carried out one constant at a time. For example, to determine modulus  $E_1$ , experimental data in  $0^\circ$ -direction has influence to  $f < 250$  kHz for  $S_0$  and to  $f < 100$  kHz for  $A_0$ . This corresponds to data points 1,...,9 for  $S_0$  and 20, 21 for  $A_0$  in Fig. 4.1(a). The rest of the experimental data is disregarded. This selection process is carried out for all of the constants by comparing Figs. 4.1 and 4.2. The selected experimental data points are given in Table 4.2.

Table 4.2. Experimental data for simplex optimization.

Elastic constant	0° – direction		90° – direction	
	$A_0$	$S_0$	$A_0$	$S_0$
$E_1$	20, 21	1,...,9	-	-
$E_2$	-	9,...,14	11,...,16	1,...,10
$E_3$	-	9,...,14	-	1,...,8
$\nu_{12}$	-	8,...,11	-	9,10
$\nu_{13}$	-	1,...,13	-	4,...,8
$\nu_{23}$	-	9,...,14	-	1,...,8
$G_{12}$	-	-	-	-
$G_{13}$	15,...,21	10,...,14	-	-
$G_{23}$	-	-	11,...,16	4,...,8

In order to show that the influence of the initial simplex is reduced, the optimization is performed starting from three different initial sets. These sets are randomly chosen, close to the estimates in Table 4.1 to cover the spectrum of possibilities.

Table 4.3. Initial sets for simplex optimization.

Initial set	$E_1$ , GPa	$E_2$ , GPa	$E_3$ , GPa	$\nu_{12}$	$\nu_{13}$	$\nu_{23}$	$G_{12}$ , GPa	$G_{13}$ , GPa	$G_{23}$ , GPa
1	38	10	10	0.28	0.28	0.35	3.50	3.50	3.70
2	42	12	12	0.30	0.30	0.40	4.00	4.00	4.29
3	45	15	15	0.32	0.32	0.45	5.00	5.00	5.17

The simplex optimization is carried out using the MATLAB function *fminsearch* (see Appendix E.1) to minimize the objective function defined in Eq. (4.1). Each constant is optimized separately from three sets of initial guesses and the experimental data relevant for this constant. Since  $G_{12}$  simply cannot be identified based on measurements in 0° and 90° directions, altogether  $8 \times 3 = 24$  optimizations were carried out. The results are shown in Table 4.4 with their means and coefficients of variation. The final optimization is carried out when the mean values are taken as the final initial set and all of the experimental data (i.e. all identified  $S_0$  and  $A_0$  data points) are employed for the optimization.

Table 4.4. The results from simplex optimization.

El. constant	from set 1	from set 2	from set 3	Mean	COV, %	Final
$E_1$ , GPa	37.7	41.1	41.7	40.2	5	39.9
$E_2$ , GPa	14.6	13.8	16.7	15.0	10	15.5
$E_3$ , GPa	16.3	17.1	17.1	16.8	3	15.4
$\nu_{12}$	0.071	0.283	0.391	0.248	66	0.37
$\nu_{13}$	0.145	0.104	0.247	0.165	45	0.13
$\nu_{23}$	0.435	0.404	0.383	0.407	6	0.30
$G_{12}$ , GPa	-	-	-	-	-	-
$G_{13}$ , GPa	3.79	4.23	5.70	4.58	22	6.0
$G_{23}$ , GPa	4.83	4.72	4.71	4.75	1	4.8

Table 4.4 shows that some of the identified constants ( $E_1$ ,  $E_2$ ,  $E_3$ ,  $G_{23}$ ) converged to very similar values from sets 1 to 3 (low COV), and also from the final optimization. It is likely that these constants are identified. The same four constants and  $G_{13}$  in addition had also good convergence in a similar optimization conducted for a glass-fiber/epoxy plate [126]. The reason for the problematic convergence of  $G_{13}$  in Table 4.4 is unknown, for example it can be related to the specific initial guesses. The Poisson's ratios  $\nu_{12}$ ,  $\nu_{23}$  seem to converge to a realistic value in the end, but the intermediate results from sets 1 to 3 are not consistent to that. As previously shown (Fig 4.2), Poisson's ratios  $\nu_{12}$ ,  $\nu_{13}$  have very low sensitivity to phase velocities.

### 4.2.3 Numerical demonstration of convergence for simplex optimization

It is of interest to study how the convergence from random initial sets (e.g. the sets in Table 4.3) takes place. To demonstrate the principle, a series of calculations are carried out.

At first, 1000 initial sets are randomly created for optimization. Each created set is enforced to comply with thermodynamic constraints (Appendix B) and constants can obtain values randomly, with a uniform distribution, from a given interval. Constant  $E_1$  is chosen from range (37, 47) GPa, constants  $E_2$  and  $E_3$  from (7, 17) GPa, all Poisson's ratios from (0, 0.5) and all shear moduli from (2, 7) GPa. The initial distributions are colored red in the histograms in Fig. 4.3.

Each of the elastic constants is optimized separately and experimental data points are taken from Table 4.2. For example, constant  $E_1$  is optimized from data points 20, 21 ( $A_0$ ) and 1,...,9 ( $S_0$ ) in the  $0^\circ$ - direction, for every one of the 1000 random initial sets. It is exactly analogous to what was done in Table 4.4, however here are 1000 initial sets instead of three and the ranges for initial sets are fairly wide. All of the 1000 results for  $E_1$  (and other constants) are plotted as overlapping blue histograms in Fig. 4.3. We see that optimized results for  $E_1$  tend to converge to approx. 42.5 GPa. However, it is also possible to get the  $E_1$  results as 32 GPa or 55 GPa – optimization is still dependent on the initial simplex or the specific initial set. Similar behaviour where the distribution has a clear peak is seen for  $E_1$ ,  $E_2$ ,  $E_3$ ,  $G_{13}$  and  $G_{23}$ . No clear peak is observed for  $\nu_{23}$ . It is also observed that the peaks in Fig. 4.3 approximately agree with the final results in Table 4.4.

Fig. 4.3 contains data from 6x1000 optimizations. Clearly, this brute force approach to evaluate the possible solution is computationally slow, but it demonstrates an important behaviour. Given an approximate initial set, the solutions for the sensitive elastic constants tend to, as shown in Table 4.4 and Fig. 4.3, converge to the final solution. Most of the random initial guesses in Fig. 4.3 resulted after optimization with values close to the final results in Table 4.4. Various other outcomes are also possible, but are not as numerous, as seen from the histograms.



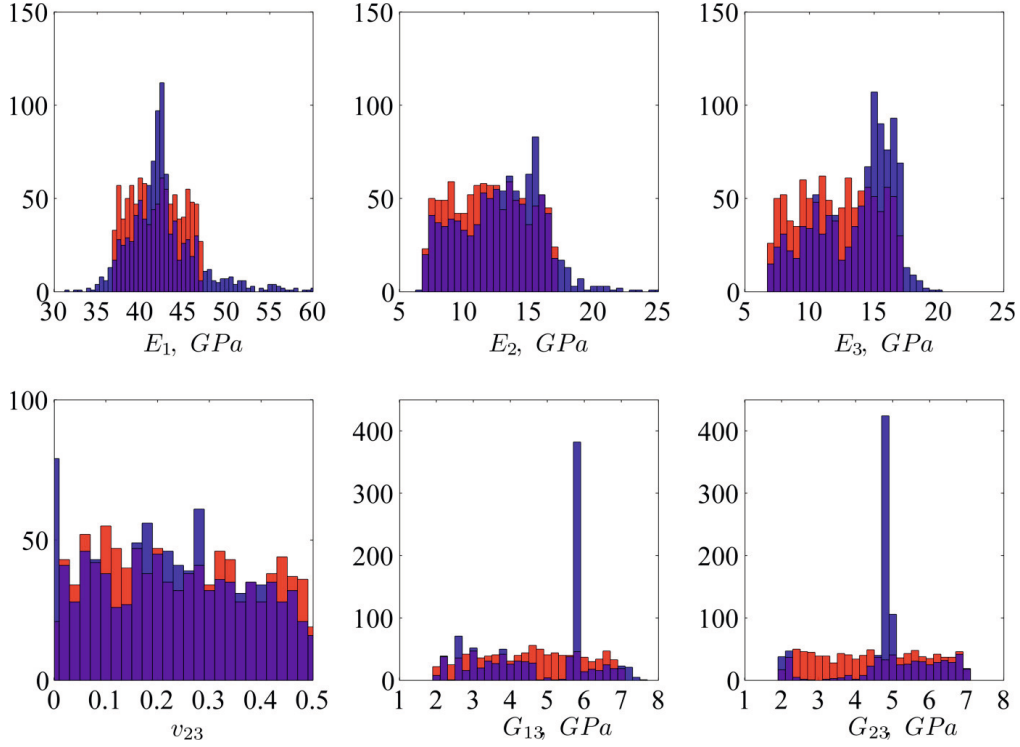


Figure 4.3. Histograms of the uniformly distributed initial sets (red) and the optimized sets (blue) for six elastic constants.

#### 4.2.4 Optimization results

The results of the simplex optimization are compared to the results from more time consuming genetic algorithm (GA) based optimization. Simple genetic algorithm (SGA) and micro genetic algorithm ( $\mu$ GA) are run from self-written toolboxes in MATLAB and their description can be found in Appendices E.2–E.3. Optimization with GA uses all of the identified data points for  $A_0$  and  $S_0$  modes from Fig. 4.1. Both Simplex and GA optimization techniques employ (also in Sections 4.2.2 and 4.2.3) the same definition of the objective function:

$$ObjF = \sum_{i=1}^4 \left\{ \frac{1}{n} \sum_{j=1}^n \left[ (c_{p,i,j}^g - c_{p,i,j}^m)^2 \frac{w_{i,j}}{\max(w_{i,j})} \right] \right\}, \quad (4.1)$$

where  $i$  denotes different dispersion curves ( $A_0$  in  $0^\circ$  and  $90^\circ$  directions, and  $S_0$  in  $0^\circ$  and  $90^\circ$  directions);  $j$  denotes the specific data point in a curve;  $n$  is the total number of measured points on a curve;  $c_{p,i,j}^g$  and  $c_{p,i,j}^m$  stand for the guessed and measured phase velocities, respectively;  $w_{i,j}$  is the weight of the data point, taken equal to the amplitude of the frequency-wavenumber representation (the third dimension of contour plots in Fig. 4.1).

It can be seen from Eq. (4.1) that the weighting is used according to experimental data, and both wave modes and directions are taken equally into account by the function (data point average is calculated for each direction/wave mode). The unknown variables are the engineering constants, constrained by the thermodynamic constraints (Appendix B). Exactly the same definition for the objective function was used in [126]. Since the GA optimization seeks to maximize fitness (instead of minimizing the objective function), the fitness for GA is defined as  $fitness = 1/ObjF$ . Table 4.5 reports the SGA and  $\mu$ GA parameters used in optimization and the variable space for unknowns. The resolution of the variable space does not have round values due to the binary-coding of candidate solutions.

SGA and  $\mu$ GA were run consecutively ten times and the evolution of  $ObjF$  (inverse of fitness) of the best individual in the population is followed in Fig. 4.4. Typical behavior of GA is evident from the figure. Relatively fast initial convergence ( $ObjF=10^4$  by  $n_{feval} = 5000$ ) is succeeded by long periods of stagnation ( $ObjF=3.7 \cdot 10^3$  by  $n_{feval} = 50\,000$ ). It is surprising that even though  $\mu$ GA showed slightly faster initial convergence, compared to SGA, its final convergence behavior in Fig. 4.4 seems poorer. As a reminder,  $\mu$ GA is generally thought to counter stagnation better than SGA (Appendix E.3).

Table 4.5. GA parameters and the search space.

(a) GA parameters

SGA		$\mu$ GA	
Pop. size	$n = 50$	Pop. size	$n = 5$
Nr. of generations	$t = 1000$	Nr. of function evaluations	$n_{feval} = 5 \cdot 10^4$
Fitness scaling parameter	$nxavg = 2$	Convergence criterion	$p_{conv} = 95 \%$
Probability of cross-over	$p_{cross} = 90 \%$	probability	
Nr. of elites	$n_{elites} = 1$	Nr. of elites	$n_{elites} = 1$
Mutation probability	$p_{mut} = 2 \%$	Mutation probability	$p_{mut} = 0$

(b) GA variable space (min; max; resol.)

$E_1$ , GPa	(35; 50; 0.0588)
$E_2, E_3$ , GPa	(5; 20; 0.0588)
all $\nu$	(0; 0.5; 0.0079)
all $G$ , GPa	(1; 8; 0.0551)

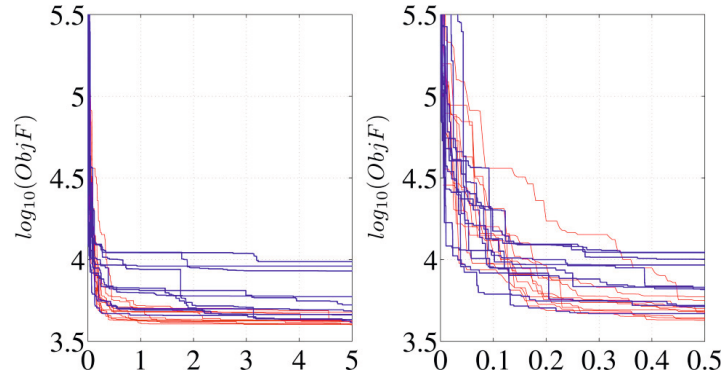


Figure 4.4. The evolution of the  $ObjF$  value of the best individual through ten SGA (red) and  $\mu$ GA (blue) runs. Hor. axis – number of  $ObjF$  evaluations [ $\cdot 10^4$ ]. Figure on the right shows an enlarged section of the figure on the left.

Each of the GA runs took 50 000  $ObjF$  evaluations and a total of 10 trial runs were carried out, which sums up to a half a million function evaluations for both SGA and  $\mu$ GA. The Simplex method took 1000 function evaluations for each of the trial runs and 10 000 for the final optimization, resulting in just 13 000 function evaluations, which shows substantial savings in computing time.

Table 4.6. Summary of optimization results.

Variable	SGA – results from 10 trials		$\mu$ GA – results from 10 trials		Simplex
	COV, %	Highest fitness result	COV, %	Highest fitness result	
$E_1$ , GPa	6	38.3	7	38.6	39.9
$E_2$ , GPa	11	15.6	12	15.5	15.5
$E_3$ , GPa	2	15.3	4	15.2	15.4
$\nu_{12}$	74	0.45	65	0.47	0.37
$\nu_{13}$	52	0.08	47	0.09	0.13
$\nu_{23}$	21	0.32	27	0.32	0.30
$G_{12}$ , GPa	-	-	-	-	-
$G_{13}$ , GPa	1	6.0	2	6.0	6.0
$G_{23}$ , GPa	1	4.7	5	4.7	4.8
$ObjF$		3990		4130	3830

Table 4.6 summarizes the results from SGA,  $\mu$ GA and Simplex optimizations. It is evident that the same moduli, which had low COV from Simplex trial runs have also low COV from GA runs. As a consequence these moduli ( $E_1$ ,  $E_2$ ,  $E_3$ ,  $G_{13}$ ,  $G_{23}$ ) result with very similar final values from all optimization strategies.

Transversely isotropic material has an intrinsic material dependency, which was not included as a constraint to the optimization. This dependency connects moduli  $E_2 = E_3$ ,  $G_{23}$  and  $\nu_{23}$  on the plane of isotropy. For example, Poisson ratio can be evaluated approximately by  $\nu_{23} = E_2/2G_{23} - 1$  which results with  $\nu_{23} = 15.5/9.5 - 1 = 0.63$ . This does not agree with the identified  $\nu_{23}$  in Table 4.6. Although the other Poisson's ratios  $\nu_{12}$ ,  $\nu_{13}$  converged to similar

values, the high COV of the results raises doubt about their correctness. In addition, for transversely isotropic materials  $\nu_{12} = \nu_{13}$  should hold, which is not seen in Table 4.6.

Altogether, the elastic moduli ( $E_1, E_2, E_3$ ) and shear moduli ( $G_{13}, G_{23}$ ) were identified and the Poisson's ratios were not identified due to low sensitivity. Shear modulus  $G_{12}$  is physically impossible to identify from current wave propagation measurements. The dispersion curves from the best results of all three optimizations are plotted with experimental data in Fig. 4.5. It is evident that minor differences in optimization results have little influence to the dispersion curves, which overlap each other almost perfectly. The fundamental modes  $A_0$  and  $S_0$  (which were used for elastic constant determination) agree well with experimental data points. For higher order modes, the agreement is less satisfactory.

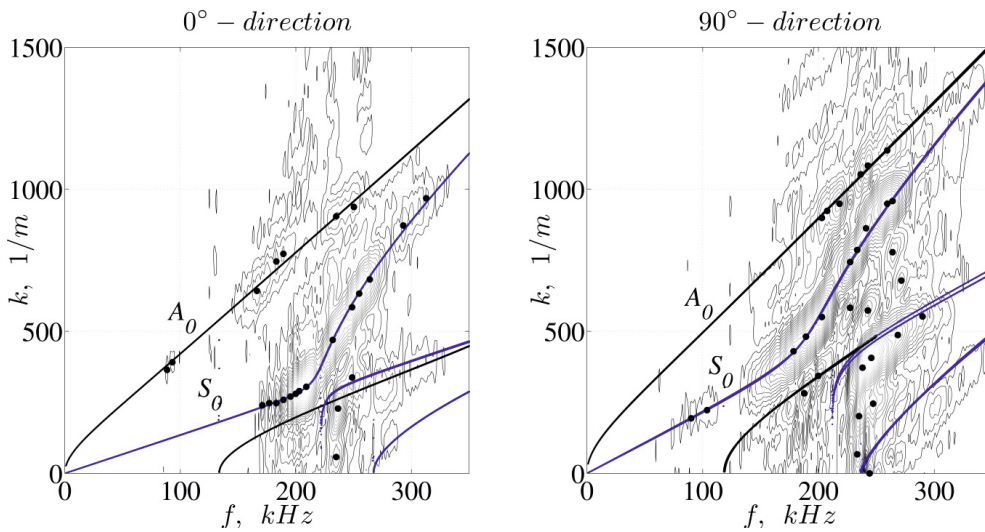


Figure 4.5. Dispersion curves as calculated from the best results of three optimizations (in near perfect agreement with each other) and experimental data. Blue lines: symmetric modes; black lines: anti-symmetric modes; dots: experimental data.

### 4.3 Interface waves on cross-plyed plates

#### 4.3.1 Scholte wave

Some interesting results were obtained while measuring (Appendix G.4) Lamb waves on cross-plyed composite plates. Several plots of experimental data revealed a slow non-dispersive wave propagating in the high-wavenumber region, e.g. as shown in Fig. 4.6. Much faster Lamb wave modes can also be seen on the same plots in the  $k < 1500$  wavenumber region. This slow wave was identified from six different measurements on both virgin and damaged laminates. Data reduction (linear least-squares curve fitting) identified the speeds of this wave in to the range 340 to 350 m/s (mean 346.5 m/s, standard deviation 5.5 m/s). This result has an excellent agreement with the speed of sound in air. However, it was obtained with a laser interferometer measuring perpendicular to the surface of the plate.

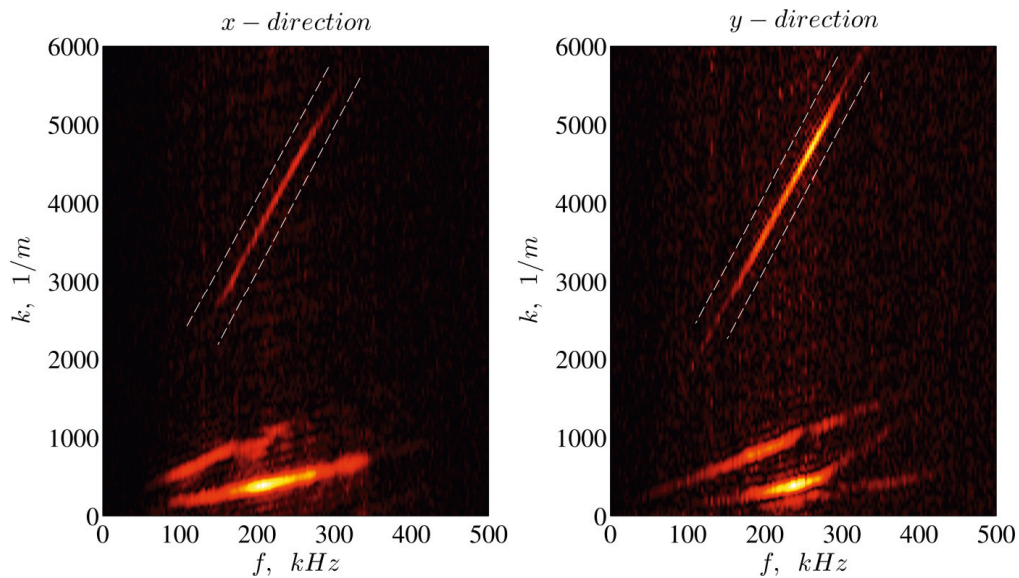


Figure 4.6. Experimental data from a damaged (transverse matrix cracks in surface plies) cross-plyed plate in air:  $x$  and  $y$  mark the wave propagation directions  $[90_2/0_2/90_2]$  and  $[0_2/90_2/0_2]$ , respectively. The slow wave is emphasized with dashed lines.

The wave identified in Fig. 4.6 is most likely a Scholte wave — an interface wave propagating between a solid and a fluid media [127–133]. Ellipses for the Scholte wave particle movement are schematically shown in Fig. 4.7. It can be noted that the vertical component amplitude (which was experimentally measured) is small, compared to horizontal amplitude of particle trajectories in the fluid. Also, the horizontal component is discontinuous across the interface. It has been reasoned that its optical detection was mostly due to air index variation and not from the surface normal displacement. It has been shown that detection works also without reflecting the probe beam on the sample [134].

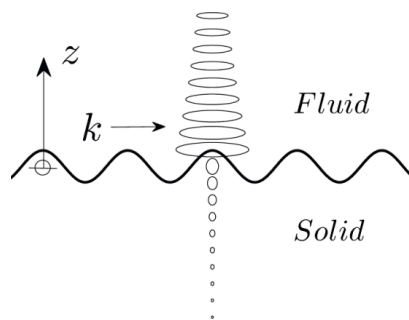


Figure 4.7. Particle movements in the Scholte wave, after [127, 129].

Relatively small displacements in the solid mean that the wave is just weakly influenced by the elastic properties of the solid and most of the wave energy is concentrated into the neighbouring layer of fluid medium. Table 4.7 shows Scholte wave velocities  $c_{sch}$  for various

solid-fluid combinations, calculated either as a special case from Stoneley equation [99] or from Eq. (4.2) [135]:

$$\sqrt[4]{1 - \left(\frac{c_{sch}}{c_{p1}}\right)^2} \sqrt{1 - \left(\frac{c_{sch}}{c_{s1}}\right)^2} - \left(2 - \left(\frac{c_{sch}}{c_{s1}}\right)^2\right)^2 = \frac{\rho_0}{\rho_1} \left(\frac{c_{sch}}{c_{s1}}\right)^4 \frac{\sqrt{1 - \left(\frac{c_{sch}}{c_{p1}}\right)^2}}{\sqrt{1 - \left(\frac{c_{sch}}{c_0}\right)^2}}, \quad (4.2)$$

where  $c_0$  and  $\rho_0$  are the phase velocity and density of the fluid,  $\rho_1$  is the density of the solid and  $c_{p1}$  and  $c_{s1}$  are the bulk wave velocities of the solid. The roots for this equation are found numerically. The bulk wave velocities for an isotropic solid (elastic modulus  $E$ , Poisson's ratio  $\nu$ ) are calculated in Eqs. (F.1), (F.2) in Appendix F. An approximate solution for Eq. (4.2) is given by Viktorov, as reported in [134]:

$$c_{sch} = (1 - \varepsilon)c_0, \quad (4.3)$$

$$\varepsilon = \frac{1}{8} \left( \frac{\rho_0}{\rho_1} \frac{c_{p1}^2 c_0^2}{c_{s1}^2 (c_{p1}^2 - c_{s1}^2)} \right)^2 \quad (4.4)$$

The Scholte wave velocity is always smaller than the velocity of any of the contacting media. However, in case of air medium, the influence of the solid is infinitesimal and the wave propagates practically at the velocity of sound in air (just slightly below). Only for “soft” solid – fluid interface (solid shear velocity is smaller than fluid velocity) a significant amount of Scholte wave energy becomes localized in the solid [130].

Table 4.7. Scholte wave velocities [m/s] for various solid-fluid combinations ( $\nu=0.3$  for all solids).

	<b>Water</b> $c_0 = 1480$ m/s $\rho_0 = 1000$ kg/m <sup>3</sup>	<b>Air</b> $c_0 = 343$ m/s $\rho_0 = 1.2$ kg/m <sup>3</sup>
<b>Steel</b> $E = 210$ GPa $\rho_1 = 7800$ kg/m <sup>3</sup>	1479.6	343.0
<b>Aluminium</b> $E = 70$ GPa $\rho_1 = 2700$ kg/m <sup>3</sup>	1476.5	343.0
<b>Pure epoxy</b> $E = 4.3$ GPa $\rho_1 = 1270$ kg/m <sup>3</sup>	893.1	343.0

For example, this is the case for epoxy-water (see Table 4.7), where Scholte wave velocity differs significantly from water velocity. The shear wave velocity of epoxy is less than water velocity and the elastic properties of the solid actually have a significant influence to the Scholte wave velocity. It appears this effect is unrealistic for gases such as air and all usual

solids, as seen from Table 4.7 and Fig 4.8. For gases and solids, Scholte wave propagates approximately with the velocity of gas.

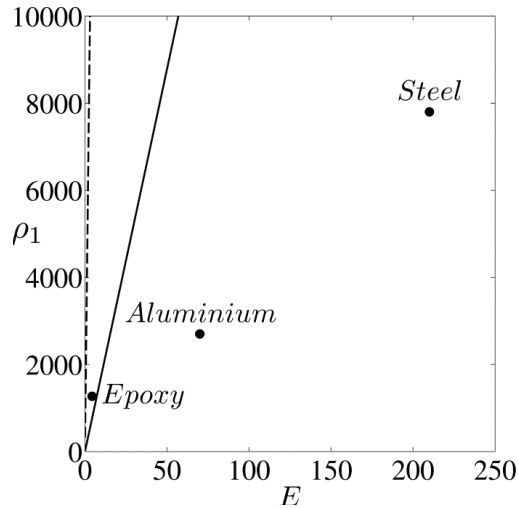


Figure 4.8. Distinction for “soft” solids with regard to the Scholte wave. Lines for air (--) and water (-) show when the shear velocity of the solid ( $E$ , GPa;  $\rho_1$ ,  $\text{kg/m}^3$ ;  $\nu=0.3$ ) is equal to fluid velocity. If the material is above and left to the lines, it is considered “soft” (after [130]).

The ability to measure Scholte waves on the plate surfaces demonstrates an additional monitoring possibility. Provided that sensors are able to register the Scholte wave, the wavespeed can easily be calculated for the surrounding gas. This principle presents a possibility for the remote detection of gas leaks. So far, the solutions for detecting gas or liquid mostly employ the waves in the plate (i.e. Lamb waves) [136–138]. However, the interface waves are more sensitive to the properties of the fluid and therefore show better potential as indicators. This was utilized by Cegla *et al.* [139] who measured the quasi-Scholte mode along a plate inserted into various liquids and obtained the properties of the immersion medium.

The literature reveals little information on the Scholte wave at the fluid-solid interface where the solid has sustained damage. There have been a few studies [127, 130, 133, 134] about Scholte wave interaction with single crack/defect geometries on the surface and large obstacles in propagation path, all for isotropic solids. Distortions of the Scholte wave signals have been reported. It was found that Scholte waves can have reflections from surface defects which are related to the depth of defects. Scholte waves also reflect from obstacles and their amplitude is reduced if surrounding media has obstacles in fluid near the solid surface. However, a different, periodic form of damage, transverse matrix cracks, is commonly observed in composite materials (and on its surface) in various structures during service life. Fig. 4.6 provides the first experimental measurement known to author about Scholte waves on such transversely cracked laminates. The work is ongoing to explain the measured data. Transverse matrix cracks are further discussed in Chapter 5.

### 4.3.2 Rayleigh wave

Another type of interface wave is Rayleigh wave [99, 140, 141]. It is the analogue of the Scholte wave when the density of the fluid approaches zero and all stresses vanish at the interface. Rayleigh wave is a non-dispersive wave to which the fundamental Lamb modes  $A_0$  and  $S_0$  asymptotically approach at high frequencies (see Figure F.1(b)). Similarly to Scholte wave, the displacement in the solid follows an elliptical orbit which decays exponentially with the coordinate from the solid surface. The displacement amplitudes are approx. 10% of their surface values at one wavelength below the surface [142]. Therefore, Rayleigh waves specifically contain information about the surface layers of the solid and much less about the insides. Rayleigh waves can in principle be used for the surface layer material characterization, for either uniform or coated solids. Unfortunately, none of the obtained experimental dispersion curves showed data in the high frequency region for glass fiber composite plates (see Figs. 4.5 and 4.6). The signal was generated with low central frequency transducers (250 kHz). Also, the high frequency spectrum is known to be heavily attenuated for composites.



## 5 Measurements about stiffness reduction in fatigue

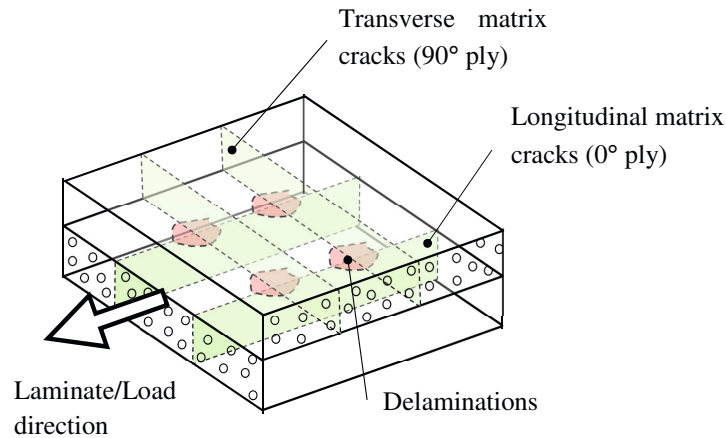
### 5.1 Introduction

Transverse matrix cracks are among the first forms of damage during service life. Although not directly detrimental, matrix cracks serve as initiation points for other forms of damage. The final objective of this study is to quantify the influence of transverse matrix cracking on elastic behavior of laminates. To achieve that, damage is created to cross-plyed specimens by uniaxial fatigue loading. Stiffness evaluation is conducted by using the same three methods as in previous chapters: static testing and NDT measurements based on natural frequencies and Lamb waves.

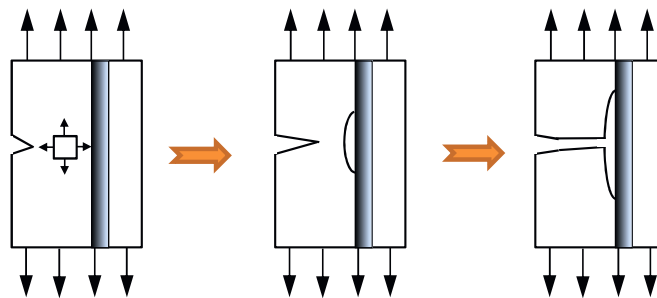
Fatigue is assumed to start from intrinsic defects. In metals, fatigue failure is divided into three stages: crack initiation, crack propagation to a critical size, and unstable fracture. A single macro-crack develops. For FRP laminates however, Highsmith and Reifsnider [143] and others have experimentally shown that a different phenomenon takes place — first damage appears in the form of distributed matrix cracking. Damage accumulates from numerous small-scale defects. At high stresses and short fatigue lives, failure results from few localized flaws, whereas at lower stresses and longer fatigue lives failure results from more dispersed flaws [144]. A general review discussing composite failure mechanisms is given in ref. [8] by Cantwell and Morton.

Matrix cracking starts from resin pockets, fiber-matrix interface, locations of stress concentrations and imperfections inside the laminate. When the crack appears, strain energy in the nearby material volume is released. The cracks appear through matrix/interphase and run parallel to fibers, as seen in Fig. 5.1(a). Fibers can carry more load than the matrix phase and therefore act as crack arresters, as seen in Fig. 5.1(b). The next crack develops at the location where matrix material fails due to stress concentrations. The crack gets arrested when reaching a ply where fibers bridge the crack. This process results with a near-periodic distribution of matrix cracks over a volume of laminate, as depicted in Fig. 5.1(a).

Matrix cracks are usually not decisive for structural integrity, since fibers carry most of the load. However, the crack tips may become nucleating sites for other forms of damage — local delaminations in the interphase between  $90^\circ$  and  $0^\circ$  plies, as seen in Fig. 5.1(a) and later fiber failure. In addition, matrix cracks enable easier introduction of harmful substances or chemicals into the composite. Matrix cracks can compromise the fluid tightness of the composite leading to earlier failures from hydrostatic pressure (relevant for pipes and pressure vessels).



(a) Schematic of matrix cracks in a cross-ply laminate



(b) Mechanism of crack stopping at the fiber-matrix interface, after [1]

Figure 5.1. Matrix cracking.

The changes in stiffness distribution, caused by matrix cracks, can modify internal forces and moments globally if the structure is statically indeterminate. Also, stiffness controlled limit states (deflection, vibration) can be compromised. Depending on the structure and its requirements, transverse cracks can be considered either damage or damage precursors. The effects of matrix cracking are described in the composite standard DNV-OS-C501 [145] as:

- causes fracture in UD laminates;
- causes fracture in cross-ply laminates loaded in in-plane shear;
- may reduce compressive fiber strength;
- may initiate delamination;
- causes leakage unless another barrier can keep the fluid out of the laminate.

Failing laminates tend to show a sequence of failure mechanisms. Some typical sequences are also given in DNV-OS-C501 [145]:

- matrix cracking → delamination → fiber failure;

- debonding and matrix cracking → fiber buckling → fiber failure;
- delamination → crack propagation due to fatigue → global buckling.

This shows that matrix fracture signifies the onset of permanent damage, later followed by additional mechanisms and types of damage.

Monitoring of stiffness by non-destructive testing is one means to detect the occurrence of matrix cracks. However, the measurement system needs to foresee which system behavior is expected to change due to damage or what type of damage does a change in behavior indicate. The dynamic behavior of composite laminates subjected to a specific form of damage is therefore of interest to the NDT community. An overview of previous work is given in the following.

### 5.1.1 Selected results from static studies

Literature [e.g. 146–151] shows that three different stages, as shown in Fig 5.2, can be distinguished from tensile fatigue induced stiffness degradation. Transverse crack density increases to saturation mainly during the first stage.

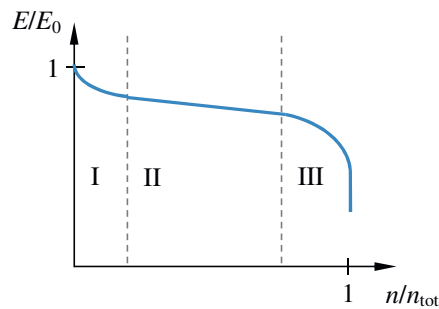


Figure 5.2. Evolution of stiffness under tensile fatigue. Hor. axis – normalized life; vert. axis – normalized stiffness.

- Stage I (initiation) is characterized by a steep decrease in stiffness due to intralaminar matrix cracking in off-axis plies. After a while (up to 20% of life) the pace of stiffness degradation stabilizes.
- Stage II (growth) displays a weak, almost linear decrease of stiffness. Delaminations continue to develop after matrix cracks have become saturated. Additional damage occurs due to longitudinal cracking in  $0^\circ$  plies, local spots of delamination and very occasional, isolated fiber fractures.
- In the final stage III (localization), delaminations become more consolidated and the fibers begin to break in clusters, resulting in material failure.

The reduction of laminate stiffness due to transverse crack density, and as a function of number of fatigue cycles has been the topic of numerous investigations, from late 1970-ies to the beginning of 2000-s, and has been thoroughly studied. An overview of these developed analytical models is out of the scope of current work. As an alternative to analytical models,

FE modelling can also provide numerical estimations for stiffness degradation, given the geometry of cracks, laminate layup and stiffness properties of intact laminae.

Hereby, a few results are mentioned, which have relevance to the experimental work presented later. Early work by Morris [152] showed that graphite/epoxy fracture surface contains “hackles”, which are essentially like roof shingles. Microscopy revealed that these hackles are present for both mating surfaces of delamination cracks. Smith and Ogin [153] discussed the stiffness reduction for bending loads on cross-ply laminates and provided a model to predict matrix cracking when laminate is subjected to bending. Displacement of neutral axis was applied, implying the assumption of bimodular material behaviour for transverse plies.

Adden and Horst [154] conducted a comprehensive study about stiffness degradation due to fatigue loads, based on classical laminate theory and representative volume elements. A modelling approach was introduced for stiffness degradation in arbitrary layups.

Beaumont [16] mentions that Poisson’s ratio values can be indicators of the presence of cracks, more sensitive than the other elastic constants. Digital image correlation (DIC) measurements in [12] confirm that full-field measured Poisson’s ratios give indications of damage locations. They also note similar connection between shear strains and damage. In addition, three stages of fatigue life are experimentally identified from acoustic emission (AE) and DIC measurements.

### **5.1.2 Vibration testing studies**

Both, the advantages and the downsides of vibration testing are due to its global character. The global nature gives additional freedom to choose the measurement points on the structure as convenient. The test time can be short if the resonant frequencies are excited by an impulse. The downside is the lack of ability to detect small damage. Also, since modal frequencies are a global property, they generally cannot provide spatial information to determine the location of damage uniquely. Literature reviews [155, 156] show that multiple studies have been conducted about local through-thickness cracks and also on the effect of delamination damage to vibration characteristics. Less is found about the influence from distributed damage such as transverse cracking to natural frequencies of composites. Of these studies, several noted that changes in damping are more sensitive to damage than changes in natural frequencies. Researchers have historically noted that natural frequencies decrease less with cracks which can open and close, than cracks which stay open. This implies that frequency drop is also affected by preload and residual stress, not just crack density. A few recent studies are reviewed below.

Bedewi and Kung [157] investigated the influence of fatigue to natural frequencies and damping ratios for graphite/epoxy specimens. The decrease of natural frequencies and the increase in damping was measured as a function of number of cycles to failure. A technique for the prediction of fatigue life was developed. Damping ratios were recommended to use as a backup approach to support predictions made by using natural frequencies.

Birman *et al.* [158–160] present calculation models (partly based on a previous model by Han and Hahn) to predict flexural stiffness and assess the natural frequencies of cracked composite beams. Transverse cracks are expected to introduce bimodular material behaviour as they are open under tension (degraded stiffness) and close under compression (restoring initial stiffness).

Kessler *et al.* [161] studied modal evaluation techniques to detect various types of damage — drilled holes, impact, compressive load, cyclic load and delaminations — in graphite/epoxy  $[90/\pm 45/0]_8$  coupons. A correspondence between the extent of damage (stiffness loss) and reduction in natural frequency was noted. It was found difficult to differentiate reliably between damage types or its location simply by observing the frequency response.

Moon *et al.* [162] developed a model based on natural frequency (flexural stiffness) degradation to predict fatigue behavior due to transverse cracking of a  $[90_2/0_2]_5$  graphite/epoxy composite. The predicted natural frequencies over fatigue life are compared to experimental frequencies measured on carbon/epoxy coupons. The prediction model parameters (connecting fatigue cycles with stiffness) were obtained from experimental data.

Yang *et al.* [163] presented a calculation model estimating the flexural stiffness and natural frequencies of a laminate for a given density of idealized, evenly distributed interlaminar transverse cracks. For compression side of the laminate, transverse cracks are assumed to close perfectly, restoring the original modulus. Theoretical predictions are compared with experimental data (cross-ply graphite/epoxy) from literature. It is noted that transverse cracks are more influential to stiffness reduction for glass-fiber laminates (as opposed to graphite or carbon).

Cheng and Hwu [164] describe an on-line real-time detection system for a composite wing structure (graphite/epoxy skin and foam core), which employed natural frequency and strain measurements as detectors and ANNs to determine the material properties inversely.

Abo-Elkhier *et al.* [165] applied bending fatigue loads to glass/polyester ( $[0]_3$ ,  $[45]_3$  and  $[90]_3$ ) specimens, interrupting it during various stages to measure natural frequencies and damping ratios. Natural frequencies were shown to reduce as 2-nd order polynomials and damping ratios to increase exponentially. Changes in damping ratios were therefore concluded as better indicators of damage.

### 5.1.3 Ultrasonic testing studies

Lamb waves are useful for detecting transverse cracking since their velocity (and particle movement) is able to characterize the in-plane stiffness of the plate. In contrast, extensional waves in through-thickness direction lie in the same plane as transverse cracks and therefore wave-crack interaction is small. Also, Lamb waves can be used for local stiffness reduction measurements, as opposed to vibrations, which typically employ the whole structure or component.

There are various focus directions for ultrasonic plate wave (Lamb wave) studies about defects and damage. Either of two defect categories is usually considered — local, single

physical defects (delaminations, cut-outs, holes) [e.g. 166–175] or distributed forms of damage such as transverse cracks and thermal/fatigue damage). The latter category of distributed damage is reviewed in more detail.

#### 5.1.3.1 Thermal-mechanical aging

In addition to fatigue damage, several studies have focused also on matrix cracking from thermal damage which is due to large changes in temperature (e.g. from  $-50^{\circ}\text{C}$  to  $+200^{\circ}\text{C}$ ).

Seale and Madaras [176] investigated graphite/polyimide specimens with  $[45/0/-45/90]_{2S}$  layup under thermal-mechanical aging by one-sided dry-coupled measurement technique. They used approximate Lamb wave equations appropriate for low frequency region and studied the sensitivity of  $A_0$  mode to plate stiffnesses. The matrix cracking led to slower  $A_0$  velocities and decreased laminate stiffnesses (out-of-plane shear stiffnesses  $A_{44}$ ,  $A_{55}$  by up to ca. 20%). In the following study, Seale and Madaras [177] investigated the effect of thermal-mechanical aging to the same material. Symmetric  $S_0$  mode velocity was shown to decrease only in the order of 5% during 5000 hours of aging (ca. 10% of predicted life).

Gélébart *et al.* [178] studied carbon/epoxy  $[0/45/-45/90]_S$  plates subjected to constant temperature exposition with air-coupled transducers. They found that the number and the length of orthogonal matrix cracks reaching the plate surface increased with aging. Only the external plies seemed to be affected. They treated the plate as homogeneous orthotropic medium and found a 20% reduction of the constant  $C_{55}$  due to cracks. The phase velocity of both  $A_0$  and  $S_0$  was measured to decrease.

Castaigns and Hosten [179] studied carbon/epoxy composite pressure vessels and plate specimens with air-coupled transducers to quantify the effects of moisture content and micro-cracking. They found that attenuation of  $A_0$  mode is sensitive to moisture content in a  $[0/90]_{6S}$  layup. Also, wave numbers of symmetric modes  $S_1$  and  $S_0$  were found to be most sensitive, followed by  $A_1$  (and rather insensitive  $A_0$ ) to cracking induced by immersion in liquid nitrogen for a  $[0/+60/-60]_{33S}$  layup laminate.

#### 5.1.3.2 Fatigue and transverse cracking

Among the first who considered using Lamb waves for detecting in-plane stiffness reduction from transverse cracking were Kinra and Dayal [5]. They studied [180] transverse cracking in  $[0_2/90_2/0]_S$ ,  $[0/90_3]_S$  and  $[0/90_4]_S$  graphite/epoxy laminates with leaky Lamb waves by using the  $S_0$  mode. Matrix cracking was found to lower the wave velocity and increase attenuation. The stiffness reduction obtained from wave measurements was up to 5%, 15% and 30% for the laminates with increasing amount of  $90^{\circ}$  plies at  $6\text{ cm}^{-1}$  crack density.

Gorman and Ziola [181] noted that AE signals from transverse cracking created both  $S_0$  and  $A_0$  Lamb waves in graphite/epoxy cross-ply laminates. The amplitude from  $S_0$  waves was much larger.

Shih *et al.* [182] used contact transducers to measure metal and polymer matrix cross-ply ( $[90/0]_S$ ) composites, subjected to  $R=0.1$  fatigue tests to induce stiffness degradation. Extensional waves were measured in  $0^{\circ}$ ,  $45^{\circ}$  and  $90^{\circ}$  directions and shear wave was measured

by through-thickness measurements. During the fatigue monitoring, stiffness values obtained from velocity measurements were higher than from static testing with a contact extensometer. This discrepancy was shown to result from crack closure, occurring when the tensile stress was removed i.e. extensional plate wave velocity in  $0^\circ$  and  $45^\circ$  directions was clearly shown to decrease when tensile stress was applied and transverse cracks opened. The stiffness determined from plate waves on “open cracks” specimens approached the stiffness measured by an extensometer. It was recommended to conduct NDE while specimen is under tensile stress.

Seale *et al.* [183] conducted studies on  $[0/90_3]_S$  cross-ply graphite/epoxy specimens to monitor both, fatigue and thermal damage with Lamb wave velocities. Experimental dispersion curves from an immersion study were compared for damaged and undamaged specimens. Roughly a 7% difference in the velocity (related to 5% in  $C_{22}$ ) is reported for  $S_0$  curve, less for  $A_0$  during fatigue damage. They also noted that crack density increased and Lamb wave velocity decreased with increasing number of fatigue cycles. Thermal damage was noted to reduce  $S_0$  velocity by up to 15%.

Toyama *et al.* [184, 185] studied the effects of transverse cracks to low frequency  $S_0$  Lamb mode velocity for CF laminates ( $[0/90_6/0]$  and  $[0/90_8/0]$ ) and GF laminates ( $[0_2/90_{12}/0_2]$ ) for AE source location measurement purposes. Their results indicated that if the number of transverse cracks was known, the  $S_0$  velocity could be evaluated by using existing analytical prediction models for degraded stiffness. The  $S_0$  wave velocity decreased up to 10% for CF and 20% for GF laminate ( $5 \text{ cm}^{-1}$  crack density) while the laminate in-plane stiffness decreased by 15% and 30%, respectively. Their final study [186] also included delaminations and showed significant increase of  $S_0$  velocity as the delaminated area increased. Their reasoning depicted separate smaller  $S_0$  waves propagating in the sub-laminates around the delamination (some with pure  $0^\circ$  ply speed).

Adden *et al.* [149] applied circumferential plate waves to GFRP tubes to measure/monitor the stiffness degradation caused by fatigue damage. By moving the transducer along a line parallel to the cylinder axis, the entire surface of the tube was scanned. Tension/torsion biaxial fatigue loads were applied to the test tubes and a steep drop in stiffness was recorded over first 10% of the fatigue life, which later slowed, as material entered stage II (Fig. 5.2) of fatigue life. In-plane shear stiffness degradation was significant, up to 23%, in comparison to elastic modulus degradation of 10%. A gradual decrease in ultrasonic wave amplitude (increase in damping) was recorded with increasing loading cycles. A correlation between ultrasonic damping and stiffness degradation was noted.

Rheinfurth *et al.* [150] studied biaxially fatigued glass/epoxy cylinders ( $[0/45/90/-45]_S$  layup, where 0 is axial direction) with static testing and air-coupled transducers. Longitudinal stiffness was reduced up to 12% for most of the specimens and in-plane shear modulus up to 29%. After crack density saturation only minor decline in stiffness took place before failure. Guided wave ( $A_0$  mode) velocity and attenuation were measured. Velocity decreased rapidly during first 15% of lifespan, similar to stiffness, their total end-of-life decline was also up to

12% of the initial. It is reported that  $A_0$  propagates separately in several plies of the delaminated areas. Incline in crack density correlates with attenuation.

Schmidt *et al.* [187] studied the effect of large or finely distributed small voids in  $[0/45/90/-45]_S$  glass/epoxy tubes, under biaxial fatigue loading. Both elastic and shear moduli were reported to decline (ca. 10% and 27%, respectively) during first two phases (Fig. 5.2), however last phase (about 5% of life) could not be monitored this way due to the local nature of critical damage. Air-coupled guided wave ( $A_0$  mode) velocity and attenuation are measured parallel to the cylinder axis. Large void detection was demonstrated by using the deviations from average signal amplitude. Guided wave velocity was shown to reduce by just below 10% over lifetime.

Rheinfurth *et al.* [151] present the results from Lamb wave  $A_0$  mode air-coupled measurements for glass/epoxy  $[0/45/90/-45/45/90/-45/0]$  flat laminates under mechanical fatigue loading. Velocity is shown to correlate with measured stiffness degradation and crack densities. Stiffness degradation was about 15% or less before stage III drop (Fig. 5.2) for all used  $R$ -ratios. Decrease in  $A_0$  phase velocities remained below 15% and 24% during ex-situ and in-situ measurements.

Paipetis *et al.* [188] used AE sensors (one as pulser, one as receiver) to measure  $S_0$  pulse velocity on glass/epoxy  $[0_4/90_4]_S$  coupons in-between tension-tension fatigue cycles. Experiments show an initial increase of velocity by 10% at stage I (Fig. 5.2), followed by a plateau of 110% velocity during stage II, and a steep drop when fiber breaking and final stage began (at ca. 60% of life). The velocity right before final failure was ca. 90% of the initial undamaged velocity. The increase in velocity is explained by cracking phenomena as top  $0^\circ$  ply becomes increasingly isolated from the rest of the laminate due to delaminations (and acts as a separate waveguide). The  $S_0$  mode velocity measurements therefore offer an indication of the extent of delaminations.

### 5.1.3.3 Interaction of crack surfaces

During ultrasonic excitation, the crack surfaces are in close proximity or even touching each other, at the tips of asperities. Either the contact areas are of microscopic size or larger, opening-closing of a crack introduces “clapping” phenomena due to the “breathing” of crack. This has been studied by Solodov *et al.* [174, 189–192]. It is reported that these phenomena can be exploited for ultrasonic non-destructive characterization and early detection of fatigue damage.

### 5.1.4 Summary of key issues and motivation for this study

Many studies have been carried out to describe the tensile stiffness degradation from transverse cracks — a partial loss of  $E_2$  modulus — and several analytical models for this purpose are available from literature. For static and vibration studies, researchers e.g. Birman, Yang *et al.* [153, 158–160, 163] recognize that transverse cracks close under compression. A complete restoration of initial modulus is assumed in compression. Morris [152] however reports that hackles are commonly present on the inner surfaces of cracks. The cracks with hackles will not be able to close perfectly. The areas of micro-contact in generally non-planar



contact interfaces are also recognized in [189]. Natural, rough contact interface includes a variety of radii and heights of asperities, resulting in a diversity of local contact pressures (stress concentrations). This discussion hints that a partial loss of  $E_2$  might be appropriate also for compressive loads. In addition, several researchers [149, 150, 187] have measured significant in-plane shear stiffness reduction from transverse cracking. It is of interest to see the same effect from NDT methods.

Early ultrasound studies about distributed damage were focused on carbon and graphite fiber composites. Only recently, papers by Toyama, Adden, Rheinfurth, Schmidt, Paipetis *et al.* [149–151, 186–188,] have also looked into the behaviour of glass fiber composites. While many studies clearly show  $A_0$  and  $S_0$  Lamb wave velocity to decrease with increasing amount of matrix cracks, some unusual phenomena have also been observed. Shih *et al.* [182] noted that progressive opening of transverse cracks (e.g. from tensile load) caused the wave velocity to decrease i.e. there is a difference in wave velocities, depending whether transverse cracks are open or closed. Toyama, Rheinfurth, Paipetis *et al.* [150, 186, 188] have noted that Lamb waves (both  $A_0$  and  $S_0$ ) can propagate separately in isolated surface plies (sub-laminates) which are created in delaminated areas. There is a discrepancy between the influences, since transverse cracks reduce the velocities and wave propagation in sub-laminates can increase the Lamb wave velocity. Overall, the effect from transverse cracks and small delaminations to plate wave velocities is not well understood.

During the last decade more focus has been put on glass-fiber composites in NDT work. However, the number of studies about the NDT detection of transverse cracks for glass-fiber laminates is limited. The referred ultrasound studies mainly compare wave velocities measured from waveforms to an initial reference. According to the knowledge of the author, experiments which characterize Lamb wave behaviour in wavenumber-frequency ( $k$ - $f$ ) axes of transversely cracked glass-fiber laminates have not been published so far. No studies have been found which characterize the same glass-fiber material from three separate and independent (static, natural vibration and Lamb wave) measurements.

Experimental data from static, natural vibration and Lamb wave measurements, characterizing glass/epoxy cross-ply laminates, is presented in the following.

## **5.2 Experimental measurements for stiffness degradation**

The description of glass fiber/epoxy cross plied specimens used for this study is found in Table G.1 in Appendix G.1.

### **5.2.1 Static measurements**

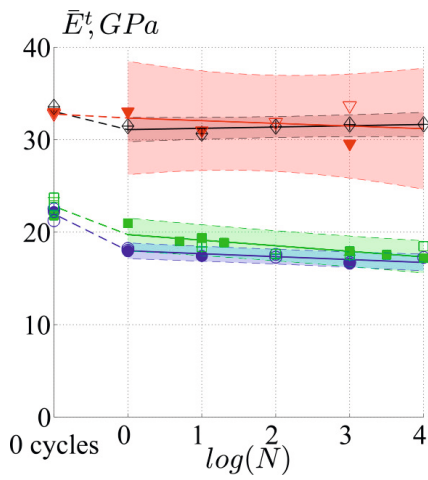
The initial (“0-cycle”) stiffness of undamaged specimens was measured in the earlier work and can be found in Table 2.2 of Section 2.4.2. Fatigue loading was then applied to the same coupon specimens, which progressively resulted in visible development of transverse and longitudinal matrix cracks, and small delaminations, as depicted in Fig. 5.1(a). At certain numbers of fatigue cycles, the tests were interrupted and the specimens were removed for static testing. Uniaxial tension and three-point flexure testing was employed, exactly the same way as for “0-cycle” stiffness (for details see Appendix G.2).

The objective of fatigue loading was to create a damage state clearly surpassing transverse crack saturation and progressively characterize laminate stiffness during this process. Triangular shaped tension-tension fatigue loading ( $R = \sigma_{\min}/\sigma_{\max} = 0.1$ ) was applied under load control and room temperature. The frequency of the fatigue load was low,  $f < 0.5$  Hz. Load control was chosen to avoid stress relaxation, which also restrains damage development, known to occur under deformation control. The maximum load for each specimen was chosen to be 400 MPa stress in the  $0^\circ$  plies, without considering  $90^\circ$  plies (approximately 40 % of the estimated ultimate tensile load for all specimens). The average stresses over entire cross-section were therefore either 133 MPa or 266 MPa. The maximum strains during fatigue were in the range  $\epsilon_{\max} \approx (0.6, 0.9)$  % for different specimens and cycle numbers. Fatigue loading was applied for 10 000 cycles, or until the specimen failed, if this occurred before.

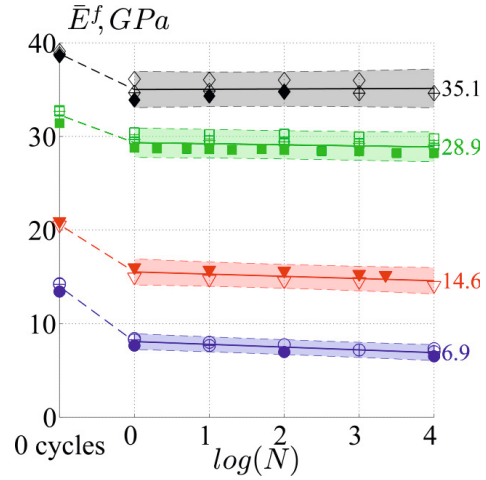
Tensile and flexural stiffness of the laminate was monitored from in-between measurements and the results are presented in Fig. 5.3. The use of numerous specimens over several fatigue cycles  $N$  enables to evaluate statistical 95 % confidence intervals for stage II (see Fig. 5.2) linear stiffness degradation in Figs. 5.3(a),(b). Figures 5.3(a) and 5.3(b) include the numerical value of layup average stiffness at  $10^4$  cycles. The abscissa in these plots is base ten logarithm of cycle numbers with values in the interval (0, 4). The undamaged “0-cycle” results from Table 2.2 are marked separately, although plotted on the same axes.

The figures show that the applied load was so high that most of the stiffness degradation took already place during the first cycle. The elastic modulus reduction during the first cycle is mostly attributed to transverse cracking. The pace of stiffness degradation between 1 and 10 000 cycles is stable and it is concluded that the laminates entered stage II of fatigue life.

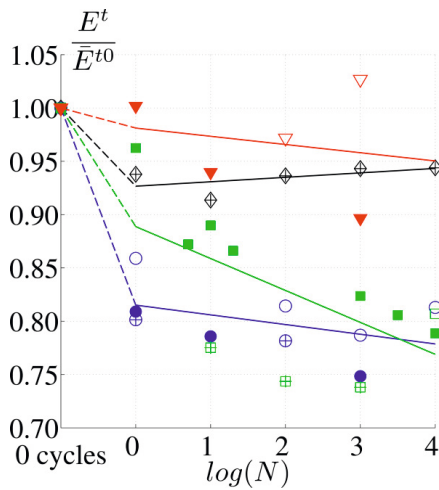
Not all of the measured data was plotted in Fig. 5.3. A filter was applied to the experimental data in order to disregard outliers and measurements with overly high variability. A single stiffness measurement (i.e. a data point) in Fig. 5.3 is the mean of at least four repeated measurements on the same specimen, as explained in Appendix G.2. The difference between highest and lowest values in force/strain or force/deformation slopes was calculated for each of the repeated measurements (see Fig. 5.4(a)). If the difference between the extremes was more than 10% of the mean, the measurement was considered as failed and the data was disregarded from further consideration. The slope variability is explained in Fig. 5.4(a) and a chart explaining the filter in Fig. 5.4(b). The data points in Fig. 5.3 have all passed this filter. A total of twenty eight stiffness measurements were disregarded from tensile experiments and four from flexural experiments.



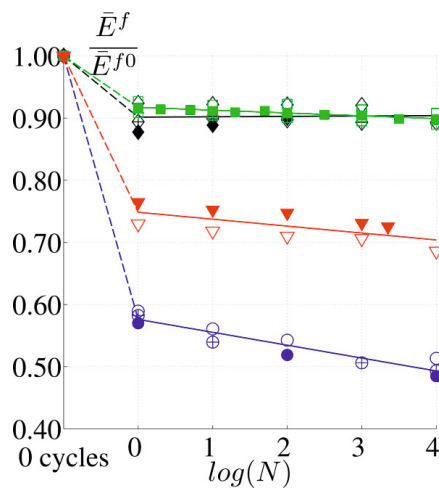
(a) Tensile stiffness and 95% CI, numerical value of layup average given at  $N=10^4$  (GPa)



(b) Flexural stiffness and 95% CI, numerical value of layup average given at  $N=10^4$  (GPa)



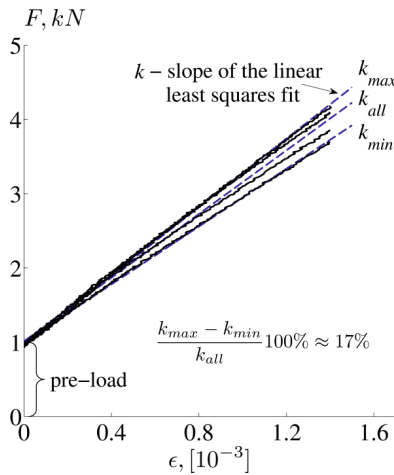
(c) Tensile stiffness, normalized



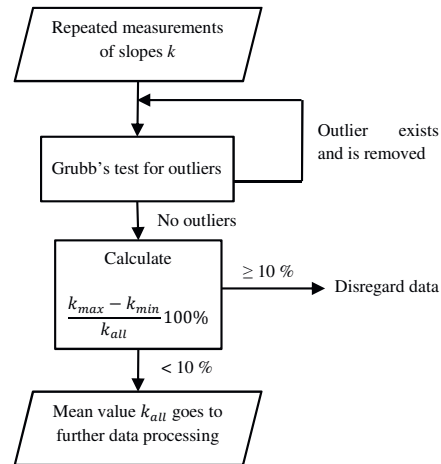
(d) Flexural stiffness, normalized

○ 1a	◇ 2a	□ 3a	▽ 4b
⊕ 1b [90 <sub>2</sub> /0 <sub>2</sub> /90 <sub>2</sub> ]	⊕ 2b [0 <sub>2</sub> /90 <sub>2</sub> /0 <sub>2</sub> ]	⊕ 3b [0/90 <sub>4</sub> /0]	▼ 4c [90/0 <sub>4</sub> /90]
● 1c	◆ 2c	■ 3c	

Figure 5.3. Tensile and flexural stiffness degradation from tensile fatigue of the laminate ( $R=0.1$ ,  $\sigma_{max} \approx 0.4 \sigma_{ult}$ ), solid lines mark the least-squares linear fit for different layups.



(a) Example of high variability in repeated tensile measurements. Specimen 3a, tensile test,  $N=10$  cycles



(b) Sequence of steps for filtering out low quality experimental data

Figure 5.4. Filter for the experimental data.

Specimen 4a was destroyed by an accident before fatigue testing. Specimen 2a had no end tabs and it failed prematurely near the grip at cycle count  $N > 1000$ . Specimens 2c and 4c began to slip in the grips and fatigue loading could not be continued after 100 and 2252 cycles, respectively. Specimen 3c was measured in more intermediate points than others in order to get a better notion of the degradation curve.

The  $90^\circ$  ply is effectively cut to sections by an increasing amount of transverse cracks as the cyclic fatigue load is applied. Single cracks are visible to the naked eye on the surfaces and sides of the specimens, when some hue is applied. Average crack spacing can be determined by counting the number of cracks per length at several places on a single specimen. Table 5.1 displays the transverse crack spacing after fatigue loading, averaged over four representative locations, each spanning ca. 5 cm, for each of the specimens. The results show that crack density is higher for laminates with thinner  $90^\circ$  plies, which is expected.

Table 5.1. Average transverse crack spacing after tensile fatigue.

Specimen	Nr. of cycles $N$	Average crack spacing, mm	Layup	Average for layup, mm
1a	10 000	2.17	[90 <sub>2</sub> /0 <sub>2</sub> /90 <sub>2</sub> ]	2.19
1b	10 000	2.26		
1c	10 000	2.13		
2b	10 000	1.41	[0 <sub>2</sub> /90 <sub>2</sub> /0 <sub>2</sub> ]	1.46
2c	100	1.50		
3a	10 000	1.72	[0/90 <sub>4</sub> /0]	1.81
3b	10 000	1.89		
3c	10 000	1.82		
4b	10 000	1.58	[90/0 <sub>4</sub> /90]	1.65
4c	2252	1.72		

## 5.2.2 Vibration measurements and optimization results

It is known that the degree of reduction in natural frequency is dependent on the position of the defect/damage relative to the mode shape of particular mode of vibration. The reduction in frequency is larger when the cracks are at regions of large curvature for the specific mode. This dependency is hereby removed by manufacturing a plate test specimen which has homogeneous damage over all its volume.

Static stiffness degradation measurements in Section 5.2.1 unsurprisingly showed that  $[90_2/0_2/90_2]$  specimens had the largest reduction of tensile or flexural stiffness observed from four layups. To investigate the possibility of detecting stiffness reduction by non-destructive measurements, two plate specimens (ca.  $30 \times 30 \text{ cm}^2$ ) of this layup were produced.



Figure 5.5. Specimen  $TR11\_1F$  in the 1000 kN test machine during fatigue loading.

Details about the glass-fiber/epoxy specimen production can be found in Table G.1 in Appendix G.1. It is noted that their production process was exactly the same as for coupon specimens. Plate  $TR11\_1$  is a virgin specimen without damage; plate  $TR11\_1F$  is an analogue which has fatigue damage; both plates have  $[90_2/0_2/90_2]$  layups.  $TR11\_1F$  was loaded with 150 cycles of sinusoidal  $R = 0.1$ ,  $\sigma_{max} \approx 0.4\sigma_{ult}$  fatigue loading in  $[90_2/0_2/90_2]$  direction (see Fig. 5.5). The uncertainty about the fatigue behavior for this specific mechanical set-up was the main reason for applying only 150 cycles. However, the behavior in Fig. 5.3 shows that 150 cycles is sufficient to arrive to transverse crack saturation for such high load. This was confirmed by the crack spacing measurements on outside plies of  $TR11\_1F$  which were 2.2 mm on average, agreeing well with the crack spacing of smaller coupons after 10 000 cycles, as seen in Table 5.1. The mean physical plate properties are reported in Table 5.2(a) and the results for the natural frequencies of all-edges-free plates in Table 5.2(b). Details about vibration measurements can be found in Appendix G.3.

Table 5.2 Experimental measurement results for  $[90_2/0_2/90_2]$  plates.

a) Physical properties

Plate	Layup	$a$ , mm	$b$ , mm	$h$ , mm	$\rho$ , kg/m <sup>3</sup>
TR11_1	[90 <sub>2</sub> /0 <sub>2</sub> /90 <sub>2</sub> ]	294	293	4.79	1958
TR11_1F		294	300	4.68	1973

b) Natural frequencies, Hz

Plate	Layup	$f_1^{\text{exp}}$	$f_2^{\text{exp}}$	$f_3^{\text{exp}}$	$f_4^{\text{exp}}$	$f_5^{\text{exp}}$
TR11_1	[90 <sub>2</sub> /0 <sub>2</sub> /90 <sub>2</sub> ]	88.7	155.9	234.8	255.2	306.3
TR11_1F		78.8	122.8	198.1	238.3	279.3
(TR11_1 → TR11_1F)		-11 %	-21 %	-16 %	-7 %	-9 %

The reduction of natural frequencies is immediately apparent for the damaged plate TR11\_1F. However, it should be noted that the physical properties of the two plates are also slightly different. Plate TR11\_1F is thinner and deviates more from the square shape (side length  $a$  is measured along the  $[90_2/0_2/90_2]$  direction).

Ply property based natural frequency calculation would require that some assumptions for damage mechanisms are introduced. For example, whether  $E_2$  of the cracked transverse ply would have similar or different stiffnesses in tension and compression. The effects of damage mechanisms for plies were left undecided and the inversion of stiffness properties for the TR11\_1F plate was carried out on plate level (i.e. treating the laminate as a single orthotropic layer). As a reminder, the inversion of TR11\_1 had also been carried out on laminate level in Section 3.6.2.

The optimization was carried out by using the same principles and objective function as for virgin plates in Section 3.6.2 previously. However, some details are explained again in the following. The parameters for SGA optimization based inversion are shown in Table 5.3.

Table 5.3. SGA parameters for plate TR11\_1F.

Pop. size	$n = 25$
Nr. of generations	$t = 30$
Fitness scaling parameter	$nxavg = 2$
Probability of cross-over	$p_{\text{cross}} = 90 \%$
Nr. of elites	$n_{\text{elites}} = 1$
Mutation probability	$p_{\text{mut}} = 2 \%$

Computation time is saved by narrowing the search space. This was possible as approximate analytical estimates, based on formulas given in ref. [60] were used to get first rough estimates for stiffnesses  $E_x$ ,  $E_y$ ,  $G_{xy}$ . The resolution is defined very finely for the sensitive moduli ( $E_x$ ,  $E_y$ ,  $G_{xy}$ ), below 0.01 GPa, and very coarsely for non-sensitive constants ( $\nu_{xy}$ ,  $G_{xz}$ ,  $G_{yz}$ ). The binary string lengths designated to the variables are 10, 9, 9 digits for  $E_x$ ,  $E_y$ ,  $G_{xy}$  and 2 digits for each of the non-sensitive moduli, resulting in a 34 binary digit individual for each

of the plates. SGA optimization was run consecutively 50 times for the plate inversion. The evolution of fitness can be seen in Fig. 5.6, with similar data from virgin plates. Each of the 50 SGA optimizations took  $n_{feval} = nt = 25 \cdot 30 = 750$  fitness function evaluations. The unique solutions resulting in  $fitness \geq 4.95$  were achieved for 10 out of 50 runs, but the maximum  $fitness = 5$  was not obtained. Three constants of these high-fitness results have converged well, as seen from Table 5.4.

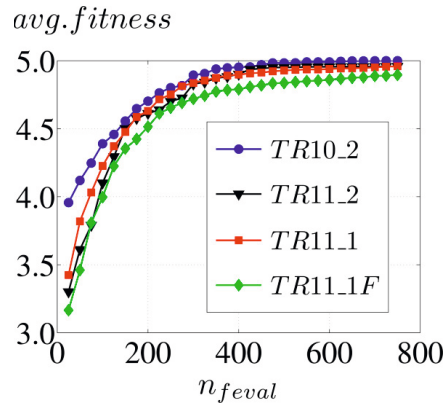


Figure 5.6 The fitness of the best individual averaged over 50 optimization runs, as a function of number of fitness function evaluations

Table 5.4. Statistical data of unique fitness  $\geq 4.95$  results from SGA optimization.

El. constant	TR11_1F	
	Mean	COV, %
$E_x$ , GPa	35.1	0.4
$E_y$ , GPa	10.2	0.5
$\nu_{xy}$	0.05	161.0
$G_{xy}$ , GPa	3.9	0.1
$G_{xz}$ , GPa	5.1	23.5
$G_{yz}$ , GPa	5.2	21.8

The flexural moduli which are believed to be identified with confidence, for both virgin and damaged plates, are given in Table 5.5. The results for the virgin plate TR11\_1 are copied from Table 3.6 in Section 3.6.2.

Table 5.5. The comparison of effective moduli measured from vibration testing.

El. constant	TR11_1 (virgin)	TR11_1F (fatigue damage)	Difference
$E_x$ , GPa ( $[0_2/90_2/0_2]$ )	38.6	35.1	- 9 %
$E_y$ , GPa ( $[90_2/0_2/90_2]$ )	14.3	10.2	-28 %
$G_{xy}$ , GPa	4.5	3.9	-13 %

Some observations, regarding the values in Table 5.5, are noted.

- Comparison of laminate moduli unambiguously shows that all three in-plane moduli decrease with fatigue damage. Therefore, all three can be used for damage detection, even when the load is only in  $y$ -direction.
- The values for  $E_x$  and  $E_y$  for the intact plate  $TR11\_1$  compare well to flexural stiffnesses measured by static tests for specimens 2 and 1, ranging (38.6, 39.1) and (13.4, 14.3), respectively, as seen from Table 2.2.
- The  $E_y = 10.2$  GPa result for plate  $TR11\_1F$  shows clearly higher result than the uncertainty range for specimen 1 in Fig 5.3(b). Since this modulus is mostly controlled by  $E_2$  and is therefore matrix dominated, it may be hypothesized that strain rate dependence makes the material behave stiffer during vibration measurements.
- The  $E_x = 35.1$  GPa value for  $TR11\_1F$  cannot in principle be compared to values of Specimen 2 in Fig 5.3(b) because the fatigue load was not applied in this direction of the plate. The static test coupons were, however fatigued in the same direction. Nevertheless, these values do compare well — the mean value from static measurements after  $10^4$  cycles was 35.1 GPa. This comparison shows that in-plane damage is also created for longitudinal stiffness in  $x$ -direction, even when the fatigue load is in  $y$ -direction, most likely due to longitudinal cracks (which are transverse in the other direction) and delaminations.

Natural frequencies vary with the square root of the flexural stiffness change, for beams and also for simple analytical formulas for plates. Modes (1,1), (2,0) and (0,2) are dominated by laminate moduli  $G_{xy}$ ,  $E_y$  and  $E_x$ , respectively. FE-modelling of plates  $TR11\_1$  and  $TR11\_1F$  with their inverted constants confirms that the order of the first five modes is the same both plates, with (1,1) being the first, (2,0) the second and (0,2) the fourth mode. Table 5.6 shows the comparison of frequency ratios and square roots of moduli ratios, which correspond to these frequencies. This shows that modulus ratio can be approximately predicted for square plates, based on the ratio of natural frequencies from these three basic modes.

Table 5.6. The comparison of frequency and moduli ratios.

Ratio	1. mode (1,1)	2. mode (2,0)	4. mode (0,2)
$f_{1, TR11\_1} / f_{1, TR11\_1F}$	1.13	1.27	1.07
$(G_{xy, TR11\_1} / G_{xy, TR11\_1F})^{0.5}$	1.07	-	-
$(E_{y, TR11\_1} / E_{y, TR11\_1F})^{0.5}$	-	1.18	-
$(E_{x, TR11\_1} / E_{x, TR11\_1F})^{0.5}$	-	-	1.05



### 5.2.3 Wave propagation measurements

As in the previous section, the virgin plate is referred as *TR11\_1* and the plate with fatigue damage as *TR11\_1F*. Peel plies (i.e. release fabrics) had been used on both faces of plates during manufacturing, and therefore the final surfaces turned out slightly corrugated. However, the corrugations were sanded down on the location of laser dot measurements. Lamb wave measurements and 2-D FFT were carried out according to the description in Appendix G.4. Two different transducers with 100 kHz and 250 kHz central frequencies were used for signal excitation on the edge of the plate.

The local maxima from the frequency-wavenumber representation (after 2-D FFT) were identified from three separate measurements:

- virgin plate *TR11\_1* with 250 kHz transducer;
- damaged plate *TR11\_1F* with 100 kHz or 250 kHz transducers.

Both plates are hereby denoted by layup  $[90_2/0_2/90_2]$  in the  $x$ -direction. Perpendicular direction  $[0_2/90_2/0_2]$  is denoted as  $y$ . Therefore, wave propagation in  $x$ -dir. is across and in  $y$ -dir. along the transverse cracks which had been created in the outer plies during fatigue loading. The results of three measurements are shown on wavenumber-frequency ( $k$ - $f$ ) axes in Fig. 5.7(a) and phase velocity vs frequency-thickness axes in Fig. 5.7(b).

Sensitive changes of the phase velocities of different propagation modes can be useful for determining damage. The following can be observed from Fig. 5.7.

- Plots in both directions show that experimentally measured changes for  $A_0$  and  $S_0$  mode are small, when compared to the overall scatter of results. Only the reduction of  $S_0$  is clearly evident (by ca. 13%) in the range (0.5, 1.5) MHz-mm for  $x$ -dir. (across the transverse cracks).
- Data for  $S_0$  velocity is scattered in the range (0.5, 1.5) MHz-mm for  $x$ -direction and (0.5, 1.0) for  $y$ -direction.
- $A_0$  mode displays more data in the low frequency spectrum,  $S_0$  becomes very inconsistent below 0.5 MHz-mm.
- Some data points are obtained for higher order modes, either  $S_1$  or  $A_1$ .

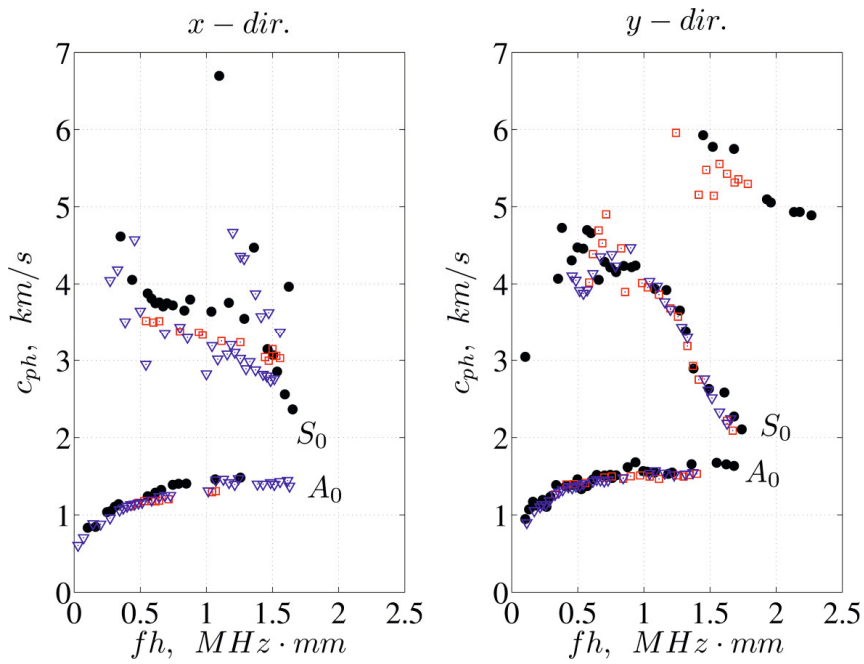
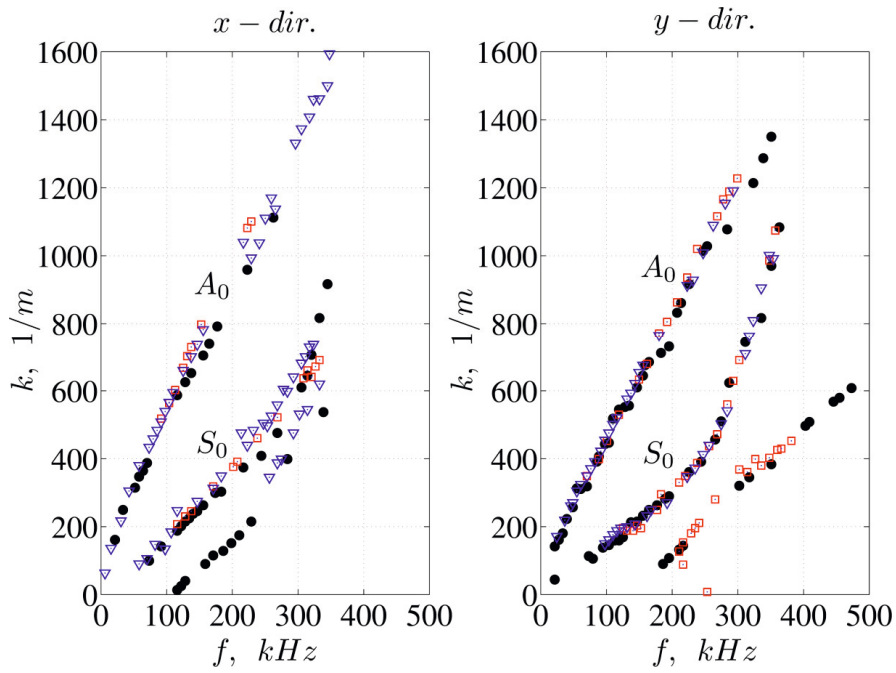


Figure 5.7. Experimental traces of Lamb wave dispersion curves. (o): TR11\_1 (virgin), 250 kHz; ( $\square$ ): TR11\_1F (fatigue damage), 250 kHz; ( $\nabla$ ): TR11\_1F (fatigue damage), 100 kHz.

### 5.3 Summary of experimental observations

Static measurements in between fatigue cycles quantified the effect of fatigue load to laminate stiffness. Most of the stiffness degradation is attributed to  $E_2$  due to transverse cracks, however longitudinal matrix cracks in  $0^\circ$  plies and small delamination spots were also observed on specimens.

- Fig. 5.3(c) shows that tensile stiffness is reduced by only 5% for specimens  $[0_2/90_2/0_2]$  and  $[90/0_4/90]$ ; and about 20% for specimens  $[90_2/0_2/90_2]$  and  $[0/90_4/0]$ .
- Fig. 5.3(d) shows that flexural stiffness drops by 10% for  $[0_2/90_2/0_2]$  and  $[0/90_4/0]$ ; up to 30% for  $[90/0_4/90]$ ; and up to 50% for  $[90_2/0_2/90_2]$ .
- Tensile stiffness degradation of 5% ( $[0_2/90_2/0_2]$  or  $[90/0_4/90]$ ) cannot be detected with confidence for usual engineering materials. The COV-s for ply properties were measured and calculated as 2.5% for  $E_1$  and 8% for  $E_2$  (see Section 2.5).
- The flexural stiffness reduction of 50% and the tensile stiffness reduction by 20% for  $[90_2/0_2/90_2]$  specimens (Fig. 5.3 (c), (d)) clearly exceeds the uncertainty intervals and should therefore be detectable.

Showing the most potential for non-destructive measurements, layup  $[90_2/0_2/90_2]$  was chosen for further non-destructive studies. Two plates with this layup were manufactured, and one of them was pre-treated with tensile  $R=0.1$  fatigue loading (up to 40% of estimated ultimate load), creating uniform damage: saturated transverse cracks, longitudinal cracks and small spots of delamination. The main observations from the vibration measurements of these two plates are as follows.

- The first five natural frequencies of two approximately similar plates decreased by ca. 10–20%.
- The in-plane moduli proved to be sensitive to fatigue loading applied in only one direction, and their values decreased: flexural moduli by 28% and 9%, shear modulus by 13%.
- The flexural stiffness of the plate in fatigue direction  $[90_2/0_2/90_2]$  is higher than the 95% confidence interval of a similar coupon measured from static testing. This flexural modulus is  $E_2$  and matrix dominated and this result shows possible strain rate dependence of  $E_2$ .

The experimental dispersion curves of Lamb waves, for the same two plates, measured by a laser interferometer, display the following results (Fig. 5.7).

- The phase velocities of the damaged plate are lower, compared to the virgin plate, in both principal directions, over full frequency spectrum. However, the reduction of the phase velocity is small, except for  $S_0$  in  $[90_2/0_2/90_2]$  direction at (0.5, 1.5) MHz-mm frequency range by ca. 13%.
- The reduction of  $A_0$  and  $S_0$  mode velocities is small ( $< 10\%$ ) elsewhere and comparable to experimental scatter.
- Data for  $S_0$  velocity is scattered in the range (0.5, 1.5) MHz-mm for  $[90_2/0_2/90_2]$  direction and (0.5, 1.0) MHz-mm for  $[0_2/90_2/0_2]$  direction.

It can be noted that three experimental quantities were evaluated to characterize laminate stiffness. The slope of force/displacement curve was measured in static testing — proportional to laminate stiffness, as e.g. seen from Eq. (2.2). Natural frequencies were measured in vibration testing — proportional to the square root of their dominant stiffnesses, as can be seen in the approximate formulas in [60, 83]. Phase velocities were measured for Lamb waves — proportional to either square root or 0.25 power of laminate stiffness in the low frequency region (see Eqs. (F.14), (F.15)). Therefore, as the frequency of measurement methods increases (static → vibration → wave) the effect of the laminate stiffness change to the experimentally measured quantity decreases (powers of 1 → 0.5 → 0.25). To summarize, the same change in stiffness is expected to affect the slope of the force/displacement curve the most, the natural frequencies by an intermediate amount, and the phase velocities of the Lamb waves the least.

Table 5.7 is compiled to summarize the experimental observations for the effect of fatigue damage to the [90<sub>2</sub>/0<sub>2</sub>/90<sub>2</sub>] glass-fiber/epoxy laminate. Changes of stiffness and dispersive velocity measurements are quantified and, where possible, compared.

Table 5.7. Changes in [90<sub>2</sub>/0<sub>2</sub>/90<sub>2</sub>] laminate behavior due to fatigue load ( $R=0.1$ ,  $\sigma_{max} \approx 0.4\sigma_{ult}$ ), exceeding transverse crack saturation.

Static*	Vibration**	Lamb wave**
[90 <sub>2</sub> /0 <sub>2</sub> /90 <sub>2</sub> ] $\bar{E}^t$ : -20% $\bar{E}^f$ : -50%	[90 <sub>2</sub> /0 <sub>2</sub> /90 <sub>2</sub> ] $\bar{E}^f$ : -28% [Both dir.] $\bar{G}_{xy}$ : -13%	[90 <sub>2</sub> /0 <sub>2</sub> /90 <sub>2</sub> ] $S_0 c_{ph}$ : -13% in (0.5, 1.5) MHz-mm
[0 <sub>2</sub> /90 <sub>2</sub> /0 <sub>2</sub> ] $\bar{E}^t$ : -5% $\bar{E}^f$ : -10%	[0 <sub>2</sub> /90 <sub>2</sub> /0 <sub>2</sub> ] $\bar{E}^f$ : -9%	Small (< 10%) reduction of $A_0$ and $S_0$ elsewhere

\* - fatigue load applied to the specimen direction

\*\* - fatigue load applied only to [90<sub>2</sub>/0<sub>2</sub>/90<sub>2</sub>] direction of the plate

Vibration testing shows that in-plane shear modulus has reduced by 13% due to transverse cracking. This is slightly less than shear modulus degradation from static measurements reported in literature (reduction ca. 20–30%).

It is evident that a discrepancy exists for flexural stiffness reduction in the [90<sub>2</sub>/0<sub>2</sub>/90<sub>2</sub>] direction — static testing shows up to 50% stiffness reduction while vibration measurement shows only a 28% reduction. The low-frequency  $A_0$  velocity is reduced less than 10%, however the scatter of experimental data has a comparable magnitude. Approximate formulas for low-frequency region  $A_0$  show that phase velocity is proportional to 0.25 power of effective flexural stiffness (as seen from Eq. (F.15)). This would predict the  $A_0$  velocity reduction to ca.  $1-(0.5)^{0.25} = 16\%$  based on static stiffness reduction, or to  $1-(0.72)^{0.25} = 8\%$  based on vibration-measured stiffness reduction.

As for the extensional behavior in the same direction — static tensile stiffness is reduced by 20%, whereas Lamb wave  $S_0$  velocity by ca. 13% in the (0.5, 1.5) MHz-mm frequency region. The  $S_0$  velocity in the low frequency region is proportional to the square root of effective extensional laminate stiffness (see Eq. (F.14)). Therefore, static tensile stiffness reduction of

20% would predict the  $S_0$  velocity reduction to  $1 - (0.8)^{0.5} = 11\%$  in this region (assuming cracks are not closing for the Lamb wave). This agrees reasonably well with the result from the  $S_0$  measurement.

Literature studies revealed three possible causes creating discrepancies between different methods:

- strain rate dependence of elastic moduli;
- transverse crack closure and opening (depending on the magnitude and direction of movements of crack surfaces);
- separate propagation of Lamb waves in the sub-laminates, separated by areas of delamination.

## 6 Conclusions

This Chapter contains the summary of main results and points out the novelty in the monograph. In addition, some suggestions are given for future work.

### 6.1 Achieving the objectives

The four objectives stated in Section 1.5 of the monograph were achieved as follows:

1. Chapter 2 and Appendix D describe a new method for analyzing experimental data. The method was developed to evaluate ply moduli (and COV) from the laminate stiffnesses of symmetric cross-ply laminates. The back-calculation method was successfully demonstrated on experimental data compiled of tensile and flexural stiffnesses (Sections 2.4.2, 2.5.3). Additionally, the same method was generalized for symmetric-balanced laminates (Section 2.4.3). The general approach was less successful as the scatter of back-calculated moduli became excessive when experimentally measured stiffness data was used as input.
2. A dynamic test method based on impulse loading and natural vibration measurements is described and experimentally demonstrated in Chapter 3. The determination of flexural plate moduli  $E_x$ ,  $E_y$  and in-plane  $G_{xy}$  is carried out for thin plates. Additionally,  $G_{xz}$ ,  $G_{yz}$  should be possible to evaluate for thick plates, or by employing higher modes, and  $\nu_{xy}$  for plates with appropriate length to width aspect ratio. The experiments are simple and fast to conduct. Data manipulation requires FE analysis and optimization, both of which were developed by means of non-commercial software (utilizing freeware toolbox for FEA and own code for SGA). Systematic errors due to approximate numerical modelling and random errors from experimental uncertainties are accounted in the fitness definition.

Another dynamic method based on wave propagation measurements was developed in Chapter 4. Experimental procedure for this method (Appendix G.4) is elaborate and currently mostly suitable in the laboratory environment. However, this can change in the future. Ply moduli  $E_1$ ,  $E_2$ ,  $E_3$ ,  $G_{13}$ ,  $G_{23}$  were obtained from the measurements in two principal directions of the UD plate. The inverse problem was solved by using three different optimization strategies: two global GA based methods (SGA,  $\mu$ GA) and a two-stage Simplex method accompanied by a preliminary sensitivity study.

3. The reader is referred forward to Section 6.2 (Tables 6.1 and 6.2) for the comparison of elastic constants measured from different test methods.
4. The influence from transverse cracking (due to fatigue) on elastic constants of cross-ply laminates was experimentally studied in Chapter 5. The detailed overview of experimental observations is given in Section 5.3 and a broad method-based summary in Section 6.2.

## 6.2 Comparison of independent measurements

The following Tables summarize and compare experimentally measured stiffnesses, obtained from different measurement methods (quasi-static, natural vibrations and Lamb waves). First, the measurements conducted on virgin glass fiber laminates are discussed. Then, a method-based summary is given about the damaged material.

Table 6.1 shows a good agreement of results for quasi-static and vibration based measurements of flexural stiffness. The results of vibration measurements can also be used for further ply modulus back-calculation, as described in Chapter 2. Vibration-measured stiffnesses, which are more matrix dominated (14.3 GPa and 21.5 GPa) seem to agree with the upper limit of stiffnesses from quasi-static measurements. This can be related to the strain rate dependence of  $E_2$  modulus. However, the vibration-measured fiber-dominated moduli (38.6 GPa and 32.0 GPa) can be noted to agree with the mid-range or lower limit of respective quasi-static measurements. More analogous measurements are needed to conclude whether this behavior is really systematic.

The results in Table 3.6 also show that in-plane shear stiffnesses  $G_{xy}$ , measured from the vibration of plates with same material and different layup ( $[90_2/0_2/90_2]$  and  $[0/90_4/0]$ ), show remarkably similar results (4.5 GPa and 4.6 GPa), as expected from theory.

Table 6.1. A comparison of laminate flexural moduli from static and vibration based measurements on virgin glass/epoxy cross-ply laminates.

Specimens: glass/epoxy (Table G.1 in Appendix G) Data: Table 2.2, Table 3.6		
Layup	Quasi-static $\bar{E}^f$ , GPa	Vibration $\bar{E}^f$ , GPa
$[90_2/0_2/90_2]$	14.3	14.3
	14.2	
	13.4	
$[0_2/90_2/0_2]$	39.1	38.6
	38.8	
	38.6	
$[0/90_4/0]$	32.8	32.0
	32.7	
	31.4	
$[90/0_4/90]$	20.3	21.5
	20.5	
	20.9	

Table 6.2 compares the elastic constants measured from the UD laminate by two dynamic methods (vibrations, Lamb waves). Again, a good agreement between the results is noted for two independent methods. Known relations  $E_2 = E_3$  and  $G_{12} = G_{13}$  for transversely isotropic symmetry are shown to hold approximately.

Table 6.2. A comparison of UD laminate moduli from vibration and Lamb wave based measurements on virgin glass/vinylester material.

Specimens: glass/vinylester (Table G.3 in Appendix G) Data: Table 3.6, Table 4.6				
Modulus	Lamb wave propagation			Vibration
	SGA	$\mu$ GA	Simplex	
$E_1$ , GPa	38.3	38.6	39.9	40.8
$E_2$ , GPa	15.6	15.5	15.5	15.1
$E_3$ , GPa	15.3	15.2	15.4	-
$G_{12}$ , GPa	-	-	-	5.5
$G_{13}$ , GPa	6.0	6.0	6.0	-
$G_{23}$ , GPa	4.7	4.7	4.8	-

Three independent measurement methods were applied to the transversely cracked (fatigued) material in the final part of the experimental work. All three methods succeeded to display stiffness reduction; however the mutual agreement was slightly less satisfactory than for virgin specimens. Reference is made back to Section 5.3 for the full discussion. Table 6.3 gives a broad, method-based summary of experimental observations. Bullet points hypothesize about the possible causes for the discrepancies. It is concluded that each of these approaches can in principle be applied for qualitative damage detection. In order to obtain quantitative agreement for stiffness degradation, more refined models need to be developed — taking account of crack-closure, strain rate influence and separate wave propagation in sub-laminates.

Table 6.3. A method-based comparison of stiffness measurements on transversely cracked laminates.

Specimens: glass/epoxy (Table G.1 in Appendix G), fatigue load $R=0.1$ , $\sigma_{\max} \approx 0.4\sigma_{\text{ult}}$ , exceeding transverse crack saturation Data: Table 5.7		
Quasi-static	Vibration	Lamb wave
Lowest stiffness (largest reduction) <ul style="list-style-type: none"> <li>• crack closure</li> </ul>	Medium stiffness (medium reduction) <ul style="list-style-type: none"> <li>• crack closure</li> <li>• strain rate influence</li> </ul>	Highest stiffness (approximately evaluated from $A_0$ , $S_0$ velocities) <ul style="list-style-type: none"> <li>• crack closure</li> <li>• strain rate influence</li> <li>• wave propagation in separated sub-laminates</li> </ul>



### 6.3 Novelty

- A new method for the back-calculation of ply moduli from laminate stiffness measurements (tensile and flexural) is described for symmetric cross-ply laminates. A stacking sequence parameter  $\delta$  is defined, which enables to estimate the standard deviation of the back-calculated moduli, both qualitatively and quantitatively. The reader is referred to Sections 2.3 and 2.5 and Appendix D for details.
- New experimental data is obtained, characterizing the behavior of transversely cracked glass-epoxy cross plied laminates from quasi-static, natural vibration and Lamb wave propagation measurements. Such data or comparison, obtained by measuring the same damaged material by three independent methods, has not been found in the open literature by the author. The results from the measurements are presented in Section 5.2 and the summary of observations is found in Section 5.3.
- Two improvements are described for the application of optimization algorithms. The author has not accounted these approaches in the open literature.
  - The fitness function used for the optimization with vibration measurements is defined to account for systematic and random error estimates. This defines the target frequencies not as distinct, but rather as plausible frequency ranges. The reader is referred to Section 3.6.2 for details.
  - A useful improvement is described for the Simplex optimization. It requires a “good” preliminary guess and previous sensitivity study about the elastic constant influence to phase velocities. The two-stage optimization is shown to converge to similar values as with global optimization (SGA,  $\mu$ GA) methods, however displaying much faster performance. The reader is referred to Sections 4.2.2 and 4.2.4 for details.
- The waves in composite plates were detected on the plate surface by a laser interferometer. Evidence about Scholte interface waves between glass-epoxy composite plate and air was detected in several measurements. Various measurements of Scholte waves have been conducted by other researchers previously. However, this is the first time known to the author, when Scholte waves are measured on a transversely cracked (damaged) composite surface in air. The measurement of Scholte waves enables to characterize the surrounding media (e.g. gas, air) rather than the plate itself in case of usual engineering solids. The work is ongoing to explain the measured data. Section 4.3 describes the results and the context to Scholte waves.

## 6.4 Summary of findings

A concise summary of most relevant findings is hereby given.

1. The back-calculation of ply moduli was carried out based on tensile and flexural stiffnesses of symmetric, cross-plyed laminates. The experimentally measured moduli resulted with coinciding results from different strategies, also agreeing with realistic expectations.  
Further, the back-calculation method was shown to be ill-conditioned for some laminates (i.e. errors in input data cause much larger errors in the output). To decide whether a combination of a laminate and a calculation strategy is ill-conditioned, and by how much, a dimensionless stacking sequence parameter  $\delta$  can be calculated. The coefficients of variation for the ply moduli were also evaluated by using the same parameter  $\delta$ .  
Altogether, a systematic methodology was developed to evaluate ply moduli (with coefficients of variation) from laminate tensile or flexural stiffnesses.
2. Quasi-static, natural frequency and Lamb wave propagation based measurements were employed to evaluate the elastic moduli of virgin glass-fiber laminates. The comparison of Young's and shear moduli shows very good agreement and expected results for these three independent methods. The flexural stiffnesses from vibration testing can be further employed for back-calculation, as described in the previous paragraph.
3. The stiffness reduction of a cross-plyed laminate due to tension-tension fatigue was investigated by employing the aforementioned three methods (static testing, natural frequency measurements and Lamb wave dispersion curves). Although the reduction of stiffness or velocity was indeed witnessed for each method, the agreement of individual results was less satisfactory than for virgin material. In general, static testing showed the largest reduction and Lamb waves the smallest reduction of stiffnesses. Vibration testing showed a clear reduction of flexural and in-plane shear moduli.
4. Scholte waves were observed in the interface between air and the surface of damaged glass-fiber/epoxy laminate (transverse cracks reaching surface).

## 6.5 Future work

Hereby, some suggestions for work directions are given, which remained undone and can be interesting for future studies.

1. An approach to obtain dispersion curves for Lamb wave propagation could be developed as a numerical in-house/freeware code for arbitrary multi-layered plate configurations (various plies made from different anisotropic materials, at arbitrary angles). Such solutions are known to exist and commercial software [116, 117] is available. Writing it as in-house code was skipped in current work since it seemed like a formidable task with little promise of scientific novelty. The extension to general layouts and the ability to use it as a module in other code would enable to study a wide variety of layered plates.
2. The generation of Scholte interface waves was not consistent by using contact transducers on the plate edge. For some measurements, the Scholte wave dispersion curve had amplitudes clearly distinguishing from the surrounding noise. However, for other measurements the detected signals were much weaker. Therefore, it is of interest to study the set-up for experimental excitation of Scholte waves on composites. In addition, the experimental results showed that the cracked surface of the composite had little influence on the Scholte wave speed. This should be further confirmed by numerical modelling.
3. Current work has approximated the behavior of composite plates as linear elastic structures, without considering the attenuation of waves or damping of natural vibrations. The relations of these energy dissipation mechanisms to the physical properties of the plate (internal reinforcement structure, viscosity of the polymer matrix, transverse cracks) could be of interest to investigate further.

## Appendix A Elastic constants of anisotropic laminae

Most of the contents of this Appendix can be found in textbooks on mechanics of composite materials, under the sections called “lamina macromechanics”. The aim of the Appendix is to introduce and summarize the nomenclature and notation used for describing the elastic behavior of composite laminates. It is mostly aimed at non-specialist readers, e.g. people with background in isotropic materials.

Table A.1 The number of elastic constants and their notation at various levels.

Material	Constants	Usual notation			
		Tensor ( $C_{ijkl}, S_{ijkl}$ )	Matrix ( $C_{ij}, S_{ij}$ )	Reduced matrix ( $Q_{ij}, S_{ij}$ )	Engineering ( $E_i, G_{ij}, \nu_{ij}$ )
General anisotropic	81	x			
	36*	x	x		
	21**	x	x		
Orthotropic	9		x		x
Transversely isotropic	5		x		x
Plane stress ply	4			x	x
Isotropic	2		x		x

\* – with consideration of symmetry of stress and strain tensors

\*\* – with strain energy considerations

Table A.1 shows the number of independent elastic constants at various levels of material generality. In addition, it shows commonly used notational principles for stiffness and compliance. In the following sections, the contents of Table A.1 are explained. The most general elastic material is considered first. Thereafter, the description for the engineering constants of a single ply is given for orthotropic and transversely isotropic symmetries. Then, plane stress approximation is introduced. The descriptions are intentionally kept brief, however, more in-depth discussion can be found e.g. in textbooks [3, 53, 85, 193, etc.]. Appendix closes with an often disregarded aspect — strain rate dependence of engineering constants.

### A.1 General material

In the most general case, stresses acting on the six sides of an infinitesimal cube, aligned with Cartesian coordinates are  $\sigma_{ij}$ , with  $i, j = 1, 2, 3$  where  $i$  denotes the normal of the plane and  $j$  the orientation of the stress. Normal stresses have  $i = j$  and shear stresses  $i \neq j$ . Static equilibrium of the cube causes  $\sigma_{ij} = \sigma_{ji}$ . Similarly, strain is defined by  $\epsilon_{ij}$ , with  $i, j = 1, 2, 3$  and  $\epsilon_{ij} = \epsilon_{ji}$ . Both of these tensor quantities have therefore six independent components. The generalized Hooke’s law reads as:

$$\sigma_{ij} = C_{ijkl} \epsilon_{kl} \quad , \quad \text{with } i, j, k, l = 1, 2, 3. \quad (\text{A.1})$$

The fourth-rank tensor  $C_{ijkl}$  is called the stiffness tensor and in its most general form has  $3^4=81$  entries, as it connects nine stresses to nine strains. However, due to aforementioned stress and strain symmetries, it only has 36 independent entries, since  $C_{ijkl} = C_{jikl} = C_{jilk} = C_{ijlk}$ .

In composite engineering it is customary to use contracted notations:  $\tau$  notation for shear stress, and engineering shear strains instead of tensor shear strains ( $\gamma_{ij} = 2\varepsilon_{ij}$ ). General stress-strain relationship can be defined by a 6x6 stiffness matrix  $[C]$  with 36 entries:

$$\begin{bmatrix} \sigma_1 \\ \sigma_2 \\ \sigma_3 \\ \tau_{23} \\ \tau_{13} \\ \tau_{12} \end{bmatrix} = \begin{bmatrix} C_{11} & C_{12} & C_{13} & C_{14} & C_{15} & C_{16} \\ C_{21} & C_{22} & C_{23} & C_{24} & C_{25} & C_{26} \\ C_{31} & C_{32} & C_{33} & C_{34} & C_{35} & C_{36} \\ C_{41} & C_{42} & C_{43} & C_{44} & C_{45} & C_{46} \\ C_{51} & C_{52} & C_{53} & C_{54} & C_{55} & C_{56} \\ C_{61} & C_{62} & C_{63} & C_{64} & C_{65} & C_{66} \end{bmatrix} \begin{bmatrix} \varepsilon_1 \\ \varepsilon_2 \\ \varepsilon_3 \\ \gamma_{23} \\ \gamma_{13} \\ \gamma_{12} \end{bmatrix}, \quad (\text{A.2})$$

The inverse of the stiffness matrix  $[C]$  is called a compliance matrix  $[S]$ . We can write Eq. (A.2) and its inverse as:

$$\sigma_i = \sum C_{ij} \varepsilon_j, \quad \varepsilon_i = \sum S_{ij} \sigma_j \quad \text{with } i, j = 1, 2, 3, 4, 5, 6. \quad (\text{A.3})$$

The stiffness matrix can be obtained from the strain energy density  $W$  (work per unit volume) as

$$C_{ij} = \frac{\partial^2 W}{\partial \varepsilon_i \partial \varepsilon_j} \quad \text{or} \quad C_{ji} = \frac{\partial^2 W}{\partial \varepsilon_j \partial \varepsilon_i}. \quad (\text{A.4})$$

Since the order of differentiation is immaterial, the stiffness and compliance matrices are symmetric, i.e

$$C_{ij} = C_{ji} \quad \text{and} \quad S_{ij} = S_{ji}. \quad (\text{A.5})$$

In stiffness tensor notation terms it means  $C_{ijkl} = C_{klij}$ . Due to this symmetry, a total of 21 independent elastic constants remain in the generalized Hooke's law in the symmetric 6x6 matrix Eq. (A.2). Experiments on single crystals have verified this number [24]. The fully populated stiffness matrix causes the material to respond in non-intuitive ways — e.g. all deformations in every direction result from a simple uniaxial stress. This is because there are no planes of symmetry for the material properties and each stress component is coupled to each strain component (and vice versa). The physical significance of the terms in stiffness or compliance matrix such as Eq. (A.2) is described in Fig. A.1.

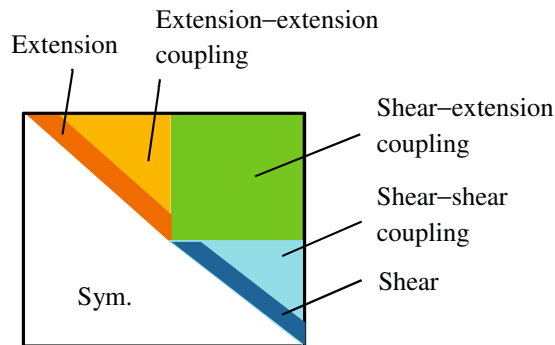
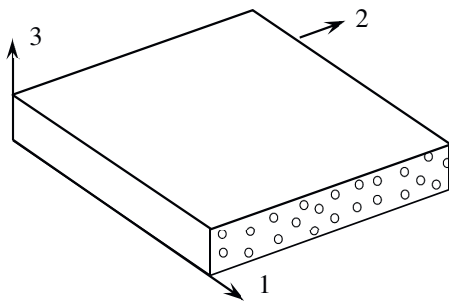


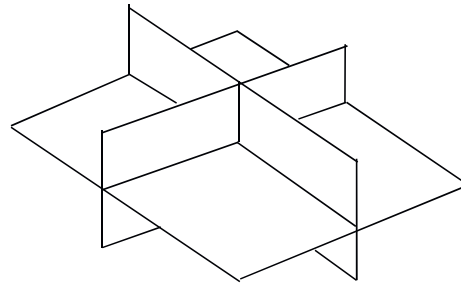
Figure A.1. The coupling terms in the 6x6 stiffness and compliance matrices for stress-strain relations, after Jones [85].

## A.2 Orthotropic ply

A lamina (a ply) is the basic building block (the simplest macro-element) in laminated fiber-reinforced composite materials. Ply thickness usually ranges from 0.1 to 1.0 mm, and is therefore much larger than the fiber diameter (ca. 0.01 mm). Orthotropy is the most general material symmetry employed for usual composite ply studies. Orthotropic material has three mutually perpendicular planes of material symmetry, as seen in Fig. A.2(b). If the material coordinate system is defined parallel to the intersections of these three planes, various stiffness and compliance terms become uncoupled. The number of independent elastic constants reduces to nine.



(a) Unidirectional ply with material axes



(b) Planes of material symmetry

Figure A.2. Orthotropic ply.

The compliance matrix components can be related to engineering constants by elementary thought experiments (uniaxial tension, shear). Stiffness matrix can then be calculated by inverting the compliance matrix. The compliance and stiffness matrices in orthotropic material principal directions read in engineering constants (zeros omitted):

$$[S] = \begin{bmatrix} \frac{1}{E_1} & -\frac{\nu_{21}}{E_2} & -\frac{\nu_{31}}{E_3} & & & \\ -\frac{\nu_{12}}{E_1} & \frac{1}{E_2} & -\frac{\nu_{32}}{E_3} & & & \\ -\frac{\nu_{13}}{E_1} & -\frac{\nu_{23}}{E_2} & \frac{1}{E_3} & & & \\ & & & \frac{1}{G_{23}} & & \\ & & & & \frac{1}{G_{13}} & \\ & & & & & \frac{1}{G_{12}} \end{bmatrix}, \quad (\text{A.6})$$

$$[C] = [S]^{-1} = \begin{bmatrix} \frac{1 - \nu_{23}\nu_{32}}{E_2 E_3 \Delta} & \frac{\nu_{12} + \nu_{13}\nu_{32}}{E_1 E_3 \Delta} & \frac{\nu_{13} + \nu_{12}\nu_{23}}{E_1 E_2 \Delta} & & & \\ \frac{\nu_{21} + \nu_{31}\nu_{23}}{E_2 E_3 \Delta} & \frac{1 - \nu_{13}\nu_{31}}{E_1 E_3 \Delta} & \frac{\nu_{23} + \nu_{21}\nu_{13}}{E_1 E_2 \Delta} & & & \\ \frac{\nu_{31} + \nu_{21}\nu_{32}}{E_2 E_3 \Delta} & \frac{\nu_{32} + \nu_{12}\nu_{31}}{E_1 E_3 \Delta} & \frac{1 - \nu_{12}\nu_{21}}{E_1 E_2 \Delta} & & & \\ & & & G_{23} & & \\ & & & & G_{13} & \\ & & & & & G_{12} \end{bmatrix}, \quad (\text{A.7})$$

and

$$\Delta = \frac{1 - \nu_{12}\nu_{21} - \nu_{23}\nu_{32} - \nu_{31}\nu_{13} - 2\nu_{21}\nu_{32}\nu_{13}}{E_1 E_2 E_3}, \quad (\text{A.8})$$

where  $E_i$  denote tensile and compressive elastic moduli along  $i$  directions. Shear moduli  $G_{ij}$  act on planes defined by axes  $i-j$ . The Poisson's ratio  $\nu_{ij}$  characterizes contraction or expansion in direction  $j$  when load is applied in direction  $i$ . Due to the symmetry of the compliance matrix (can also be obtained from Betti's reciprocal law), an important relationship exists between Young's moduli and Poisson's ratios:

$$\frac{E_i}{\nu_{ij}} = \frac{E_j}{\nu_{ji}} \quad i, j = 1, 2, 3 \quad \text{and} \quad i \neq j. \quad (\text{A.9})$$

Orthotropic material, when stressed in principal material coordinates 1, 2, 3 displays (see Fig. A.1, Eqs.(A.6)–(A.7)):

- no shear–extension coupling
- no shear–shear coupling

However, orthotropic materials stressed along non-principal material axes exhibit apparent anisotropy i.e. they have fully populated stiffness and compliance matrices, just as in Eq. (A.2). For such material, the number of input values defining the elastic response increases, because the angles from the material principal directions to the load axis are also required for the transformation.

### A.3 Transversely isotropic ply (hexagonal fiber packing)

The cross-sections of the continuous fibers used in this study are circular. The placement of fibers in the actual ply is not regular but rather chaotic, as can be observed under a microscope (depicted in Fig. A.3(a)). Since the actual fiber distribution is unknown, typical idealized fiber packing placements are studied, e.g. cross-sectional arrays with hexagonal, square, rectangular and layer-wise distributions. Composites with low fiber volume ratio tend to have a random fiber distribution whereas high volume ratios result with nearly hexagonal packing (Fig. A.3(b)).

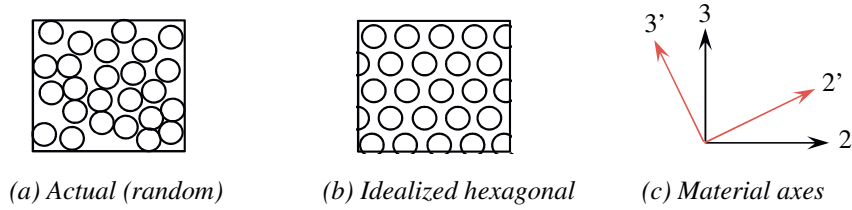


Figure A.3. Examples of fiber distributions in the lamina cross-section and the plane of isotropy for hexagonal packing.

The fiber volume fraction for idealized hexagonal packing is given by [3]:

$$V^f = \frac{\pi}{2\sqrt{3}} \left(\frac{r}{R}\right)^2, \quad (\text{A.10})$$

where  $r$  is the radius of fibers and  $2R$  is the distance between neighboring fibers. The maximum physically possible volume fraction for hexagonal packing is  $V^f = 0.907$ . Real unidirectional composite materials, manufactured by vacuum assisted resin infusion, have usually  $V^f$  values from 0.50 to 0.65.

In case of hexagonal packing, the lamina has just five independent elastic constants. Assuming axis 1 along the fibers (Fig. A.3(b),(c)), all axes 2'–3' obtained by rotation around axis 1 do not change the elastic constants from the initial reference 2–3. Axis 1 possesses rotational symmetry, as any plane containing this axis is a plane of mirror symmetry. Plane 2–3 is called the plane of isotropy and indices 2 and 3 are interchangeable for elastic constants. The independent constants can be chosen as  $E_1$ ,  $E_2$ ,  $G_{12}$ ,  $G_{23}$ ,  $\nu_{12}$ , as described in



Table A.2. Sometimes Poisson's ratio  $\nu_{23}$  is chosen as the independent constant instead of  $G_{23}$ . The material symmetry described in Table A.2 is known as transversely isotropic.

Table A.2. Elastic constants for unidirectional transversely isotropic ply (hexagonal fiber packing or close to it).

Category	Independent constants	Dependent constants
Young's moduli	$E_1$	-
	$E_2$	$E_2 = E_3 = E_{2'} = E_{3'}$
Shear moduli	$G_{12}$	$G_{12} = G_{13} = G_{12'} = G_{13'}$
	$G_{23}$	-
Poisson's ratios	$\nu_{12}$	$\nu_{12} = \nu_{13} = \nu_{12'} = \nu_{13'}$ $G_{23} = \frac{E_2}{2(1 + \nu_{23})}$

The stiffness and compliance matrices in Eqs. (A.6), (A.7) remain the same, since transverse isotropy is a special case of orthotropy. However, the number of independent constants is reduced to five, as seen from Table A.2. The following four relationships hold in addition to nine components of the symmetric stiffness matrix, see Eqs. (A.2), (A.7):

$$C_{22} = C_{33}; \quad C_{55} = C_{66}; \quad C_{12} = C_{13}; \quad 2C_{44} + C_{23} = C_{22} \quad (\text{A.11})$$

The compliance matrix is the inverse of the stiffness matrix just as for orthotropic or general anisotropic materials.

#### A.4 Plane stress ply (CLT)

In typical structural elements, plies in the composite are mostly loaded in-plane. Thus, plane stress is a very good practical approximation for a large number of real life applications. This means, all stress components in the out-of-plane direction are set zero, as seen in Fig. A.4.

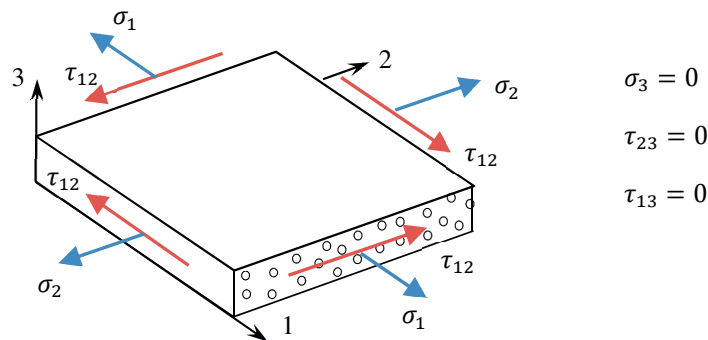


Figure A.4. Non-zero and zero stress components for the plane stress assumption.

The state of plane stress in plies is employed also in the equations of Classical Laminate Theory (CLT). In reality, significant through-thickness stresses exist in the locations where external out-of-plane load is applied or through-thickness changes occur in geometry. For these (often local) situations, plane stress assumption does not work.

Introducing the zero conditions for the out of plane stresses (Fig. A.4) into the Hooke's law and eliminating the out-of-plane strain  $\epsilon_3 \neq 0$  from the equations results with the reduced stress-strain relations as:

$$\begin{bmatrix} \sigma_1 \\ \sigma_2 \\ \tau_{12} \end{bmatrix} = \begin{bmatrix} Q_{11} & Q_{12} & \\ Q_{12} & Q_{22} & \\ & & Q_{66} \end{bmatrix} \begin{bmatrix} \epsilon_1 \\ \epsilon_2 \\ \gamma_{12} \end{bmatrix}, \quad (\text{A.12})$$

$$Q_{11} = \frac{E_1}{1 - \nu_{12}\nu_{21}}, \quad (\text{A.13})$$

$$Q_{22} = \frac{E_2}{1 - \nu_{12}\nu_{21}}, \quad (\text{A.14})$$

$$Q_{12} = \frac{\nu_{21}E_1}{1 - \nu_{12}\nu_{21}} = \frac{\nu_{12}E_2}{1 - \nu_{12}\nu_{21}}, \quad (\text{A.15})$$

$$Q_{66} = G_{12}. \quad (\text{A.16})$$

The inverse relations with lamina compliances read:

$$\begin{bmatrix} \epsilon_1 \\ \epsilon_2 \\ \gamma_{12} \end{bmatrix} = \begin{bmatrix} S_{11} & S_{12} & \\ S_{12} & S_{22} & \\ & & S_{66} \end{bmatrix} \begin{bmatrix} \sigma_1 \\ \sigma_2 \\ \tau_{12} \end{bmatrix} \quad (\text{A.17})$$

$$S_{11} = \frac{1}{E_1}, \quad (\text{A.18})$$

$$S_{22} = \frac{1}{E_2}, \quad (\text{A.19})$$

$$S_{12} = -\frac{\nu_{12}}{E_1} = -\frac{\nu_{21}}{E_2}, \quad (\text{A.20})$$

$$S_{66} = \frac{1}{G_{12}}. \quad (\text{A.21})$$

As previous expressions show, elastic plane stress behaviour of the ply is characterized by four independent constants — expressed either by reduced stiffnesses  $[Q]$ , compliances  $[S]$  or engineering constants  $E_1$ ,  $E_2$ ,  $G_{12}$  and  $\nu_{12}$ . Additional elastic constants are needed if nonzero out-of-plane strain  $\epsilon_3$  is calculated. Because of the inverse relationship of Eqs. (A.12) and (A.17) reduced  $[Q]$  and  $[S]$  matrices are also the inverses of each other.

### A.5 Strain rate influence

It has been recognized that strain rate has substantial influence to composite stiffness. The strain rate during quasi-static or dynamic loading events (impact or vibrations) can vary over a wide range of values. For a general material characterization, experimental measurements need to be conducted on the specific range of strain rates, which is of particular interest. Shokrieh and Omidì have studied the behavior of glass-epoxy laminates (fiber volume fraction 50%) under low and intermediate strain rates in a recent series of papers [194–197]. They concluded that for strain rates  $\dot{\epsilon}$  from 0.001 to 100 s<sup>-1</sup>, the change in stiffness can be approximated by an empirical regression function:

$$M(\dot{\epsilon}) = \alpha + \beta \dot{\epsilon}^\gamma, \quad (\text{A.22})$$

where  $M$  is the stiffness modulus under investigation. Material constants  $\alpha$ ,  $\beta$ ,  $\gamma$  were determined by curve fitting from the experimental data. Table A.3 presents an overview of such material constants for various modes of loading.

Another reference for glass-epoxy strain rate characterization can be found in [198]. A large number of references on the subject are found in the aforementioned papers, regarding also strength dependence of strain rate and other material systems (carbon, graphite fibers).

The strain rate required in quasi-static test standards [17, 18, 20] is 1% per minute, which translates into 0.00017 s<sup>-1</sup>. Figure A.5 shows the moduli relative to their quasi-static values, if strain rate is increased from 0.001 (may be regarded as nearly quasi-static) to 100 s<sup>-1</sup>, based on the approach by Shokrieh and Omidì (Eq. (A.22), Table A.3). The observed trends indicate that compressive longitudinal modulus in particular is strongly influenced by variations in the

strain rate, for glass-epoxy laminates. Surprisingly, the shear modulus actually decreases with strain rate, as seen from Table A.3. Researchers have hypothesized that strain rate dependence is attributed to the viscous nature of polymeric matrix material.

Table A.3. Material constants for glass/epoxy UD laminate, for strain rates  $0.001$  to  $100 \text{ s}^{-1}$ , from [194–197].

Mode of loading/related modulus	Material constant			Correlation coefficient $R$
	$\alpha$	$\beta$	$\gamma$	
Tension, $0^\circ$ – dir.	37.243	1.139	0.276	0.9836
Compression, $0^\circ$ – dir.	7.223	24.449	0.0529	0.9938
Shear *	5.173	-1.177	0.043	0.9879
Tension, $90^\circ$ – dir.	10.037	0.4370	0.2624	0.9877
Compression, $90^\circ$ – dir.	11.419	0.0259	1.0216	0.9886

\* measured by uniaxial tensile loading on symmetric, balanced  $\pm 45^\circ$  specimens composed of UD plies. Stress, longitudinal and transverse strains (biaxial rosette) were measured and shear modulus calculated from this data. The reported function is expressed with regard to shear strain rate (from  $0.002$  to  $140 \text{ s}^{-1}$ ).

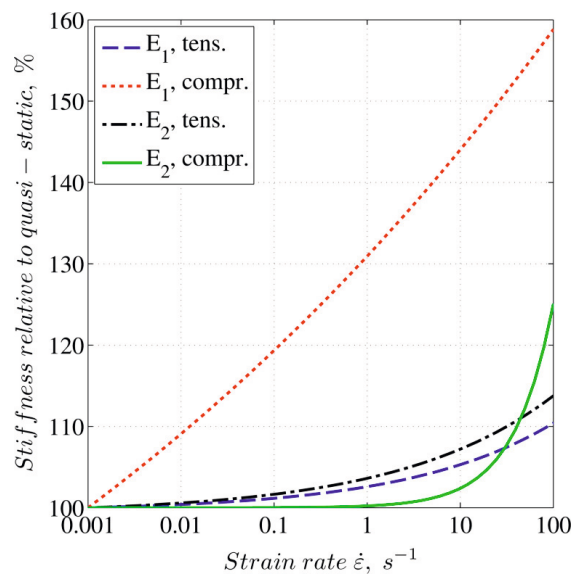


Figure A.5. Change of elastic moduli from  $0.001 \text{ s}^{-1}$  (quasi-static) to  $100 \text{ s}^{-1}$  for glass-epoxy.

## Appendix B Constraints and invariants for elastic moduli

This Appendix reviews the thermodynamic constraints for the ply material. Also, their applicability to laminates or damaged material constants is discussed. In the end, invariants for the laminate stiffnesses during coordinate transformations are discussed.

### B.1 Isotropic material

The physical arguments below, regarding isotropic material, were obtained from Jones [85]. Consider that only one normal strain is applied to the material. Then, in order to have positive change in the strain energy, elastic modulus  $E$  has to be positive. Similar argument in shear requires that shear modulus  $G$  has to be positive. There is a well-known relation between elastic and shear moduli:

$$G = \frac{E}{2(1 + \nu)}. \quad (\text{B.1})$$

Since  $E$  and  $G$  are both positive, Eq. (B.1) states that Poisson's ratio  $\nu > -1$ . In case of hydrostatic pressure  $p$ , the volumetric strain (sum of three extensional strains) is:

$$\varepsilon_x + \varepsilon_y + \varepsilon_z = \frac{3(1 - 2\nu)}{E} p. \quad (\text{B.2})$$

In order to prevent the expansion of elementary cube under hydrostatic pressure, the upper constraint to Poisson's ratio becomes  $\nu < 0.5$ .

### B.2 Orthotropic material

The previous arguments for isotropic materials were first generalized for orthotropic materials by Lempriere [199]. Discussion about thermodynamic constraints can be found in textbooks e.g. [85, 193, 200]. The general constraint for elastic constants originates from the condition that arbitrary deformation on a solid must result in a positive change in the strain energy. That is, the sum of the work done by all stress components must be positive in order to prevent the creation of energy. For a general state of strain acting on an anisotropic solid (with  $[\bar{C}]$  as the stiffness matrix), it means:

$$[\varepsilon_x \ \varepsilon_y \ \varepsilon_z \ \gamma_{yz} \ \gamma_{xz} \ \gamma_{xy}][\bar{C}][\varepsilon_x \ \varepsilon_y \ \varepsilon_z \ \gamma_{yz} \ \gamma_{xz} \ \gamma_{xy}]^T > 0 \quad (\text{B.3})$$

$$\text{when } [\varepsilon_x \ \varepsilon_y \ \varepsilon_z \ \gamma_{yz} \ \gamma_{xz} \ \gamma_{xy}] \neq 0.$$

This inequality effectively requires that stiffness matrix  $[\bar{C}]$  in an arbitrary coordinate system is positive definite. Correspondingly, the inverse of the stiffness matrix, known as compliance matrix  $[\bar{S}]$ , must also be positive definite. Therefore, the conditions to ensure positive definiteness of symmetric matrices  $[C]$  or  $[S]$  (in material coordinates) also formulate the

thermodynamic constraints to elastic moduli. Positive definiteness of a matrix can be evaluated through eigenvalues, which all must be positive. Calculating eigenvalues with numerical software poses no difficulty and this is how the thermodynamic constraints are applied in this work.

However, positive definiteness can also be evaluated from the condition that its sub-determinants must be positive. Applying this condition to compliance and stiffness matrices enables to formulate the constraints on the engineering constants, as described in Table B.1.

*Table B.1. The constraints on engineering constants, by Kollár and Springer [193].*

Orthotropic	$E_1 > 0, \quad E_2 > 0, \quad E_3 > 0$ $G_{23} > 0, \quad G_{13} > 0, \quad G_{12} > 0$ $1 - \nu_{23}^2 \frac{E_3}{E_2} - \nu_{13}^2 \frac{E_3}{E_1} - \nu_{12}^2 \frac{E_2}{E_1} - 2\nu_{12}\nu_{13}\nu_{23} \frac{E_3}{E_1} > 0$ $\nu_{23}^2 < \frac{E_2}{E_3}, \quad \nu_{13}^2 < \frac{E_1}{E_3}, \quad \nu_{12}^2 < \frac{E_1}{E_2}$
Transversely isotropic	$E_1 > 0, \quad E_2 > 0, \quad G_{12} > 0$ $-1 < \nu_{23} < 1 - 2\frac{E_2}{E_1}\nu_{12}^2$ $\nu_{12}^2 < \frac{E_1}{E_2}$
Isotropic	$E_1 > 0$ $-1 < \nu_{12} < 0.5$

### B.3 Laminate constraints and invariants

#### B.3.1 Thermodynamic constraints for a laminate

The composite plate is a laminate with various angles for individual laminae in the stacking sequence. But as a model simplification it is sometimes considered as a single orthotropic entity with effective stiffness properties. This laminate may also have sustained damage, altering the stiffnesses of its layers in different ways. It can be assumed, that thermodynamic constraints for such an approximated “material” (which includes various internal layers and cracks) must be different from considerations based on uniform continuum. A simple set of constraints for these effective engineering moduli requires that all constants are positive, e.g. as used in ref. [81] for cross-ply laminates. Positive Young’s and shear moduli are obvious from intuitive basis. In anisotropic materials, negative Poisson’s ratios are perfectly possible; however these materials are quite rare and tend to have a specific internal structure.

### B.3.2 Stiffness invariants for in-plane coordinate transformation

Invariants present a convenient way to check the results if the stiffnesses are experimentally obtained along different coordinate axes.

Consider the coordinate transformation of a ply or a laminate, with rotation around out-of-plane 3-axis. It has been shown that there are two combinations of reduced stiffness matrix  $[Q]$  components (see Appendix A.4) and six combinations of laminate  $ABD$ -matrix components which remain invariant to rotation around axis 3. These invariants were defined by Tsai and Pagano [53, 85] as:

$$L_1 = Q_{11} + Q_{22} + 2Q_{12}, \quad (\text{B.4})$$

$$L_2 = Q_{66} - Q_{12}. \quad (\text{B.5})$$

$$P_1 = A_{11} + A_{22} + 2A_{12} = hL_1, \quad (\text{B.6})$$

$$P_2 = A_{66} - A_{12} = hL_2, \quad (\text{B.7})$$

$$P_3 = B_{11} + B_{22} + 2B_{12} = 0, \quad (\text{B.8})$$

$$P_4 = B_{66} - B_{12} = 0, \quad (\text{B.9})$$

$$P_5 = D_{11} + D_{22} + 2D_{12} = L_1 \frac{h^3}{12}, \quad (\text{B.10})$$

$$P_6 = D_{66} - D_{12} = L_2 \frac{h^3}{12}, \quad (\text{B.11})$$

where  $h$  is total thickness of the plate.

Should one work directly with stiffness matrix  $[C]$  of the laminate, instead of engineering constants (typical in ultrasound), five irreducible invariants exist for the laminate stiffness matrices. These five irreducible invariants for laminates (orthotropic symmetry and built up from the same elementary ply) have been described by Hosten in [201].

## Appendix C Micromechanics based estimation of elastic moduli

Micromechanics formulas help to evaluate the elastic properties of composites based on the properties of the constituents. Micromechanics views the composite material as a heterogeneous entity, on contrary to macromechanics where a large enough homogeneous piece of material is analyzed. The macromechanical elastic properties of interest are usually four in-plane constants employed in the laminate theory:  $E_1$ ,  $E_2$ ,  $\nu_{12}$ ,  $G_{12}$ . Micromechanical modelling is successful if its predictions agree with the measured macro properties.

The description of composite ingredients includes fiber properties, matrix properties, fiber packing assumption and fiber volume fraction. Most precise estimations can be obtained by using finite element analysis or elasticity solutions on the concept of representative volume element. These elaborate models can reveal the influence from fiber packing arrangements, or give detailed description of stresses in the fibers, matrix and their interface.

There is a group of models in micromechanics, which are based on mechanics of materials considerations, the so-called rule-of-mixture models. These approaches result in relatively simple algebraic formulas, convenient to use for quick estimations. Characteristic feature to rule-of-mixture models is that the shape of the fiber cross-section or their packing is not relevant. Only the cross-sectional areas of the fiber and matrix are important (assumed to be proportional to the fiber and matrix volume fractions  $V^f$  and  $V^m$ , respectively).

Variations in composite manufacturing cause variations in fiber array geometry and hence composite moduli. Thus, one should not hope to predict composite moduli precisely. Approximate approaches such as mechanics of materials and Halpin-Tsai equations should satisfy many practical cases, and therefore only these simple approaches are reviewed in the following. Micromechanics formulas are thoroughly discussed in a number of textbooks, such as [3, 41, 85, 200], which also serve as the basis for the excerpts in this Appendix.

### C.1 Strength of materials models (rule-of-mixtures)

In the following, it is assumed that the amount of voids is negligible and therefore:

$$V^m = 1 - V^f \quad (C.1)$$

Rule-of-mixtures estimates are derived based on simple assumptions, such as uniform strain or uniform stress in the constituents. Springs-in-parallel ( $E_1$ ) or springs-in-series ( $E_2$ ) or similarly simple models in 2-D ( $\nu_{12}$ ,  $G_{12}$ ) are used in the derivations. An overview of several rule-of-mixtures estimations is presented in Table C.1.



Table C.1. Rule-of-mixtures estimates for elastic constants.

$E_1$	$E_1 = E_1^f V^f + E^m V^m$
$E_2$	<p>Regular expression:</p> $\frac{1}{E_2} = \frac{V^f}{E_2^f} + \frac{V^m}{E^m}$ <p>Modified expression (Ekvall) accounts for the triaxial stress state in the matrix due to fiber restraint:</p> $E_2 = \frac{E^f E'^m}{V^f E'^m + V^m E^f (1 - (v^m)^2)}, \quad E'^m = \frac{E^m}{1 - 2(v^m)^2}$ <p>Modified expression, accounting for the constraint imposed on the matrix by the fibers in the fiber direction:</p> $E_2 = \frac{E_2^f E'^m}{V^f E'^m + V^m E_2^f}, \quad E'^m = \frac{E^m}{1 - (v^m)^2}$ <p>Modified expression (stress partitioning, accounts for the error in assumption that fiber and matrix are both subjected to full stress):</p> $\frac{1}{E_2} = \frac{\frac{V^f}{E_2^f} + \frac{\eta V^m}{E^m}}{V^f + \eta V^m}$ <p>Modified expression (accounts for the error in assumption that fiber and matrix are not bonded together):</p> $\frac{1}{E_2} = \frac{\eta^f V^f}{E_2^f} + \frac{\eta^m V^m}{E^m}$ <p>where</p> $\eta^f = \frac{E_1^f V^f + [(1 - v_{12}^f v_{21}^f) E^m + v^m v_{21}^f E_1^f](1 - V^f)}{E_1^f V^f + E^m (1 - V^f)}$ $\eta^m = \frac{[(1 - v^{m2}) E_1^f - (1 - v^m v_{12}^f) E^m] V^f + E^m V^m}{E_1^f V^f + E^m (1 - V^f)}$
$G_{12}$	<p>Regular expression:</p> $\frac{1}{G_{12}} = \frac{V^f}{G_{12}^f} + \frac{V^m}{G^m}$ <p>Modified expression (stress partitioning):</p> $\frac{1}{G_{12}} = \frac{\frac{V^f}{G_{12}^f} + \frac{\eta' V^m}{G^m}}{V^f + \eta' V^m}$
$\nu_{12}$	$\nu_{12} = \nu_{12}^f V^f + \nu^m V^m$

where:

$E^m, \nu^m, G^m, V^m$  — elastic properties and fiber volume fraction of the matrix

$E_1^f, E_2^f, \nu_{12}^f, \nu_{21}^f, G_{12}^f, V^f$  — elastic properties and fiber volume fraction of the fibers (longitudinal and the transverse directions of the fiber are denoted by 1 and 2, respectively). Although fibers are usually treated as isotropic (indices 1, 2 omitted), they can have more complex material behavior, e.g. graphite fibers are transversely isotropic.

$0 < \eta < 1$  — stress partitioning factor for  $E_2$  ( $\eta=0.4$  compares well with square-packed array of fibers,  $\eta=0.5$  compares well with hexagonal packing). In general is determined empirically.

$0 < \eta' < 1$  — stress partitioning factor for  $G_{12}$  ( $\eta'=0.6$  leads to a good correlation with the elasticity solution).

The dominant constituent material (for usual  $V^f$  values) and general agreement with more precise models and experimental data is overviewed for mechanics of materials models in Table C.2. Since the Poisson's ratios of the constituents ( $\nu^f, \nu^m$ ) are usually quite similar, the major Poisson's ratio  $\nu_{12}$  of the composite is neither matrix or fiber-dominated. The modified expressions in Table C.1 are mostly concerned with the properties which do not have a good agreement with experiments ( $E_2, G_{12}$ ).

Table C.2. Features of mechanics of materials estimates.

El. property	Dominant constituent	Agreement with complex models (FEM, elasticity) and experiments
$E_1$	Fibers	Very good
$E_2$	Matrix	Underestimates the value
$\nu_{12}$	Neutral	Very good
$G_{12}$	Matrix	Underestimates the value

## C.2 Halpin-Tsai equations

Halpin and Tsai developed an approximate representation of more complicated micromechanics results, which are also simple and easy to use in the design. These equations generalize more exact micromechanics results. Halpin-Tsai expressions for  $E_1$  and  $\nu_{12}$  are the usual rule-of-mixtures results (Table C.1), which have shown good enough precision. For matrix dominated elastic constants  $E_2, G_{12}$  and Poisson's ratio  $\nu_{23}$ , the semiempirical equations read:

$$M = M^m \frac{1 + \xi \eta V^f}{1 - \eta V^f}, \quad (C.2)$$

and

$$\eta = \frac{\frac{M^f}{M^m} - 1}{\frac{M^f}{M^m} + \xi}, \quad (\text{C.3})$$

where  $M$  denotes the composite material constant ( $E_2, G_{12}, \nu_{23}$ ),  $M^f$  corresponding fiber constant ( $E^f, G^f, \nu^f$ ) and  $M^m$  the corresponding matrix constant ( $E^m, G^m, \nu^m$ ).

Parameter  $\xi$  (can range from 0 to  $\infty$ ) is a measure of fiber reinforcement of the composite material that depends on the fiber geometry, packing geometry and loading conditions. For small values of  $\xi$  the fibers are not very effective whereas for large values of  $\xi$ , the fibers are extremely effective in increasing the composite stiffness. One extreme,  $\xi = 0$ , results in the series model (such as regular  $E_2$  expression in Table C.1) and the other extreme,  $\xi = \infty$ , in the parallel model (such as rule-of-mixtures  $E_1$  expression).

The difficulty of using Halpin-Tsai equations lies in the determination of a suitable value for  $\xi$ . If experimental data is available,  $\xi$  can be determined e.g. from curve fitting. For circular fibers in a square array,  $\xi = 2$  has been successfully used for  $E_2$  and  $\xi = 1$  for  $G_{12}$  at  $V^f = 0.55$ . Experimental values for  $E_2$  fall within  $1 < \xi < 2$  ( $\xi = 1$  for hexagonal,  $\xi = 2$  for square arrays). It has been noted that the predictions of  $G_{12}$  by Halpin-Tsai equations with  $\xi = 1$  agree exactly with the results from self-consistent field method and lower bound for the bounding method. Despite this, the predictions tend to underestimate the moduli, in comparison to experimental measurements. For shear modulus  $G_{12}$ , it has also been suggested to use the empirical value:

$$\xi = 1 + 40(V^f)^{10}. \quad (\text{C.4})$$

For experimentally obtained values of composite property  $M$  and fiber volume ratio  $V^f$ , the parameter  $\xi$  can be calculated from:

$$\xi = \frac{M^f(M - M^m) - V^f M(M^f - M^m)}{M^m[(M^f - M) - V^m(M^f - M^m)]}. \quad (\text{C.5})$$

### C.3 Estimations for a glass-epoxy material

The Halpin-Tsai equations are employed in the following to estimate four elastic constants ( $E_1, E_2, G_{12}, \nu_{12}$ ) for an arbitrary glass-epoxy material. Glass fibers and epoxy matrix are both assumed to be isotropic and their properties are arbitrary handbook values (from ref. [3]), as reported in Table C.3. It should be noted that these estimates are also reasonable for other polymer matrix composites (e.g. polyester or vinylester). The estimates for elastic constants are calculated for a range of fiber volume fractions  $V^f = (0.50, 0.65)$  and Halpin-Tsai parameters  $\xi = (0, 2)$ , as shown in Fig. C.1.

Table C.3. Estimates for constituent properties.

El. property	E-Glass fibers	Epoxy matrix
$E$	73 GPa	3.9 GPa
$\nu$	0.23	0.35
$G$	30 GPa	1.4 GPa

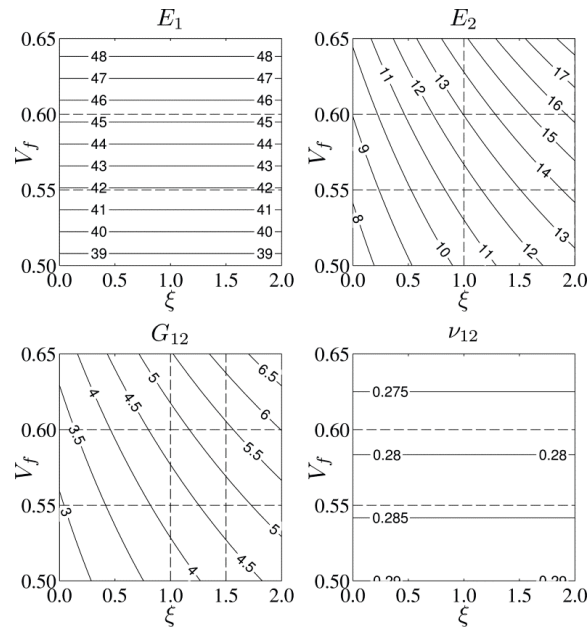


Figure C.1. Halpin-Tsai estimates for elastic moduli.

Since  $E_1$  and  $\nu_{12}$  are actually calculated from rule-of-mixtures estimates, they are independent of parameter  $\xi$ . The reasonable values of  $\xi$  range between (1, 2) for  $E_2$  and (1, 1.5) for  $G_{12}$  according to literature (see Appendix C.2). Practical experience with vacuum assisted resin infusion estimates the fiber volume fraction as (0.55, 0.60). These ranges for  $V^f$  and  $\xi$  are marked with dashed lines in Fig. C.1. The estimates for elastic moduli are obtained from Fig. C.1 and summarized in Table C.4. The results show that even if the properties of constituents are exactly known, the reasonable uncertainty of  $V^f$  and  $\xi$  causes the typical estimates for  $E_2$  and  $G_{12}$  to range on a wide scale.

Table C.4. Halpin-Tsai estimates for glass-epoxy material ( $V^f=0.55-0.60$ ).

El. property	Estimated range	(max-min)/mean, %
$E_1$ , GPa	(42.0, 45.3)	8 %
$E_2$ , GPa	(11.5, 16.2)	34 %
$G_{12}$ , GPa	(4.2, 5.4)	25 %
$\nu_{12}$	(0.278, 0.284)	2 %

## Appendix D Formulas for the back-calculation of ply moduli

### D.1 Symmetric cross-plyed composites

Symmetric cross-plyed composites are particularly suitable for tensile and flexural testing in their principal directions. The layup symmetry with regard to midplane results with no coupling between extension and bending ( $[B] = 0$ ). In addition, balanced laminates (each  $+\theta$  ply has a corresponding  $-\theta$  ply) have no in-plane normal and shear coupling ( $A_{xs} = A_{ys} = 0$ ). For a special case of cross-plyed laminates, the bending-twist coupling ( $D_{xs} = D_{ys} = 0$ ) also vanishes. Since shear deformations are uncoupled from extension and bending, shear modulus  $G_{12}$  has theoretically no influence on the testing in principal directions. The experimentally measured quantities can be laminate tensile stiffnesses  $\bar{E}_x^t, \bar{E}_y^t$  and flexural stiffnesses  $\bar{E}_x^f, \bar{E}_y^f$ . The unknowns are ply moduli  $E_1, E_2$  and Poisson's ratio  $\nu_{12}$ .

For the notation, numbers 1, 2 denote the ply and  $x, y$  the laminate coordinates, such that fibers are aligned with  $x$  in  $0^\circ$  plies and with  $y$  in  $90^\circ$  plies. Overbar distinguishes the laminate effective (averaged) properties and superscripts  $t$  and  $f$  denote tension and flexure.

#### D.1.1 Single direction specimen (TF1)

In this testing strategy, specimens from only one principal laminate direction are available for testing. They are measured for both, tensile and flexural stiffness. The influence of Poisson's ratio can be shown as near-negligible and therefore it is either estimated or assumed to be zero. Moduli  $E_1, E_2$  are back-calculated from two measured stiffnesses.

This approach is more physically sound than measuring on two different specimens. The drawback of using the test results from a single specimen is that tensile and flexural stiffnesses become mixed. The experimental uncertainties for tensile or flexural stiffness measurement are different due different stress distribution and test configuration. These calculations will mix these uncertainties from tension and flexure.

The following laminate geometry coefficients can be defined, representing the volume fractions of  $0^\circ$  and  $90^\circ$  plies in the whole laminate ( $\psi + \xi = 1$ ):

$$\psi = \frac{1}{h} \sum_{k=1}^n (z_k - z_{k-1}) \quad \text{for those } k, \text{ for which } \theta_k = 0^\circ, \quad (\text{D.1})$$

$$\xi = \frac{1}{h} \sum_{k=1}^n (z_k - z_{k-1}) \quad \text{for those } k, \text{ for which } \theta_k = 90^\circ. \quad (\text{D.2})$$

For flexural calculations, the following geometry coefficients are additionally defined:

$$\alpha = \frac{1}{3h^3} \sum_{k=1}^n (z_k^3 - z_{k-1}^3) \quad \text{for those } k, \text{ for which } \theta_k = 0^\circ, \quad (\text{D.3})$$

$$\beta = \frac{1}{3h^3} \sum_{k=1}^n (z_k^3 - z_{k-1}^3) \quad \text{for those } k, \text{ for which } \theta_k = 90^\circ. \quad (\text{D.4})$$

The total laminate thickness is denoted as  $h$ , the total number of plies as  $n$ , and  $z$  are the distances from the laminate midplane to the ply surfaces. Coefficients  $\psi$  and  $\xi$  represent the relative contributions of  $0^\circ$  and  $90^\circ$  plies to tensile stiffness,  $\alpha$  and  $\beta$  represent similar contributions to flexural stiffness. It can be shown that  $\alpha + \beta = 1/12$ .

Based on CLT, the laminate effective stiffnesses in  $x$ -direction can be derived:

$$\bar{E}_x^t = \frac{1}{1 - \nu_{12}^2 \frac{E_2}{E_1}} \left[ \psi E_1 + \xi E_2 - \frac{(\nu_{12} E_2)^2}{\psi E_2 + \xi E_1} \right], \quad (\text{D.5})$$

$$\bar{E}_x^f = \frac{12}{1 - \nu_{12}^2 \frac{E_2}{E_1}} \left[ \alpha E_1 + \beta E_2 - \frac{(\nu_{12} E_2)^2}{12^2 (\alpha E_2 + \beta E_1)} \right]. \quad (\text{D.6})$$

For a cross-plyed symmetric laminate without Poisson's effect ( $\nu_{12} = 0$ ), laminate stiffnesses become:

$$\bar{E}_x^t = \psi E_1 + \xi E_2, \quad (\text{D.7})$$

$$\bar{E}_x^f = 12(\alpha E_1 + \beta E_2). \quad (\text{D.8})$$

These two general equations (D.5) and (D.6) appear to have no simple forms of solutions for moduli  $E_1$  and  $E_2$ . However, they can be solved for  $E_1$  and  $E_2$  by numerical methods, e.g. optimization. The complex form of Eqs. (D.5), (D.6) is caused by the Poisson's ratios, as seen from the comparison to Eqs. (D.7), (D.8). Should one define Poisson's ratios into coefficients  $c$  as:

$$c_t = \frac{1 - \bar{v}_{xy}^t \bar{v}_{yx}^t}{1 - \nu_{12} \nu_{21}}, \quad (\text{D.9})$$

$$c_f = \frac{1 - \bar{v}_{xy}^f \bar{v}_{yx}^f}{1 - \nu_{12} \nu_{21}}, \quad (\text{D.10})$$

the solution for ply moduli can be shown as

$$\begin{bmatrix} E_1 \\ E_2 \end{bmatrix} = \frac{1}{\psi\beta - \alpha\xi} \begin{bmatrix} \beta & -\xi \\ -\alpha & \psi \end{bmatrix} \begin{bmatrix} \frac{\bar{E}_x^t}{c_t} \\ \frac{\bar{E}_x^f}{12c_f} \end{bmatrix}. \quad (\text{D.11})$$

Equation (D.11) clearly shows that once the Poisson's ratio is disregarded ( $\nu_{12} = 0$ ,  $c_t = c_f = 1$ ), the solution for ply moduli becomes straightforward, depending only on the dimensionless geometry coefficients.

Equations (D.9) and (D.10) defining coefficients  $c$  contain the Poisson's ratios for the lamina,  $\nu_{12}$  and  $\nu_{21} = \nu_{12}E_2/E_1$ , and effective Poisson's ratios for the laminate,  $\bar{v}^t$  and  $\bar{v}^f$ . The physical meaning of the laminate Poisson's ratios is:

$$\bar{v}_{xy}^t = \frac{A_{xy}}{A_{yy}}, \quad \bar{v}_{yx}^t = \frac{A_{xy}}{A_{xx}}, \quad (\text{D.12})$$

$$\bar{v}_{xy}^f = \frac{D_{xy}}{D_{yy}}, \quad \bar{v}_{yx}^f = \frac{D_{xy}}{D_{xx}}. \quad (\text{D.13})$$

Laminate Poisson's ratios are also involved in the derivations in the following sections.

### D.1.2 Multiple specimens

In these methods, two different specimens are measured, one in either principal directions of the plate. This means that experimental data is collected from two physically different specimens. Two specimens will inevitably have small differences, although they are expected to represent the same material. However, if the number of experimental specimen pairs is large enough, the small differences of individual specimens even out for the evaluation of the mean.

### D.1.2.1 Tension-Tension (*TT*)

In the following, the case where two different specimens are both measured for tension is considered. This derivation was carried out previously by Echtermeyer [26], however it was never published and therefore is repeated here for completeness. The laminate stiffness matrix  $[A]$  can be expressed as a linear combination of  $0^\circ$  and  $90^\circ$  transformed ply matrices  $[Q]$ :

$$[A] = (\psi[Q^{(0)}] + \xi[Q^{(90)}])h , \quad (\text{D.14})$$

where  $h$  is the total thickness of the laminate and  $\psi$ ,  $\xi$  are defined in Eqs. (D.1), (D.2). The components of ply stiffness matrices can be shown from Eq. (D.14) to be:

$$Q_{11} = \frac{\psi A_{xx} - \xi A_{yy}}{h(\psi^2 - \xi^2)} , \quad (\text{D.15})$$

$$Q_{22} = \frac{\psi A_{yy} - \xi A_{xx}}{h(\psi^2 - \xi^2)} , \quad (\text{D.16})$$

$$Q_{12} = \frac{A_{xy}}{h} . \quad (\text{D.17})$$

Ply engineering constants can be calculated from stiffness matrix  $[Q]$  formulation (see Appendix A.4) as:

$$E_1 = \frac{Q_{11}Q_{22} - Q_{12}^2}{Q_{22}} , \quad (\text{D.18})$$

$$E_2 = \frac{Q_{11}Q_{22} - Q_{12}^2}{Q_{11}} , \quad (\text{D.19})$$

$$\nu_{12} = \frac{Q_{12}}{Q_{22}} . \quad (\text{D.20})$$



When inserting Eqs. (D.15)–(D.17) into Eqs. (D.18)–(D.20) with the knowledge that the components of laminate stiffness matrix  $[A]$  can be calculated from laminate effective tensile properties as:

$$A_{xx} = \frac{\bar{E}_x^t h}{1 - \bar{\nu}_{xy}^t \bar{\nu}_{yx}^t}, \quad (\text{D.21})$$

$$A_{yy} = \frac{\bar{E}_y^t h}{1 - \bar{\nu}_{xy}^t \bar{\nu}_{yx}^t}, \quad (\text{D.22})$$

$$A_{xy} = \frac{\bar{E}_x^t \bar{\nu}_{yx}^t h}{1 - \bar{\nu}_{xy}^t \bar{\nu}_{yx}^t} = \frac{\bar{E}_y^t \bar{\nu}_{xy}^t h}{1 - \bar{\nu}_{xy}^t \bar{\nu}_{yx}^t}. \quad (\text{D.23})$$

Then after some simplification, direct relationships between laminate and ply engineering constants are established in tension:

$$E_1 = \frac{1}{\gamma} \left[ \frac{\psi \bar{E}_x^t - \xi \bar{E}_y^t}{\psi^2 - \xi^2} - \frac{(\bar{E}_y^t \bar{\nu}_{xy}^t)^2 (\psi^2 - \xi^2)}{\psi \bar{E}_y^t - \xi \bar{E}_x^t} \right], \quad (\text{D.24})$$

$$E_2 = \frac{1}{\gamma} \left[ \frac{\psi \bar{E}_y^t - \xi \bar{E}_x^t}{\psi^2 - \xi^2} - \frac{(\bar{E}_y^t \bar{\nu}_{xy}^t)^2 (\psi^2 - \xi^2)}{\psi \bar{E}_x^t - \xi \bar{E}_y^t} \right], \quad (\text{D.25})$$

$$\nu_{12} = \frac{(\psi - \xi) \bar{E}_y^t \bar{\nu}_{xy}^t}{\psi \bar{E}_y^t - \xi \bar{E}_x^t}, \quad (\text{D.26})$$

where

$$\gamma = 1 - (\bar{\nu}_{xy}^t)^2 \frac{\bar{E}_y^t}{\bar{E}_x^t}. \quad (\text{D.27})$$

Eqs. (D.24)–(D.27) are directly applicable for the calculation of ply engineering constants  $E_1, E_2$  with the knowledge of laminate effective tensile stiffnesses in principal directions  $\bar{E}_x^t, \bar{E}_y^t$ , Poisson's ratio  $\nu_{12}$  and coefficients  $\psi, \xi$  describing the relative amount of layers in both laminate directions.

### D.1.2.2 Flexure-Flexure (FF)

The case where two different specimens are both measured for flexure is considered here. This derivation is in many ways analogous to what was carried out in the previous section. Geometry coefficients  $\alpha$  and  $\beta$  are defined in Eqs. (D.3), (D.4) to represent the contributions of  $0^\circ$  and  $90^\circ$  plies to the laminate bending stiffness  $[D]$ , from the transformed ply matrices  $[Q]$ :

$$[D] = (\alpha[Q^{(0)}] + \beta[Q^{(90)}])h^3. \quad (D.28)$$

After a similar derivation than was previously carried out for tension, direct relationships between ply and laminate effective moduli are established in flexure:

$$E_1 = \frac{1}{\gamma} \left[ \frac{\alpha\bar{E}_x^f - \beta\bar{E}_y^f}{12(\alpha^2 - \beta^2)} - \frac{12(\bar{E}_y^f \bar{\nu}_{xy}^f)^2 (\alpha^2 - \beta^2)}{\alpha\bar{E}_y^f - \beta\bar{E}_x^f} \right], \quad (D.29)$$

$$E_2 = \frac{1}{\gamma} \left[ \frac{\alpha\bar{E}_y^f - \beta\bar{E}_x^f}{12(\alpha^2 - \beta^2)} - \frac{12(\bar{E}_y^f \bar{\nu}_{xy}^f)^2 (\alpha^2 - \beta^2)}{\alpha\bar{E}_x^f - \beta\bar{E}_y^f} \right], \quad (D.30)$$

$$\nu_{12} = \frac{(\alpha - \beta)\bar{E}_y^f \bar{\nu}_{xy}^f}{\alpha\bar{E}_y^f - \beta\bar{E}_x^f}, \quad (D.31)$$

where

$$\gamma = 1 - (\bar{\nu}_{xy}^f)^2 \frac{\bar{E}_y^f}{\bar{E}_x^f}. \quad (D.32)$$

The similarity of Eqs. (D.29)–(D.32) to (D.24)–(D.27) can be observed due to the similar formulation of laminate stiffness as a linear combination of ply reduced stiffnesses  $[Q]$ . Eqs. (D.29)–(D.32) are directly applicable for the calculation of ply elastic constants  $E_1, E_2$  from

laminate effective flexural stiffnesses  $\bar{E}_x^f, \bar{E}_y^f$ , Poisson's ratio  $\nu_{12}$  and coefficients  $\alpha, \beta$  which characterize the geometry of the layup.

### D.1.2.3 Tension-Flexure (TF2)

The specimen in one principal direction is measured in tension and the specimen in the other direction in flexure. Here, the uncertainties arising from having two physically different specimens, and from testing them by two different principles, are combined. The calculation can be carried out using Eqs. (D.5) and (D.6) derived in Appendix D.1.1 previously. The modification that two specimens are in different directions (one in  $x$  and the other in  $y$ ) needs to be introduced, i.e. geometry coefficients need to be switched for one of the equations.

## D.2 Symmetric balanced composites

Classical laminate theory shows that symmetric cross plied layups are the most general laminate type which can be used to carry out both tensile and flexural tests without stiffness coupling issues. They possess beneficial characteristics for extension-bending ( $[B] = 0$ ), in-plane normal and shear ( $A_{xs} = A_{ys} = 0$ ) and bending-twist coupling ( $D_{xs} = D_{ys} = 0$ ).

The symmetric angle ply laminates  $[\pm\theta]_s$  or their symmetric combinations with cross plies are more general, of greater practical interest, and they also have ( $[B] = 0$ ) and ( $A_{xs} = A_{ys} = 0$ ). This means uncoupled tensile testing can be carried out in their principal directions. There is a problem with flexure due to coupling between bending and twist ( $D_{xs} \neq 0, D_{ys} \neq 0$ ). However, if this coupling is relatively small, flexural testing becomes a practical possibility as well.

Laminates of symmetric balanced layup, consisting of plies with  $0^\circ, 90^\circ, \pm\theta_1, \pm\theta_2, \pm\theta_3$ , etc. are considered in this section. An example of such laminate can be  $[0/45/-45/90/60/-60]_s$ . It should be noted that due to the angle plies, in-plane shear modulus  $G_{12}$  also contributes to the longitudinal stiffness.

There are three unknowns  $E_1, E_2, G_{12}$ , even if Poisson's ratio is estimated or disregarded. This means that on contrary to the cross-plyed plate, the three unknown moduli  $E_1, E_2$  and  $G_{12}$  cannot be directly determined from just two stiffness measurements (e.g. tension-flexure on the same specimen). Further, this raises a question of what would be the best way of using the input data (stiffness measurements in principal directions) to estimate the three unknown moduli. One approach could be to optimize for the unknown moduli, minimizing the difference between the measured and estimated stiffnesses. Another approach could be similar to what was used for cross-plyed specimens — two stiffness measurements would give a certain set of data, which can then be analyzed. Exact solution cannot be obtained this way, but a graphical representation for ranges of moduli is possible. The latter approach gives a better overview of outliers and scatter. The specific formulations are discussed in the following sections.

### D.2.1 Tensile stiffness

Assuming tensile stress applied in the  $x$ -direction and a boundary condition of zero stress applied in the  $y$ -direction, the effective tensile stiffness of the laminate can be derived as:

$$\bar{E}_x^t = \left\{ [\rho(\psi E_1 + 2\chi \nu_{12} E_2 + \xi E_2) + 4\chi G_{12}] - \frac{[\rho(\chi E_1 + (\psi + \xi)\nu_{12} E_2 + \chi E_2) - 4\chi G_{12}]^2}{[\rho(\xi E_1 + 2\chi \nu_{12} E_2 + \psi E_2) + 4\chi G_{12}]} \right\}, \quad (D.33)$$

where  $\rho$  represents the Poisson's ratio influence as

$$\rho = \frac{1}{1 - \nu_{12}\nu_{21}} = \frac{1}{1 - \nu_{12}^2 \frac{E_2}{E_1}}, \quad (D.34)$$

and the layup geometry coefficients are

$$\psi = \frac{1}{h} \sum_{k=1}^n m^4 (z_k - z_{k-1}), \quad (D.35)$$

$$\xi = \frac{1}{h} \sum_{k=1}^n n^4 (z_k - z_{k-1}), \quad (D.36)$$

$$\chi = \frac{1}{h} \sum_{k=1}^n m^2 n^2 (z_k - z_{k-1}). \quad (D.37)$$

Ply angles are represented in  $m = \cos\theta_k$  and  $n = \sin\theta_k$ , and  $h$  is the thickness of the laminate. The total number of plies is  $n$  and the distances from the laminate midplane to the ply surfaces are denoted by  $z$ . Eqs. (D.35), (D.36) can be seen as generalizations of Eqs. (D.1), (D.2). For a cross-plyed symmetric laminate ( $\chi = 0$  and  $\psi + \xi = 1$ ), Eqs. (D.33), (D.34) reduce to Eq. (D.5).

### D.2.2 Flexural stiffness

Assume a bending moment applied on the laminate in  $x$ -direction and a boundary condition of zero moment applied in  $y$ -direction. In addition, a boundary condition of zero twist curvature ( $\kappa_s = 0$ ) is assumed to cancel the small valued, however non-zero coupling terms  $D_{xs}$  and  $D_{ys}$ . The error introduced by  $\kappa_s = 0$  assumption is hereby acknowledged, however not further analyzed, implicitly assuming that its influence to the overall result is sufficiently small.

Following the aforementioned assumptions, the expression for the effective flexural modulus of the laminate can be derived:

$$\bar{E}_x^f = 12 \left\{ [\rho(\alpha E_1 + 2\eta v_{12} E_2 + \beta E_2) + 4\eta G_{12}] - \frac{[\rho(\eta E_1 + (\alpha + \beta)v_{12} E_2 + \eta E_2) - 4\eta G_{12}]^2}{[\rho(\beta E_1 + 2\eta v_{12} E_2 + \alpha E_2) + 4\eta G_{12}]} \right\}, \quad (\text{D.38})$$

where  $\rho$  is previously given in Eq. (D.34), and the layup geometry coefficients are

$$\alpha = \frac{1}{3h^3} \sum_{k=1}^n m^4 (z_k^3 - z_{k-1}^3), \quad (\text{D.39})$$

$$\beta = \frac{1}{3h^3} \sum_{k=1}^n n^4 (z_k^3 - z_{k-1}^3), \quad (\text{D.40})$$

$$\eta = \frac{1}{3h^3} \sum_{k=1}^n m^2 n^2 (z_k^3 - z_{k-1}^3). \quad (\text{D.41})$$

It is easy to see that the coefficients defined in Eqs. (D.39), (D.40) are the generalized version of definitions in Eqs. (D.3), (D.4). In case of a cross-plyed symmetric laminate ( $\eta = 0$  and  $\alpha + \beta = 1/12$ ), Eq. (D.38) reduces to Eq. (D.6).

## Appendix E Optimization algorithms

### E.1 Nelder-Mead Simplex method

The basic version of MATLAB software includes *fminsearch* function [202]. This function finds the minimum of a scalar function of several variables, starting at an initial estimate. The algorithm is based on simplex search method of Lagarias *et al.* [203] whereas the original Nelder-Mead Simplex method is discussed in [204].

The number of unknown variables for the objective function is  $n$ . The search method is based on the propagation of a simplex through the search space. Simplex is the generalized notion of a triangle to  $n$ -dimensions which is characterised by  $n + 1$  vectors that are its vertices. If  $n = 2$ , the simplex is triangle, if  $n = 3$ , the simplex is a pyramid. During each search iteration, a new simplex is created as a result of basic operations (reflection, expansion, contraction, reduction/shrinkage) by replacing the worst vertex/vertices in the simplex, and following a certain logic of operations. Iterations are repeated until a stopping criterion is exceeded. The stopping criterion can be set for the number of function evaluations, the number of iterations, etc.

If a maximization problem is encountered, the objective function is recommended to be defined as the negative value of the given function. Various constraints (e.g. constraints for the elastic moduli of composite materials) can be imposed to the unknowns by giving a very large value to the objective function when these constraints are violated.

The simplex method is fast and able to handle discontinuities of the objective function; nevertheless it has limitations. For one, the variables can only be real numbers. This can be overcome, since the complex number can be expressed by an ordered pair of two real numbers. The most severe limitation is its requirement of the initial simplex. This defines the starting location of the search and the consequences of an inappropriate choice can be dramatic. If the objective function has numerous minima, the initial simplex actually defines the minimum to where the final simplex converges. Given a poor initial guess, it is not likely to converge to the global minimum for large  $n$  and a complicated shape of the objective function. Heavy dependence on the initial guess is a well-known drawback of traditional (non-stochastic) search techniques. Another problem arises when the function has numerous global minima; again, the starting location defines if and which of these minima will be found.

The experience of the author from the elastic constant inversion is that while the function *fminsearch* works well for up to  $n=3$  and relatively simple objective functions (e.g. see Chapter 2), it is unsuitable for the direct inversion of e.g. 9 elastic constants from numerous dispersion curve data points. A different strategy is needed there.

## E.2 SGA

Genetic algorithms (GA) are search and optimization methods which employ the process of natural selection. The foundation for contemporary developments of GAs was established by John Henry Holland in 1970-s. GAs are stochastic global search methods, fundamentally different from traditional gradient based techniques as they avoid the local character of conventional exploration, escaping the local minima. No derivatives or any auxiliary information is necessary. GAs are commonly used in various fields in both industry and academia, and are known for their robustness in dealing with complicated problems and large number of variables. Examples of their use for elastic constant inversion can be seen in [78–82, 119, 205], etc.

The simple genetic algorithm (SGA) toolbox described below was developed by the author in MATLAB, early 2011, based on the classic textbook reference on the subject by Goldberg [206]. It is acknowledged that some of the approaches used in the toolbox are not most convenient (e.g. binary coding) or contemporary (e.g. roulette wheel selection). The aim of the work was to produce a robust and reliable algorithm where the user has good control over the details.

SGA is mimicking the natural evolution as described in the diagram in Fig. E.1. The contents of the flowchart are explained as follows. The variable space is defined in matrix  $G$  by discrete groups of values, given for each of the search variables. The initial population of  $n$  individuals is created in random. Each of the individuals is a candidate solution for the problem, i.e. a candidate set of search variables is coded into a binary string which constitutes the individual. The individuals develop through  $t$  iterations (also called generations). During each generation, the fitness of every individual is evaluated by the non-negative fitness function. The binary string of the individual is coded back to real variables and a fitness function value  $f_{pre}$  is evaluated. The aim of the genetic algorithm is to maximize the fitness. The fitness of the whole population  $f_{pre}$  is then scaled to  $f$  in order to slightly reduce the unevenness and the dominance of a few fit individuals (can be thought as “socialist” scaling – author’s remark). Linear scaling is employed through parameter  $nxavg$ . The probability of an individual to enter the mating pool is proportional to its fitness  $f$ . A number  $n_{elites}$  of best solutions go directly to the next generation without competing with others. This does not allow the best fitness to decrease in the population. The rest are chosen to the mating pool for reproduction according to fitness-biased roulette wheel selection. A single cut cross-over of the pairs in the mating pool takes place with a probability  $p_{cross}$  at a random location in the binary string. Finally, the new generation is mutated (zero to one and vice versa) with a probability  $p_{mut}$  for each integer in the binary code. The algorithm terminates when the final generation  $t$  has been simulated. The individual with the highest fitness in the final population is the best solution.

Some known remarks about SGA:

- it handles well large variable spaces (large number of variables with large ranges) and discontinuities in the objective function;

- initial convergence (or increase of fitness) is very good, however the final convergence is very slow;
- after a number of generations all individuals become similar (also known as premature convergence or stagnation) and new information arrives to the population only through mutation. To counter stagnation better and improve the convergence, another version of genetic algorithm,  $\mu$ GA is introduced in the following section;
- generally, more evaluations of the objective function are required by GAs than traditional search methods, making it computationally costly.

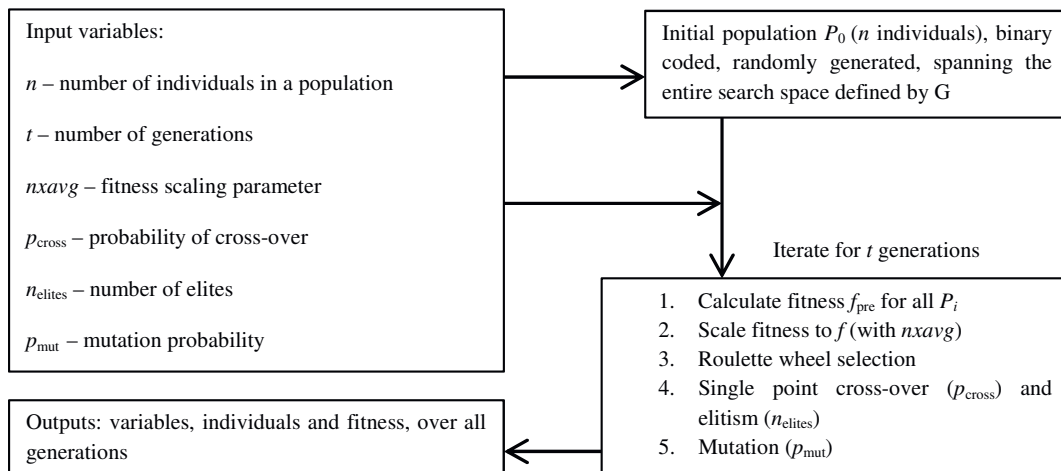


Figure E.1. Schematic overview of the SGA toolbox.

To verify the reliability of the programmed SGA toolbox, it was tested on various test functions, where the solution(s) were known beforehand. These test functions included: polynomial equations, systems of equations, trigonometric equations, Rosenbrock's, Himmelblau's, Rastrigin's, Schwefel's and Ackley's functions for up to ten variables. The SGA toolbox performed well and found the solutions for all of the aforementioned functions. Some notes were taken during the tests:

- a population size of 5 to 10 times the number of search variables seems to be enough;
- if the problem has several equally good solutions, they all cannot be identified with a single optimization. Multiple solutions are found by running the program several times;
- some global minima were obtained with a single optimization, but this was not always the case. A good strategy to solve a problem is to run the program a number of consecutive times (e.g. 10) and to decide about the final result based on the distribution of results and their fitness;
- the initial population is generated in random, the mating pool is compiled biased-random, the cross-over procedure happens in random and the mutation process is random, so there is no possibility to exactly replicate previous optimization. Randomness can be "avoided" by introducing pseudo-random numbers which could be reproduced (as in [110]), but this was not hereby employed.



### E.3 $\mu$ GA

Micro genetic algorithm ( $\mu$ GA) was outlined by D. E. Goldberg in 1988 and applied first by Krishnakumar [207] in 1989. An overview of the algorithm can be found in a report by Senecal [208] and some applications in [110, 111, 122, 209].

In essence,  $\mu$ GA is a number of serially implemented small population SGA-s. Its outline is described in the diagram in Fig. E.2. A small initial population (ca.  $n = 5$  individuals) is generated at random. Usual SGA genetic operations (see Fig. E.1) are performed with this small population until nominal convergence. The nominal convergence of individuals can be judged from the values of their bits, e.g.  $p_{\text{conv}} = 0.95$  means 95% of the bits are required to be the same for all individuals. The convergence for a small population arrives in a few generations. Then  $n_{\text{elites}}$  (usually  $n_{\text{elites}} = 1$ ) best individual(s) are directly transferred to the next “initial” population. The other individuals in the new small population are generated at random and SGA operations are again performed until convergence. These iterations are carried out until the number of fitness function evaluations  $n_{\text{feval}}$  is exceeded. Since new information constantly flows in with each iteration (random new individuals), the mutation is not applied.

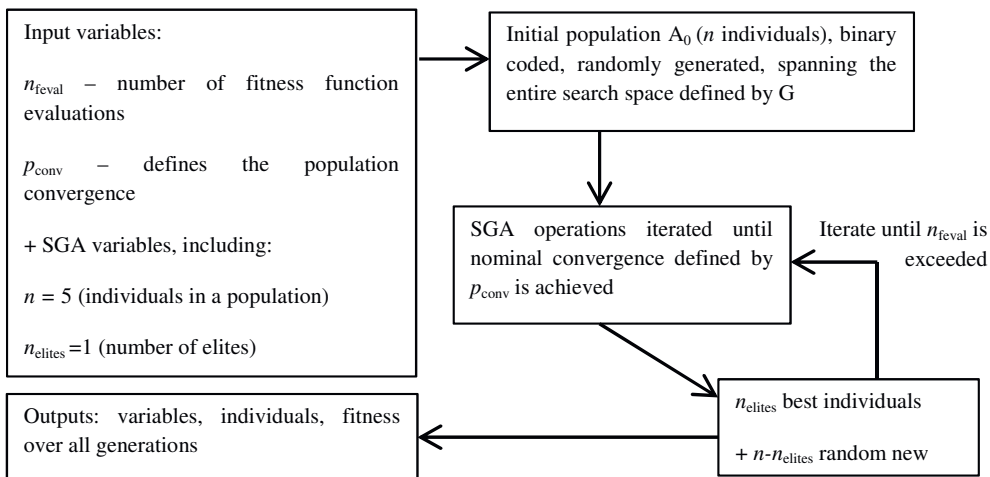


Figure E.2. Schematic overview of the  $\mu$ GA toolbox.

The SGA is known for premature convergence (or stagnation) when new information is only gained by mutation.  $\mu$ GA counters this by employing a kind of “start and restart” procedure, which helps to avoid premature convergence, as explained by Krishnakumar [207]. It is reported that  $\mu$ GA reaches the near-optimal region much quicker than big population genetic algorithms.  $\mu$ GA code performance was tested with test functions similar to SGA in the previous section.

## Appendix F Wave propagation

### F.1 Isotropic media – bulk wave velocities

Isotropic materials have three elastic constants: elastic modulus  $E$ , shear modulus  $G$  and Poisson's ratio  $\nu$ , two of which are independent. Bulk waves propagate in infinite media. Bulk velocities in boundless isotropic media can be calculated, if the mass density  $\rho$  is known for the material [99, 210]. The velocity of the longitudinal wave (also referred to as compression or dilatational wave — where particle motion coincides with the direction of wave travel) is

$$c_L = \sqrt{\frac{E(1-\nu)}{\rho(1+\nu)(1-2\nu)}}. \quad (\text{F.1})$$

The shear wave velocity (also referred to as transverse, distortional, torsional or rotational wave — where particle displacement is perpendicular to the propagation vector), is calculated from

$$c_T = \sqrt{\frac{E}{2\rho(1+\nu)}} = \sqrt{\frac{G}{\rho}}. \quad (\text{F.2})$$

Shear waves can only propagate in solids, whereas compressional waves propagate in all media (liquids, gases). Bulk longitudinal and shear waves are non-dispersive and depend only on material constants (geometry has no influence since the medium has no boundaries and the material is isotropic). The ratio of bulk wave velocities depends only on Poisson's ratio:

$$\frac{c_L}{c_T} = \sqrt{\frac{2(1-\nu)}{(1-2\nu)}}. \quad (\text{F.3})$$

### F.2 Orthotropic media – Christoffel equation

The relationship between material elastic properties and bulk wave velocities in anisotropic material is given by the Christoffel equation [100]. The dispersion equation is obtained by setting the characteristic determinant of the Christoffel equation to zero as:

$$|\Gamma_{ik} - \rho c^2 \delta_{ik}| = 0 \quad (\text{F.4})$$

Where  $\rho$  is mass density, and  $c$  is the phase velocity.  $\Gamma_{ik}$  is called the Christoffel matrix or the Christoffel stiffness, which has elements dependent only on the plane wave propagation

direction with unit normal  $n_i = (l, m, n)$ . The components of the symmetric Christoffel matrix for the most general material (21 elastic constants given by the  $[C]$  matrix) read:

$$\Gamma_{ij} = \begin{bmatrix} \Gamma_{11} & \Gamma_{12} & \Gamma_{13} \\ \Gamma_{12} & \Gamma_{22} & \Gamma_{23} \\ \Gamma_{13} & \Gamma_{23} & \Gamma_{33} \end{bmatrix}, \quad (\text{F.5})$$

where

$$\Gamma_{11} = l^2 C_{11} + m^2 C_{66} + n^2 C_{55} + 2mn C_{56} + 2nl C_{15} + 2lm C_{16},$$

$$\Gamma_{22} = l^2 C_{66} + m^2 C_{22} + n^2 C_{44} + 2mn C_{24} + 2nl C_{46} + 2lm C_{26},$$

$$\Gamma_{33} = l^2 C_{55} + m^2 C_{44} + n^2 C_{33} + 2mn C_{34} + 2nl C_{35} + 2lm C_{45},$$

$$\begin{aligned} \Gamma_{12} = & l^2 C_{16} + m^2 C_{26} + n^2 C_{45} + mn(C_{46} + C_{25}) \\ & + nl(C_{14} + C_{56}) + lm(C_{12} + C_{66}), \end{aligned} \quad (\text{F.6})$$

$$\begin{aligned} \Gamma_{13} = & l^2 C_{15} + m^2 C_{46} + n^2 C_{35} + mn(C_{45} + C_{36}) \\ & + nl(C_{13} + C_{55}) + lm(C_{14} + C_{56}), \end{aligned}$$

$$\begin{aligned} \Gamma_{23} = & l^2 C_{56} + m^2 C_{24} + n^2 C_{34} + mn(C_{44} + C_{23}) \\ & + nl(C_{36} + C_{45}) + lm(C_{25} + C_{46}) \end{aligned}$$

are its components. Eq. (F.4) is a general equation, which can be written for other more constrained material symmetries. It is necessary however that the propagation direction and the stiffness constants  $[C]$  refer to the same coordinate system. The wavespeed can be calculated from an equation cubic in  $(\rho c^2)$ , which reads [100]:

$$(\rho c^2)^3 - \Gamma_1(\rho c^2) + \Gamma_2(\rho c^2) - \Gamma_3 = 0, \quad (\text{F.7})$$

where

$$\Gamma_1 = \Gamma_{11} + \Gamma_{22} + \Gamma_{33} ,$$

$$\Gamma_2 = \Gamma_{11}\Gamma_{22} + \Gamma_{22}\Gamma_{33} + \Gamma_{33}\Gamma_{11} - \Gamma_{12}^2 - \Gamma_{23}^2 - \Gamma_{13}^2 , \quad (\text{F.8})$$

$$\Gamma_3 = \Gamma_{11}\Gamma_{22}\Gamma_{33} - \Gamma_{11}\Gamma_{23}^2 + \Gamma_{22}\Gamma_{13}^2 - \Gamma_{33}\Gamma_{12}^2 + 2\Gamma_{12}\Gamma_{23}\Gamma_{31} .$$

Equation (F.7) has three solutions for  $(\rho c^2)$ , showing three possible modes, each with a polarization vector corresponding to the material motion for that mode. In general, material motion is not parallel to the wave velocity, which is along the normal of the wavefront.

### F.3 Guided waves in isotropic plates – Lamb waves

The difference between bulk wave and guided wave propagation is due to the applied boundaries. Wave properties are now also determined by the boundaries and these waves are therefore referred as guided waves. In case of a plate, the boundary conditions are applied on the top and bottom surfaces of the plate which are usually assumed to be stress free. As the ultrasonic energy is introduced into the plate, the waves begin to reflect from the plate surfaces and mode conversion occurs (longitudinal wave to shear wave and vice versa). The superposition of these waves (constructive and destructive interference) causes the formation of “wave packets” or “wave modes” that travel in the plate structure. The relationship between material properties, plate dimension and Lamb wave velocity is complex, as explained below.

Through mode conversion and reflection from the surfaces of the plate, resulting wave modes propagate along the plate structure. It is common practice to analyse the propagation characteristics of these wave modes by using dispersion curves. Dispersion curves essentially show the possibilities for combinations of frequency and wavenumber (or frequency and phase velocity) that can propagate in the wave guide structure. For the derivation of dispersion equations, reference is made to ([99, 210]). The equations connect the wave angular frequency  $\omega = 2\pi f$ , wavenumber  $k$ , half-thickness of the plate  $h = d/2$  and the bulk wave velocities. Rayleigh-Lamb dispersion equations (also known as frequency equations) are expressed as:

$$\frac{\tan(qh)}{\tan(ph)} + \left[ \frac{4k^2 pq}{(q^2 - k^2)^2} \right]^B = 0 , \quad (\text{F.9})$$

$B = 1$  for the symmetric waves (or S-modes), where displacement is an even function of the transverse coordinate with its origin on the plate midplane i.e. displacements are symmetric to midplane;

$B = -1$  for the antisymmetric waves (or A-modes), where displacement is an odd function of the transverse coordinate i.e. displacements are anti-symmetric to midplane.

Parameters  $p$  and  $q$  are defined as:

$$p^2 = \frac{\omega^2}{c_L^2} - k^2 \quad (\text{F.10})$$

$$q^2 = \frac{\omega^2}{c_T^2} - k^2. \quad (\text{F.11})$$

Dispersion equation (F.9) can be solved for wavenumber  $k$  for a given the angular frequency  $\omega = 2\pi f$ . Although Eq. (F.9) looks relatively simple, it can only be solved by numerical methods [99]. It is known that for any given frequency, there is an infinite number of wavenumbers that will satisfy Eq. (F.9). A finite number of these wavenumbers will be purely real or purely imaginary, while infinitely many will be complex. Wavenumber  $k$  can in general be complex  $k = k_r + ik_{im}$ . Rose [99] discusses that time harmonic factor  $\exp[i(kx - \omega t)]$  becomes  $\exp[i(k_r x - \omega t)] \exp[-k_{im} x]$  and therefore the values for the real number  $k_{im}$  have the following physical interpretation:

- $k_{im} < 0$ , waves grow exponentially with distance;
- $k_{im} = 0$ , waves propagate without damping;
- $k_{im} > 0$ , wave decay exponentially with distance.

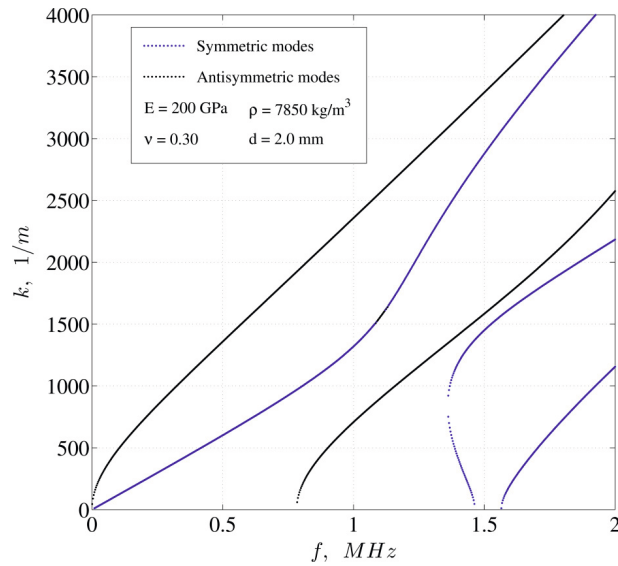
The growing waves have not been physically observed and the decaying waves will disappear as their amplitude decreases exponentially from the source. A typical example of  $k_{im} > 0$  is seen in the water immersed plate where part of the energy “leaks” into the fluid. The plates in current study reside in air and it is concluded that only the real values for  $k$  are necessary to supply information about propagating waves. Therefore, only the real solutions or the undamped propagating modes of Eq. (F.9) are here of interest. A numerical approach employing the bisection method is employed to search for the roots.

The phase velocity of the wave is established from

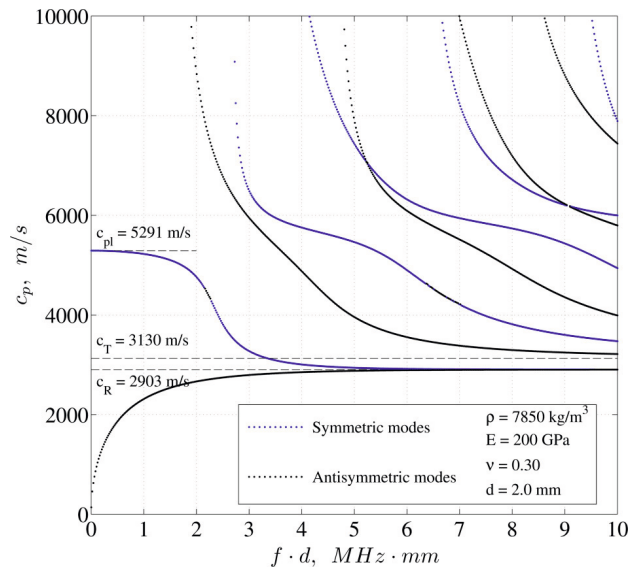
$$c_p = \frac{\omega}{k}. \quad (\text{F.12})$$

Examples of dispersion curves for steel are plotted in Figure F.1. The limiting value for large  $fd$  values of fundamental  $A_0$  and  $S_0$  phase velocity is the non-dispersive Rayleigh surface wave velocity  $c_R$ , as seen from Fig. F.1(b). The high-frequency limiting velocity for other modes besides the fundamental is  $c_T$ . Long wavelength (small  $f$ ) plate velocity  $c_{pl}$  for  $S_0$  can be calculated as:

$$c_{pl} = \sqrt{\frac{E}{\rho(1-\nu^2)}} \quad (F.13)$$



(a) wavenumber- frequency axes



(b) phase velocity and frequency-thickness axes

Figure F.1. Dispersion curves for a 2 mm thick steel plate.

Fig. F.1(b) displays the following two important characteristics of Lamb waves:

- Lamb waves are dispersive (wave velocity depends on frequency);
- there is an infinite number of wave modes, usually labelled  $S_n$  and  $A_n$  according to order in which they appear on frequency axis. However, the fundamental  $S_0$  and  $A_0$  are the only modes which span the entire frequency spectrum.

## F.4 Guided waves in orthotropic plates

### F.4.1 Solutions for the low frequency region

The phase velocity in the long wavelength (wavelength  $\gg$  plate thickness) limit of the fundamental symmetric mode  $S_0$ , in the principal directions of an orthotropic plate, becomes non-dispersive and simplifies to [e.g. 211]:

$$c_{pe,x} = \sqrt{\frac{A_{xx}}{\rho h}} = \sqrt{\frac{\bar{E}_x^t}{\rho(1 - \bar{\nu}_{xy}^t \bar{\nu}_{yx}^t)}}, \quad (\text{F.14})$$

$$c_{pe,y} = \sqrt{\frac{A_{yy}}{\rho h}} = \sqrt{\frac{\bar{E}_y^t}{\rho(1 - \bar{\nu}_{xy}^t \bar{\nu}_{yx}^t)}},$$

where  $h$  denotes the plate thickness,  $\rho$  is the density and  $A_{xx}$ ,  $A_{yy}$  are in-plane laminate stiffnesses. The  $E$ ,  $\nu$  expressions with overbars denote effective laminate in-plane moduli, just as in Appendix D (see Eqs. (D.21), (D.22)). The analogy of Eqs. (F.14) to Eq. (F.13) is obvious. The approximate solution for the long wavelength flexural wave is dispersive and reads:

$$c_{pf,x} = \sqrt[4]{\frac{D_{xx}}{\rho h}} \sqrt{\omega} = \sqrt[4]{\frac{\bar{E}_x^f h^2}{12\rho(1 - \bar{\nu}_{xy}^f \bar{\nu}_{yx}^f)}} \sqrt{\omega} \quad (\text{F.15})$$

$$c_{pf,y} = \sqrt[4]{\frac{D_{yy}}{\rho h}} \sqrt{\omega} = \sqrt[4]{\frac{\bar{E}_y^f h^2}{12\rho(1 - \bar{\nu}_{xy}^f \bar{\nu}_{yx}^f)}} \sqrt{\omega}$$

Where  $D_{xx}$  and  $D_{yy}$  are laminate flexural stiffnesses and expressions with overbars denote effective laminate flexural moduli in principal directions. The use of Eqs. (F.14), (F.15) for laminate stiffness determination is however limited, due to their approximate nature and narrow low frequency range.

#### F.4.2 A solution for orthotropic plate in principal directions

The Lamb wave dispersion equation for an anisotropic medium has been derived by Rhee *et al.* [124] based on elasticity (not approximated plate theory). For the sake of overview, and due to a small misprint in the original paper, the dispersion equation results are re-printed in the following.

Symmetric mode dispersion equation can be written as

$$\begin{aligned} (C_{33}R_-k_{z-} + C_{13}k_x)(R_+k_x + k_{z+}) \sin(k_{z+}h) \cos(k_{z-}h) \\ - (C_{33}R_+k_{z+} + C_{13}k_x)(R_-k_x + k_{z-}) \sin(k_{z-}h) \cos(k_{z+}h) = 0 . \end{aligned} \quad (\text{F.16})$$

Anti-symmetric mode dispersion equation can be written as

$$\begin{aligned} (C_{33}R_+k_{z+} + C_{13}k_x)(R_-k_x + k_{z-}) \sin(k_{z+}h) \cos(k_{z-}h) \\ - (C_{33}R_-k_{z-} + C_{13}k_x)(R_+k_x + k_{z+}) \sin(k_{z-}h) \cos(k_{z+}h) = 0 , \end{aligned} \quad (\text{F.17})$$

where  $h = d/2$  is the half thickness of the plate and

$$R_{\pm} = \frac{(\rho\omega^2 - C_{11}k_x^2 - C_{55}k_{z\pm}^2)}{(C_{55} + C_{13})k_xk_{z\pm}} , \quad (\text{F.18})$$

$$k_{z\pm}^2 = \left( \frac{-M \pm \sqrt{M^2 - 4N}}{2} \right) k_x^2 , \quad (\text{F.19})$$

where

$$M = \frac{C_{11}C_{33} - 2C_{55}C_{13} - C_{13}^2 - \frac{\rho\omega^2}{k_x^2}(C_{33} + C_{55})}{C_{33}C_{55}} , \quad (\text{F.20})$$

$$N = \frac{\rho^2 \left( \frac{\omega^2}{k_x^2} - \frac{C_{11}}{\rho} \right) \left( \frac{\omega^2}{k_x^2} - \frac{C_{55}}{\rho} \right)}{C_{33}C_{55}} . \quad (\text{F.21})$$



$k_x$  and  $k_z$  indicate the wave numbers of directions 1 and 3, respectively, and  $\omega = 2\pi f$  is the angular frequency of the wave. Dispersion equations for direction 2 can also be written as Eqs. (F.16)–(F.21), when the values for directions 1 and 2 are switched in the stiffness matrix  $[C]$ .

## Appendix G Experiments and data reduction

### G.1 Composite specimens

Test specimens used for the experiments employ various materials systems. These material systems, their physical properties and specimen production are described here for an easy reference throughout the study. Only the information which could be confirmed by the author is reported.

#### G.1.1 Glass/epoxy

*Table G.1. Details of cross-plyed glass-fiber/epoxy specimen production.*

Fibers	UD Devold PPG 2002 E-glass fibers (layer weights 1152 g/m <sup>2</sup> and 51.2 g/m <sup>2</sup> in 0° and 90° directions)
Matrix	<i>Epikote MGS RIMR</i> 135 epoxy resin, <i>Epikure MGS RIMH</i> 137 curing agent
Production	VARI, post curing at 80 °C for 15 hours, following the manufacturer's recommendations
Specimen cutting	Diamond saw
Fiber volume fraction	58 % on average (burn-off)
Details	Release fabrics (peel plies) were used on both faces of the plates Thickness: 4.86 mm (average) Density: 1946 kg/m <sup>3</sup> (average)
Specimens	3 straight sided specimens: 1a, 1b, 1c [90 <sub>2</sub> /0 <sub>2</sub> /90 <sub>2</sub> ] 3 straight sided specimens: 2a, 2b, 2c [0 <sub>2</sub> /90 <sub>2</sub> /0 <sub>2</sub> ]  3 straight sided specimens: 3a, 3b, 3c [0/90 <sub>4</sub> /0] 3 straight sided specimens: 4a, 4b, 4c [90/0 <sub>4</sub> /90]  1 plate, ca. 30x30 cm <sup>2</sup> , TR11_1 [90 <sub>2</sub> /0 <sub>2</sub> /90 <sub>2</sub> ] 1 plate, ca. 30x30 cm <sup>2</sup> , TR11_1F [90 <sub>2</sub> /0 <sub>2</sub> /90 <sub>2</sub> ] (with fatigue damage to create transverse cracks in the outside layers) 1 plate, ca. 30x30 cm <sup>2</sup> , TR11_2 [0/90 <sub>4</sub> /0]

Table G.2. Details of symmetric-balanced glass-fiber/epoxy specimen production.

Fibers	R-Glass fibers in stitchbonded UD fabric (layer weights 1150 g/m <sup>2</sup> and 36 g/m <sup>2</sup> in 0° and 90° directions)
Matrix	<i>Epikote MGS RIMR 135</i> epoxy resin, <i>Epikure MGS RIMH 137</i> curing agent
Production	VARI, post curing at 80 °C for 15 hours, following the manufacturer's recommendations
Specimen cutting	Water jet cutting
Fiber volume fraction	55–61% (calculated estimation)
Details	Laminate layup [90/45/-45/0 <sub>2</sub> ] <sub>s</sub> was built up from unidirectional plies (±45° plies were manually placed at these angles). Release fabrics (peel plies) were used on both faces of the plates
Specimens	3 straight sided specimens [90/45/-45/0 <sub>2</sub> ] <sub>s</sub> 3 straight sided specimens [0/-45/45/90 <sub>2</sub> ] <sub>s</sub>
Additional information	The following elastic constants of exactly the same material have been measured independently from standard tensile tests on flat specimens (ASTM D3039 [20], ASTM D3518 [212]), as reported by Perillo [213]. They are reported with coefficients of variation (COV). <i>t</i> – tension, <i>c</i> – compression.  $V_f = 54\%$ (Burn-off) $E_1^t = 44.9$ GPa, COV = 2.1 % $E_1^c = 45.0$ GPa, COV = 4.1 % $E_2^t = 12.1$ GPa, COV = 6.2 % $E_2^c = 12.4$ GPa, COV = 4.5 % $G_{12} = 3.4$ GPa, COV = 4.2 %

It can be noted that the measurement results from Perillo [213] in Table G.2 agree with micromechanics Halpin-Tsai estimates, as given in Table C.4 in Appendix C.3. Both  $E_1$  and  $E_2$  are within the estimated range. Shear modulus  $G_{12} = 3.4$  GPa, is for some reason lower than the predicted range of (4.2, 5.4) GPa.

### G.1.2 Glass/vinylester

Table G.3. Details of unidirectional GF/vinylester specimen production.

Fibers	Glass fiber, unidirectional: 0° ply weight 1134 g/m <sup>2</sup> , 90° ply weight 50.2 g/m <sup>2</sup>
Matrix	Vinylester ( <i>DION IMPACT 9102-75 SERIES</i> )
Production	VARI, post curing at 80 °C for 15 hours
Specimen cutting	Diamond saw
Fiber volume fraction	55–61% (calculated estimation)
Details	Thickness: 6.6 mm (average) Density: 1930 kg/m <sup>3</sup> (average)
Specimens	1 unidirectional plate, ca. 30x30 cm <sup>2</sup> , TR10_1 [0 <sub>8</sub> ] 1 unidirectional plate, ca. 30x30 cm <sup>2</sup> , TR10_2 [0 <sub>8</sub> ]

### G.1.3 Carbon/vinylester

Table G.4. Details for CF/vinylester specimens.

Fibers	Devold DB420, LT450 carbon fiber layers. All plies (0°, 90°, +45° or -45°) have similar nominal area weight of fibers, varying from 201 to 208 g/m <sup>2</sup>
Matrix	DION 9500-501 vinylester resin (Reichhold)
Production	post curing at 80 °C for 15 hours
Specimen cutting	Water jet, diamond saw
Fiber volume fraction	30...40 % (burn-off)
Details	–
Specimens	4 straight sided specimens [(+45/-45/0/90) <sub>7</sub> (+45/-45)] (30 layers in total)

## G.2 Static measurements

### G.2.1 Tensile testing

A Zwick/Roell Z250 test machine with mechanical wedge grips was used for tensile testing. Load was measured with a standard 250 kN load cell, elongation and the initial gauge length were measured with a mounted optical extensometer videoXtens. Tensile test set-up is shown in Fig. G.1.

During the test, the specimen was elongated along its longitudinal axis in force control, until strain reached a predetermined value. Time, load sustained by the specimen, elongation and strain were recorded with 10 Hz sampling frequency. The highest applied strain rate was 0.3% min<sup>-1</sup>. Since all tests were carried out in room temperature, at low strain rates and load values, any viscoelastic effects of the material are expected to be negligible (see also Appendix A.5). A pre-load was set for all specimens, to avoid possible onset effects disturbing the beginning of the stress-strain curve. The strains were measured over an interval of  $\epsilon = (0.03, 0.20)\%$ , slightly different sub-interval for each specimen. The modulus was obtained by linear regression. The systematic component for uncertainty is evaluated as  $\pm 0.3\%$  for force measurement and  $\pm 0.7\%$  for strain measurement.

Tensile tests (e.g. Fig. G.2(a)) were repeatedly carried out from four up to ten times for the same specimen, releasing it from the grips in between. This accounts for the imperfect alignment of the specimen and the test machine. The reported result for one specimen is the mean of these repeated measurements.

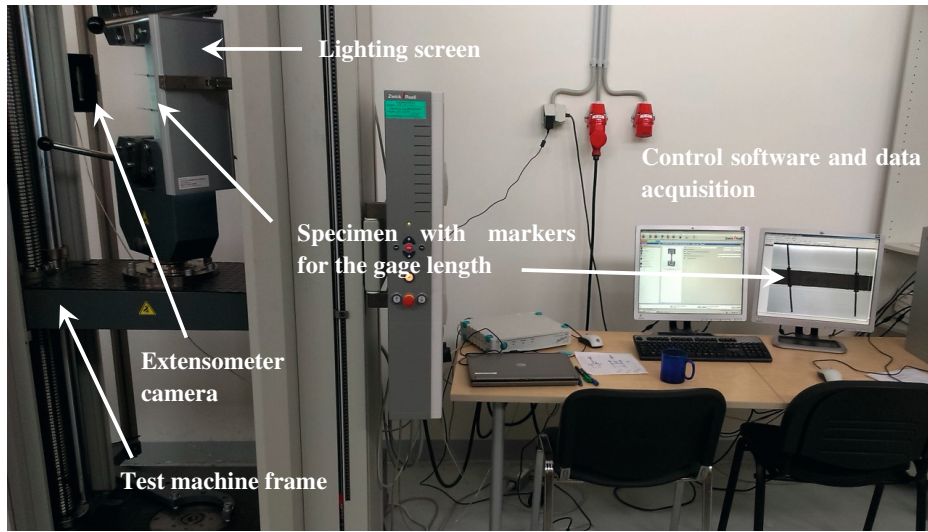
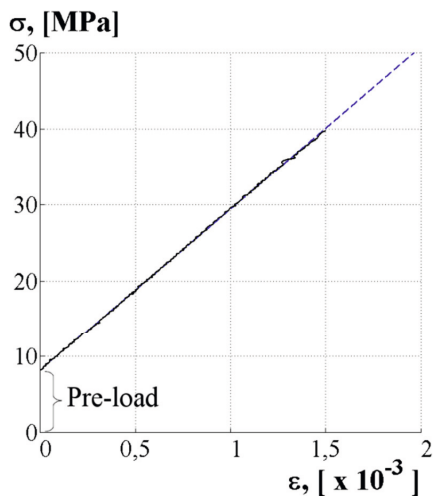
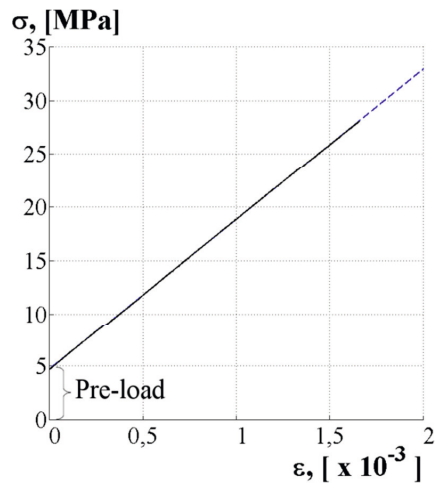


Figure G.1. Tensile test set-up.



a) Tensile testing (specimen 1a)



b) Flexural testing (specimen 1a), calculated tensile stress value at the beam midpoint, outer surface

Figure G.2. Examples of experimental stress-strain curves and their linear regression lines (actual strains are higher than the values on horizontal axis, due to the pre-load).

### G.2.2 Flexural testing

A table top test machine Zwick/Roell Z2.5 was used for flexural tests under three-point loading. The load application device and the supports were 10 mm diameter steel cylinders, as shown in Fig. G.3. The load and the deflection were measured with a standard 2.5 kN load cell and machine grip movements.

Test specimen, supported as a beam under central load, was deflected under load control until the maximum load reached a pre-determined value. The time history of the central load sustained by the specimen and the corresponding central deflection were recorded with 10 Hz frequency. The highest applied strain rate was estimated as  $0.3\% \text{ min}^{-1}$ . The undamaged ply was assumed to have equal compressive and tensile stiffnesses. Maximum deflections remained below 3% of the span length and therefore large deflection corrections needed not to be accounted for. The load to deflection ratio was obtained by using linear regression. A pre-load was set for all specimens to avoid onset effects from seating or fitting of the specimen. The maximum strains were measured in the interval  $\epsilon = (0.01 \dots 0.20) \%$ , a slightly different sub-interval for each specimen. The systematic component for uncertainty is evaluated as  $\pm 0.3\%$  for force measurement and  $\pm 0.5\%$  for deflection measurement.

An example result of a single flexural test is shown in Fig. G.2(b). These flexural tests were repeated for a minimum of four times (for some specimens it was up to ten times) for one specimen. The reported result for one specimen is the mean of these repeated measurements.

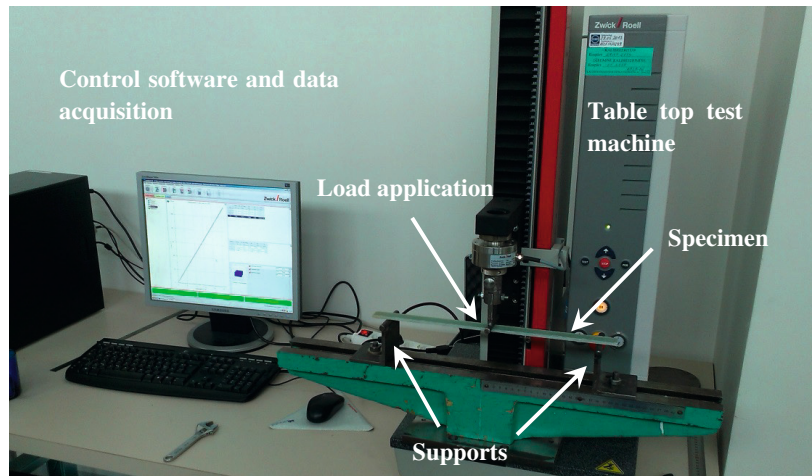


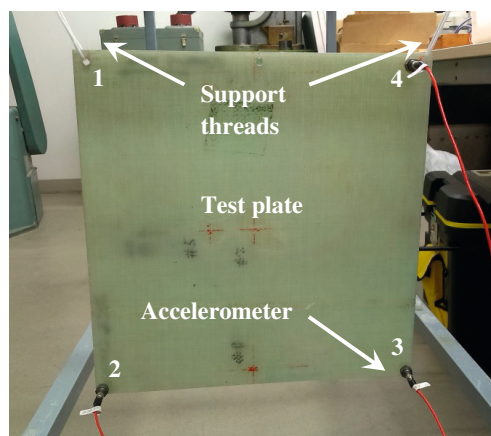
Figure G.3. Test set-up for three-point flexure.

## G.3 Vibration measurements

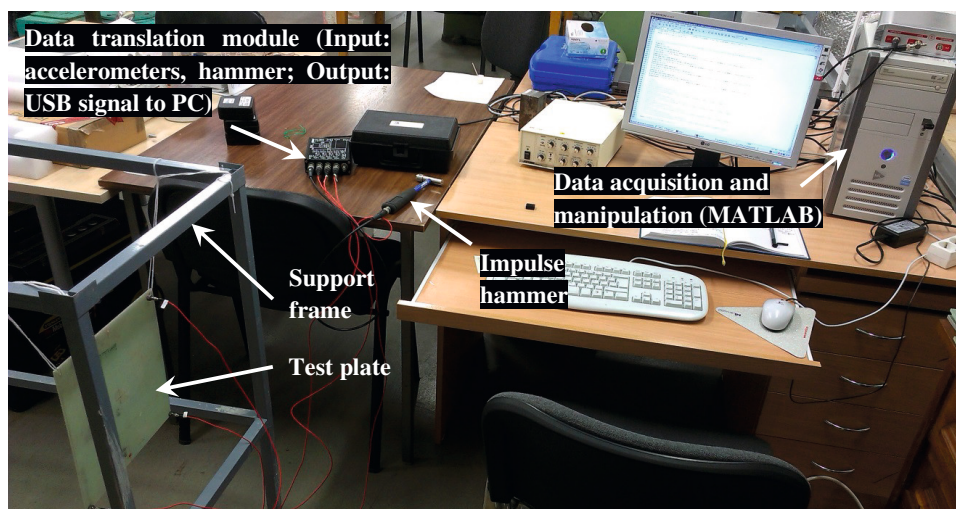
### G.3.1 Test set-up

The free vibration testing was carried out by the impulse technique. Impulse technique stimulates all frequencies in the specimen simultaneously and therefore permits a rapid determination of natural frequencies. The test plate was vertically suspended by two threads, as seen in Fig. G.4(a). Three corners of the composite plate were instrumented with one-axis, model 3049E1 accelerometers (mass 3.3 g) from Dytran Instruments Inc., as also seen in Fig. G.4(a). The accelerometers were mounted on the plate using two component strain-gage glue X60 from HBM, to ensure a stiff connection (glueline thickness small,  $E \approx 13 \text{ GPa}$ ). The plate was excited with a hand held model 5800B3 DYNAPULSE impulse hammer from Dytran Instruments Inc. A small impulse was applied to all four corners of the plate (1, 2, 3, 4) during separate sub-measurements. Hardness of the hammer tip controls the excited vibration range.

The metal tip was used to ensure the widest range of excitation. Since three accelerometers were recording during four separate impulse loads, one full measurement produced twelve sets of time-acceleration series. The data was acquired through Data Translation *DT9837B* module into the PC USB Port, as seen in Fig G.4(b). Data acquisition was triggered by the force transducer in the impulse hammer.



(a) vertically suspended plate with three accelerometers



(b) workplace and equipment

Figure G.4. Vibration test set-up.

The test set-up enabled the measurement of time domain data: input force (voltage) signal  $F(t)$  from the impulse hammer and the voltage signals  $u(t)$  from the accelerometers, with 10 kHz sampling frequency. The input channels saved 8000 data points each, i.e. the lengths of all saved signals were 0.8 s. Acceleration can be obtained from voltage via specific accelerometer sensitivity, which is ca.  $10 \text{ mV}/(9.8 \text{ m/s}^2)$ . The locations of excitation and measurement are at four different plate corners, denoted by numbers in Fig. G.4(a).

### G.3.2 Data reduction

A short description of data reduction is given in the following by an example of one measurement. The example is taken from the measurement of *TR10\_2* glassfiber/vinylester plate. Hammer strikes corner at location 1 and accelerometer signal is measured from the corner of location 4 (Fig. G.4(a)). Recorded temporal signals are shown in Fig. G.5. Windows (e.g. exponentially decaying window) for the data were not used, since decay of the signal is already well captured within 0.8 s.

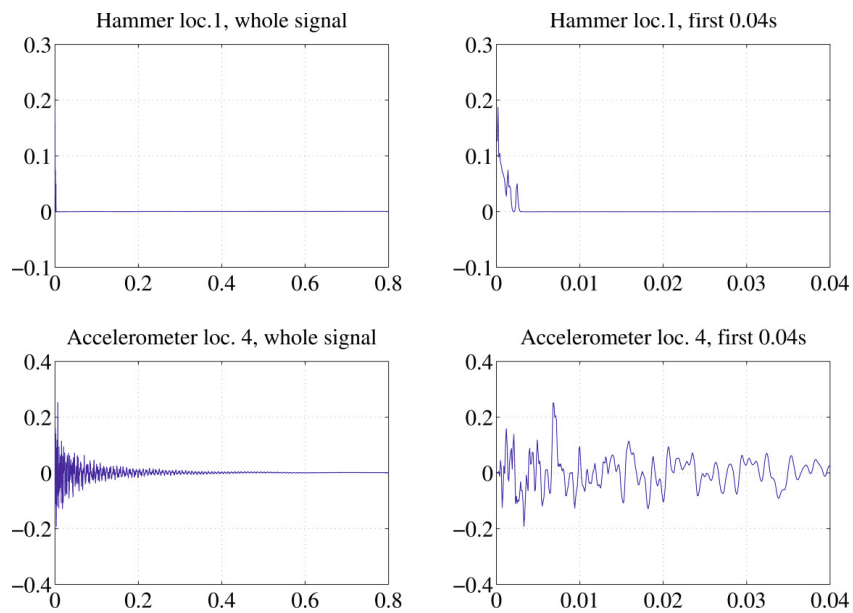


Figure G.5. Recorded temporal signals for hammer  $F(t)$  and accelerometer  $u(t)$ . All horizontal axes: time, s; all vertical axes: measurement signal in V.

To identify the frequency components of the signal, discrete Fourier transform is found by taking the fast Fourier transform (FFT). Figure G.6 displays the frequency domain components of the hammer impulse and the accelerometer. It can be noted that the peaks of higher frequencies in Fig. G.6 are blunted. This makes the direct eigenfrequency identification from FFT spectrum difficult. To overcome this, a frequency response function (FRF) is calculated by dividing the FFT of accelerometer  $u(t)$  by the FFT of the impulse hammer  $F(t)$ . The phase angle of the complex FRF reveals the natural frequencies as it passes through  $\pm 90^\circ$  (see Fig. G.7).

A comparison of natural frequencies with the results from a state-of-the-art experimental set-up (laser scanning vibrometer and commercial software) proved the results from current set-up and data reduction satisfactory.



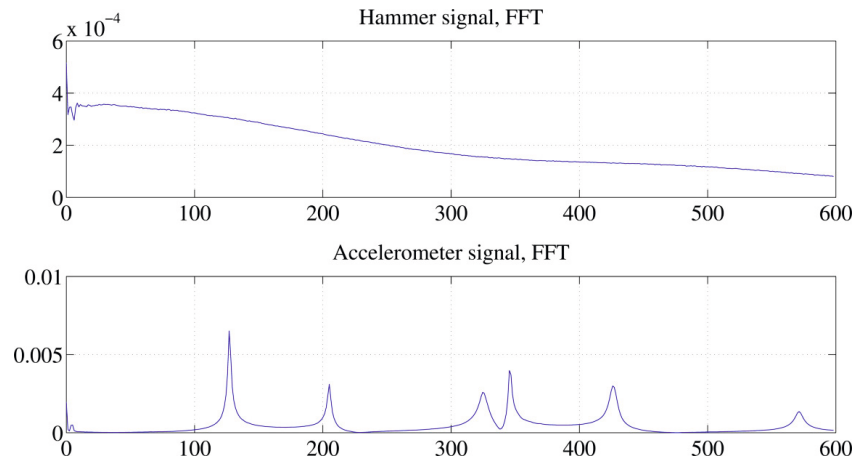


Figure G.6. Single-sided amplitude spectrum shows frequency components of hammer and accelerometer signals. Horizontal axes in Hz.

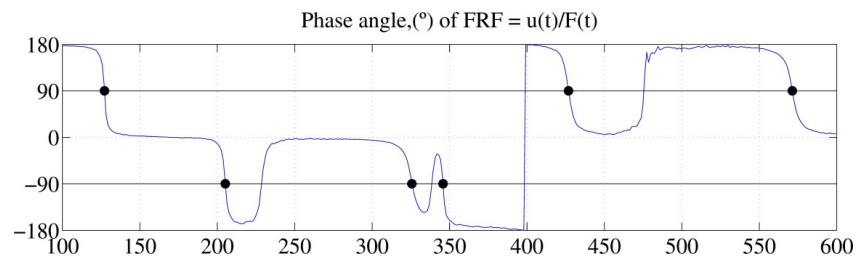


Figure G.7. The phase of the frequency response function (FRF) reveals the locations of resonances ( $\pm 90^\circ$ ) in freq. domain. Horizontal axis in Hz, vertical axis in degrees ( $^\circ$ ).

### G.3.3 Results

The length  $a$ , width  $b$ , thickness  $h$  and mass  $m$  of the specimen plates were measured on various separate locations. The density was calculated from mass and linear dimensions. The physical properties in Table G.5 were accordingly evaluated with a coefficient of variation (COV).

Table G.5. Physical properties of the plates.

Specimen plate	$a$ , mm		$b$ , mm		$h$ , mm		$\rho$ , kg/m <sup>3</sup>	
	mean	COV, %	mean	COV, %	mean	COV, %	mean	COV, %
TR10_2	300.0	0.0	300.7	0.2	6.51	2.0	1953	2.0
TR11_1	294.0	0.3	293.0	0.7	4.79	1.2	1958	1.2
TR11_1F	294.3	0.2	300.0	0.0	4.68	1.3	1973	1.3
TR11_2	295.0	0.0	296.7	0.2	4.81	1.0	1973	1.0
Mean COV, %	0.2				1.4			

Since each sub-measurement was carried out under similar conditions (same duration, sampling rate and assumed noise level), the measured frequency from a single test was calculated as a mean of twelve individual measurements (four hammer strikes measured by three accelerometers each).

Each of the plates was measured independently on at least two occasions ( $n=2$ ); the damaged plate *TR11\_1F* was measured on five ( $n=5$ ) separate occasions. These separate measurements took place on some occasions a few years apart. The mean, minimum and maximum frequency from all measurements is presented in Table G.6. The variation in measurements is characterized by the relative difference between min/max and the mean of  $n$  measurements.

Table G.6. Experimental natural frequencies (Hz) and relative variations (%).

1:  $f_{mean}$  ; 2:  $f_{min}$  ; 3:  $f_{max}$  ; 4:  $\frac{f_{mean}-f_{min}}{f_{mean}} \cdot 100\%$  ; 5:  $\frac{f_{max}-f_{mean}}{f_{mean}} \cdot 100\%$  ;

Plate	Property	$f_1^{exp}$	$f_2^{exp}$	$f_3^{exp}$	$f_4^{exp}$	$f_5^{exp}$	Mean
<i>TR10_2</i>	1	126.8	205.6	327.4	345.3	424.1	0.37
	2	126.5	205.2	325.6	344.6	421.5	
	3	127.2	206.1	329.2	346.0	426.6	
	4	0.28	0.24	0.55	0.2	0.6	
	5	0.28	0.24	0.55	0.2	0.6	
<i>TR11_1</i>	1	88.7	155.9	234.8	255.2	306.3	0.32
	2	88.5	155.7	233.3	254.2	305.5	
	3	88.9	156.0	236.3	256.1	307.1	
	4	0.24	0.09	0.64	0.37	0.27	
	5	0.24	0.09	0.64	0.37	0.27	
<i>TR11_1F</i>	1	78.8	122.8	198.1	238.3	279.3	0.71
	2	78.5	121.7	197.2	237.3	278.0	
	3	79.2	125.0	198.9	239.7	282.8	
	4	0.34	0.93	0.43	0.44	0.47	
	5	0.47	1.75	0.44	0.56	1.23	
<i>TR11_2</i>	1	88.4	185.9	230.9	255.0	287.7	0.32
	2	87.8	185.8	230.5	254.4	287.0	
	3	89.0	186.1	231.7	255.5	289.1	
	4	0.74	0.08	0.18	0.24	0.26	
	5	0.65	0.07	0.35	0.19	0.48	

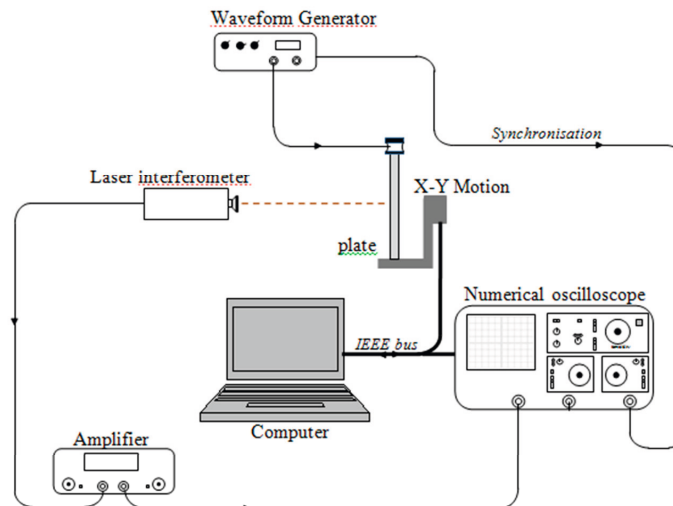
## G.4 Lamb wave measurements

It is acknowledged that the experiments and initial data manipulation for Lamb wave measurements were conducted by two colleagues (F. Chati, D. Décultot) at the acoustics laboratory LOMC at the University of Le Havre, France. Hereby, a description of the experiment is presented for completeness, however it is emphasized that this specialized experimental work was not carried out by the author.

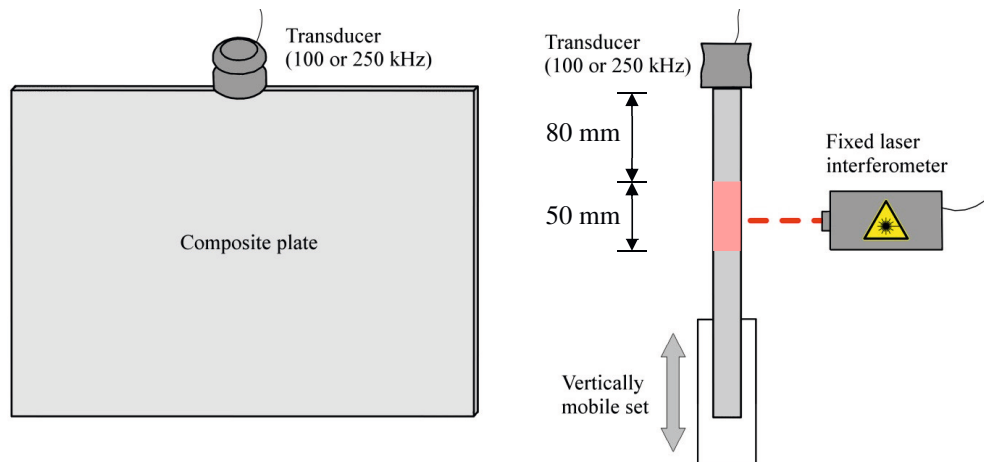
### G.4.1 Test set-up

Illustration of the equipment for Lamb wave measurements is presented in Fig. G.8(a). The contact transducer is fixed on the edge of the studied composite plate and *Metalscan UT5* gel is used to ensure a good ultrasonic coupling. The thickness of the gel layer between transducer and the plate is kept unchanged during the measurements. The excitation signal which was applied to the transducer consisted of *Hanning* windowed sinusoid with 1 cycle duration, generated with an *Agilent 33220A* arbitrary waveform generator. The normal displacements at the composite surface were measured using a single point laser interferometer. Each displacement measurement is enhanced by taking 200 averages in order to improve the signal to noise ratio. The time signals obtained from the laser probe are visualized on a *Lecroy 9310M* numerical oscilloscope and recorded on a PC via IEEE Bus.

The set-up shown in Fig. G.8(b) allows to generate longitudinal, symmetric modes from the edge section of the plate. Due to imperfections on the plate edge, anti-symmetric waves can also be occasionally generated. In addition, Scholte interface waves are generated. The set is vertically mobile by means of a motion set-up which generates movements with a displacement step of 0.1 mm (see Fig. G.8(a)). Laser spot starts measuring at 80 mm from the transducer and ends at 130 mm thus making measurements at 500 locations in total.



(a) The equipment



(b) The measurement

Figure G.8. Illustration of the experimental set-up.

#### G.4.2 Transducers

Two transducers were used for specimen excitation.

- A broadband Panametrics transducer, model V1012 is characterized by a central frequency 250 kHz and the useful frequency range of ca. 125–375 kHz. The excitation signal is a narrow 250 kHz band signal consisting of one sinusoid train with a period of 10 ms.
- A broadband Panametrics transducer, model V1011 is characterized by a central frequency 100 kHz and the useful frequency range of ca. 50–150 kHz. The excitation signal is a narrow 100 kHz band signal consisting of one sinusoid train with a period of 10 ms.

#### G.4.3 Laser interferometer

The detection of signal was carried out using a BMI heterodyne probe SH140 to measure the out-of-plane (normal) displacement on the surface of the plate. The main characteristics of the laser interferometer (Nd<sub>2</sub>YAG laser) are:

Laser Power: 532 nm

Sensitivity: 10 mV/Å

Maximum: 20 kHz – 30 MHz

Power: 100 mW

#### G.4.4 2-D FFT

After the measurement of temporal signals, a 2-D FFT is applied to the temporal data (time histories at various positions). The method was developed in [123] and is commonly used when multimode wave propagation with dispersion is measured.

The input signals are the time histories of waves received at a series of equally spaced positions along the propagation path. First, a Fourier transform is carried out on the temporal signal at each monitored position. This gives the spectral information for each position. A spatial Fourier transform is then carried out at all given frequencies, which gives the spatial spectrum (wavenumber).

This 2-D FFT procedure separates different propagating modes from raw data in spatial-temporal domain into a frequency-wavenumber ( $f-k$  or  $\omega-k$ ) representation. The amplitude scale in the third dimension reflects the out of plane displacements and its intensity shows the energy distribution between various modes and frequencies. Similar data manipulation is also carried out by other researchers, e.g. in [115, 121]. The 2-D FFT used in current work is calculated by specialized software.

## References

1. Vasiliev, Valery V., and Evgeny V. Morozov. "Chapter 3 - Mechanics of a Unidirectional Ply." In *Advanced Mechanics of Composite Materials (Third Edition)*, 53–124. Boston: Elsevier, 2013.
2. Ashby, Michael F., and David R. H. Jones. "Part B: The Elastic Moduli." In *Engineering Materials 1 (Fourth Edition)*, 29–82. Boston: Butterworth-Heinemann, 2012.
3. Daniel, Isaac M., and Ori Ishai. *Engineering Mechanics of Composite Materials (Second Edition)*. New York: Oxford University Press, 2006.
4. Scott, I. G., and C. M. Scala. "A Review of Non-Destructive Testing of Composite Materials." *NDT International* 15, no. 2 (April 1982): 75–86.
5. Kinra, Vikram K., and Vinay Dayal. "Ultrasonic Nondestructive Evaluation of Fibre-Reinforced Composite Materials — a Review." *Sadhana* 11, no. 3–4 (December 1, 1987): 419–32.
6. Reynolds, W. N. "Recent European Work on the NDT of Composite Materials." *Materials & Design* 9, no. 4 (July 1988): 183–91.
7. Adams, R. D., and P. Cawley. "A Review of Defect Types and Nondestructive Testing Techniques for Composites and Bonded Joints." *NDT International* 21, no. 4 (August 1988): 208–22.
8. Cantwell, W. J., and J. Morton. "The Significance of Damage and Defects and Their Detection in Composite Materials: A Review." *The Journal of Strain Analysis for Engineering Design* 27, no. 1 (January 1, 1992): 29–42.
9. Yolken, H. Thomas, and George A. Matzkanin. Nondestructive Evaluation of Advanced Fiber Reinforced Polymer Matrix Composites: A Technology Assessment, *NASA/CR-2009-215566*, February 1, 2009.
10. Ibrahim, M. E. "Nondestructive Evaluation of Thick-Section Composites and Sandwich Structures: A Review." *Composites Part A: Applied Science and Manufacturing* 64 (September 2014): 36–48.
11. E07 Committee. ASTM E2533 – 09. Guide for Nondestructive Testing of Polymer Matrix Composites Used in Aerospace Applications. ASTM International, 2009.
12. Cuadra, Jefferson, Prashanth A. Vanniamparambil, Kavan Hazeli, Ivan Bartoli, and Antonios Kontsos. "Damage Quantification in Polymer Composites Using a Hybrid NDT Approach." *Composites Science and Technology* 83 (June 28, 2013): 11–21.
13. Pagnotta, Leonardo. "Recent Progress in Identification Methods for the Elastic Characterization of Materials." *International Journal of Mechanics* 4, no. 2 (2008): 129–40.
14. Su, Zhongqing, Lin Ye, and Ye Lu. "Guided Lamb Waves for Identification of Damage in Composite Structures: A Review." *Journal of Sound and Vibration* 295, no. 3–5 (August 22, 2006): 753–80.
15. Broda, D., W. J. Staszewski, A. Martowicz, T. Uhl, and V. V. Silberschmidt. "Modelling of Nonlinear Crack-wave Interactions for Damage Detection Based on

- ultrasound—A Review.” *Journal of Sound and Vibration* 333, no. 4 (February 14, 2014): 1097–1118.
16. Beaumont, Peter W. R. “On the Problems of Cracking and the Question of Structural Integrity of Engineering Composite Materials.” *Applied Composite Materials* 21, no. 1 (February 1, 2014): 5–43.
  17. ISO/TC 61/SC 13 Committee. ISO 14125:1998(en). Fibre-Reinforced Plastic Composites — Determination of Flexural Properties. ISO, 1998.
  18. ISO/TC 61/SC 2 Committee. ISO 527-1:2012(en). Plastics — Determination of Tensile Properties — Part 1: General Principles. ISO, 2012.
  19. D30 Committee. ASTM D7264 / D7264M – 07. Test Method for Flexural Properties of Polymer Matrix Composite Materials. ASTM International, 2007.
  20. D30 Committee. ASTM D3039 / D3039M – 14. Test Method for Tensile Properties of Polymer Matrix Composite Materials. ASTM International, 2014.
  21. Leif A. Carlsson, Donald F. Adams, and R. Byron Pipes. *Experimental Characterization of Advanced Composite Materials*, Third Edition. CRC Press, 2002.
  22. Hodgkinson, J M, ed. *Mechanical Testing of Advanced Fibre Composites*. Woodhead Publishing Series in Composites Science and Engineering. Woodhead Publishing, 2000.
  23. Tarnopol’skii, Yu M., and V. L. Kulakov. “Tests Methods for Composites. Survey of Investigations Carried out in the PMI of Latvian Academy of Sciences in 1964-2000.” *Mechanics of Composite Materials* 37, no. 5–6 (September 1, 2001): 431–48.
  24. Sheldon M. Wiederhorn, Richard J. Fields, Samuel Low, Gun-Woong Bahng, Alois Wehrsted, Junhee Hahn, Yo Tomota, *et al.* “Springer Handbook of Materials Measurement Methods. 7. Mechanical Properties.” In *Springer Handbook of Materials Measurement Methods*, edited by Horst Czichos, Tetsuya Saito, and Leslie Smith. Springer Science & Business Media, 2006.
  25. Ng, Yeow-Cheong. “Deriving Composite Lamina Properties from Laminate Properties Using Classical Lamination Theory and Failure Criteria.” *Journal of Composite Materials* 39, no. 14 (July 1, 2005): 1295–1306.
  26. Andreas T. Echtermeyer. *Laminate Theory Manual*. DNV Research, 1991.
  27. Lecompte, David, Arwen Smits, Hugo Sol, John Vantomme, and Danny Van Hemelrijck. “Mixed Numerical–experimental Technique for Orthotropic Parameter Identification Using Biaxial Tensile Tests on Cruciform Specimens.” *International Journal of Solids and Structures* 44, no. 5 (March 1, 2007): 1643–56.
  28. Gurvich, Mark R., and Patrick L. Clavette. “Probabilistic Characterization of Elastic Properties of Composites Using Digital Image Correlation Technique.” In *Composite Materials and Joining Technologies for Composites, Volume 7*, edited by Eann Patterson, David Backman, and Gary Cloud, 93–98. New York, NY: Springer New York, 2013.
  29. Pagnotta, Leonardo. “Determining Elastic Constants of Materials with Interferometric Techniques.” *Inverse Problems in Science and Engineering* 14, no. 8 (December 1, 2006): 801–18.

30. Caminero, M. A., M. Lopez-Pedrosa, C. Pinna, and C. Soutis. "Damage Assessment of Composite Structures Using Digital Image Correlation." *Applied Composite Materials* 21, no. 1 (February 1, 2014): 91–106.
31. Kam, T. Y., C. M. Chen, and S. H. Yang. "Material Characterization of Laminated Composite Materials Using a Three-Point-Bending Technique." *Composite Structures* 88, no. 4 (May 2009): 624–28.
32. Munjal, A.K. "Test Methods for Determining Design Allowables for Fiber Reinforced Composites." In *Test Methods and Design Allowables for Fiber Composites: Second Symposium*, edited by C.C Chamis, 93–110. ASTM International, 1989.
33. Hart-Smith, L.J. "Some Observations About Test Specimens and Structural Analysis for Fibrous Composites." In *Composite Materials: Testing and Design (Ninth Volume)*, edited by S.P Garbo, 86–120. ASTM International, 1990.
34. Adams, Donald F. "5.06 - Test Methods for Mechanical Properties." In *Comprehensive Composite Materials*, edited by Anthony Kelly and Carl Zweben, 113–48. Oxford: Pergamon, 2000.
35. Joseph R. Davis. *Tensile Testing, 2nd Edition*. ASM International, 2004.
36. MIL-HDBK-17-1F Composite Materials Handbook. Volume 1. Polymer Matrix Composites. Guidelines for Characterization of Structural Materials. USA Department of Defense, 2002.
37. Hart-Smith, L. J. "5.07 - Backing-out Composite Lamina Strengths from Cross-Ply Testing." In *Comprehensive Composite Materials*, edited by Anthony Kelly and Carl Zweben, 149–61. Oxford: Pergamon, 2000.
38. Welsh, J.S, and D.F Adams. "Unidirectional Composite Compression Strengths Obtained by Testing Cross-Ply Laminates." *Journal of Composites Technology and Research* 18, no. 4 (1996): 241.
39. Carlsson, L. A., D. F. Adams, and R. B. Pipes. "Basic Experimental Characterization of Polymer Matrix Composite Materials." *Polymer Reviews* 53, no. 2 (April 18, 2013): 277–302.
40. Ghaemi, Hamid, and Zouheir Fawaz. "Experimental Evaluation of Effective Tensile Properties of Laminated Composites." *Advanced Composite Materials* 11, no. 3 (January 1, 2002): 223–37.
41. Hyer, M. W. *Stress Analysis of Fiber-Reinforced Composite Materials*. WCB McGraw-Hill, 1998.
42. A.H.J. Nijhof. "7 - Analysis of Laminated Composites." In *Composite Materials in Maritime Structures*, edited by R. A. Sheno and J. F. Wellicome, 1:172–204. Cambridge: Cambridge University Press, 1993.
43. Nettles, A. T. *NASA Reference Publication 1351. Basic Mechanics of Laminated Composite Plates*. National Aeronautics and Space Administration MSFC, October 1994.
44. Van Vinckenroy, G., and W. P. de Wilde. "The Use of Monte Carlo Techniques in Statistical Finite Element Methods for the Determination of the Structural Behaviour of Composite Materials Structural Components." *Composite Structures*, Eighth International Conference on Composite Structures, 32, no. 1–4 (1995): 247–53.



45. Shaw, Andrew, Srinivas Sriramula, Peter D. Gosling, and Marios K. Chryssanthopoulos. "A Critical Reliability Evaluation of Fibre Reinforced Composite Materials Based on Probabilistic Micro and Macro-Mechanical Analysis." *Composites Part B: Engineering* 41, no. 6 (September 2010): 446–53.
46. Gayathri, P., K. Umesh, and R. Ganguli. "Effect of Matrix Cracking and Material Uncertainty on Composite Plates." *Reliability Engineering & System Safety* 95, no. 7 (July 2010): 716–28.
47. Sarangapani, G., and Ranjan Ganguli. "Effect of Ply-Level Material Uncertainty on Composite Elastic Couplings in Laminated Plates." *International Journal for Computational Methods in Engineering Science and Mechanics* 14, no. 3 (January 23, 2013): 244–61.
48. Lekou, D. J., and T. P. Philippidis. "Mechanical Property Variability in FRP Laminates and Its Effect on Failure Prediction." *Composites Part B: Engineering* 39, no. 7–8 (October 2008): 1247–56.
49. Berg, C.A, J Tirosh, and M Israeli. "Analysis of Short Beam Bending of Fiber Reinforced Composites." In *Composite Materials: Testing and Design (Second Conference)*, edited by H.T Corten, 206–18. ASTM International, 1972.
50. Stinchcomb, W.W, E.G Henneke, and H.L Price. "Use of the Short-Beam Shear Test for Quality Control of Graphite-Polyimide Laminates." In *Reproducibility and Accuracy of Mechanical Tests*, edited by J.M Holt, 96–109. ASTM International, 1977.
51. Adams, Donald F., Todd R. King, and Donald M. Blackketter. "Evaluation of the Transverse Flexure Test Method for Composite Materials." *Composites Science and Technology* 39, no. 4 (1990): 341–53.
52. Zweben, C, W.S Smith, and M.W Wardle. "Test Methods for Fiber Tensile Strength, Composite Flexural Modulus, and Properties of Fabric-Reinforced Laminates." In *Fifth Conference on Composite Materials: Testing and Design*, edited by S.W Tsai, 228–62. ASTM International, 1979.
53. Whitney, James M. *Structural Analysis of Laminated Anisotropic Plates*. CRC Press, 1987.
54. Berube, Keith A., and Roberto A. Lopez-Anido. "Variability in the Material Properties of Polymer Matrix Composites for Marine Structures." *Journal of ASTM International* 7, no. 4 (2010): 1–18.
55. E28 Committee. ASTM E1875 - 13. Test Method for Dynamic Youngs Modulus, Shear Modulus, and Poisson's Ratio by Sonic Resonance. ASTM International, 2008.
56. E28 Committee. ASTM E1876 - 09. Test Method for Dynamic Youngs Modulus, Shear Modulus, and Poisson's Ratio by Impulse Excitation of Vibration. ASTM International, 2009.
57. Technical Committee CEN/TC 184. EN 843-2. Advanced Technical Ceramics. Mechanical Properties of Monolithic Ceramics at Room Temperature. Part 2: Determination of Young's Modulus, Shear Modulus and Poisson's Ratio. CEN, 2006.
58. Larsson, P.-O. "Determination of Young's and Shear Moduli from Flexural Vibrations of Beams." *Journal of Sound and Vibration* 146, no. 1 (April 8, 1991): 111–23.

59. Viens, Michael J., and Jeffrey J. Johnson. NASA Technical Memorandum 104629. Determination of Elastic Moduli of Fiber-Resin Composites Using an Impulse Excitation Technique, February 1, 1996.
60. McIntyre, M. E., and Woodhouse, J. "On Measuring the Elastic and Damping Constants of Orthotropic Sheet Materials." *Acta Metall.* 36, no. 6 (1988): 1397–1416.
61. Fällström, K.-E., and M. Jonsson. "A Nondestructive Method to Determine Material Properties in Anisotropic Plates." *Polymer Composites* 12, no. 5 (October 1, 1991): 293–305.
62. Pedersen, P., and P. S Frederiksen. "Identification of Orthotropic Material Moduli by a Combined Experimental/numerical Method." *Measurement* 10, no. 3 (July 1992): 113–18.
63. Soares, C.M. Mota, M. Moreira de Freitas, A.L. Araújo, and P. Pedersen. "Identification of Material Properties of Composite Plate Specimens." *Composite Structures* 25, no. 1–4 (1993): 277–85.
64. Araújo, A. L., C. M. Mota Soares, and M. J. Moreira de Freitas. "Characterization of Material Parameters of Composite Plate Specimens Using Optimization and Experimental Vibrational Data." *Composites Part B: Engineering* 27, no. 2 (1996): 185–91.
65. Frederiksen, Per S. "Application of an Improved Model for the Identification of Material Parameters." *Mechanics of Composite Materials and Structures* 4, no. 4 (October 1, 1997): 297–316.
66. Gibson, Ronald F., and Emmanuel O. Ayorinde. "Method and Apparatus for Non-Destructive Measurement of Elastic Properties of Structural Materials," July 9, 1996. <http://www.google.com/patents/US5533399>.
67. Gibson, Ronald F. "Modal Vibration Response Measurements for Characterization of Composite Materials and Structures." *Composites Science and Technology* 60, no. 15 (November 2000): 2769–80.
68. Rikards, R., and A. Chate. "Identification of Mechanical Properties of Composites Based on Design of Experiments." *Mechanics of Composite Materials* 34, no. 1 (January 1, 1998): 1–11.
69. Rikards, R., and A. Chate. "Identification of Elastic Properties of Composites by Method of Planning of Experiments." *Composite Structures* 42, no. 3 (July 1998): 257–63.
70. Rikards, R., A. Chate, W. Steinchen, A. Kessler, and A. K. Bledzki. "Method for Identification of Elastic Properties of Laminates Based on Experiment Design." *Composites Part B: Engineering* 30, no. 3 (April 1999): 279–89.
71. Bledzki, A. K., A. Kessler, R. Rikards, and A. Chate. "Determination of Elastic Constants of Glass/epoxy Unidirectional Laminates by the Vibration Testing of Plates." *Composites Science and Technology* 59, no. 13 (October 1999): 2015–24.
72. R. Rikards. "Method for Identification of Elastic Properties of Laminates." In *Inverse Problems in Engineering Mechanics II*, edited by G. S. Dulikravich and Mana Tanaka. Elsevier, 2000.

73. Rikards, R, A Chate, and G Gailis. "Identification of Elastic Properties of Laminates Based on Experiment Design." *International Journal of Solids and Structures* 38, no. 30–31 (July 2001): 5097–5115.
74. Rikards, R., H. Abramovich, T. Green, J. Auzins, and A. Chate. "Identification of Elastic Properties of Composite Laminates." *Mechanics of Advanced Materials and Structures* 10, no. 4 (October 1, 2003): 335–52.
75. Akishin, Pavel, Andrejs Kovalovs, and Evgeny Barkanov. "Non-Destructive Technique for Determination of Elastic Material Properties." *Construction Science* 14 (2013): 13–19.
76. Lauwagie, Tom, Hugo Sol, Gert Roebben, Ward Heylen, Yinming Shi, and Omer Van der Biest. "Mixed Numerical–experimental Identification of Elastic Properties of Orthotropic Metal Plates." *NDT & E International* 36, no. 7 (October 2003): 487–95.
77. Gsell, D., G. Feltrin, S. Schubert, R. Steiger, and M. Motavalli. "Cross-Laminated Timber Plates: Evaluation and Verification of Homogenized Elastic Properties." *Journal of Structural Engineering* 133, no. 1 (2007): 132–38.
78. Cunha, Jesiel, Scott Cogan, and Christophe C. "Application of Genetic Algorithms for the Identification of Elastic Constants of Composite Materials from Dynamic Tests." *International Journal for Numerical Methods in Engineering* 45, no. 7 (July 10, 1999): 891–900.
79. Teixeira Silva, Mariana Ferreira, Lavinia Maria Sanabio Alves Borges, Fernando Alves Rochinha, and Luís Alfredo Vidal De Carvalho. "A Genetic Algorithm Applied to Composite Elastic Parameters Identification." *Inverse Problems in Science and Engineering* 12, no. 1 (February 1, 2004): 17–28.
80. He, Rong-Song, and Shun-Fa Hwang. "Damage Detection by an Adaptive Real-Parameter Simulated Annealing Genetic Algorithm." *Computers & Structures* 84, no. 31–32 (December 2006): 2231–43.
81. Hwang, Shun-Fa, Jen-Chih Wu, and Rong-Song He. "Identification of Effective Elastic Constants of Composite Plates Based on a Hybrid Genetic Algorithm." *Composite Structures* 90, no. 2 (September 2009): 217–24.
82. Beluch, Witold. "Evolutionary Identification and Optimization of Composite Structures." *Mechanics of Advanced Materials and Structures* 14, no. 8 (November 16, 2007): 677–86.
83. L. Gaul, K. Willner, and S. Hurlbaas. "Determination of Material Properties of Plates from Modal ESPI Measurements." *Proc. 17th International Modal Analysis Conference*, 1999, 1756–63.
84. Hwang, Shun-Fa, and Chao-Shui Chang. "Determination of Elastic Constants of Materials by Vibration Testing." *Composite Structures* 49, no. 2 (June 2000): 183–90.
85. Jones, Robert M. *Mechanics Of Composite Materials (2nd Ed.)*. Taylor & Francis, 1999.
86. A.J.M. Ferreira. "Chapter 13 – Laminated Plates." In *MATLAB Codes for Finite Element Analysis*, 203–30. Solid Mechanics and Its Applications 157. Springer Netherlands, 2009.
87. Abaqus 6.12. Analysis User's Manual. Volume IV: Elements. Dassault Systèmes SIMULIA, 2012.

88. Tittmann, Bernhard R., and Robert L. Crane. "5.12 - Ultrasonic Inspection of Composites." In *Comprehensive Composite Materials*, edited by Carl Zweben and Anthony Kelly, 259–320. Oxford: Pergamon, 2000.
89. C08 Committee. ASTM C1419 - 14. Standard Test Method for Sonic Velocity in Refractory Materials at Room Temperature and Its Use in Obtaining an Approximate Youngs Modulus. ASTM International, 2014.
90. E07 Committee. ASTM E494 - 10. Standard Practice for Measuring Ultrasonic Velocity in Materials. ASTM International, 2010.
91. Chimenti, Dale E., and Yoseph Bar-Cohen. "Properties of Composite Laminates Using Leaky Lamb Waves," June 23, 1987. <http://www.google.com/patents/US4674334>.
92. Lareau, John P., and Mark V. Brook. "Lamb Wave Ultrasonic Probe for Crack Detection and Measurement in Thin-Walled Tubing," June 16, 1998. <http://www.google.com/patents/US5767410>.
93. Wang, Weicheng David. "Ultrasonic Lamb Wave Technique for Measurement of Pipe Wall Thickness at Pipe Supports," October 12, 1999. <http://www.google.com/patents/US5965818>.
94. Lichtenwalner, Peter F., James P. Dunne, Ronald S. Becker, and Erwin W. Baumann. "Active Damage Interrogation Method for Structural Health Monitoring," December 21, 1999. <http://www.google.com/patents/US6006163>.
95. Giurgiutiu, Victor, Jingjing Bao, and Andrei N. Zagari. "Structural Health Monitoring System Utilizing Guided Lamb Waves Embedded Ultrasonic Structural Radar," February 7, 2006. <http://www.google.com/patents/US6996480>.
96. Kessler, Seth S., Christopher T. Dunn, and Dong-Jin Shim. "Triangulation with Co-Located Sensors," May 19, 2009. <http://www.google.com/patents/US7533578>.
97. Kim, Hyeung-Yun. "Systems and Methods for Identifying Damage in a Structure," September 15, 2009. <http://www.google.com/patents/US7590510>.
98. Dunne, James P. "Identification of Lamb Wave Modes," March 25, 2014. <http://www.google.com/patents/US8677825>.
99. Rose, Joseph L. *Ultrasonic Waves in Solid Media*. Cambridge; New York: Cambridge University Press, 1999.
100. Lempriere, Brian M. *Ultrasound and Elastic Waves. Frequently Asked Questions*. Burlington: Academic Press, 2003.
101. Dean, G. D. "Use of Plate Bending Waves for Elastic Property Determination of Polymers." *Composites* 20, no. 6 (November 1989): 575–83.
102. Tang, B., and E. G. Henneke. "Long Wavelength Approximation for Lamb Wave Characterization of Composite Laminates." *Research in Nondestructive Evaluation* 1, no. 1 (March 1, 1989): 51–64.
103. Hosten, Bernard. "Elastic Characterization of Orthotropic Composite Materials from Ultrasonic Inspection through Non-Principal Planes." In *Review of Progress in Quantitative Nondestructive Evaluation*, edited by Donald O. Thompson and Dale E. Chimenti, 1437–44. Springer US, 1991.

104. Hosten, Bernard, David A. Hutchins, and David W. Schindel. "Measurement of Elastic Constants in Composite Materials Using Air-coupled Ultrasonic Bulk Waves." *The Journal of the Acoustical Society of America* 99, no. 4 (April 1, 1996): 2116–23.
105. Prosser, William H. "The Propagation Characteristics of the Plate Modes of Acoustic Emission Waves in Thin Aluminum Plates and Thin Graphite/Epoxy Composite Plates and Tubes." PhD Thesis, Johns Hopkins University, 1991.
106. Rogers, W. P. "Elastic Property Measurement Using Rayleigh-Lamb Waves." *Research in Nondestructive Evaluation* 6, no. 4 (December 1, 1995): 185–208.
107. Wu, T. -T., and Y. -H. Liu. "On the Measurement of Anisotropic Elastic Constants of Fiber-Reinforced Composite Plate Using Ultrasonic Bulk Wave and Laser Generated Lamb Wave." *Ultrasonics* 37, no. 6 (September 1999): 405–12.
108. Castaings, M., B. Hosten, and T. Kundu. "Inversion of Ultrasonic, Plane-Wave Transmission Data in Composite Plates to Infer Viscoelastic Material Properties." *NDT & E International* 33, no. 6 (September 2000): 377–92.
109. Reverdy, F., and B. Audoin. "Elastic Constants Determination of Anisotropic Materials from Phase Velocities of Acoustic Waves Generated and Detected by Lasers." *The Journal of the Acoustical Society of America* 109, no. 5 (May 1, 2001): 1965–72.
110. Xi, Z, and G Liu. "Chapter 18. Inverse Determination of Material Constants of Composite Laminates." In *Elastic Waves in Anisotropic Laminates*. CRC Press, 2001.
111. Liu, G. R, W. B Ma, and X Han. "An Inverse Procedure for Determination of Material Constants of Composite Laminates Using Elastic Waves." *Computer Methods in Applied Mechanics and Engineering* 191, no. 33 (June 21, 2002): 3543–54.
112. Rose, Joseph L. "A Baseline and Vision of Ultrasonic Guided Wave Inspection Potential." *Journal of Pressure Vessel Technology* 124, no. 3 (July 26, 2002): 273–82.
113. Giurgiutiu, Victor, Andrei Zagari, and JingJing Bao. "Embedded Active Sensors for In-Situ Structural Health Monitoring of Thin-Wall Structures." *Journal of Pressure Vessel Technology* 124, no. 3 (July 26, 2002): 293–302.
114. Van Otterloo, Douglas L., and Vinay Dayal. "How Isotropic Are Quasi-Isotropic Laminates." *Composites Part A: Applied Science and Manufacturing* 34, no. 1 (January 2003): 93–103.
115. Gao, Weimin, Christ Glorieux, and Jan Thoen. "Laser Ultrasonic Study of Lamb Waves: Determination of the Thickness and Velocities of a Thin Plate." *International Journal of Engineering Science* 41, no. 2 (January 2003): 219–28.
116. Lowe, M. J. S., P. Cawley, and B. N. Pavlakovic. "A General Purpose Computer Model for Calculating Elastic Waveguide Properties, with Application to Non-Destructive Testing." In *Surface Waves in Anisotropic and Laminated Bodies and Defects Detection*, edited by Robert V. Goldstein and Gerard A. Maugin, 241–56. NATO Science Series II: Mathematics, Physics and Chemistry 163. Springer Netherlands, 2005.
117. Gómez, P., J.P. Fernandez, and P.D. García. "Lamb Waves and Dispersion Curves in Plates and It's Applications in NDE Experiences Using Comsol Multiphys." *Proceedings of the 2011 Comsol Conference*, 2011.

118. Predoi, Mihai V., Michel Castaings, Bernard Hosten, and Christophe Bacon. "Wave Propagation along Transversely Periodic Structures." *The Journal of the Acoustical Society of America* 121, no. 4 (April 1, 2007): 1935–44.
119. Vishnuvardhan, J., C. V. Krishnamurthy, and Krishnan Balasubramaniam. "Genetic Algorithm Reconstruction of Orthotropic Composite Plate Elastic Constants from a Single Non-Symmetric Plane Ultrasonic Velocity Data." *Composites Part B: Engineering* 38, no. 2 (March 2007): 216–27.
120. Vishnuvardhan, J., C. V. Krishnamurthy, and Krishnan Balasubramaniam. "Blind Inversion Method Using Lamb Waves for the Complete Elastic Property Characterization of Anisotropic Plates." *The Journal of the Acoustical Society of America* 125, no. 2 (February 1, 2009): 761–71.
121. Tian, Zhenhua, and Lingyu Yu. "Lamb Wave Propagation Study Using Frequency-Wavenumber Analysis," *Proceedings of SMASIS2012*, September 19, 2012, 713–21.
122. Glushkov, Evgeny, Natalia Glushkova, and Artem Eremin. "Efficient Mathematical Representations for Computing the Forced Wave Dynamics of Anisotropic Laminated Composites." *CEAS Aeronautical Journal* 4, no. 1 (April 1, 2013): 11–19.
123. Alleyne, D., and P. Cawley. "A Two-Dimensional Fourier Transform Method for the Measurement of Propagating Multimode Signals." *The Journal of the Acoustical Society of America* 89, no. 3 (March 1, 1991): 1159–68.
124. Rhee, Sang-Ho, Jeong-Ki Lee, and Jung-Ju Lee. "The Group Velocity Variation of Lamb Wave in Fiber Reinforced Composite Plate." *Ultrasonics* 47, no. 1–4 (December 2007): 55–63.
125. Karim, M. R., A. K. Mal, and Y. Bar-Cohen. "Inversion of Leaky Lamb Wave Data by Simplex Algorithm." *The Journal of the Acoustical Society of America* 88, no. 1 (July 1, 1990): 482–91.
126. Lasn, K., A. Klauson, F. Chati, and D. Décultot. "Experimental Determination of Elastic Constants of an Orthotropic Composite Plate by Using Lamb Waves." *Mechanics of Composite Materials* 47, no. 4 (September 1, 2011): 435–46.
127. Tinel, A., and J. Duclos. "New Scholte Wave Emitter: Application to Nondestructive Evaluation." *Review of Scientific Instruments* 64, no. 12 (December 1, 1993): 3651–52.
128. Desmet, C., V. Gusev, W. Lauriks, C. Glorieux, and J. Thoen. "Laser-induced Thermoelastic Excitation of Scholte Waves." *Applied Physics Letters* 68, no. 21 (May 20, 1996): 2939–41.
129. Meegan, G. D., M. F. Hamilton, Yu A. Il'inskii, and E. A. Zabolotskaya. "Nonlinear Stoneley and Scholte Waves." *The Journal of the Acoustical Society of America* 106, no. 4 (October 1, 1999): 1712–23.
130. Glorieux, Christ, Kris Van de Rostyne, Keith Nelson, Weimin Gao, Walter Lauriks, and Jan Thoen. "On the Character of Acoustic Waves at the Interface between Hard and Soft Solids and Liquids." *The Journal of the Acoustical Society of America* 110, no. 3 (September 1, 2001): 1299–1306.
131. Glorieux, C., K. Van de Rostyne, J. D. Beers, W. Gao, S. Petillion, N. Van Riet, K. A. Nelson, *et al.* "Acoustic Waves at Interfaces Studied by Laser Ultrasonics (invited)." *Review of Scientific Instruments* 74, no. 1 (January 1, 2003): 465–69.

132. Ruo-Long, Peng, and Qian Meng-Lu. "Scholte Wave at Air-Metal Interface Generated by a Pulsed Disc-Like Source." *Chinese Physics Letters* 22, no. 9 (September 1, 2005): 2342.
133. Zhao, Yan, Zhonghua Shen, Jian Lu, and Xiaowu Ni. "Laser-Induced Scholte Wave Detection at Air-Solid Interfaces by Beam Deflection Technique." *Optical Engineering* 46, no. 2 (2007): 024302–024302 – 5.
134. Jenot, F., M. Ouaftouh, M. Duquennoy, and M. Ourak. "Interferometric Detection of Acoustic Waves at Air-Solid Interface Applications to Non-Destructive Testing." *Journal of Applied Physics* 97, no. 9 (May 1, 2005): 094905.
135. Dong, Hefeng, and Jens M. Hovem. "Ch. 6. Interface Waves." In *Waves in Fluids and Solids*, edited by Ruben Pico Vila. InTech, 2011.
136. Sakharov, V. E., S. A. Kuznetsov, B. D. Zaitsev, I. E. Kuznetsova, and S. G. Joshi. "Liquid Level Sensor Using Ultrasonic Lamb Waves." *Ultrasonics* 41, no. 4 (June 2003): 319–22.
137. Song, Hyeong-Doo, Seung Hyun Cho, Insu Jeon, and Chang-Doo Kee. "A Sensing Medium Exchangeable Hydrogen Sensor Using Lamb Waves." *Sensors and Actuators B: Chemical* 162, no. 1 (February 20, 2012): 348–52. doi:10.1016/j.snb.2011.12.095.
138. Yu, Lingyu, Zhenhua Tian, and Liuxian Zhao. "Gas Accumulation Detection in a Water Tank Using Lamb Waves," Proceedings of the ASME 2012 Conference on Smart Materials, Adaptive Structures and Intelligent Systems, 2012.
139. Cegla, F. B., P. Cawley, and M. J. S. Lowe. "Material Property Measurement Using the Quasi-Scholte mode — A Waveguide Sensor." *The Journal of the Acoustical Society of America* 117, no. 3 (March 1, 2005): 1098–1107.
140. Li, Xian-Fang. "On Approximate Analytic Expressions for the Velocity of Rayleigh Waves." *Wave Motion* 44, no. 2 (December 2006): 120–27.
141. Cerv, J., and J. Plešek. "Implicit and Explicit Secular Equations for Rayleigh Waves in Two-Dimensional Anisotropic Media." *Wave Motion, Advanced Modelling of Wave Propagation in Solids*, 50, no. 7 (November 2013): 1105–17.
142. Worden, K. "Rayleigh and Lamb Waves - Basic Principles." *Strain* 37, no. 4 (November 1, 2001): 167–72.
143. Highsmith, AL, and KL Reifsnider. "Stiffness-Reduction Mechanisms in Composite Laminates." In *Damage in Composite Materials: Basic Mechanisms, Accumulation, Tolerance, and Characterization, ASTM STP 775*, edited by KL Reifsnider, 103–17. ASTM International, 1982.
144. Daniel, I. M., and A. Charewicz. "Fatigue Damage Mechanisms and Residual Properties of Graphite/epoxy Laminates." *Engineering Fracture Mechanics* 25, no. 5–6 (1986): 793–808.
145. *Offshore Standard DNV-OS-C501 "Composite Components."* Det Norske Veritas AS, November 2013. exchange.dnv.com.
146. Brøndsted, P., S. I. Andersen, and H. Lilholt. "Fatigue Performance of Glass/polyester Laminates and the Monitoring of Material Degradation." *Mechanics of Composite Materials* 32, no. 1 (January 1, 1996): 21–29.

147. Li, Chingshen, F. Ellyin, and A. Wharmby. "A Damage Meso-Mechanical Approach to Fatigue Failure Prediction of Cross-Ply Laminate Composites." *International Journal of Fatigue* 24, no. 2–4 (February 2002): 429–35.
148. Li, Chingshen, Fernand Ellyin, and Alan Wharmby. "On Matrix Crack Saturation in Composite Laminates." *Composites Part B: Engineering* 34, no. 5 (July 1, 2003): 473–80.
149. Adden, S., K. Pfleiderer, I. Solodov, P. Horst, and G. Busse. "Characterization of Stiffness Degradation Caused by Fatigue Damage in Textile Composites Using Circumferential Plate Acoustic Waves." *Composites Science and Technology* 68, no. 7–8 (June 2008): 1616–23.
150. Rheinforth, M., F. Schmidt, D. Döring, I. Solodov, G. Busse, and P. Horst. "Air-Coupled Guided Waves Combined with Thermography for Monitoring Fatigue in Biaxially Loaded Composite Tubes." *Composites Science and Technology* 71, no. 5 (March 22, 2011): 600–608.
151. Rheinforth, Martin, Nils Kosmann, Dorothee Sauer, Gerd Busse, and Karl Schulte. "Lamb Waves for Non-Contact Fatigue State Evaluation of Composites under Various Mechanical Loading Conditions." *Composites Part A: Applied Science and Manufacturing* 43, no. 8 (August 2012): 1203–11.
152. Morris, GE. "Determining Fracture Directions and Fracture Origins on Failed Graphite/Epoxy Surfaces." In *Nondestructive Evaluation and Flaw Criticality for Composite Materials, ASTM STP 696*, edited by RB Pipes, 274–297. ASTM International, 1979.
153. Smith, P. A, and S. L Ogin. "On Transverse Matrix Cracking in Cross-Ply Laminates Loaded in Simple Bending." *Composites Part A: Applied Science and Manufacturing* 30, no. 8 (August 1999): 1003–8.
154. Adden, Stephan, and Peter Horst. "Stiffness Degradation under Fatigue in Multiaxially Loaded Non-Crimped-Fabrics." *International Journal of Fatigue*, Fourth International Conference on Fatigue of Composites (ICFC4), 32, no. 1 (January 2010): 108–22.
155. Salawu, O. S. "Detection of Structural Damage through Changes in Frequency: A Review." *Engineering Structures* 19, no. 9 (September 1997): 718–23.
156. Scott W. Doebling, Charles R. Farrar, Michael B. Prime, and Daniel W. Shevitz. LA-13070-MS. *Damage Identification and Health Monitoring of Structural and Mechanical Systems from Changes in Their Vibration Characteristics: A Literature Review*. Los Alamos National Laboratory, 1996.
157. Bedewi, N. E., and D. N. Kung. "Effect of Fatigue Loading on the Modal Properties of Composite Structures and Its Utilization for Prediction of Residual Life." *Composite Structures* 37, no. 3–4 (March 1997): 357–71.
158. Birman, V, and L. W Byrd. "Matrix Cracking in Transverse Layers of Cross-Ply Beams Subjected to Bending and Its Effect on Vibration Frequencies." *Composites Part B: Engineering* 32, no. 1 (2001): 47–55.
159. Birman, Victor, and George J. Simitzes. "Vibrations of Sandwich Panels and Beams with Matrix Cracks in the Facings." *Composites Science and Technology* 61, no. 11 (August 2001): 1605–13.



160. Birman, Victor, and Larry W. Byrd. "Effect of Matrix Cracking in Cross-Ply Ceramic Matrix Composite Beams on Their Mechanical Properties and Natural Frequencies." *International Journal of Non-Linear Mechanics* 38, no. 2 (March 2003): 201–12.
161. Kessler, Seth S., S. Mark Spearing, Mauro J. Atalla, Carlos E. S. Cesnik, and Constantinos Soutis. "Damage Detection in Composite Materials Using Frequency Response Methods." *Composites Part B: Engineering* 33, no. 1 (January 2002): 87–95.
162. Moon, Tae-Chul, Hyeung-Yun Kim, and Woonbong Hwang. "Natural-Frequency Reduction Model for Matrix-Dominated Fatigue Damage of Composite Laminates." *Composite Structures* 62, no. 1 (October 2003): 19–26.
163. Yang, Taoling, Zheng Li, J. Wang, and L. Tong. "Overall Moduli and Natural Frequencies of Composite Laminates Containing Multiple Interlaminar Transverse Cracks." *Composite Structures*, Twelfth International Conference on Composite Structures, 66, no. 1–4 (October 2004): 223–30.
164. Cheng, S. H., and Chyanbin Hwu. "On-Line Measurement of Material Properties for Composite Wing Structures." *Composites Science and Technology* 66, no. 7–8 (June 2006): 1001–9.
165. Abo-Elkhier, M., A. A. Hamada, and A. Bahei El-Deen. "Prediction of Fatigue Life of Glass Fiber Reinforced Polyester Composites Using Modal Testing." *International Journal of Fatigue*, SI: Theory and experiments in fatigue lifetime assessment, 69 (December 2014): 28–35.
166. Maslov, K., and T. Kundu. "Selection of Lamb Modes for Detecting Internal Defects in Composite Laminates." *Ultrasonics* 35, no. 2 (March 1997): 141–50.
167. Castaings, M., P. Cawley, R. Farlow, and G. Hayward. "Single Sided Inspection of Composite Materials Using Air Coupled Ultrasound." *Journal of Nondestructive Evaluation* 17, no. 1 (March 1, 1998): 37–45.
168. Ghosh, T., T. Kundu, and P. Karpur. "Efficient Use of Lamb Modes for Detecting Defects in Large Plates." *Ultrasonics* 36, no. 7 (May 1998): 791–801.
169. Valdés, Sergio H. Díaz, and Costas Soutis. "Real-Time Nondestructive Evaluation of Fiber Composite Laminates Using Low-Frequency Lamb Waves." *The Journal of the Acoustical Society of America* 111, no. 5 (May 1, 2002): 2026–33.
170. Basri, R., and W. K. Chiu. "Numerical Analysis on the Interaction of Guided Lamb Waves with a Local Elastic Stiffness Reduction in Quasi-Isotropic Composite Plate Structures." *Composite Structures*, Twelfth International Conference on Composite Structures, 66, no. 1–4 (October 2004): 87–99.
171. Duflo, H., B. Morvan, and J. -L. Izbicki. "Interaction of Lamb Waves on Bonded Composite Plates with Defects." *Composite Structures* 79, no. 2 (July 2007): 229–33.
172. Predoi, Mihai V., Michel Castaings, and Ludovic Moreau. "Influence of Material Viscoelasticity on the Scattering of Guided Waves by Defects." *The Journal of the Acoustical Society of America* 124, no. 5 (November 1, 2008): 2883–94.
173. Kim, Inho, and Ratneshwar Jha. "Effect of Lamb Wave Excitation Frequency on Detection of Delamination in Composite Plates," *Proceedings of SMASIS2011*: 1-8.

174. Shen, Yanfeng, and Victor Giurgiutiu. "Simulation of Interaction Between Lamb Waves and Cracks for Structural Health Monitoring With Piezoelectric Wafer Active Sensors," *Proceedings of SMASIS2012* September 19, 2012, 615–23.
175. Ben, B. S., B. A. Ben, K. A. Vikram, and S. H. Yang. "Damage Identification in Composite Materials Using Ultrasonic Based Lamb Wave Method." *Measurement* 46, no. 2 (February 2013): 904–12.
176. Seale, Michael D., and Eric I. Madaras. "Lamb Wave Characterization of the Effects of Long-Term Thermal-Mechanical Aging on Composite Stiffness." *The Journal of the Acoustical Society of America* 106, no. 3 (September 1, 1999): 1346–52.
177. Seale, Michael D., and Eric I. Madaras. "Lamb Wave Evaluation of the Effects of Thermal-Mechanical Aging on Composite Stiffness." *Journal of Composite Materials* 34, no. 1 (January 1, 2000): 27–38.
178. Gélébart, Y., H. Duflo, and J. Duclos. "Air Coupled Lamb Waves Evaluation of the Long-Term Thermo-Oxidative Ageing of Carbon-Epoxy Plates." *NDT & E International* 40, no. 1 (January 2007): 29–34.
179. Castaings, M., and B. Hosten. "Ultrasonic Guided Waves for Health Monitoring of High-Pressure Composite Tanks." *NDT & E International* 41, no. 8 (December 2008): 648–55.
180. Dayal, Vinay, and Vikram K. Kinra. "Leaky Lamb Waves in an Anisotropic Plate. II: Nondestructive Evaluation of Matrix Cracks in Fiber-Reinforced Composites." *The Journal of the Acoustical Society of America* 89, no. 4 (April 1, 1991): 1590–98.
181. Gorman, M. R., and S. M. Ziola. "Plate Waves Produced by Transverse Matrix Cracking." *Ultrasonics* 29, no. 3 (May 1991): 245–51.
182. Shih, J.-H., A. K. Mal, and M. Vemuri. "Plate Wave Characterization of Stiffness Degradation in Composites During Fatigue." *Research in Nondestructive Evaluation* 10, no. 3 (September 1, 1998): 147–62.
183. Seale, Michael D., Barry T. Smith, and W. H. Prosser. "Lamb Wave Assessment of Fatigue and Thermal Damage in Composites." *The Journal of the Acoustical Society of America* 103, no. 5 (May 1, 1998): 2416–24.
184. Toyama, Nobuyuki, Tomonaga Okabe, Nobuo Takeda, and Teruo Kishi. "Effect of Transverse Cracks on Lamb Wave Velocity in CFRP Cross-Ply Laminates." *Journal of Materials Science Letters* 21, no. 4 (February 1, 2002): 271–73.
185. Toyama, N., T. Okabe, and N. Takeda. "Lamb Wave Evaluation and Localization of Transverse Cracks in Cross-Ply Laminates." *Journal of Materials Science* 38, no. 8 (April 1, 2003): 1765–71.
186. Toyama, N., J. Noda, and T. Okabe. "Quantitative Damage Detection in Cross-Ply Laminates Using Lamb Wave Method." *Composites Science and Technology* 63, no. 10 (August 2003): 1473–79.
187. Schmidt, F., M. Rheinfurth, P. Horst, and G. Busse. "Multiaxial Fatigue Behaviour of GFRP with Evenly Distributed or Accumulated Voids Monitored by Various NDT Methodologies." *International Journal of Fatigue* 43 (October 2012): 207–16.
188. A.S. Paipetis, D.G. Aggelis, N.M. Barkoula, T.E. Matikas, and N. Melanitis. "Chapter 44. Damage Monitoring of Composite Laminates Using Ultrasonics." In

- Emerging Technologies in Non-Destructive Testing V*, edited by Paipetis *et al.*, 281–86. CRC Press, 2012.
189. Solodov, Igor Yu. “Ultrasonics of Non-Linear Contacts: Propagation, Reflection and NDE-Applications.” *Ultrasonics* 36, no. 1–5 (February 1998): 383–90.
  190. Nagy, Peter B. “Fatigue Damage Assessment by Nonlinear Ultrasonic Materials Characterization.” *Ultrasonics* 36, no. 1–5 (February 1998): 375–81.
  191. Solodov, I. Yu., N. Krohn, and G. Busse. “CAN: An Example of Nonclassical Acoustic Nonlinearity in Solids.” *Ultrasonics* 40, no. 1–8 (May 2002): 621–25.
  192. Solodov, I., K. Pfleiderer, H. Gerhard, S. Predak, and G. Busse. “New Opportunities for NDE with Air-Coupled Ultrasound.” *NDT & E International*, Emerging Technologies in NDT - Third International Conference 3rd Emerging Technologies in NDT, 39, no. 3 (April 2006): 176–83.
  193. Kollár, László P., and George S. Springer. *Mechanics of Composite Structures*. Cambridge: Cambridge University Press, 2003.
  194. Shokrieh, Mahmood M., and Majid Jamal Omid. “Tension Behavior of Unidirectional Glass/epoxy Composites under Different Strain Rates.” *Composite Structures* 88, no. 4 (May 2009): 595–601.
  195. Shokrieh, Mahmood M., and Majid Jamal Omid. “Compressive Response of Glass–fiber Reinforced Polymeric Composites to Increasing Compressive Strain Rates.” *Composite Structures* 89, no. 4 (August 2009): 517–23.
  196. Shokrieh, Mahmood M., and Majid Jamal Omid. “Investigation of Strain Rate Effects on in-Plane Shear Properties of Glass/epoxy Composites.” *Composite Structures* 91, no. 1 (November 2009): 95–102.
  197. Shokrieh, Mahmood M., and Majid Jamal Omid. “Investigating the Transverse Behavior of Glass–Epoxy Composites under Intermediate Strain Rates.” *Composite Structures* 93, no. 2 (January 2011): 690–96.
  198. Okoli, O.I., and G.F. Smith. “High Strain Rate Characterization of a Glass/Epoxy Composite.” *Journal of Composites Technology and Research* 22, no. 1 (2000): 3–11.
  199. Lempriere, B. M. “Poisson’s Ratio in Orthotropic Materials.” *AIAA Journal* 6, no. 11 (1968): 2226–27.
  200. Staab, George H. *Laminar Composites*. Woburn: Butterworth-Heinemann, 1999.
  201. Hosten, Bernard. “Stiffness Matrix Invariants to Validate the Characterization of Composite Materials with Ultrasonic Methods.” *Ultrasonics* 30, no. 6 (1992): 365–70.
  202. “fminsearch. Find Minimum of Unconstrained Multivariable Function Using Derivative-Free Method.” Matlab online documentation, [se.mathworks.com](http://se.mathworks.com).
  203. Lagarias, J., J. Reeds, M. Wright, and P. Wright. “Convergence Properties of the Nelder-Mead Simplex Method in Low Dimensions.” *SIAM Journal on Optimization* 9, no. 1 (January 1, 1998): 112–47.
  204. Nelder, J. A., and R. Mead. “A Simplex Method for Function Minimization.” *The Computer Journal* 7, no. 4 (January 1, 1965): 308–13.
  205. He, Rong-Song, and Shun-Fa Hwang. “Damage Detection by an Adaptive Real-Parameter Simulated Annealing Genetic Algorithm.” *Computers & Structures* 84, no. 31–32 (December 2006): 2231–43.

206. Goldberg, David Edward. *Genetic Algorithms in Search, Optimization, and Machine Learning*. Addison-Wesley, 1989.
207. Krishnakumar, Kalmanje. "Micro-Genetic Algorithms For Stationary And Non-Stationary Function Optimization," *SPIE* Vol.1196:289–96, 1990.
208. Peter Kelly Senecal. *Numerical Optimization Using The GEN4 Micro Genetic Algorithm Code*. Engine Research Center. University of Wisconsin-Madison, August 2000.
209. Zhou, Zhongfu, and Kenneth D. M. Harris. "Counteracting Stagnation in Genetic Algorithm Calculations by Implementation of a Micro Genetic Algorithm Strategy." *Physical Chemistry Chemical Physics* 10, no. 48 (2008): 7262.
210. Graff, Karl F. *Wave Motion in Elastic Solids*. Courier Dover Publications, 1975.
211. Gorman, Michael R. "Plate Wave Acoustic Emission." *The Journal of the Acoustical Society of America* 90, no. 1 (July 1, 1991): 358–64.
212. D30 Committee. ASTM D3518 / D3518M - 13. Test Method for In-Plane Shear Response of Polymer Matrix Composite Materials by Tensile Test of a  $\pm 45^\circ$  Laminate. ASTM International, 2013.
213. Perillo, Giovanni. "Numerical and Experimental Investigation of Impact Behaviour of GFRP Composites." Doctoral thesis, Norwegian University of Science and Technology, 2014.

## Curriculum Vitae

Name: **KASPAR LASN**  
DOB: 24.08.1982  
Nationality: Estonian  
E-mail: kaspar.lasn@ttu.ee, kaspar.lasn@ntnu.no

### Education

2008 – ... **PhD Student** in Tallinn University of Technology (TUT) and Norwegian University of Science and Technology (NTNU), in accordance with the Cotutelle Agreement.

2011 – 2011 **Exchange student** at Norwegian University of Science and Technology (NTNU), Department of Engineering Design and Materials, Composites and Polymers group

2006 – 2008 Chalmers University of Technology (CTH), **MSc degree** in Structural Engineering, an International Master's Programme

2000 – 2006 Tallinn University of Technology (TUT), **BSc degree** in Construction Engineering, a 4-year programme. Mandatory one-year military service in 2002 – 2003

### Work experience

2012 – ... NTNU, Department of Engineering Design and Materials, Composites and Polymers group, **Researcher**. Part-time (75%) during 2012 – 2014

2008 – 2014 TUT, Faculty of Civil Engineering, Department of Mechanics, **Teaching Assistant**. Part-time (25%) during 2011 – 2014

2004 – 2006 KPME Engineering OÜ (architectural and structural design), **Engineer**

2003 – 2003 AS Renet (construction company), **Assistant Project Manager**

### Peer-reviewed publications in International Journals

Lasn, K.; Echtermeyer, A. T.; Klauson, A.; Chati, F.; Décultot, D. (2015). Comparison of laminate stiffness as measured by three experimental methods. *Polymer Testing*, 44, 143-152.

Lasn, K.; Klauson, A.; Echtermeyer, A. T. (2015). Back-calculation of ply elastic moduli for cross-ply laminates. *Mechanics of Composite Materials*, 51(1), 55-68.

Lasn, K.; Echtermeyer, A. T. (2014). Safety approach for composite pressure vessels for road transport of hydrogen. Part 1: Acceptable probability of failure and hydrogen mass. *International Journal of Hydrogen Energy*, 39(26), 14132 - 14141.

Echtermeyer, A. T.; Lasn, K. (2014). Safety approach for composite pressure vessels for road transport of hydrogen. Part 2: Safety factors and test requirements. *International Journal of Hydrogen Energy*, 39(26), 14142 - 14152.

Lasn, K.; Klauson, A.; Chati, F.; Décultot, D. (2011). Experimental determination of elastic constants of an orthotropic composite plate by using Lamb waves. *Mechanics of Composite Materials*, 47(4), 435 - 446.

### Published dissertations

Jaramillo De Leon, O.; Lasn, K. (2008). Dynamics of railway bridges subjected to high-speed trains. SDOF models for the approximate evaluation of resonance, Chalmers University of Technology. Chalmers reproservice/ Department of Civil and Environmental Engineering.

### Conference presentations

Maze, G.; Chati, F.; Léon F.; Décultot D.; Lasn, K.; Klauson, A.; Echtermeyer, A. T. (2014). Characterization of a composite plate immersed in water by acoustic scattering. *5th International Symposium on Aircraft Materials (ACMA 2014)*, Marrakech, Morocco, April 23-26, 2014.

Lasn, K.; Klauson, A. (2011). Non-destructive identification of elastic constants by vibration measurements and optimization. In: *OAS 2011: International Conference on Optimization and Analysis of Structures*, August 25-27, Tartu, Estonia. (Eds.)E. Puman, J. Lellep., 2011, 22 – 22.

Lasn, K.; Klauson, A.; Chati, F.; Décultot, D. (2011). Experimental identification of elastic constants of an orthotropic composite plate. In: *Proceedings of 16th International Conference on Composite Structures (ICCS16): 16th International Conference on Composite Structures*, Porto, Portugal, June 28-30, 2011. (Eds.)A.J.M. Ferreira., 2011.

Lasn, K.; Klauson, A.; Chati, F.; Décultot, D. (2010). The determination of mechanical properties of orthotropic composites. In: *Book of Abstracts - XVI International Conference Mechanics of Composite Materials*, 2010, 117.

### Public technical/research reports

Burman, M.; Berggreen, C.; Echtermeyer, A.; Jönsson, D.; Melasani, S.; Anyfantis, K.; Lasn, K. (2014). LiFT – End of Project Report. (<http://www.energiogtransport.net/content/wp-content/uploads/2012/06/Final-report-LiFT-Energy-Transport-submitted-small.pdf>)

Echtermeyer, A.T., Lasn K. (2013). Safety Factors and Test Methods for Composite Pressure Vessels. ([http://www.deliverhy.eu/publications/docs/DeliverHy\\_Report\\_D6.3\\_DEC2013.pdf](http://www.deliverhy.eu/publications/docs/DeliverHy_Report_D6.3_DEC2013.pdf))

**DISSERTATIONS DEFENDED AT  
TALLINN UNIVERSITY OF TECHNOLOGY ON  
CIVIL ENGINEERING**

1. **Heino Mölder**. Cycle of Investigations to Improve the Efficiency and Reliability of Activated Sludge Process in Sewage Treatment Plants. 1992.
2. **Stellian Grabko**. Structure and Properties of Oil-Shale Portland Cement Concrete. 1993.
3. **Kent Arvidsson**. Analysis of Interacting Systems of Shear Walls, Coupled Shear Walls and Frames in Multi-Storey Buildings. 1996.
4. **Andrus Aavik**. Methodical Basis for the Evaluation of Pavement Structural Strength in Estonian Pavement Management System (EPMS). 2003.
5. **Priit Vilba**. Unstiffened Welded Thin-Walled Metal Girder under Uniform Loading. 2003.
6. **Irene Lill**. Evaluation of Labour Management Strategies in Construction. 2004.
7. **Juhan Idnurm**. Discrete Analysis of Cable-Supported Bridges. 2004.
8. **Arvo Iital**. Monitoring of Surface Water Quality in Small Agricultural Watersheds. Methodology and Optimization of monitoring Network. 2005.
9. **Liis Sipelgas**. Application of Satellite Data for Monitoring the Marine Environment. 2006.
10. **Ott Koppel**. Infrastruktuuri arvestus vertikaalselt integreeritud raudtee-ettevõtja korral: hinnakujunduse aspekt (Eesti peamise raudtee-ettevõtja näitel). 2006.
11. **Targo Kalamees**. Hygrothermal Criteria for Design and Simulation of Buildings. 2006.
12. **Raido Puust**. Probabilistic Leak Detection in Pipe Networks Using the SCEM-UA Algorithm. 2007.
13. **Sergei Zub**. Combined Treatment of Sulfate-Rich Molasses Wastewater from Yeast Industry. Technology Optimization. 2007.
14. **Alvina Reihan**. Analysis of Long-Term River Runoff Trends and Climate Change Impact on Water Resources in Estonia. 2008.
15. **Ain Valdmann**. On the Coastal Zone Management of the City of Tallinn under Natural and Anthropogenic Pressure. 2008.
16. **Ira Didenkulova**. Long Wave Dynamics in the Coastal Zone. 2008.
17. **Alvar Toode**. DHW Consumption, Consumption Profiles and Their Influence on Dimensioning of a District Heating Network. 2008.
18. **Annely Kuu**. Biological Diversity of Agricultural Soils in Estonia. 2008.
19. **Andres Tolle**. Hiina konteinerveod läbi Eesti Venemaale ja Hiinasse tagasisaadetavate tühjade konteinerite arvu vähendamise võimalused. 2008.
20. **Heiki Onton**. Investigation of the Causes of Deterioration of Old Reinforced Concrete Constructions and Possibilities of Their Restoration. 2008.
21. **Harri Moora**. Life Cycle Assessment as a Decision Support Tool for System optimisation – the Case of Waste Management in Estonia. 2009.
22. **Andres Kask**. Lithohydrodynamic Processes in the Tallinn Bay Area. 2009.
23. **Loreta Kelpšaitė**. Changing Properties of Wind Waves and Vessel Wakes on the Eastern Coast of the Baltic Sea. 2009.

24. **Dmitry Kurennoy**. Analysis of the Properties of Fast Ferry Wakes in the Context of Coastal Management. 2009.
25. **Egon Kivi**. Structural Behavior of Cable-Stayed Suspension Bridge Structure. 2009.
26. **Madis Ratassepp**. Wave Scattering at Discontinuities in Plates and Pipes. 2010.
27. **Tiia Pedusaar**. Management of Lake Ülemiste, a Drinking Water Reservoir. 2010.
28. **Karin Pachel**. Water Resources, Sustainable Use and Integrated Management in Estonia. 2010.
29. **Andrus Räämet**. Spatio-Temporal Variability of the Baltic Sea Wave Fields. 2010.
30. **Alar Just**. Structural Fire Design of Timber Frame Assemblies Insulated by Glass Wool and Covered by Gypsum Plasterboards. 2010.
31. **Toomas Liiv**. Experimental Analysis of Boundary Layer Dynamics in Plunging Breaking Wave. 2011.
32. **Martti Kiisa**. Discrete Analysis of Single-Pylon Suspension Bridges. 2011.
33. **Ivar Annus**. Development of Accelerating Pipe Flow Starting from Rest. 2011.
34. **Emlyn D. Q. Witt**. Risk Transfer and Construction Project Delivery Efficiency – Implications for Public Private Partnerships. 2012.
35. **Oxana Kurkina**. Nonlinear Dynamics of Internal Gravity Waves in Shallow Seas. 2012.
36. **Allan Hani**. Investigation of Energy Efficiency in Buildings and HVAC Systems. 2012.
37. **Tiina Hain**. Characteristics of Portland Cements for Sulfate and Weather Resistant Concrete. 2012.
38. **Dmitri Loginov**. Autonomous Design Systems (ADS) in HVAC Field. Synergetics-Based Approach. 2012.
39. **Kati Kõrbe Kaare**. Performance Measurement for the Road Network: Conceptual Approach and Technologies for Estonia. 2013.
40. **Viktoria Voronova**. Assessment of Environmental Impacts of Landfilling and Alternatives for Management of Municipal Solid Waste. 2013.
41. **Joonas Vaabel**. Hydraulic Power Capacity of Water Supply Systems. 2013.
42. **Inga Zaitseva-Pärnaste**. Wave Climate and its Decadal Changes in the Baltic Sea Derived from Visual Observations. 2013.
43. **Bert Viikmäe**. Optimising Fairways in the Gulf of Finland Using Patterns of Surface Currents. 2014.
44. **Raili Niine**. Population Equivalence Based Discharge Criteria of Wastewater Treatment Plants in Estonia. 2014.
45. **Marika Eik**. Orientation of Short Steel Fibers in Concrete. Measuring and Modelling. 2014.
46. **Maija Viška**. Sediment Transport Patterns Along the Eastern Coasts of the Baltic Sea. 2014.
47. **Jana Pöldnurk**. Integrated Economic and Environmental Impact Assessment and Optimisation of the Municipal Waste Management Model in Rural Area by Case of Harju County Municipalities in Estonia. 2014.
48. **Nicole Delpeche-Ellmann**. Circulation Patterns in the Gulf of Finland Applied to Environmental Management of Marine Protected Areas. 2014.
49. **Andrea Giudici**. Quantification of Spontaneous Current-Induced Patch Formation in the Marine Surface Layer. 2015.
50. **Tiina Nuuter**. Comparison of Housing Market Sustainability in European Countries Based on Multiple Criteria Assessment. 2015.



51. **Erkki Seinre.** Quantification of Environmental and Economic Impacts in Building Sustainability Assessment. 2015.

52. **Artem Rodin.** Propagation and Run-up of Nonlinear Solitary Surface Waves in Shallow Seas and Coastal Areas. 2015.

